Thermomechanical Processing of Metallic Glasses

Carolina Maria Meylan

Clare Hall

Department of Materials Science & Metallurgy

University of Cambridge

This dissertation is submitted for the degree of Doctor of Philosophy

April 2019

Preface

This dissertation, submitted for the degree of Doctor of Philosophy, is the result of my own work under the supervision of Prof. A.L. Greer in the Department of Materials Science & Metallurgy at the University of Cambridge. This dissertation includes nothing which is the outcome of work done in collaboration except as specified in the text and acknowledgements. I declare that the work described here, or any part of it, is not substantially the same as any that I have submitted or is being concurrently submitted for a degree at the University of Cambridge or at any other University or similar institution. The length of this dissertation does not exceed the prescribed word limit of 60,000 words for the relevant Degree Committee.

Carolina Maria Meylan

April 2019

Thermomechanical Processing of Metallic Glasses

Carolina Maria Meylan

Summary

Depending on its thermal and kinetic history, a metallic glass (MG) of a given composition can show a wide range of energetic states. One central parameter determining the initial state of a glass is the cooling rate used to form it upon quenching from the melt. A faster cooling rate will give rise to a glass of higher energy with a more disordered structure. The energy, structure and properties of a glass can also be modified after glass formation. Through various thermomechanical methods, it is possible to bring the glass either to a more relaxed, ordered state of lower energy – this process is called *relaxation* – or to a more unrelaxed, disordered state of higher energy, a process called *rejuvenation*.

In the present work, the effects of several thermomechanical processing methods were explored on the properties of various MG samples. One well-known method to rejuvenate MGs is by introducing damage through plastic deformation. Here, an infrequently used approach to reach large plastic strains was tested, in which brittle fracture was avoided by deforming samples with a low aspect ratio through uniaxial compression. In this manner, large plastic strains of up to 85% were achieved in La-based MG rods, which led to an average energy increase of ≈670 J/mol, determined by ultra-fast differential scanning calorimetry (FDSC). But for this MG, room temperature (RT) is a relatively high fraction of the glass-transition temperature T_g; thus RT storage led to significant ageing and the deformation-induced energy was found to relax away with time.

Another method studied here was thermal cycling (TC), which is a novel technique to rejuvenate MGs and consists of introducing non-affine thermal strains by cycling between cryogenic and room temperatures. TC was applied to three MG compositions and different aspects were investigated. From elastic bending experiments on a La-based MG ribbon, TC was observed to accelerate the relaxation of anelastic strain. Nanoindentation measurements on a CuZr-based MG plate showed that TC decreased the yield stress, but barely affected the hardness or modulus. Finally, TC was also applied to a Fe-based MG; but for this composition, around 100 cycles were necessary to observe a significant effect, whereas only 5–10 cycles were needed to affect the other two compositions. But for all three compositions, TC was found to target mainly the individual flow units of the MG without affecting much the global structure.

While rejuvenation of MGs is often desired with the aim of improving plasticity, relaxation also has advantages, e.g. it increases thermal stability and hardness. Annealing is the common method for relaxation, but may pose the risk of inducing crystallization. Therefore, there is an interest in relaxing MGs through other means. The application of loading cycles in the elastic regime has been reported to relax MGs. Elastic cycling (EC) by nanoindentation was tested here on a CuZr-based MG and compared directly to annealing. Although EC indeed increased the yield strength of the sample, its hardening effect differed from that of annealing. The obtained results show that EC did not necessarily lead to a more relaxed state of the MG; instead the induced strengthening seemed to be rather due to the build-up of anelastic strains.

Finally, relaxation and rejuvenation of an Au-based MG through annealing was studied by FDSC. Due to its low T_g, storage at RT leads to significant relaxation, which gives rise to a characteristic endothermic sub-T_g peak in the heat flow curve measured by FDSC. This peak corresponds to the disordering of highly relaxed zones in the glass upon heating. This disordering event was analysed here, and its activation energy was observed to depend on the initial energy of the sample. Furthermore, by annealing a heavily aged sample for short times above its fictive temperature followed by fast cooling, it could be successfully returned to a state thermally equivalent to that of a freshly formed glass.

Acknowledgements

I would like to thank my supervisor Prof. A.L. Greer for his continued support, advice and guidance throughout this work. I would also like to acknowledge the financial support of this work by the funding scheme of the European Commission, Marie Curie Actions — Initial Training Networks (ITN) in the frame of the project VitriMetTech — Vitrified Metals Technologies and Applications in Devices and Chemistry, 607080 FP7-PEOPLE-2013-ITN. I am also thankful to the former and present members of the Microstructural Kinetics group (Jiri, Sarig, Yonghao, Nikos, Yurii, Jonathan, Adeline, Lindsay) for their daily support on technical matters and their companionship. Many thanks to all staff of the Department of Materials Science & Metallurgy who assisted me during my studies.

Some parts of the experimental work reported in this thesis were carried out in collaboration with or with the support of several people, whose help I deeply appreciate. I would like to acknowledge the work and help of the following people:

- Dr Jiri Orava, who taught me how to use the ultra-fast differential scanning calorimeter, and supported me with the initial measurements of the La-based and Au-based metallic-glass samples in Chapters 4 and 7,
- Dr Sarig Nachum, who showed me how to carry out experiments on the nanoindenter, and guided me through the initial measurements on elastic cycling by nanoindentation in Chapter 5,
- Dr Yonghao Sun, who showed me the thermal cycling method and supported me with the ribbon bending experiments in §6.3,
- Federico Papparotto, who carried out his Master thesis in Prof. A.L. Greer's research group, and who performed the thermal cycling treatment and nanoindentation measurements on the Fe-based metallic-glass ribbons in §6.4 under my co-supervision,
- Dr Jaroslaw Ferenc and Dr Viktoriia Basykh (Warsaw University of Technology, Poland), who helped me carry out the magnetic hysteresis loop measurements of the Fe-based ribbons in §6.4,
- Prof. Marcel B. Miglierini (Slovak University of Technology in Bratislava, Slovakia), who kindly performed the Mössbauer spectroscopy measurements on the Fe-based ribbons in §6.4,
- Dr Nikolaos T. Panagiotopoulos, who performed X-ray diffraction measurements and the conventional differential scanning calorimetry measurements on the Au-based ribbons in Chapter 7, and

– Dr Yurii P. Ivanov, who observed the structure of the "re-melted" Au-based samples by transmission electron microscopy in Chapter 7.

Finally, I am very grateful to my family for all their support, as well as for continuously offering me their help. I would especially like to thank my husband Jeremy and daughter Emily for always being there for me, for making me laugh and cheering me up, and for helping me stay confident in myself and never giving up.

Table of Contents

1 Introduction to Metallic Glasses

The world of metallic glasses has grown a lot since their first published discovery by Duwez and his students in 1960 [1]: the glass-forming ability of different compositions has been tested, their properties characterized and numerous simulations have been carried out in hope of better determining their structure and behaviour. In spite of their interesting characteristics, and in some respects improved mechanical properties compared to crystalline alloys, they still have limited applications and there has not yet been a strong adoption of these materials in industry. This is mainly due to their effective brittleness and limitation in size, as well as the insufficient understanding of their structure and detailed mechanism of mechanical behaviour.

But thanks to continuous research, more and more glass-forming alloy compositions have been discovered, and a wider range of metallic glasses are now available in the form of bulk (typical dimensions are given in §1.1). In addition, a large variety of glass states can be reached through various thermal and mechanical treatments, thereby creating the opportunity to tailor their properties.

1.1 What is a metallic glass?

Metallic glasses are amorphous, that means, in comparison to crystalline materials, they lack long-range order. To obtain a metallic glass, a metal alloy has to be cooled from the liquid state sufficiently fast to avoid crystallization. Once the melt is cooled below the melting temperature T_m (or, in the case of alloys, below the liquidus temperature $T_{liquidus}$) into the supercooled liquid region (Fig. 1.1), the liquid viscosity (which is a measure of atomic mobility) increases by several orders of magnitude upon decrease in temperature. At the higher temperature range of this state, the atomic mobility is still high enough to allow crystallization, which can be prevented if the cooling rate is fast enough. But at lower temperatures, atomic mobility decreases quickly with decreasing temperature, and crystal growth becomes more difficult. Once cooled below the glass-transition temperature T_g, which experimentally occurs typically at a viscosity of around 10^{12} Pa s [2], the supercooled liquid is frozen and a glassy state is reached. The formed metallic glass is thermodynamically unstable: upon annealing, it relaxes to a denser, less energetic state. Furthermore, the glass is metastable with respect to the crystal, meaning that if enough energy is provided (e.g. by heating it above its crystallization temperature) it will crystallize. It should be

noted that T_g is kinetically defined; if a liquid is cooled more slowly, a lower T_g is reached, whereas a higher cooling rate increases T_g (Fig. 1.1).

The range of quench rates needed to avoid crystallization is now known to be very wide, as least as wide as $10–10^{14}$ K s^{-1}. This critical cooling rate depends on the composition of the alloy. In the early years of research on metallic glasses, only a limited range of alloys with relatively high critical cooling rates were known which could be formed into a glass, and therefore fabrication techniques with rapid cooling were required. The most common technique was melt-spinning, which produces samples in the form of ribbons (Fig. 1.2a) with thicknesses of 10–100 µm. But in the last 20–30 years, a wide range of new compositions requiring lower quenching rates were discovered, and larger samples with a minimum dimension of up to 8 cm [3] can now be produced. Samples with the smallest dimension of at least 1 mm are considered as bulk metallic glasses (BMG). BMG samples are typically produced by casting in the form of rods (Fig. 1.2b). A range of different casting techniques for obtaining BMGs exist; information on these is given in ref. [4].

The critical cooling rate of a composition is determined by its glass-forming ability (GFA), i.e. its resistance to crystallization upon cooling from the liquid. Many attempts have been made to predict the GFA of various systems. A generally good indicator of the GFA is the reduced glass-transition temperature T_{rg}, defined as $T_{rg} = T_g/T_{liquidus}$ [2, 4]. The closer T_g and $T_{liquidus}$ are (i.e. the higher the value of T_{rg}), the easier it is to avoid crystallization and the better is the GFA. Therefore, GFA is

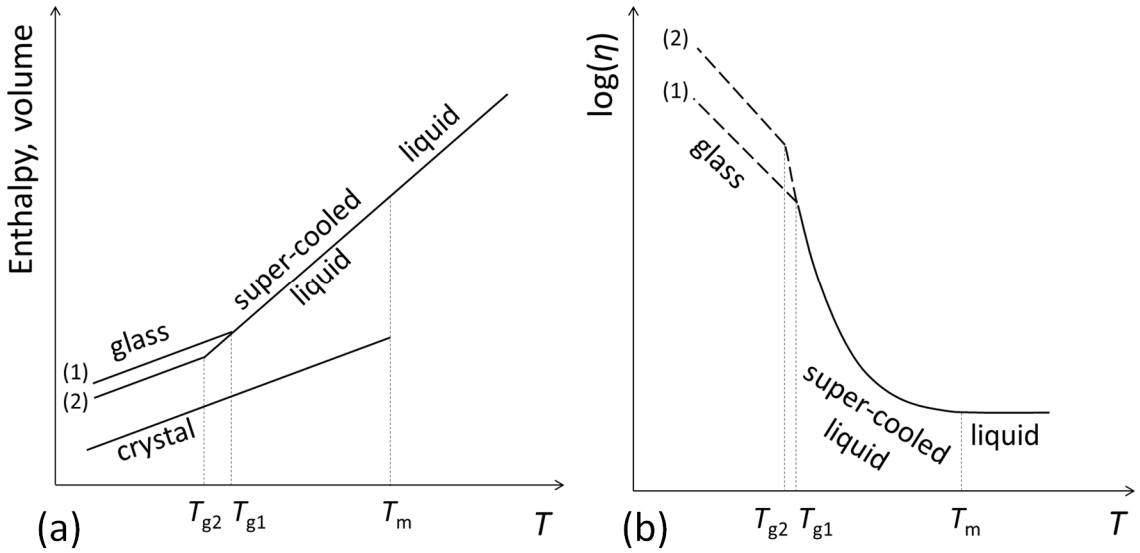

Fig. 1.1. Schematic diagrams of the variation of enthalpy or volume (a) and of liquid viscosity η (b) upon decreasing the temperature T from the liquid state. The glass transition temperature T_g at which the liquid is frozen into a glass depends on the cooling rate: faster cooling (e.g. line 1) produces a glass at T_{g1}, whereas upon slower cooling (line 2) a glass is formed at the lower temperature T_{g2}. Adapted from [5] and [2].

typically good near eutectic compositions [2]. Other guidelines for predicting a good GFA exist, for example the following 'three empirical rules' set by Inoue [6]: (1) the alloy should have three or more elements, (2) the three main constituent elements should have atomic diameters differing by more than 12%, and (3) they should also have negative heats of mixing with each other.

Due to their amorphous structure, metallic glasses present different properties compared to their crystalline counterparts, though this difference varies in scale from one property to another. For example, the density of metallic glasses is in general only 0.5–3% lower than that of their crystalline state [4]. In comparison, the electrical resistivity is around two orders of magnitude higher than that of crystalline metals [4]. The lack of a grain structure can be advantageous: the corrosion resistance tends to be better, and a higher quality of surface finish can be attained, allowing for improved aesthetics [7]. Furthermore, because no grain boundaries (or other microstructural features) are present in metallic glasses, some compositions show excellent soft magnetic properties.

Another attractive property of metallic glasses is their high yield stress σ_y compared to conventional metals [2, 7]. Interestingly, their Young's modulus E (which is typically about 30% smaller than of the corresponding crystal [8]) scales with σ_y, giving a universal elastic strain limit of around 2%, which is considerably larger than for crystalline alloys [9]. Furthermore, amorphous alloys are also known for their high hardness and correspondingly good wear resistance [7]. Metallic

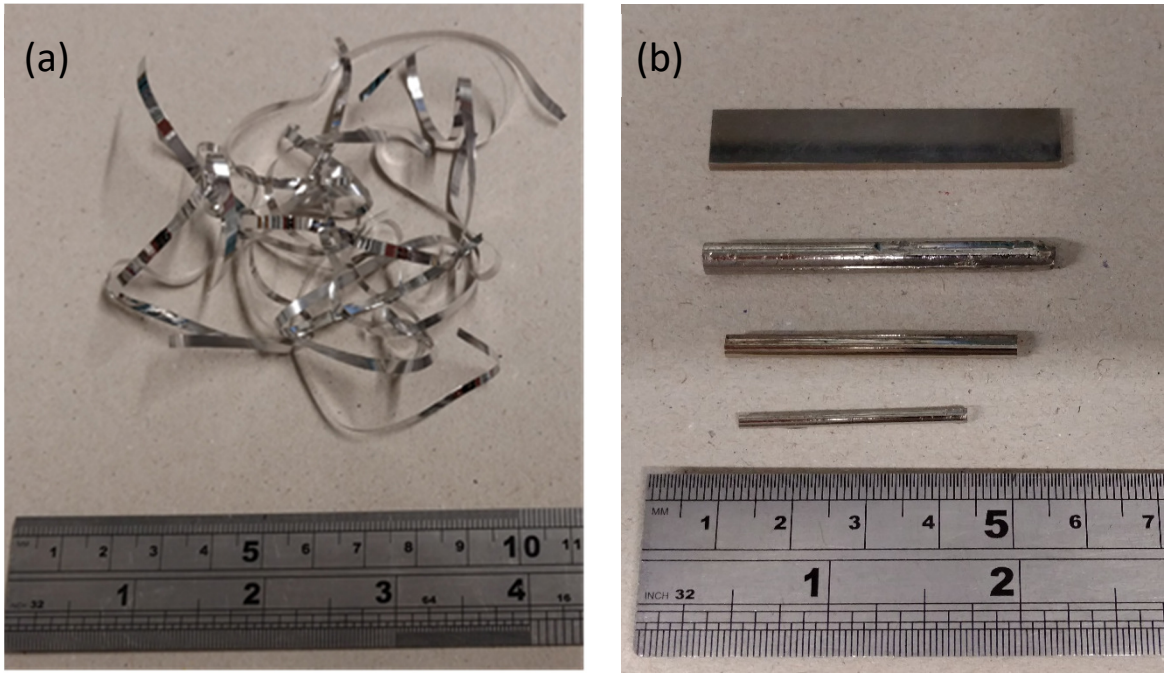

Fig. 1.2. An example of a melt-spun Al-based metallic glass ribbon (a) and various as-cast bulk-metallic-glass samples in the form of rods and a plate (CuZr- and Zr-based) (b).

glasses also have a relatively high resilience (which is the capacity to store and release elastic energy) and low loss coefficient, making them good candidates for elastic energy-storing applications. But a main disadvantage is their low or even non-existent plasticity. Plastic deformation at room temperature usually occurs in highly localized regions called shear bands, which are about 10–20 nm thick [10] and oriented at around 45° to the principal stress axis. This localized flow is associated with shear-softening and can cause the material to break catastrophically. Under tensile loading, the operation of a single shear band often dominates, leading to failure with an effective tensile ductility of nearly zero for the majority of metallic-glass compositions. But when loaded in compression, which is a more constrained loading geometry, the density of shear bands is likely to be higher, and some plastic flow may occur before failure, although it is usually limited to a strain of a few %. Therefore, a lot of research on metallic glasses is focused on increasing the plasticity in tension as well as in compression. The main idea of achieving this is to generate a fine pattern of multiple shear bands, which intersect, branch out and thus avoid the growth of one dominant shear band. This can be achieved by introducing a more inhomogeneous structure of the glass through various treatments (see Chapter 2), or by creating a type of composite, e.g. a metallic-glass matrix with embedded crystalline particle dispersions [2].

Despite their generally low plasticity, metallic glasses do have highly promising properties for certain applications [2, 7, 9]. A wide spread industrial use, which is probably their most significant and which has already been established many years ago, is in the field of magnetism (exploiting their low coercivity and high permeability). Due to the excellent soft-magnetic properties of some metallic-glass compositions, they can be used as transformer cores, sensors, choke coils, actuator yokes, magnetic recording heads or for magnetic shielding [4, 11]. Metallic glasses show also potential for structural applications. For example, because of their high elastic energy storage and low damping, combined with high strength, they are excellent candidates for springs, and have even already been successfully used in golf-club heads. Furthermore, their high hardness and wear resistance is attractive for precision tools, cutting materials or micro-gears. It should also be noted that the possibility of thermoplastic-forming of certain metallic-glass compositions has opened up a large range of potential applications. If a glass has a good GFA, it can be heated above its T_g into the supercooled-liquid region, then plastically formed into complex shapes [12]. In addition, it was found that atomically smooth surfaces can be obtained upon thermoplastic forming [13]. This thermoplastic-forming capability combined with the attractive aesthetics of metallic glasses makes them interesting for jewellery and containers; for example, metallic glasses have already been used for watch and smartphone casings.

1.2 Structure

Because of the lack of periodicity, it is difficult to characterize the structure of metallic glasses. As the glass is in fact a frozen liquid, its structure is inherited from the liquid. Since liquids and glasses have no microstructure and their atomic arrangement seems random (i.e. no periodicity), one might expect the atoms to be arranged homogeneously, with no order. However, metallic glasses as well as other glassy systems and liquids do in fact have a structure [14]. Although glasses and liquids appear disordered in the long-range, they do show some degree of ordering on a more local scale. Progress has been made on determining the short-range order, i.e. at the level of the nearest-neighbour shell, whereas the medium-range order (order over 1–2 nm) still remains poorly understood.

The structure can be described statistically through the pair distribution function (PDF) obtained from Fourier inversion of scattering data [2, 14, 15]. The PDF gives the probability $G(r)$ of finding atoms at a certain distance r from another atom. A typical PDF curve of a metallic glass shows a large first peak, a smaller and broader second peak, followed by progressively smaller peaks. The first peak of the PDF curve provides information on the average distance between nearest neighbours and the average coordination number.

Different structural models for glasses were proposed over the years, ranging from the simplified 'dense random packing' model, which considers a pure metallic liquid to consist of hard spheres of a single size, to more advanced models, which assumed that the atoms are arranged in polyhedral clusters (a brief description of the different models can be found in refs.[2, 14]). Frank

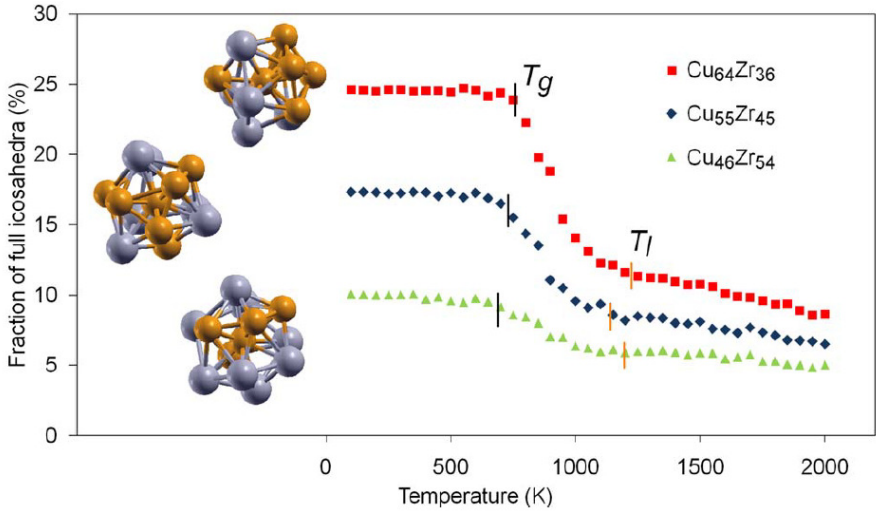

Fig. 1.3. Evolution of the fraction of atoms in Cu-centred icosahedra upon cooling from the liquid for three Cu-Zr compositions, according to molecular-dynamics simulations. The orange spheres correspond to Cu atoms, and the grey to Zr atoms. Reprinted figure from [17], Copyright 2008 by the American Physical Society.

[16] was the first to propose that the nucleation of crystals in supercooled-liquid metals was mainly inhibited due to atoms in the liquid having an icosahedral packing that is incompatible with simple crystal structures. Molecular-dynamics simulations have shown that icosahedra are indeed predominantly present in liquid metals and the fraction of atoms that are in icosahedral clusters increases drastically upon glass formation [17] (Fig. 1.3).

Even though the atom clusters contained in a glassy structure have been relatively well determined now, it is also essential to know how these clusters are ordered on a larger length scale in order to understand the relationship between structure and properties in glasses. It is now a well-accepted view that metallic glasses, and glasses in general, are in fact inhomogeneous, meaning that their structure and therefore also their properties vary from place to place. The length-scales of these variations have been observed to be in the order of 1–2 nm up to several µm [18]. The degree of heterogeneity was found to depend on the composition as well as on the processing history of the glass [19, 20, 21]; furthermore, the presence of heterogeneities seemed to affect some global properties of the sample. For example, an increase in heterogeneity was found to be linked to improved plasticity in some metallic-glass samples [19, 22]. The heterogeneity of glasses is usually visualized as different zones of various densities, degrees of ordering or atomic mobility. Often, the structure is simplified as a composite-like model of 'soft spots', i.e. liquid-like zones of higher atomic mobility, embedded in an elastic, solid-like matrix of lower mobility [23, 24].

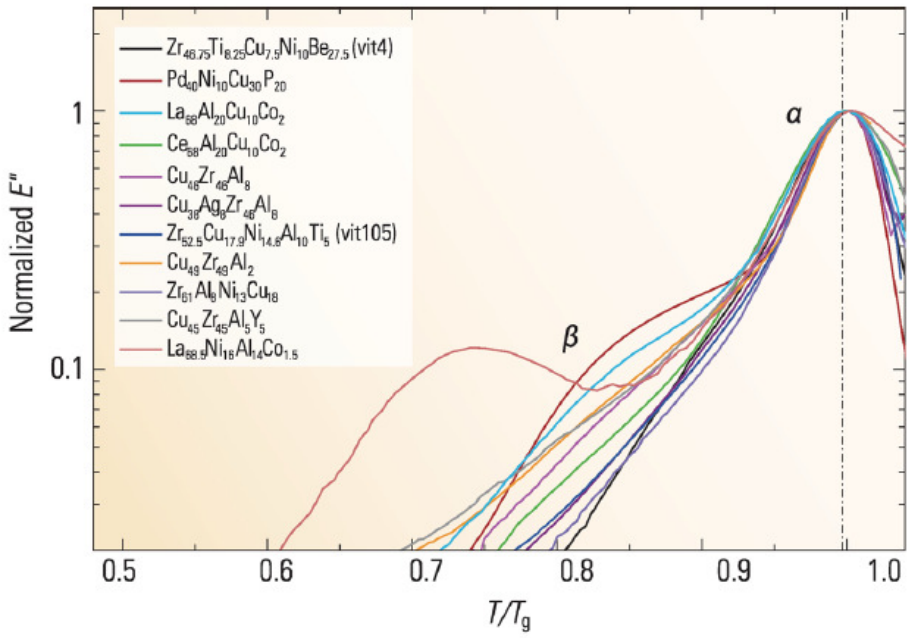

Fig. 1.4. Normalized loss modulus *E*'' as a function of temperature of different metallic-glass compositions, measured by dynamic mechanical analysis. Reprinted from ref.[26] by permission of Oxford University Press.

Several approaches exist to characterize the structural state of the different zones, or of the glass in general [14]. A common approach is the concept of free volume, which is relatively simple and easy to visualize. The free volume of a glass can be considered as the excess volume it has relative to the volume of an ideal glass formed upon infinitely slow cooling. The concept of free volume was originally used to model transport in a liquid of hard spheres [25] and describes well van der Waals liquids. Although the description of metallic liquids through free volume may be, from a physical point of view, inadequate, it remains a useful way to model metallic glasses phenomenologically.

Another important aspect of metallic glasses is their structural evolution with temperature. Two main structural relaxations are commonly observed in metallic glasses, namely the α (primary) and β (secondary) relaxations [26, 27]. The first is connected to viscous flow and the glass transition, whereas the second is related to more localized atom rearrangements. These relaxations are typically observed by dynamic mechanical analysis by measuring the variation of the storage *E*' and loss modulus *E*'' with temperature or frequency. The β relaxation is only, if at all, observed as a shoulder or excess wing of the α peak (Fig. 1.4). Nevertheless, it has attracted a lot of interest, as it seems to be correlated with the mechanical behaviour of metallic glasses [26], especially plastic deformation.

1.3 Mechanical behaviour

Since it is challenging to determine the structure, it is also difficult to understand in detail how deformation occurs in metallic glasses. Even though metallic glasses are in many respects similar to crystalline alloys, the underlying mechanisms of their mechanical behaviour is relatively different, in the plastic as well as in the elastic domain. In crystalline alloys, elastic deformation corresponds to stretching, or compression, of bonds between atoms (like springs), and plastic deformation is due to the movement of dislocations. The yield point can be accurately defined as the moment the shear stresses are large enough to operate the glide of dislocations.

But dislocations do not exist in metallic glasses; plastic deformation instead usually occurs in the form of shear-banding (Fig. 1.5). Although the atomic mechanisms of deformation are not yet well understood, it is generally believed that the fundamental units of deformation are local rearrangement of atoms. Two major models of these local rearrangements are generally considered [8, 29]. In the free-volume model [30], macroscopic flow is based on the occurrence of numerous individual atomic jumps upon the application of an external shear stress (Fig. 1.6a). The

probability that an atomic jump takes place depends mainly on the free volume in the vicinity of that atom. In the second model, local displacement is considered to occur within a flow defect zone consisting of several atoms, commonly called a “shear transformation zone” (STZ) (Fig. 1.6b). The STZ was originally imagined as a thin disc-shaped volume of two rows of 4–6 atoms around a free volume site [31]. STZs are difficult to detect or image, but more recent simulation studies found that, in average, these zones can contain a few tens to a few hundred atoms and have a length-scale of the order of 1 nm [32, 33].

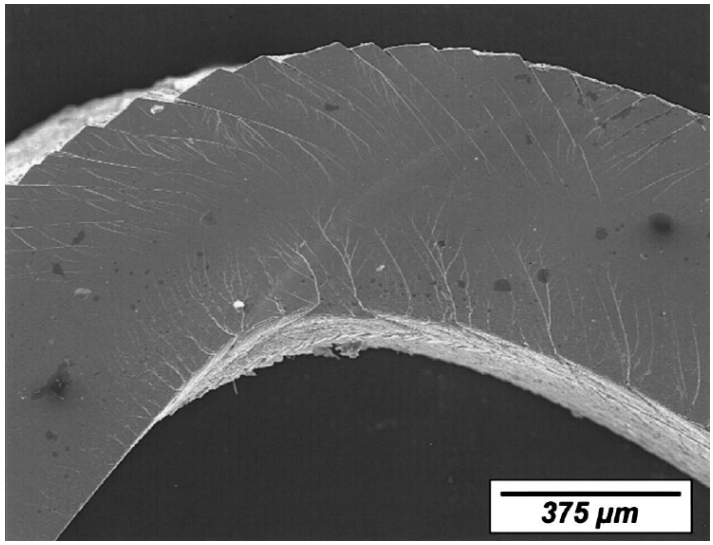

Fig. 1.5. Observation by scanning electron microscopy of shear offsets due to the formation of shear-banding in a plastically bent Zr-based metallic-glass plate of 500 µm thickness. Reprinted from ref.[28], with the permission of AIP Publishing.

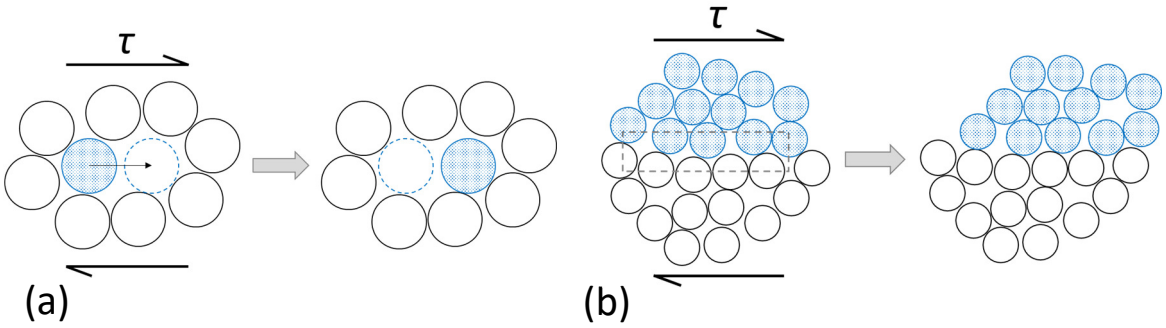

Fig. 1.6. Two-dimensional schematics of local atomic arrangements upon the application of a shear stress τ. According to the free-volume model, macroscopic flow and diffusion occur though individual atomic jumps (a). In the shear transformation zone model, shear is accommodated by a local cluster of atoms, with the upper part of the cluster (atoms in blue) moving with respect to the lower part (b). A shear transformation zone was originally considered to consist of two atom rows around a free volume site (shown as a dashed grey rectangle). Reproduced from [30] and [31].

STZs are considered as the elementary events of plastic deformation in metallic glasses. When the stress increases, more and more STZs are activated; but the distribution in time and location of these zones depend on the temperature and applied strain rate, and therefore different modes of plastic flow can occur [2, 8, 30, 34]. At relatively high temperatures and/or low strain rates, the flow is homogeneous and Newtonian (i.e. viscosity is constant) (Fig. 1.7). In this mode, structural relaxation (ordering) occurs, and cancels out any free volume generated though the local atomic disordering. At lower temperatures or higher strain rates, the flow is still homogeneous but non-Newtonian (i.e. the viscosity decreases with increasing strain rate). Here, the degree of ordering is lower and does not fully annihilate the flow-induced disorder, instead a steady-state level of free volume is formed. Although flow-thinning occurs, catastrophic failure is avoided in this mode. At even lower temperatures and higher strain rates, plastic flow is inhomogeneous; flow is highly localized in shear bands, in which there is a continuous increase in free volume (i.e. decrease in viscosity), leading to even faster localized flow until catastrophic failure occurs.

It should also be noted that although elastic deformation of metallic glasses is macroscopically similar to that of crystalline materials (in the sense that the elastic strain of the sample increases linearly with the applied stress, and returns to zero once the stress is removed), differences do exist on the atomic level. In a simple crystal, all atoms have the same surrounding and the atomic displacements are defined by the macroscopic strain; the elastic strains are in this case affine. But in a glass, each atom has a different surrounding, and the local strain is not necessarily the same for all atoms; the atomic displacements consist of an affine and a non-affine component [8, 35, 36].

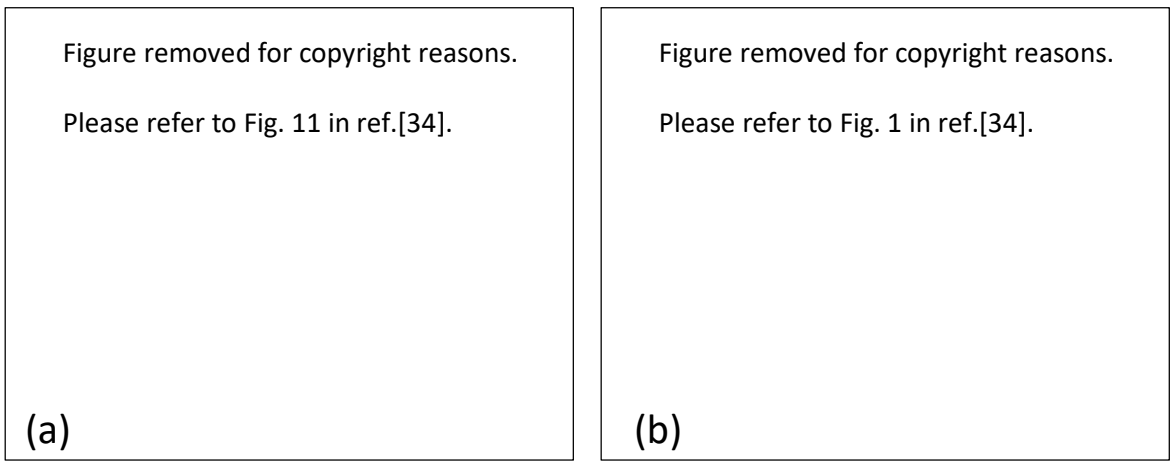

Fig. 1.7. Dependence of flow behaviour on strain-rate and temperature T of a Zr-based BMG (T_g = 623 K) tested under uniaxial compression. Deformation map showing the three flow regimes observed (a): Newtonian homogeneous flow at high T and low rates, non-Newtonian homogeneous flow at lower T and higher rates, and shear localization (inhomogeneous flow) at even lower T and higher rates. Stress-strain curves measured at a strain rate of 10^{-1} s^{-1} at various temperatures (b). From ref.[34].

Even before macroscopic yielding, some local strains may be large enough to lead to an atomic rearrangement (i.e. activation of a STZ) which does not recover fully upon stress removal [36]. These rearrangements were proposed to be the reason for the 30% lower shear modulus of amorphous alloys compared to their corresponding crystalline states [8, 36]. As will be shown in the following chapters (e.g. §2.2), such local atomic rearrangements which lead to a change in structure are the reason why treatments using merely elastic strains can change the properties of metallic glasses.

1.4 Glassy states

Depending on its thermal and kinetic history, a metallic glass of a given composition can show a wide range of energetic states. As already discussed in connection with Fig. 1.1a, the temperature at which a glass forms upon quenching from the liquid depends on the cooling rate. Upon fast cooling, the glass will form at a higher temperature than if cooled slowly, and its energy will correspondingly be higher. Therefore, in principle, a large variety of glassy states can be reached of

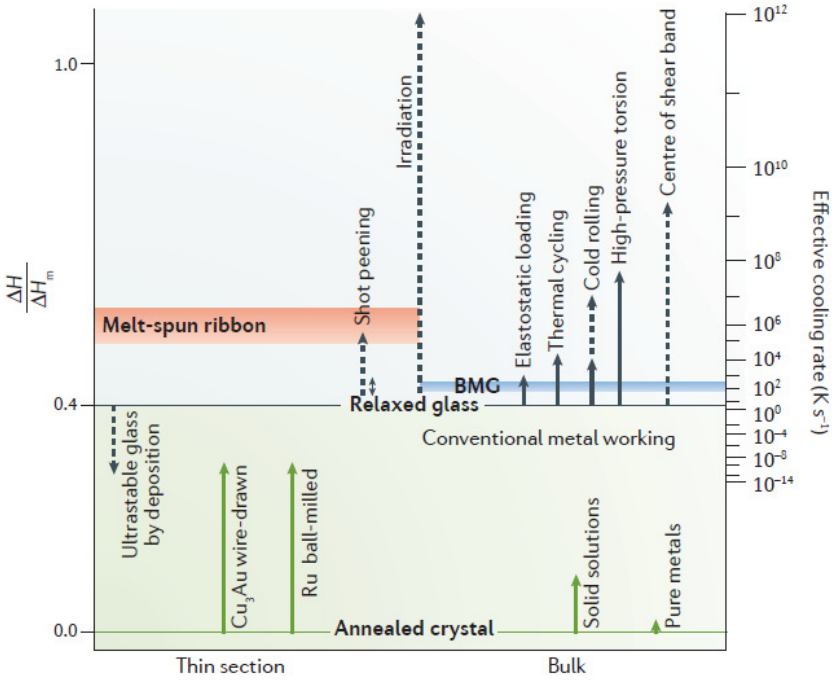

Fig. 1.8. Enthalpy levels ΔH of metallic glasses in different states, normalized to the heat of melting ΔH_m, with an annealed crystalline state taken as the baseline. The arrows indicate the maximum change in energy reported for each treatment type (solid arrows are direct measurements, dashed arrows are estimates). For every value of enthalpy, an effective cooling rate can be estimated, which corresponds to the cooling rate required to form a glass of the same enthalpy from the melt. Reprinted by permission from Springer Nature from ref.[5] Copyright 2016.

various structures and properties simply by changing the cooling rate. But the range of accessible cooling rates can be quite limited, depending on the composition and desired sample dimensions. For example, for a composition of relatively bad GFA, the critical cooling rate will be high, meaning that a glass of this composition can only be achieved in the form of a ribbon with a relatively high energy. On the other hand, if the GFA of a composition is good, a bulk metallic glass can be obtained, but forming a bulk sample implies that the cooling rate cannot be too high, and therefore the produced bulk sample will have a lower energy than if it were melt-spun in the form of a ribbon.

But fortunately, the energy, structure and properties of a glass can also be modified after glass formation. Through various thermal or mechanical methods, it is possible to bring the glass either to a more relaxed, ordered state of lower energy – this process is called *relaxation* – or to a more unrelaxed, disordered state of higher energy, a process called *rejuvenation*. The most common method for relaxing a glass is by annealing, i.e. heating up a glass, typically to a temperature close to but below T_g, for a certain time which can range from several minutes to days or even months. Relaxation is of interest for increasing the thermal stability of a glass (i.e. increasing its resistance to crystallization), as well as increasing its hardness, yield stress, chemical stability and creep resistance [5]. However, the glass generally becomes more brittle upon relaxation, which is especially disadvantageous if the glass is intended to be used as a structural material. Therefore, a large part of research on metallic glasses has been focused on increasing the plasticity. Besides achieving better plasticity by embedding a second (typically crystalline) phase in the metallic glass [37, 38], the plasticity of monolithic metallic glasses can also be improved through rejuvenation. A variety of methods to achieve rejuvenation (e.g. through mechanical deformation, heat treatments, irradiation) have been explored [5], and a range of different increases in energy have been achieved (Fig. 1.8). Through some treatments, it was possible to increase the energy of bulk samples to values equivalent to or even higher than of melt-spun ribbons. However, several treatments, especially those which can induce high degrees of rejuvenation, affect only the surface (such as ion irradiation) or deform the sample drastically (e.g. high-pressure torsion).

1.5 Aim of this work

As mentioned above, there is a high interest in being able to change the properties of metallic glasses through thermomechanical treatments, not only during, but also after glass formation, with the general goal of optimizing the sample's behaviour for a specific application. But studying the effects of various treatments on the structure and properties of metallic glasses is also interesting from a fundamental point of view, in terms of gaining some insight on the underlying mechanisms.

For example, why are some metallic glasses more susceptible to certain treatments than others, or what characteristics does the glass need to have to be affected by a treatment? Furthermore, is there a limit to the degree of relaxation or rejuvenation a metallic glass can be brought to?

In the present work, several thermomechanical processing methods will be explored and their effects on various metallic-glass samples determined by measuring their change in mechanical properties and through thermal analysis. Rejuvenation of metallic glasses is currently highly sought-after in order to improve the plasticity of these materials, and therefore two methods for increasing the disorder in metallic glasses will be explored. The first is through plastic deformation, one of the processing techniques applied earliest to metallic glasses. Upon deformation, local atomic rearrangements create free volume (i.e. disorder). In order to induce plastic strains without catastrophic failure due to shear-banding, the sample has to be mechanically constrained (as is done for example upon cold-rolling). In the present case, high plastic deformation through uniaxial compression will be induced by carefully controlling sample shape and strain rate (Chapter 4).

The second method for rejuvenation studied here is thermal cycling, a recently discovered method, which consists of cycling the metallic glass between cryogenic and room temperatures, and thereby introducing thermal strains. As this method is relatively new, its mechanisms and effects are not yet fully understood and described. Here, thermal cycling will be applied to three different metallic-glass compositions, and its effect on various properties investigated (Chapter 6).

Metallic glasses with high stability also have their advantages. So-called “ultrastable” metallic glasses could successfully be obtained in the literature for some compositions [39, 40], but only in the form of thin films through vapour deposition. The stability of ribbon or bulk samples can be increased (though not to the same degree of stability as ultrastable glasses) by bringing them to a more relaxed and ordered state, which is typically achieved by annealing. But annealing increases the brittleness, and there is also the risk of crystallization if the annealing temperature is too high. Therefore, there is an interest in being able to relax a glass through other means, such as mechanically. One method which was found in the literature to relax metallic glasses is elastic cycling, which consists of applying several loading-unloading cycles to the sample within the elastic limit. This treatment will be applied here and its effects on the mechanical properties will be measured and compared directly to those of annealing (Chapter 5).

As annealing has already been studied since the early years of research on metallic glasses, it seems to be considered nowadays as a basic and conventional technique, which is not the focus of much attention. However, annealing should not be set aside, since it may occur frequently and sometimes even unintentionally, depending on how the metallic glass is stored and for what it is

applied. For example, ageing at room temperature can be quite pronounced if the metallic glass has a relatively low T_g, which is the case for Au-based glasses. In this work, a significantly aged Au-based glass was studied by thermal analysis and compared to a less relaxed sample (Chapter 7).

But first, in Chapter 2, a review will be given of various treatments found in the literature for changing the energetic states and modifying the properties of metallic glasses.

2 Overview of Methods Inducing Relaxation and Rejuvenation

2.1 Plastic deformation

Some typical processing methods for metallic materials which make use of plastic deformation are listed in this section. These methods are usually carried out at room temperature, though it should be noted, as will be seen below, that these processes tend to have a larger effect when performed at lower (e.g. cryogenic) temperatures.

One of the first processes tested on metallic glasses which involves plastic deformation is cold-rolling. This method consists of passing a sample in the form of a ribbon or plate between rolls multiple times and thereby reducing its thickness (Fig. 2.1a). As the sample is mechanically constrained between the rolls, large plastic strains can be introduced in the form of shear bands without leading to fracture of the sample, and thus thickness reductions of up to 97% [41] could be achieved. Cold-rolling was found to increase the energy of metallic glasses [41, 42, 43, 44, 45, 46, 47], which is usually determined by measuring the change in enthalpy ΔH by differential scanning calorimetry (Fig. 2.2). The majority of studies in the literature reported a continuous increase of ΔH with the degree of deformation. However, Cao et al. [41, 44] observed that from around 70–90% thickness reduction on, ΔH of a $Cu_{60}Zr_{20}Ti_{20}$ metallic glass decreased slightly with further deformation when rolling at room temperature. This reduction in ΔH was found to be due to the occurrence of crystallization at high degrees of deformation. But when rolling at 150 K, no crystallization was observed; instead, phase separation took place and the value of ΔH was found to saturate at high strains. Furthermore, even at low degrees of deformation, the increase in energy was higher than when rolling at room temperature (Fig. 2.2). Cao et al. [41] explained these differences due to temperature with the concept of free volume. Upon plastic deformation, local

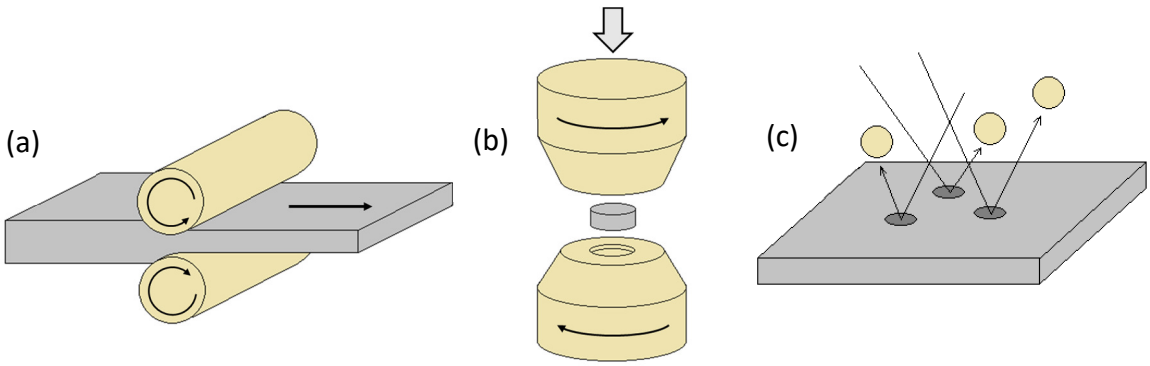

Fig. 2.1. Schematics of cold-rolling (a), high-pressure torsion (b) and shot-peening (c).

atomic rearrangements take place (§1.3) which create free volume. However, annihilation of free volume can also occur, the rate of which increases with temperature and the amount of free volume. At low degrees of deformation, the generation rate of free volume is higher than the annihilation rate, and the net amount of free volume (and therefore the energy of the glass) increases with strain. When rolling to higher degrees of deformation, the annihilation rate increases. At 150 K, a steady state between free volume generation and annihilation is thought to be established, therefore the increase in Δ*H* saturates at high strains. At RT, the annihilation rate is higher than at 150 K, and the induced free volume and energy increase is in general lower. In addition, crystallization was observed at RT at high strains; this caused the annihilation rate to increase even more since free volume is more likely to annihilate at crystal/amorphous boundaries, explaining why the free volume content decreased at high degrees of deformation [41]. Besides the dependence on temperature, Cao et al. [44] also observed that the strain rate during cold-rolling affects the degree of rejuvenation: at higher strain rates, more free volume is created, and therefore more energy is stored in the metallic glass [44].

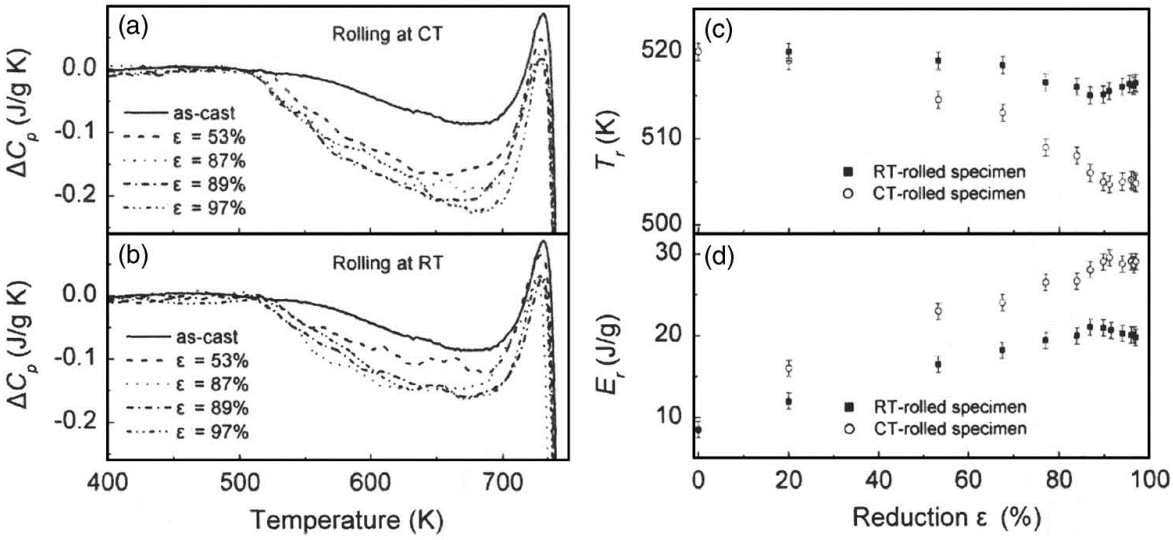

Fig. 2.2. Change in specific heat ΔC_p (= $C_p(T) - C_p(323\ K)$) measured by differential scanning calorimetry of $Cu_{60}Zr_{20}Ti_{20}$ samples rolled at 150 K (a) and at room temperature (b) to various strains ε. The samples present an exothermic peak before the glass transition at T_g = 706 K, which corresponds to the energy released upon structural relaxation. The area between the traces of the as-cast and the rolled samples represents the change in enthalpy Δ*H*. Cold-rolling at 150 K caused a larger increase in Δ*H* than at room temperature. Onset temperature of structural relaxation (c) and energy Δ*H* released during structural relaxation (d) as a function of the reduction in sample thickness at room temperature (RT) and 150 K (CT). Reprinted from ref.[41], with the permission of AIP Publishing.

Cold-rolling was also found to affect several other properties of metallic glasses. For example, tensile testing of Zr-based samples showed a decrease in yield stress and Young's modulus after rolling [48, 49]. In addition, the rolled samples were observed to show apparent work-hardening and up to 0.8% plastic strain [48, 49, 50], whereas the as-cast samples showed catastrophic failure under tensile stress. Cold-rolling was also reported to lead to a decrease in density [46, 49], an increase in Poisson ratio [49] and in heterogeneity of the glass [49, 50], and promoted less serrated flow during indentation [51]. The hardness was also found to be affected; some studies found the hardness to decrease [45, 51], whereas others observed an increase after rolling [49]. This is because rolling induces not only an increase in excess free volume, which should lead to softening of the sample, but also residual stresses, which may cause the hardness to decrease or increase, depending on whether tensile or compressive stresses are introduced upon rolling [47].

Another method to change the properties of metallic glasses is high-pressure torsion (HPT). Severe plastic deformation is induced here by holding a disc-shaped sample between two anvils, then applying torsion to the sample by rotating one anvil at the same time as applying a high pressure of several GPa (Fig. 2.1b). As was the case of cold-rolling, HPT was also found to rejuvenate metallic glasses and increase their energy [21, 52, 53, 54]; however, it should be noted that HPT can induce much higher strains than cold-rolling, and the achievable energy increase is consequently larger.

HPT was also observed to increase the degree of heterogeneity [21] and the disordering of the structure [53, 55]. This disordering, measured by high-energy X-ray diffraction, was found to take place not only at short-range, but to extend to more than 20 Å [55]. In addition, besides the creation of excess free volume, the disordering apparently also introduces "antifree" volume, meaning that local compression as well as dilatation occurs during HPT [55]. Interestingly, the induced structural changes were found to remain even after heating the glass above the glass-transition temperature into the supercooled-liquid region [53]. In addition, the crystallization behaviour was affected: the crystallization mode was modified, and the onset temperature of crystallization was decreased [53, 54].

The changes in mechanical properties after HPT were as expected after rejuvenation of metallic glasses: compression tests showed a decrease in yield stress and an increase in plastic strain [21], and deformation was found to occur more homogeneously, with a reduction in shear localization [21, 52, 54]. Furthermore, the Young's modulus and hardness decreased [52, 54].

Another interesting point is that the degree of rejuvenation achieved by HPT was found to depend on the initial ordering of the metallic glass. Qiang et al. [54] applied HPT to two ZrCu-based

metallic glasses of different Zr/Cu ratios, and observed that the HPT-induced increase in energy and change in properties was larger for the alloy with a lower Zr/Cu ratio, which is the sample with a more ordered initial structure (Fig. 2.3).

A further method which can change the structure and properties of metallic glasses is shot-peening, which consists of bombarding the surface of the sample with beads at high speeds (Fig. 2.1c). In the literature, shot-peening was typically applied to metallic glasses using fused-silica beads of 300–400 µm diameter, accelerated by air pressures of 6–7 bar, for several tens of seconds [56, 57, 58]. It should be noted that shot-peening is a surface treatment, with the affected layer estimated to be in the order of 100 µm thick [56, 57, 58]. Nevertheless, by shot-peening the surfaces of Zr-based bulk-metallic-glass samples, the plastic strain upon bending as well as compression was found to increase, and a more uniform deformation was observed [56]. This was concluded to be caused by the shear bands and compressive residual stresses introduced into the surface layer upon peening [56]. The compressive residual stresses were also found to affect hardness measurements: when indenting the sample on the peened surface, the hardness was found to increase, whereas indentation of the cross-section showed a decrease in hardness after peening [56].

Concerning the energy, shot-peening was found to either relax or rejuvenate the affected surface layer of a Pd-based metallic glass depending on its initial glass state. As-cast samples were found to relax after peening, whereas an increase in energy was observed for pre-annealed samples

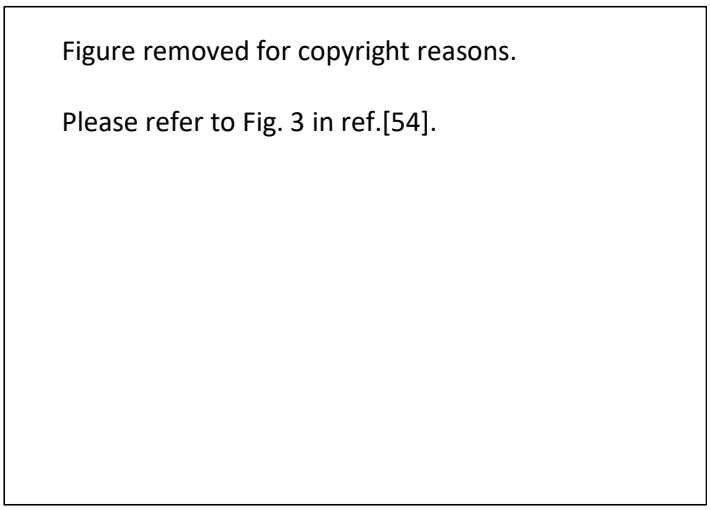

Fig. 2.3. Evolution of the structural relaxation enthalpy ΔH_{rel} upon high-pressure torsion of $Zr_{55}Cu_{30}Ni_5Al_{10}$ (Zr55), $Zr_{65}Cu_{18}Ni_7Al_{10}$ (Zr65) measured by ref.[54] and of $Zr_{50}Cu_{40}Al_{10}$ (Zr50) measured by ref.[52]. The cold-rolling induced increase in energy was found to be higher for the compositions with a lower Zr/Cu ratio, which in their as-cast state are more ordered [54]. From ref.[54].

[57, 58]. Furthermore, the change in energy upon shot-peening, regardless if an energy decrease or increase occurred, was more pronounced at lower temperatures (e.g. 77 K) than at room temperature [58]. This is because upon deformation, there is a competition between the introduction of damage, caused by the deformation, and damage repair through structural relaxation, which is greater at higher temperatures [58].

Rejuvenation of metallic glasses was also observed upon uniaxial compression [59, 60, 61]: by compressing rod-shaped Zr-based samples of low aspect ratios (i.e. height/diameter < 0.5–1) and applying low strain rates in the order of 10^{-4} s^{-1}, large plastic strains of up to 46–80% could be reached without fracture of the sample (whereas samples of a conventional aspect ratio of ≈ 2 broke in a brittle manner after < 1% plastic strain [59]). After deformation, multiple shear bands were observed on the sample surface [59, 61], and the hardness was found to decrease [59]. An increase in the structural heterogeneity of the metallic glass was also measured: while some local areas were rejuvenated, other (though minor) parts were relaxed [60]. Furthermore, the effect on the yield strength and plasticity was studied by He et al. [61]. After pre-compressing their low-

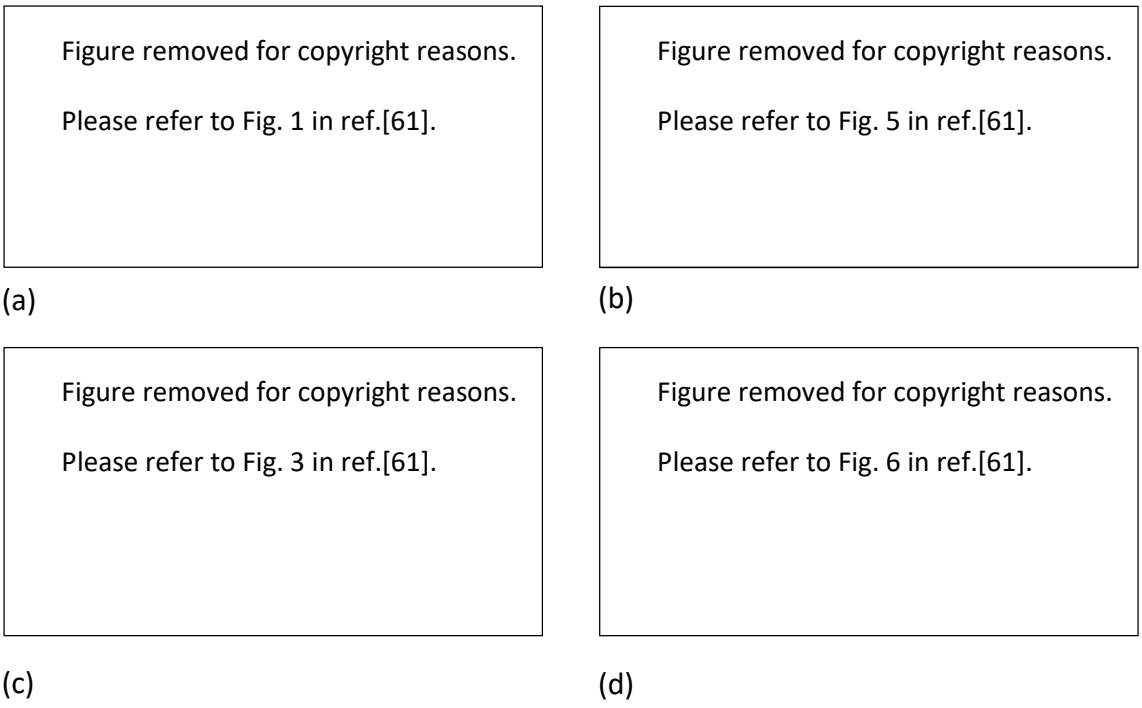

Fig. 2.4. After compressing their low aspect-ratio Zr-based metallic glass rod sample to large strains, He et al. [61] cut a new specimen with a 2:1 aspect ratio from that sample for a subsequent compression test (a). This new specimen contained primary and secondary shear bands introduced during the first compression (b). Scanning electron microscopy images showing the primary and secondary shear bands introduced in the samples compressed to 8%, 29% and 46% plastic strain (panels (a), (b) and (c) in (c), respectively). Stress-strain curves during subsequent compression (d). From ref.[61].

aspect ratio sample to large strains, a new sample was cut from it, this time with a conventional aspect ratio of 2 (Fig. 2.4a). They then applied a subsequent compression to this new sample, which showed a lower yield strength and an increased plasticity compared to the as-cast state (Fig. 2.4d). But they also observed that the orientation of the shear bands induced during pre-compression (Fig. 2.4b) affected the degree of increase in plasticity. After pre-compression to 29% strain, mostly primary shear bands were introduced (Fig. 2.4c). These shear bands were found to facilitate the formation of new shear bands during the subsequent compression because of their similar orientation, which led to a multiplication of shear bands and an increase in plastic strain from 1.1% (as-cast state) to 12.1%. But after pre-straining to 46%, less primary and more secondary shear bands were formed. These secondary shear bands had an orientation far from the direction of the maximum shear stress during the subsequent compression, and a lower plastic strain of only 6% was observed [61].

Instead of using uniaxial compression of low-aspect ratio samples to achieve rejuvenation, Pan et al. [62] could increase the energy of a Zr-based metallic glass by plastically deforming it under tri-axial stresses. By cutting a circumferential notch into the rod-shaped sample and loading the whole under uniaxial compression, the notched region was submitted to a tri-axial stress state, which allowed higher stresses to be reached while avoiding shear-banding. Compression of an un-notched sample induced many shear bands at the sample surface; in contrast, only a few shear bands were observed on the notched sample, and homogeneous plastic flow was concluded to have occurred in the latter case. The increase in energy and decrease in hardness after compression to 40% plastic strain was much larger in the notched sample than in an un-notched one. Especially the root of the notch was found to be strongly rejuvenated: the energy in the root increased by

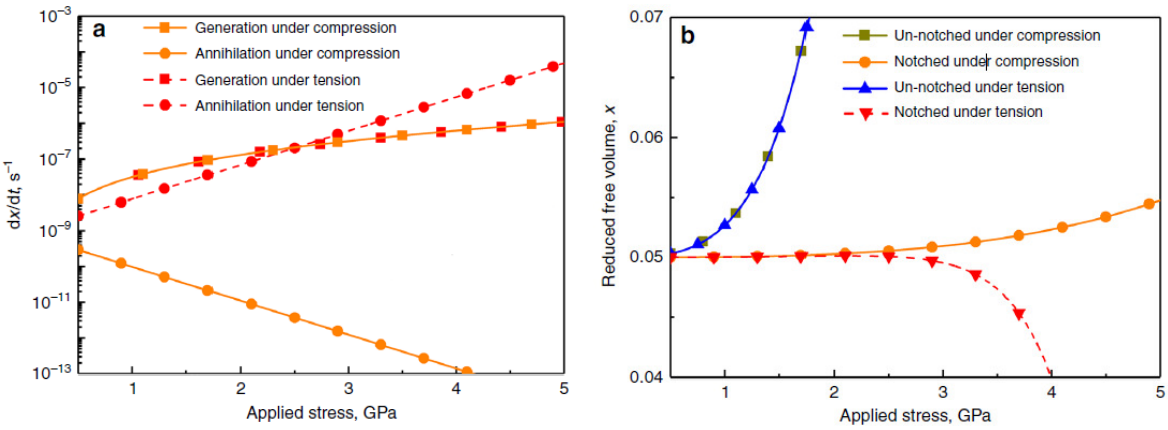

Fig. 2.5. Generation and annihilation rate of free volume under compression and tension in the case of a notched rod (a). Evolution of net free volume of un-notched and notched specimens under compression and tension (b). Reprinted from ref.[62] (https://creativecommons.org/licenses/by/4.0/).

almost 3 kJ/mol, which is larger than any other increase in energy of a macroscopic volume reported so far in the literature (comparable increases in energy were only measured at the centre of shear bands) [62].

Interestingly, relaxation rather than rejuvenation occurred after plastically deforming the Zr-based notched sample under tension instead of compression [63]. Due to the notch, stable plastic flow of up to 10% strain could be reached at room temperature, whereas an un-notched sample broke directly upon yielding when loaded under tension. After tensile deformation, the notched region was found to have a lower energy and higher hardness compared to the as-cast sample. The fact that tensile deformation led to relaxation of the notched metallic-glass sample, and compression led to rejuvenation, can be explained by considering how free volume evolves during deformation [62, 63]. Whereas the generation rate of free volume is the same for compressive and tensile loading, the annihilation rate is faster for the latter (Fig. 2.5a). Although there is a net increase in free volume at the beginning of tensile deformation, from a critical stress on, the annihilation rate becomes larger than the generation rate, and the amount of free volume decreases [63] (Fig. 2.5b).

2.2 Elastic deformation

As mentioned in §1.3, deforming metallic glasses even below their macroscopic yield point can lead to local atomic rearrangements which do not recover fully upon stress removal [36]. These strains that appear elastic at a macroscopic level were found to be able to affect the structural state of metallic glasses and change their properties. A range of methods which led to relaxation or rejuvenation of metallic glasses through elastic deformation have been reported in the literature. One example is elastostatic loading, which consists of applying a static uniaxial load in the elastic regime for a certain period of time. During the compression of rod-shaped bulk-metallic-glass samples for 12 h or more at stresses of around 80–95% of their yield strength, viscoelastic deformation (besides elastic and anelastic) was found to occur, which did not recover after unloading [64, 65, 66, 67]. This plastic flow was homogeneous, i.e. no shear bands were observed. After loading, the metallic-glass samples were found to be rejuvenated: an increase in energy was measured [64, 65, 66, 67, 68], as well as an increase in interatomic distance [67] and a decrease in density [69]. Simulations also showed structural disordering; a fraction of densely packed clusters were found to break down and form new loosely packed clusters [64, 65, 66]. In addition, the mechanical properties also showed changes that are typically related to rejuvenation. Subsequent compression tests revealed an increase in plastic strain of the pre-loaded sample in comparison to

the as-cast state [65, 67] and a decrease in yield strength and Young's modulus [65, 67, 69]. Furthermore, the degree of rejuvenation was found to depend on the initial structural state of the sample. For example, elastostatic loading of the composition $Cu_{65}Zr_{35}$, which has a higher initial packing density than the composition $Cu_{50}Zr_{50}$, led to bigger changes in energy and properties than loading of the latter (Fig. 2.6) [64, 65]. The temperature during loading was also found to play a role: a larger rejuvenation effect was observed when loading at 77 K than at room temperature [68]. This effect of temperature was explained by the fact that there is always a competition between structural disordering (which is induced by the deformation itself) and ordering, which is thermally activated. At 77 K, the rate of ordering is lower than at room temperature, and therefore the net degree of disordering is higher [68].

Besides rejuvenation, elastostatic loading in compression was also found to cause relaxation of metallic glasses [70, 71, 72, 73]. While some studies [70, 73] reported only a 'mechanical annealing' effect (i.e. relaxation), others found a transition between rejuvenation and relaxation, depending on the loading stress and duration [71, 72]. For example, Gu et al. [71] compressed a Zr-based sample for 30–120 min at stresses of 20–80% of its yield strength, and found that longer loading times and higher loads led to relaxation, whereas intermediate times and loads led to rejuvenation. Zhang et al. [72] applied elastostatic compressive loading for 48 h to another Zr-based glass, and observed that there exists a critical stress level (of around 70% of the yield strength), below which relaxation occurs, and above which rejuvenation takes place.

Changes in the properties of metallic glasses, which are usually expected from relaxation, were also observed upon elastic cycling. Packard et al. [74, 75] found that after applying of the order of

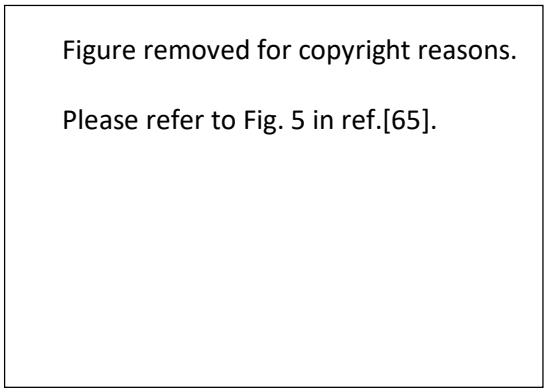

(a)

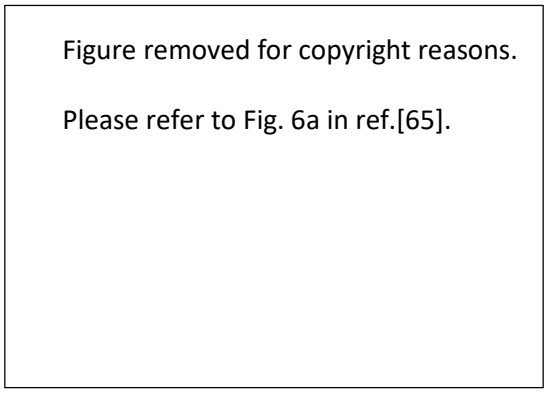

(b)

Fig. 2.6. Evolution of the heat of structural relaxation as a function of elastostatic compression time of $Cu_{50}Zr_{50}$ and $Cu_{65}Zr_{35}$ metallic-glass rods (a). Compression stress-strain curves of as-cast and elastostatically pre-compressed rods in the case of three Cu-Zr compositions (b). From ref.[65].

10 loading-unloading cycles within the elastic regime with a spherical nanoindenter tip, the yield strength (measured upon a subsequent loading cycle) of several metallic-glass compositions increased (Fig. 2.7). But the maximum load applied during the cycling was found to be critical: below a certain threshold value, no strengthening upon cycling was observed [74, 76]. Furthermore, the increase in yield strength saturated after a certain number of cycles [74, 76]. The effect of the loading rate during cycling was also studied: higher rates led to a larger increase in yield strength [76]. It was suggested that the observed strengthening was caused by the back-and-forth activation of local shear transformation zones during cycling, leading to the accumulation of small and permanent structural changes which bring the glass to a state of higher structural order [74, 75].

Molecular-dynamics simulation of cyclic nanoindentation showed consistent results with the experiments by Packard et al. [77, 78]; furthermore, they showed a decrease in excess free volume [78] and increase in elastic modulus [77] after cycling. The simulations also presented evidence that cycling may harden the preferred shear banding path, forcing yield to take place along a secondary path at a higher load [77].

The effect of macroscopic elastic cycling under uniaxial compression was also tested. Caron et al. [79] observed that cycling well below the yield load led to a decrease in the heat of relaxation (i.e. decrease in energy) and caused structural densification; this relaxation was concluded to be due to the accumulation of anelastic strains, which were frozen in during cycling because their

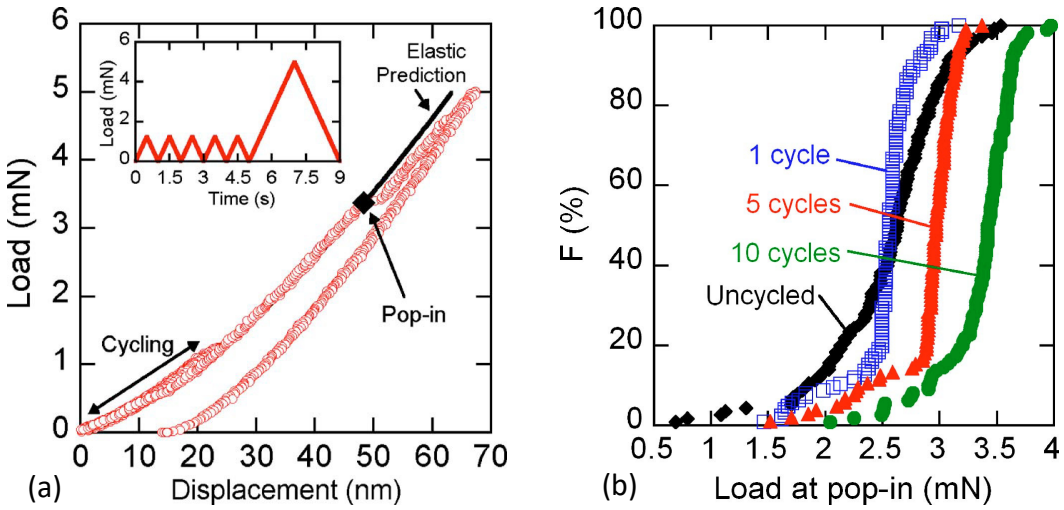

Fig. 2.7. Load-displacement curve of elastic cycling followed by a final loading cycle into the elasto-plastic region by nanoindentation using a spherical tip (a); displacement bursts called "pop-ins" are correlated to the activation of shear events. Cumulative distribution curves of the load at the first pop-in, which corresponds to the yield load, of an uncycled Fe-based bulk metallic glass sample and after 1, 5 and 10 cycles (b). Reprinted from ref.[75], with the permission of AIP Publishing.

recovery times were probably longer than the applied cycling period [79]. Another study measured the change in hardness after macroscopic elastic cycling [80]: the hardness measured on the end face of the sample (i.e. the face on which the uniaxial load was applied) was found to increase by around 8–12% after cycling, which is a similar increase as upon annealing, but the hardness measured on the side surface did not change. Furthermore, the increase in hardness of the end-face was found to decrease again upon room-temperature ageing. In addition, this study observed (in contrast to the results by Caron et al.) an increase in the heat of relaxation. It was concluded, in this case, that the hardening observed after cycling is not due to relaxation of the glass, but to residual stresses [80].

The time after cycling was also found to be critical for elastic cycling by nanoindentation. When introducing a resting time after cycling, a reduced strengthening-effect of the cycling was observed [76]. The importance of time was also investigated for cyclic stress relaxation experiments under elastic strains [81]. With increasing number of cycles, the relaxation rate of stress decreased, which corresponds to an apparent hardening effect. It was hypothesized that upon cycling, deformation units are gradually exhausted, and thereby the internal relaxation process is suppressed. But this was found to be not a permanent effect: when increasing the time intervals between the cycles, deformation units could recover, and the decrease in stress relaxation was reduced.

Another way to excite a material mechanically, within the elastic region, is by ultrasound. In the case of metallic glasses, Ichitsubo et al. [82, 83, 84, 85] investigated the effect of ultrasound during

Figure removed for copyright reasons.

Please refer to Fig. 3 in ref.[85].

Fig. 2.8. Time required for complete crystallization of two Pd-based metallic-glass compositions (a, b) upon isothermal annealing at various temperatures without and with the application of ultrasound. From ref.[85].

heating. At each temperature step, the resonance spectrum was measured by an electromagnetic acoustic resonance technique using frequencies of 300-1500 kHz. At the glass transition, the resonance frequencies abruptly jumped up, as well as the elastic constants. Such drastic shifts were only seen when ultrasound was applied, and XRD measurements confirmed them to be due to nanocrystallization [83]. With the application of ultrasound during heating, crystallization was found to occur at lower temperatures than without ultrasound, and the time required for complete crystallization decreased (Fig. 2.8); furthermore, the crystalline phases formed with the assistance of ultrasound were the same as those formed by mere heating [85]. Ichitsubo et al. also concluded that since the strain energy induced by the ultrasound vibrations is by several orders of magnitude smaller than the thermal energy [82], it cannot help the thermal agitation of atoms and therefore the ultrasound-assisted crystallization must be due to another phenomenon. They proposed that the applied ultrasound frequencies "accidentally match the jump frequency of atoms" [83], allowing them to move to more favourable sites, and thereby change the interatomic potential. Accumulation of such jumps alters the glass structure and facilitates nucleation. It was also concluded that these atom jumps are linked to the β relaxation [84, 85].

An earlier study [86] detected ultrasound-accelerated crystallization as well; in this case a Fe-based metallic glass was subjected to vibrations of 1 MHz at elevated temperatures for several hours. Another example of ultrasonic treatment is given by the work of Wang et al. [87]; in contrast to the above-mentioned studies, they report an effect of ultrasound at room temperature. After exposing a Zr-based bulk metallic glass to 20 kHz vibrations for 48 h at room temperature, the sample remained amorphous, but the average hardness and elastic modulus measured by nanoindentation were found to increase by 14% and 9%, respectively. In addition, they found that the activation energies of the glass transition and crystallization increased, which suggested an enhancement of the thermal stability of the glass [87].

2.3 Thermal methods

The most common method to relax metallic glasses is annealing close to but below the glass-transition temperature T_g. Upon isothermal heating, the glassy structure evolves towards the metastable equilibrium state of the supercooled liquid given by the annealing temperature [2]. This structural change, linked to a decrease in energy, is accompanied by changes of many properties. Examples include an increase in density, Young's modulus, hardness, yield stress, corrosion resistance and viscosity, and a decrease in thermal expansion coefficient, diffusivity and internal friction. Several electrical and magnetic properties (e.g. electrical resistivity, saturation

magnetization, magnetostriction coefficient, Curie temperature) were also observed to be affected by annealing. References to the literature reporting changes in these properties can be found in Table 5 of ref.[2].

The property changes often occur approximately linearly with the logarithm of the annealing time, until, after long times, the metastable equilibrium state is reached, which depends on the annealing temperature. At higher temperatures, the changes take place faster, and the metastable equilibrium is reached sooner than at lower annealing temperatures, but the total degree of change is smaller (as is shown in the case of the Curie temperature in Fig. 2.9).

Because relaxation is a thermally activated process and its rate increases with temperature, no structural change of glasses is expected when storing them at cryogenic temperatures. However, it was found that after quenching magnetic metallic glasses into liquid nitrogen and keeping them at that temperature for several hours, there was an irreversible change in their magnetic properties [89, 90, 91, 92, 93]. This low-temperature treatment decreased the coercive force and the saturation magnetization of several Fe- and Ni-based metallic-glass ribbons. Furthermore, the mechanical properties were also observed to be affected (decrease in the yield stress and slight increase in the elastic modulus [89]) and a decrease in the heat of relaxation was measured [89, 93]. Diffraction and Mössbauer studies found that this treatment changed the short- and medium-range order, and caused homogenisation of the glassy structure [93].

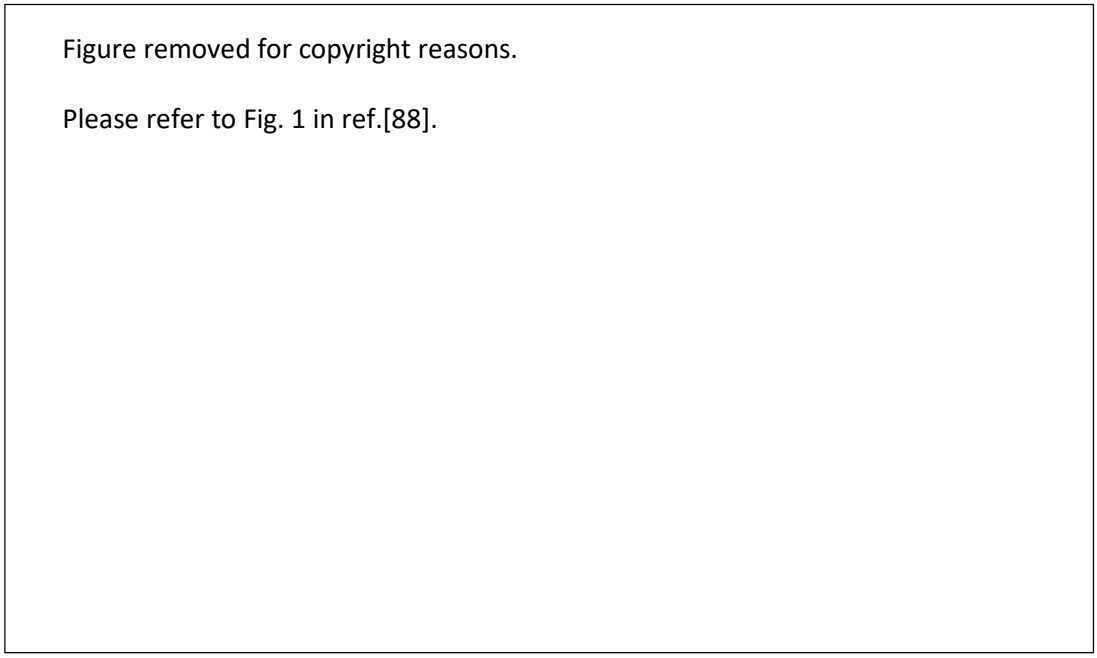

Fig. 2.9. The evolution of the Curie temperature of a $Fe_{80}B_{20}$ metallic glass upon isothermal annealing at various temperatures. From ref.[88].

The observed changes were thought to be due to the high cooling rate upon quenching into liquid nitrogen, which was estimated to be around 10^4–10^5 K/s [90]. This thermal shock was proposed to introduce thermoelastic stresses, large enough to break up the atomic bonds of certain clusters, and thereby cause a reordering of the structure and relaxation of internal stresses. The holding time at liquid-nitrogen temperature also seemed to play a role, as a larger change in magnetic properties as well as heat of relaxation was observed at longer holding times [90, 91, 93].

Besides inducing relaxation, temperature-related treatments were also found to be able to cause rejuvenation. For example, after relaxing a metallic glass by annealing, it was found to be possible to bring it again to a more unrelaxed state through 'recovery annealing' [94, 95, 96, 97]. This thermal treatment consists of heating the metallic glass above the glass transition into the supercooled-liquid region, then cooling at high rates back to lower temperatures, so that a glassy state is reached again. This was first demonstrated by Wakeda et al. [94] through simulations as well as experimentally. They first relaxed a metallic-glass sample by pre-annealing it at a temperature close to the glass transition T_g, followed by cooling at a rate of α_i. They then applied the recovery annealing treatment, i.e. heating to a temperature above T_g, followed by cooling at a rate of α_c (Fig. 2.10). In order to achieve rejuvenation, α_c had to be higher than α_i, and the annealing temperature had to be above a critical temperature T_c, which was in their case around 1.1 T_g. Further work showed that T_c is higher for a lower ratio of α_c/α_i [95]. Besides an increase in energy after recovery annealing, a decrease in hardness, Young's modulus and density were also measured [94, 95, 97].

It should be noted that through recovery annealing, the metallic-glass samples were only rejuvenated with respect to their relaxed states: although their energies were higher than after pre-annealing, they were still lower than of their as-cast states. This is because α_c (which was in the

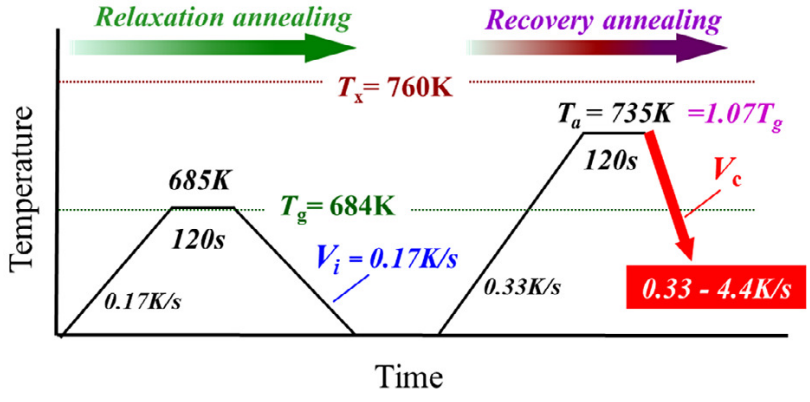

Fig. 2.10. Temperature protocol of recovery annealing, as applied by Saida et al. [95]. Reprinted from ref.[95] (https://creativecommons.org/licenses/by/4.0/).

order of several K/s) was lower than the quench rate $\alpha_{as\text{-}cast}$ needed to form the as-cast glass from the melt. In order to rejuvenate the as-cast glass, α_c would have to have been higher than $\alpha_{as\text{-}cast}$, which is difficult to achieve for many metallic-glass compositions.

A slight variant of recovery annealing was used by Küchemann et al. [98] to rejuvenate a Zr-based metallic-glass sheet; they called their treatment 'flash-annealing'. Using a capacitor discharge technique, they heated the sample through Joule heating at rates of around 10^6 K/s to temperatures above T_g (determined calorimetrically at a heating rate of 40 K/min), followed by "slow" cooling without crystallization (though it should be noted that although they termed their cooling as "slow", it was in the order of 100 K/s, which is much faster than the cooling rates applied for the recovery annealing treatment of Wakeda et al. [94]). After flash-annealing "as-cast" samples (which were apparently annealed for several seconds slightly below T_g after fabrication) to temperatures above 1.05 T_g, an increase in the heat of relaxation of around 515 kJ/mol was observed. Furthermore, flash-annealing was found to narrow the distribution of hardness and Young's modulus values measured by nanoindentation, as well as decrease the average values. Küchemann et al. claimed that, in contrast to recovery annealing, no specific quenching protocol after heating is necessary to obtain rejuvenation, but that the importance lies in the high heating rate [98] (though this was not demonstrated experimentally).

Another thermal method which was found to rejuvenate metallic glasses is thermal cycling. The effect of this treatment was first reported by Ketov et al. [99], who observed that by applying cycles between cryogenic temperatures (e.g. liquid-nitrogen temperature) and room temperature,

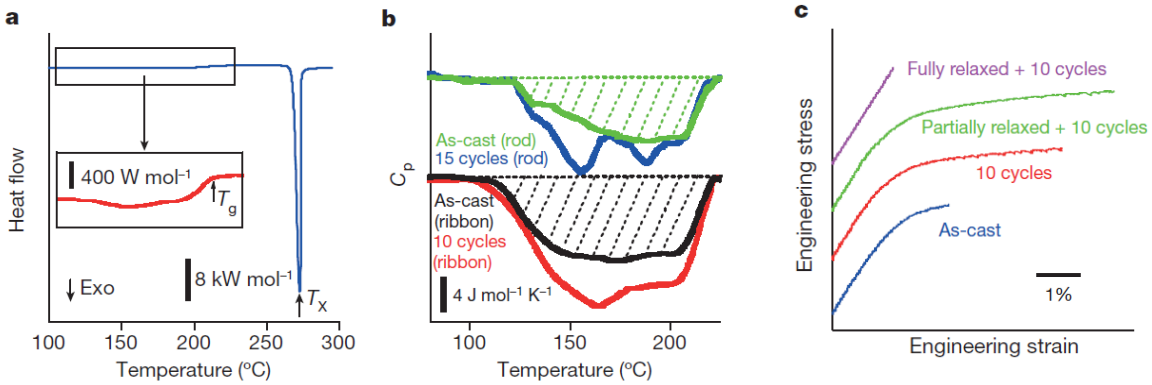

Fig. 2.11. Effect of thermal cycling on the energy and plasticity of metallic glasses observed by Ketov et al. [99]. After cycling of La-based ribbons and rods, the heat of relaxation observable as the exothermic peak before the glass transition step in the heat flow curve (inset in (a)) was found to increase (b). Thermal cycling of as-cast as well as partially relaxed CuZr-based bulk-metallic-glass samples led to an increase in compressive plasticity, but fully relaxed samples were not affected (c). Reprinted by permission from Springer Nature from ref.[99], Copyright 2015.

several metallic-glass compositions could be rejuvenated; their heat of relaxation and their plasticity in compression were found to increase (Fig. 2.11a and b), and the yield stress and hardness measured by nanoindentation decreased [99]. The rejuvenation was interpreted to be caused by non-affine thermal strains, which arise during thermal cycling due to the heterogeneity of metallic glasses [35, 99]. As the structure and many properties, including the elastic modulus, were found to be non-uniform within the glass [18, 100], the thermal expansion coefficient is also expected to differ from one region to another, leading to thermal stresses upon change in temperature.

Since the initial work on thermal cycling of metallic glasses [99], several other research groups have observed changes in properties linked to rejuvenation. Thermal cycling was also found to increase the heat of relaxation of other bulk-metallic-glass compositions which were not studied by Ketov et al., and improve their plasticity [97, 101, 102]. Furthermore, a decrease in density [102], and an increase in impact toughness and fatigue strength [103] were also manifested. On the other hand, thermal cycling was found to barely have an effect on a Ti-based bulk-metallic-glass composite (i.e. amorphous matrix with a dendritic second phase) [104]. By investigating the effect of thermal cycling on three similar metallic-glass compositions ($Zr_{60}Cu_{20}Fe_{10}Al_{10}$, $Zr_{60}Cu_{20}Ni_{10}Al_{10}$ and $Zr_{60}Cu_{20}Co_{10}Al_{10}$), it was found that the result of this treatment can be diverse and depend on the nature of the atomic bonding [105]. The maximum plastic strain under compression was observed to increase upon thermal cycling for the alloy containing Fe, decrease for the one with Co, and was not significantly affected for the sample containing Ni.

In the initial work by Ketov et al., it was proposed that a certain degree of heterogeneity is necessary in order for thermal cycling to have an effect, since rejuvenation induced by cycling was observed for an as-cast as well as a partially relaxed sample (which are probably rather heterogeneous), but not for a fully relaxed (and therefore assumingly rather homogeneous) sample (Fig. 2.11c) [99]. The importance of the heterogeneity of the glass was further demonstrated by Guo et al. [106]. They applied thermal cycling to two metallic-glass samples. Both had the same composition, but their casting temperatures were different. The sample formed from a higher temperature, which was found to have a homogeneous structure, was not affected by the cycling treatment, whereas the sample quenched from a lower temperature and which contained nano-sized clusters did show rejuvenation after cycling.

The effect of thermal cycling has also been tested on the magnetic properties of Fe-based metallic glasses. Ri et al. [107] found the magnetic induction B, coercivity H_c and Curie temperature T_C of $Fe_{78}Si_9B_{13}$ metallic-glass ribbons to fluctuate with increasing number of thermal cycles. This was understood to be due to the competition between relaxation and rejuvenation. However the

overall trend, according to the authors, showed rejuvenation of the Fe-based glass [107]. Another study on $Fe_{80}Si_{8.75}B_{10}Cu_{1.25}$ amorphous ribbons [108] found that thermal cycling led to a "compaction" of the glass, enhancing the thermal stability and soft magnetic properties (i.e. H_c decreased and B increased). But the cycling procedure was slightly different: the sample was also cycled between room temperature and liquid nitrogen, but the holding times at these temperatures were 12 h (instead of 1 min as applied in the work of Ketov et al. [99]), and a maximum of only three cycles were performed [108].

2.4 Other methods

An increase in the energy of metallic glasses is usually correlated with a decrease in density; more unrelaxed glassy states are more disordered and are considered to have more free volume. That this is however not always necessarily the case has been shown through the application of high pressure during annealing on metallic glasses. After applying hydrostatic pressures in the range

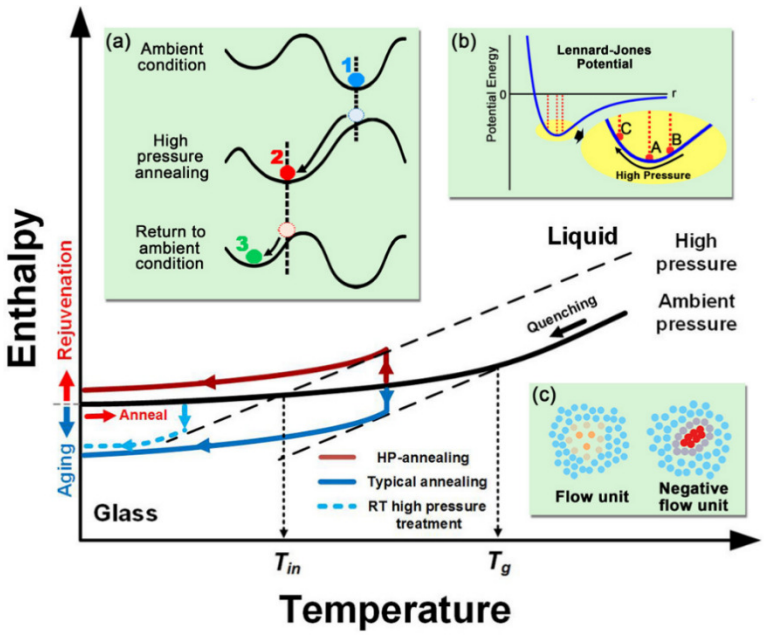

Fig. 2.12. Schematic of the enthalpy vs. temperature plot. Upon annealing at a certain temperature at ambient pressure (as shown by the solid blue line), the glassy state will relax towards the metastable equilibrium state of the supercooled liquid at that temperature (given by the lower dashed black line). If the pressure is increased, the enthalpy line of the supercooled liquid will increase as well (given by the upper dashed line), and will now intersect with the glass line (black line) at T_{in}. If the annealing temperature is between T_{in} and T_g, the enthalpy of the glass will increase in order to reach that of the supercooled liquid, as shown by the red line. Reprinted from ref. [109], with the permission of AIP Publishing.

of 2–5.5 GPa to La-based [109] and Ce-based [110] bulk-metallic-glass samples at temperatures in the range of 0.8–0.99 T_g, the enthalpies of the samples were found to increase by up to around 300 J/mol (in the case of the Ce-based sample) and 900 J/mol (for the La-based sample). The combined application of pressure and temperature was necessary to observe this increase [109]. The treatment time also seemed to play a role: longer times led to a larger increase [110]. The fact that annealing, when performed at high pressures, can cause rejuvenation instead of relaxation was explained in ref. [109] with the enthalpy vs. temperature plot (Fig. 2.12).

But besides an increase in energy, the samples treated to high-pressure annealing showed also an increase in the elastic modulus of around 2–6%, in hardness of around 7%, and in density of around 1% [109, 110]. This degree of change in modulus, hardness and density was found to be

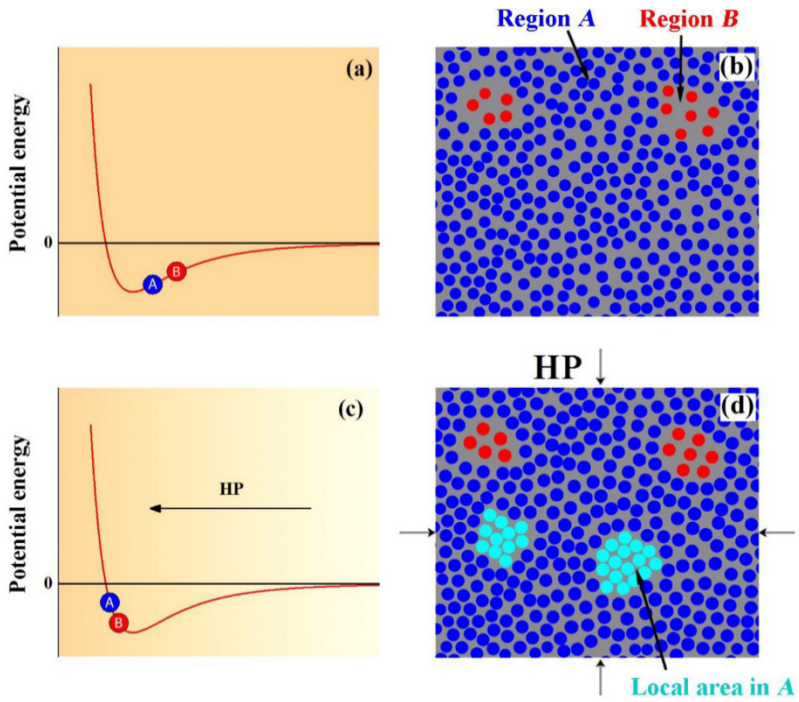

Fig. 2.13. Schematics of the Lennard-Jones-like curve describing the interatomic potential between atoms (a, c) and of the distribution of atoms within the glass (b, d). Blue circles (region A) correspond to denser regions of the glass, whereas red circles (e.g. region B) represent flow units of lower density. Upon annealing at ambient pressure (a, b), mainly regions like B are thought to be affected. The interatomic distances in such regions become smaller, and the energy decreases. At longer annealing times, parts of region A also relax. But if high pressure is applied during annealing (c, d), it is proposed that regions of type A and B relax at the same time; the average distances in both types of region decrease. Some parts of region A (light blue) become much denser than the surrounding regions, and have a higher potential energy. These regions form negative flow units. Reprinted from ref. [110], with the permission of AIP Publishing.

similar to that caused by conventional annealing (which, as expected, led to a decrease in energy) [110]. The fact that high-pressure annealing caused a higher energy as well as a higher density was proposed to be due to an increase in "negative" flow units, which have a higher atomic packing density than the surrounding glass (whereas "normal" flow units have a lower atomic packing density) but also have a higher energy [109, 110], as schematized in Fig. 2.13.

Rejuvenation was also observed upon high-temperature, or 'thermo-mechanical', creep. Tong et al. [111, 112, 113] loaded Zr-based bulk-metallic-glass samples under a uniaxial compressive stress below the elastic limit at temperatures of around 0.8–0.9 T_g for 40 min [111] or several hours [113]. The samples were then cooled under stress and unloaded at room temperature. After treatment, structural studies showed that disordering had occurred and anisotropy had been introduced. In addition, subsequent uniaxial compression tests showed an improved plasticity after treatment. The observed structural rejuvenation was concluded to be caused by the frozen-in anelastic strains. Furthermore, this rejuvenation was found to be an opposing process to structural relaxation induced by annealing: after treating a pre-annealed sample to high-temperature creep, the plasticity of the sample, which had decreased after pre-annealing, was restored to its initial value [111].

Another method which can modify the state and properties of metallic glasses is irradiation with for example electrons, ions or neutrons. Observed changes upon irradiation include a decrease in density, structural disordering, improved ductility, lower strain localization upon compression, suppression of shear-banding and decrease in the yield stress and Young's modulus [114, 115, 116]. In addition, irradiation was also found to be able to restore the bending plasticity of samples embrittled by pre-annealing [117]. These changes are all typical for rejuvenation, but irradiation can also cause relaxation: a shortening of the atomic distances and an increase in yield strength, elastic modulus and hardness were also observed [118]. Furthermore, for some metallic glasses, irradiation was even found to cause nanocrystallization [119, 120].

The effect that irradiation induces depends on the initial state of the sample, the composition of the glass, and the irradiation parameters [117, 120, 121]. For example, molecular-dynamics simulations showed that relaxation or rejuvenation occurred upon irradiation of a Cu-Ti metallic glass, depending on its initial energy [121]: an increase in enthalpy, structural ordering and a decrease in the Young's modulus (i.e. all characteristic signs of rejuvenation) were observed in the case of an initially relaxed sample, whereas the opposite occurred in an initially more unrelaxed sample. Furthermore, by increasing the irradiation dose, both samples were found to converge towards the same steady state [121].

2.5 General comments

As seen in the sections above, a large variety of thermomechanical processes have been applied in the literature to try to modify the structure and properties of metallic glasses, and to obtain a wide range of glassy states.

But naturally, not all methods are easily applied to any type of sample. In fact, many of the mechanical methods mentioned here require the sample to have a specific shape. Cold-rolling, for example, is only possible on ribbons or plates, high-pressure torsion needs the sample to be in the form of a disc, and the large degree of rejuvenation obtained upon compressive loading by Pan et al. [62] was due to the tri-axial stress state, made possible by the circumferential notch applied to the rod-shape sample. Other treatments, such as shot-peening or electron and ion irradiation, can in principle be applied to any sample shape, but affect only the surface of the sample (but it should be noted that surface treatments can affect the macroscopic behaviour of samples; e.g. the compressive plasticity of a bulk-metallic-glass rod was improved by shot-peening of the surface [56]).

An interesting point to consider, when comparing different methods with one another, is their efficiency. By inducing damage through plastic deformation, large energy increases of more than 1000 J/mol could be obtained [41, 44, 52, 62], whereas methods using elastic deformation typically led to changes in energy of only around 200–300 J/mol [66, 68, 72]. But processes using plastic deformation seem to be less efficient than those using elastic strains. In the case of plastic deformation, usually less than 10% of the work done during deformation is stored in metallic glasses [42, 57, 60, 62]. Upon elastic straining, on the other hand, the energy stored in the glass can be considerably higher than the mechanical work done. Greer and Sun [122] estimated the ratio of the increase in energy (defined as the increase in heat of relaxation ΔH_{rel}) to the work done (WD) in the case of elastostatic loading under compression performed in refs.[64, 65, 66, 67], and found that $\Delta H_{rel}/WD > 1$. This ratio was found to be even larger in the case of thermal cycling, which can also be considered as a type of elastic straining method (since the thermal strains introduced upon temperature change are well within the elastic limit): the energy increase of 340 J/mol measured in ref.[99] upon thermal cycling was estimated to correspond to a ratio $\Delta H_{rel}/WD$ of the order of 10^2–10^3 [122]. It is clear that the energy stored in the metallic glass in these cases cannot originate only from the mechanical work done; instead, it was suggested that the disordering processes here are probably endothermic, and energy in the form of heat is drawn into the sample from the surroundings [122].

In the case of several mechanical treatments mentioned in the sections above, the extent by which the glass was modified was found to depend on the temperature or the applied strain rate (Fig. 2.14). Larger effects were observed at cryogenic temperatures than at room temperature in the case of cold-rolling [41], shot-peening [58] as well as elastostatic loading [68]. The induced changes were also larger when using higher strain rates, as was shown upon cold-rolling [44] or elastic cycling [76]. Upon mechanical deformation, there is always a competition between the creation of damage and structural relaxation, which repairs the damage. At higher temperatures and lower strain rates, the atomic mobility is higher, and thus the rate of damage repair is higher, and the net induced damage is lower.

The initial state of the metallic glass also affects the outcome of the applied treatment, as shown schematically in Fig. 2.14. For example, initially more relaxed and ordered glasses experienced a larger rejuvenation effect upon high-pressure torsion [54] and elastostatic loading [64, 65] than glasses which were already relatively unrelaxed. This is because, as explained in ref.[5], the induced changes in structure and properties saturate after long processing times towards a steady state at which the rate of damage introduction is balanced by the rate of structural relaxation. The reached steady state does not depend on the thermal history of the metallic glass but on the applied

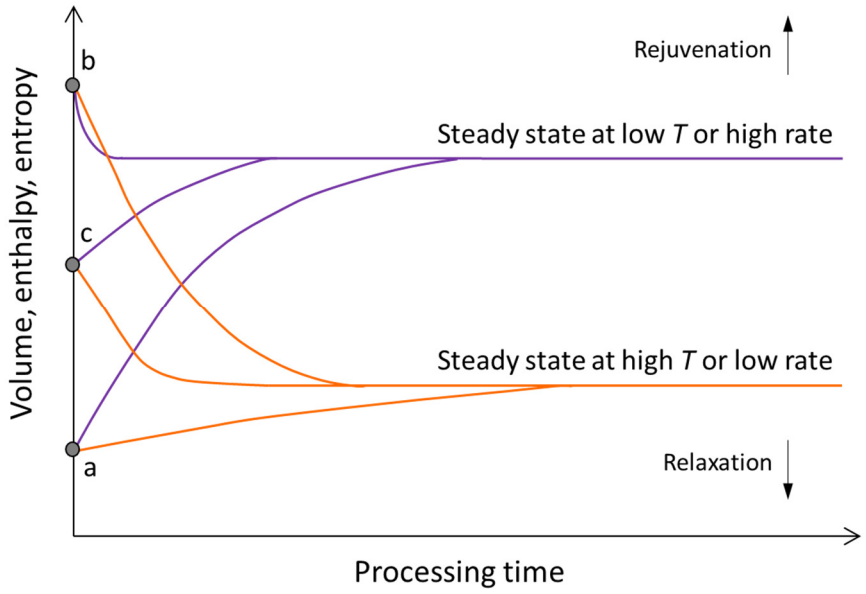

Fig. 2.14. Schematic diagram of the evolution of metallic glasses, depending on their initial energy and on the temperature *T* or strain rate applied during mechanical treatments. If the processing time is long enough, the induced changes will eventually saturate; the steady state thereby reached depends on *T* and the strain rate. The cases of three metallic glasses of different initial energies are shown: glass (a) is initially relatively relaxed, glass (b) unrelaxed, and the energy of glass (c) lies in between those of (a) and (b). Schematic was adapted from ref.[5].

temperature and strain rate. This also explains why some treatments, such as shot-peening [58] and irradiation [121], were found to cause relaxation or rejuvenation, depending on the initial energy of the sample. If the initial energy of the sample is higher than the energy of the steady state, the sample will relax, whereas if the sample has initially a lower energy, it will rejuvenate towards the energy level of the steady state.

The importance of the initial sample state was also shown in the case of thermal cycling, though here, not the energy was suggested to be critical, but the structural heterogeneity. As mentioned in §2.3, a certain degree of heterogeneity was found to be required in order for rejuvenation to be observed [99, 106].

Finally, when measuring the change in properties caused by a treatment, attention should be paid to the additional effect of residual stresses, which can build-up during deformation. For example, rejuvenation is often correlated with an increase in excess free volume, which is expected to lead to a decrease in hardness. However, upon cold-rolling in ref.[47] and elastic cycling in ref.[80], an increase in hardness was measured even though the energy increased as well; this apparent hardness increase was concluded to be caused by residual stresses [47, 80].

3 Experimental Methods

An overview of the metallic-glass compositions studied and experimental techniques employed are given below in §3.1. Two methods, nanoindentation and ultra-fast differential scanning calorimetry (FDSC), were extensively used in this work, and a more detailed description of them is provided in §3.2 and §3.3.

3.1 Overview of general methods

3.1.1 Sample compositions

Experiments were performed on the following metallic-glass compositions (given in at. %):

- $La_{55}Ni_{20}Al_{25}$: Rods (of 2 mm diameter) and ribbons (with an average thickness of 30 µm) were used. This composition was chosen for exploring rejuvenation by plastic deformation in Chapter 4, because it has a relatively low yield strength compared to other compositions, making it easier to deform to large plastic strains. Furthermore, its glass transition, crystallization peak and onset of melting are within the temperature limits of the ultra-fast differential scanning calorimeter (FDSC) used to characterize the sample after compression. This composition was also used in §6.3 to study the effect of thermal cycling on the recovery of anelastic strain due to its relatively low glass-transition temperature and Young's modulus. The $La_{55}Ni_{20}Al_{25}$ samples were kindly provided by the group of Prof. W.H. Wang (Institute of Physics, Chinese Academy of Sciences, Beijing, China).
- $Cu_{46}Zr_{46}Al_7Gd_1$: A sample of this composition was cut from a plate (thickness of 2 mm), kindly provided by the group of Prof. W.H. Wang (Institute of Physics, Chinese Academy of Sciences, Beijing, China). This sample was used for studying the effect (and combined effects) of elastic cycling, thermal cycling and annealing on the mechanical properties measured by nanoindentation in Chapter 5 and §6.2. This composition was chosen for these experiments because it can be formed as a bulk glass, making it convenient to manipulate during the various treatments without damage. In addition, this composition is relatively easy to polish to a surface finish good enough for nanoindentation measurements. Furthermore, the possibility of rejuvenating this glass by thermal cycling was already demonstrated in the literature [99].

- $Fe_{73.5}Cu_1Nb_3Si_{15.5}B_7$: Amorphous ribbons (19 µm thick) of this composition were kindly provided by Vacuumschmelze GmbH (Germany). The effect of thermal cycling was tested on this ribbon in §6.4. This composition is commercially available and of interest for current industrial applications due to its soft-magnetic properties. Fe-based glasses are often thermally annealed to relax internal stresses in order to minimize the coercivity; this however also severely embrittles the glass. There is therefore an interest in finding a method (maybe thermal cycling?) which can relax stresses without causing embrittlement, or which can increase again the plasticity.

- $Au_{49}Cu_{26.9}Si_{16.3}Ag_{5.5}Pd_{2.3}$: Two metallic-glass ribbons, of 16 µm and 40 µm thickness, were used in Chapter 7. They were kindly provided by the group of Prof. J. Löffler (ETH, Zurich, Switzerland) and by K. Georgarakis (SIMaP, Grenoble INP, France). Information on the thermal histories of both ribbons can be found in §7.2.1. This composition is well suited for FDSC measurements, because as it has a relatively low melting temperature and critical cooling rate, it can be melted and even vitrified again upon cooling in the FDSC. FDSC is a relatively new technique, and so far a large part of the published research using FDSC, in the domain of metallic glasses, was on studies of this composition.

3.1.2 Sample treatments

A list of the sample treatments applied in this work is given below:

- *Annealing*: Annealing for several hours (as performed in Chapter 5) was performed in a furnace in air. Shorter annealings were carried out using conventional or ultra-fast differential scanning calorimeters, as used to anneal the Fe-based ribbon in §6.4, Fig. 6.14 and the Au-based ribbon in §7.3.2.

- *Elastic cycling*: This mechanical treatment was performed by nanoindentation; experimental details are given in §5.2.3.

- *Thermal cycling*: This treatment was performed as in ref.[99]. Metallic-glass samples were encased in wire baskets, then dipped into a dewar filled with liquid nitrogen (77 K). After 1 min, the samples were taken out of the dewar, brought back to room temperature with an air blower and kept at room temperature for 1 min. This was repeated until the desired number of cycles was reached. After thermal cycling, the samples were cleaned with acetone.

- *Compression*: A compression test was used to induce large degrees of plastic deformation in La-based metallic-glass samples in Chapter 4. Details on the equipment and compression

procedure are given in §4.2.1. The displacement of the cross-head was measured, and therefore the compliance of the machine had to be first defined (by performing a separate compression test without any sample) and then used to correct the load-displacement curves of the sample.

- *Bending*: In order to study the strain relaxation behaviour of La-based ribbons in §6.3, elastic strain was imposed to the ribbons by bending them, under different conditions, around mandrels for several minutes. Detailed information on this treatment is given in §6.3.2.

3.1.3 Characterization of structure and properties

The effect of the treatments on the metallic-glass samples was mainly determined by measuring the change in mechanical properties and by thermal analysis.

The mechanical properties were measured by nanoindentation, which is a non-destructive technique, where only the surface (up to less than 1 μm deep in the case of the measurements performed here) is affected. This means that the properties of a single sample can be measured multiple times, and after undergoing multiple treatments. A description of this technique and its experimental parameters applied can be found in §3.2.

Thermal analysis was performed by differential scanning calorimetry (DSC). Two types of DSC were used here: 'conventional' DSC (CDSC), as well as the recently commercialized ultra-fast DSC (FDSC). The latter was extensively used for the experiments in §4 and §7, because fast heating and cooling rates are available and only a small sample weighing up to several μg is needed for this technique. Therefore many experiments could be performed on the limited amount of samples available, within a relatively short time. A description of DSC in general is given in §3.3.1. Section §3.3.2 provides the experimental parameters used for the CDSC measurements, and detailed information on FDSC can be found in §3.3.3–§3.3.7.

Structural characterization by X-ray diffraction (XRD) was occasionally performed in order to verify that the metallic-glass sample remained amorphous after the treatment. XRD was carried out on a Bruker D8 instrument, using Cu Kα radiation (1.54 Å wavelength).

3.2 Nanoindentation

3.2.1 Introduction to nanoindentation

Information on nanoindentation mentioned in this and the following sub-sections (§3.2.1–§3.2.5) can be found in refs. [123, 124, 125].

The principle of indentation methods is to indent the material to be tested with another material of known properties. If the indenter material is harder than the material to be tested (which is the aim of indentation tests, and therefore diamond is usually chosen as indenter material), an imprint will be left on the latter. By knowing the force applied during indentation and measuring the size of the residual imprint, the hardness of the unknown material can be determined.

Hardness is commonly measured by macro- or microindentation tests, during which a fixed load in the range of several N (in the case of microindentation) up to kN (in the case of macroindentation) is applied for a fixed time, of typically several seconds, onto the indenter. This leads the indenter to penetrate the sample to depths of several µm to mm, leaving a residual impression which can be determined visually by an optical microscope once the load is removed. The shape of the indenter is usually pyramidal (e.g. for Vickers and Knoop tests), spherical (for Brinell test) or conical (for Rockwell test).

In the case of nanoindentation, the applied force is of the order of mN, and the indentation depth is in the range of nm up to several µm. The residual impression is therefore too small to be measured optically in a convenient and accurate manner. Instead, the area of the impression has to be defined indirectly, by first measuring the indentation depth of the indenter, from which the area of contact can then be derived. Furthermore, nanoindentation is an instrumented indentation testing technique, meaning that the indentation depth is continuously recorded during the application and removal of the load, and a load-displacement curve is correspondingly obtained from the measured data. This means that besides the hardness, the elastic modulus can also be determined from this testing method.

Nanoindentation tests are typically carried out with spherical, conical or pyramidal indenters, with the three-sided pyramidal Berkovich indenter being the most commonly used. The advantage of pyramidal and conical indenters is their geometric similarity, meaning that the ratio of the diagonal of the area of contact (in the case of pyramidal indenters, or the radius of circle of contact for conical indenters) to the indentation depth is a constant, and therefore the applied strain is independent of the load. This is not the case for spherical indenters, for which the measured hardness value depends on the applied load. But the advantage of spherical indenters is that a low

contact stress is obtained at the beginning of the loading procedure, which produces a purely elastic deformation of the sample. At higher loads, the deformation transitions from elastic to elastic-plastic, and a yield stress can be determined from this transition point.

Since nanoindentation probes only up to several µm of material, it is a suitable method to measure the mechanical properties of samples that are small or thin (such as coatings or thin films), as well as to determine the effects of surface treatments. In addition, nanoindentation is a non-destructive technique, and thus the properties of a single sample can be measured before as well as after a treatment. This is important for characterizing metallic glasses, since their structure is susceptible to many factors (cooling rate upon glass formation, thermal history etc.), thus the properties of one sample can differ from another, even if the composition is the same. It is therefore advisable to define the effect of a treatment by comparing the states of the same sample before and after the treatment.

3.2.2 Nanoindenter instrument

As nanoindentation deals with relatively low indentation displacements, any vibration, thermal variation or acoustic noise may affect the measurement. Therefore, the nanoindenter equipment is normally enclosed in a cabinet, as shown in Fig. 3.1 in the case of the MTS Nanoindenter XP,

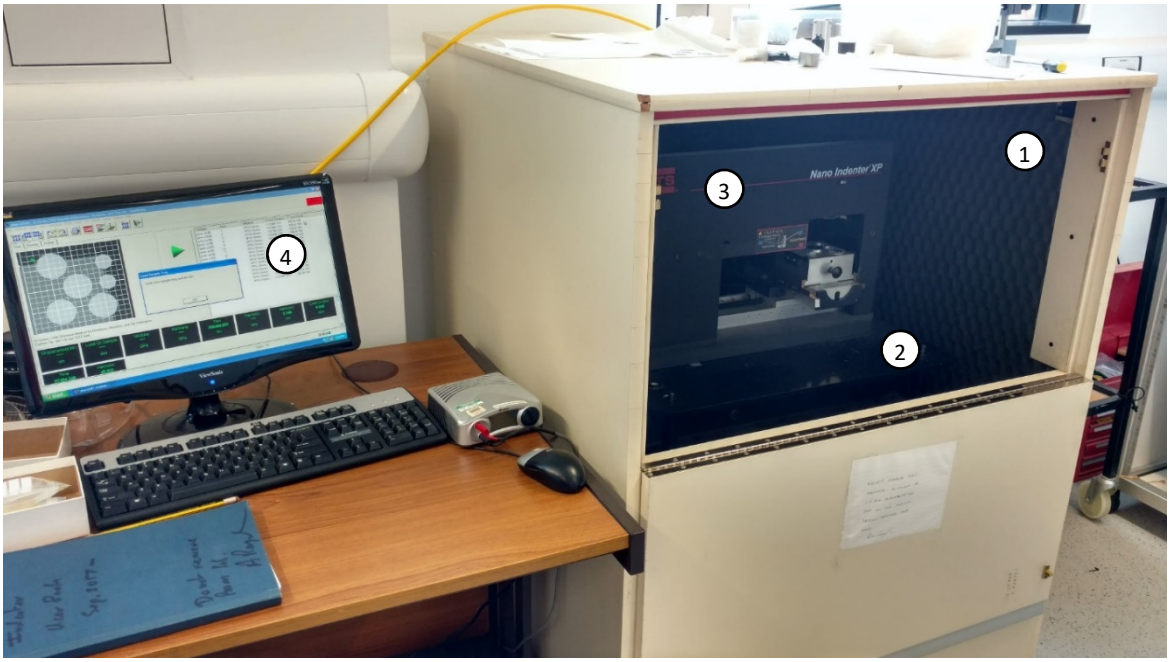

Fig. 3.1. MTS Nanoindenter XP set-up: vibration isolation cabinet (1), vibration isolation table (2), nanoindenter (3), computer linked to the nanoindenter with specific nanoindenter software (4).

which was the instrument used for the experiments in this thesis, and set up on a suspended vibration isolation table.

The MTS Nanoindenter XP consists of the nanoindenter "head" and the sample stage (Fig. 3.2a). The head contains the force actuator, the displacement measurement system, the indenter shaft and an optical microscope objective (of a 10× or 40× magnification).

The MTS Nanoindenter XP is a load-controlled machine, like most nanoindenters. The load is typically applied via an electromagnetic coil to the indenter, which is mounted onto the indenter shaft. When applying current through the coil, a magnetic field is generated which interacts with the magnetic upper end of the indenter shaft, thereby moving it towards or away from the sample. The applied force is not measured directly, but instead derived from the current applied to the coil (i.e. the force is in theory proportional to the current). The displacement of the indenter is commonly measured with a capacitance gauge. In the case of the MTS Nanoindenter XP, a three-plate capacitor is used, with holes in the centre of the plates in which the indenter shaft sits. The two outer plates are fixed to the nanoindenter head. The inner plate is attached to the indenter shaft, and moves vertically along with the indenter during indentation. This movement of the inner plate with respect to the outer ones creates a change in capacitance, which is measured and from which the indenter displacement is calculated.

The sample stage (Fig. 3.2b) of the MTS Nanoindenter XP contains six sample positioning holes, into which sample holders can be clamped. Samples are either attached to sample holders with mounting wax or glue, or mounted in resins of the right shape and size. The sample stage can be moved laterally by linear screw drives. The minimum step size of this movement is usually smaller than 0.5 µm.

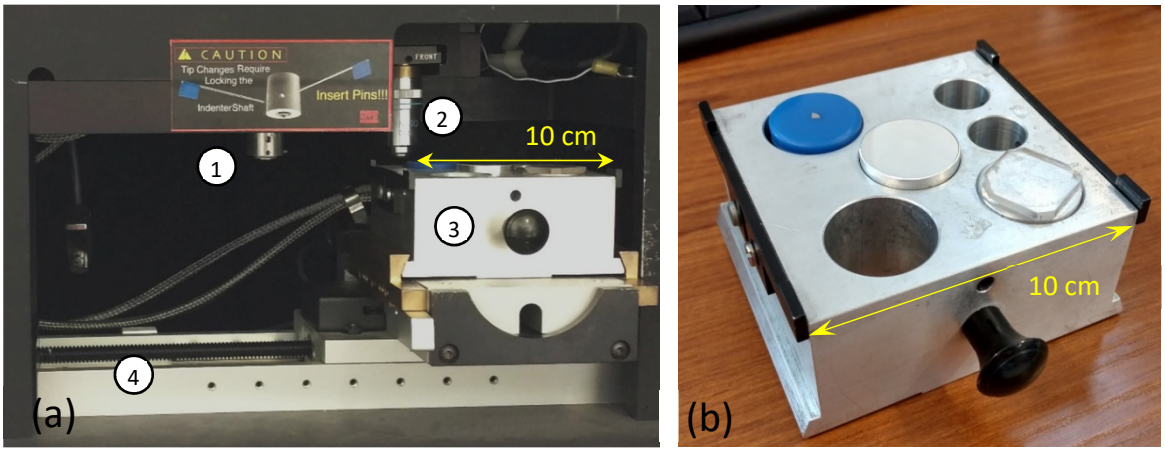

Fig. 3.2. Close-up view of the nanoindenter (a): the head contains the indenter shaft (1) and a microscope objective (2), the sample stage (3) can be moved laterally by linear screw drives (4). Samples are attached to sample holders and clamped onto the sample stage (b).

The movement of the sample stage, as well as the set-up of the experiments, is controlled via the nanoindenter software on the linked computer. For the experiments performed in this work, the software TestWorks 4 was used. The sample surface can be observed in the software through the optical microscope objective attached to the nanoindenter head, and the position of the indents subsequently defined.

Below is a list of some specifications of the MTS Nanoindenter XP used for the experiments performed in this work:

- Maximum indentation depth: 500 µm
- Maximum load: 500 mN
- Displacement resolution: <0.01 nm
- Load resolution: 50 nN
- Accuracy of indentation position: 1.5 µm

3.2.3 Determination of mechanical properties from nanoindentation measurements

This section deals with the determination of mechanical properties from measurements using a spherical indenter tip. The information below was taken from refs.[124, 126, 127].

If a purely elastic contact is considered between a rigid spherical indenter and a flat surface (Fig. 3.3), Hertz found that the radius of the circle of contact a is related to the load F applied to the indenter by [124]:

$$a^3 = \frac{3}{4}\frac{F \cdot R}{E_r} \tag{3.1}$$

where R is the indenter radius and E_r the indentation modulus, which combines the elastic modulus of the sample E_{sample} and of the indenter $E_{indenter}$:

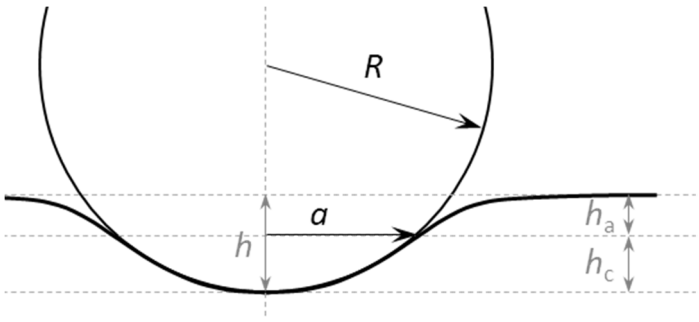

Fig. 3.3. Schematic of contact between a rigid spherical indenter of radius R and a flat sample surface. a is the radius of the circle of contact, h the total indentation depth, h_a the distance from the free surface to the circle of contact, and h_c the contact depth. Schematic was adapted from [124].

$$\frac{1}{E_{\mathrm{r}}} = \frac{1-\nu_{\mathrm{sample}}{}^{2}}{E_{\mathrm{sample}}} + \frac{1-\nu_{\mathrm{indenter}}{}^{2}}{E_{\mathrm{indenter}}} \tag{3.2}$$

where ν_{sample} and ν_{indenter} are the Poisson ratio of the sample and indenter, respectively. If the indentation depth h is relatively small compared with R, then:

$$a = \sqrt{h \cdot R} \tag{3.3}$$

By inserting Eq. (3.3) into Eq. (3.1), it follows that:

$$F = (4/3) \cdot E_r \cdot R^{1/2} \cdot h^{3/2} \tag{3.4}$$

It should be noted that the Hertzian theory assumes that no friction occurs and that the sample and indenter are regarded as elastic half-spaces. This means that a must be small compared with the dimensions of the bodies and the radii of curvature of both surfaces [124].

The mean contact pressure P_{mean} is defined as the indenter load F divided by the projected contact area:

$$P_{\mathrm{mean}} = \frac{F}{\pi a^2} \tag{3.5}$$

In metallic glasses, plastic flow occurs through shear-banding when the temperature is relatively low and the strain rate high. Under load control, the formation and operation of shear bands is manifested in nanoindentation by a sudden increase in displacement, resulting in a so-called "pop-in" event (Fig. 3.4). The load at which the first pop-in appears can be determined as the yield load

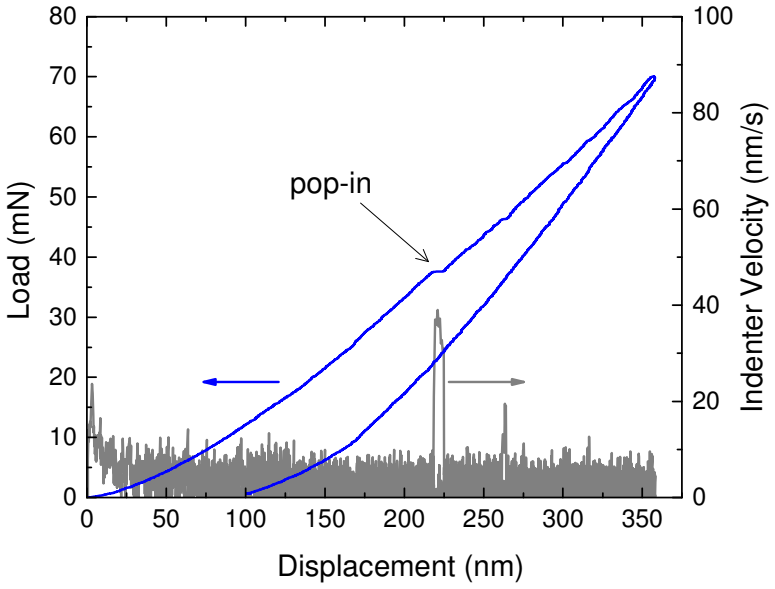

Fig. 3.4. Example load-displacement curve (in blue) and the corresponding velocity of the indenter (in grey). A sudden increase in displacement, called "pop-in", is thought to be due (in the case of metallic glasses) to the initiation and propagation of shear bands [128].

F_y of the glass [128]. These pop-ins are usually easily recognizable on load–displacement curves. They are also detectable as a peak of the indenter velocity $v = \mathrm{d}h/\mathrm{d}t$, where h is the indentation depth and t the time. After determining the load F_y and displacement h_y at which the first pop-in occurred from the nanoindentation results, the pressure at yield P_y can be calculated by combining Eq. (3.3) and Eq. (3.5):

$$P_y = \frac{F_y}{\pi \cdot R \cdot h_y} \tag{3.6}$$

In nanoindentation, the indentation modulus E_r is typically determined from the unloading curve, as will be shown below. But since the loading curve can be considered as purely elastic up to the first pop-in, a value for E_r can also be determined upon loading. E_r determined by this manner is termed here *Hertzian indentation modulus*. By rearranging Eq. (3.4), the Hertzian modulus $E_{r,\mathrm{Hertzian}}$ is given by:

$$E_{r,\,\mathrm{Hertzian}} = \frac{F}{(4/3) \cdot R^{1/2} \cdot h^{3/2}} \tag{3.7}$$

After yielding, the contact between indenter and sample is not anymore elastic, but elastic-plastic. In this regime, plastic deformation exists below the indenter tip, but it is constrained by the surrounding elastic material. By increasing the load, the pressure beneath the indenter increases and the zone of plastic deformation becomes bigger. Eventually, the plastic zone extends to the sample surface and is not anymore constrained by the surrounding material. The deformation is now purely plastic, and further increase in load causes little or no increase in P_{mean}. In the plastic regime, P_{mean} is equal to the hardness H, which is calculated as:

$$H = \frac{F}{\pi \cdot a^2} \tag{3.8}$$

The relationship between a and h is not anymore given by Eq. (3.3), but is now defined as:

$$a = \sqrt{2R \cdot h_c - {h_c}^2} \tag{3.9}$$

since the deformation is not anymore purely elastic. h_c is the contact depth, as shown schematically in Fig. 3.5b. The value of h_c is typically defined with the multiple-point unload method (also known as the "Oliver and Pharr" method applied to the spherical indenter) or the single-point unload method (sometimes called the "Field and Swain" method). For the nanoindentation measurements carried out here, the single-point method was applied. According to this method, h_c is given by:

$$h_c = h_{max} - \frac{h_e}{2} = h_{max} - \frac{h_{max} - h_r}{2} = \frac{h_{max} + h_r}{2} \tag{3.10}$$

where h_{max} is the total indenter displacement at maximum load, h_e the elastic portion of the displacement and h_r the depth of the residual impression (Fig. 3.5).

If unloading is purely elastic, the shape of the load-displacement curve upon unloading should be the same as that upon re-loading of the same indent. Taking this to be the case, then the Hertzian equation for elastic contacts can also be applied to the unloading curve, and a value for E_r, called here the *unloading indentation modulus* $E_{r,unloading}$, can be calculated as:

$$E_{\mathrm{r,\,unloading}} = \frac{F_{\max}}{(4/3) \cdot {R_{\mathrm{x}}}^{1/2} \cdot {h_{\mathrm{e}}}^{3/2}} \tag{3.11}$$

where F_{max} is the maximum load. It should be noted that the radius in Eq. (3.11) is not anymore the indenter radius R, but a larger radius R_x. This is because the shape of the load-displacement curve upon unloading should be the same as that upon re-loading. However, upon re-loading, the sample surface is not anymore flat at $F = 0$ but contains a residual impression with a radius of curvature R_r. This can be taken into account by considering a relative radius of curvature R_x, given by $1/R_{\mathrm{x}} = 1/R - 1/R_{\mathrm{r}}$. Since $h_{\mathrm{e}} = h_{\max} - h_{\mathrm{r}}$, the equation for $E_{r,unloading}$ can now be written as:

$$E_{\mathrm{r,\,unloading}} = \frac{F_{\max}}{(4/3) \cdot (1/R - 1/R_{\mathrm{r}})^{-1/2} \cdot (h_{\max} - h_{\mathrm{r}})^{3/2}} \tag{3.12}$$

where R_r is given by:

$$R_{\mathrm{r}} = \frac{2Rh_{\mathrm{c}} - {h_{\mathrm{c}}}^2 + {h_{\mathrm{r}}}^2}{2h_{\mathrm{r}}} \tag{3.13}$$

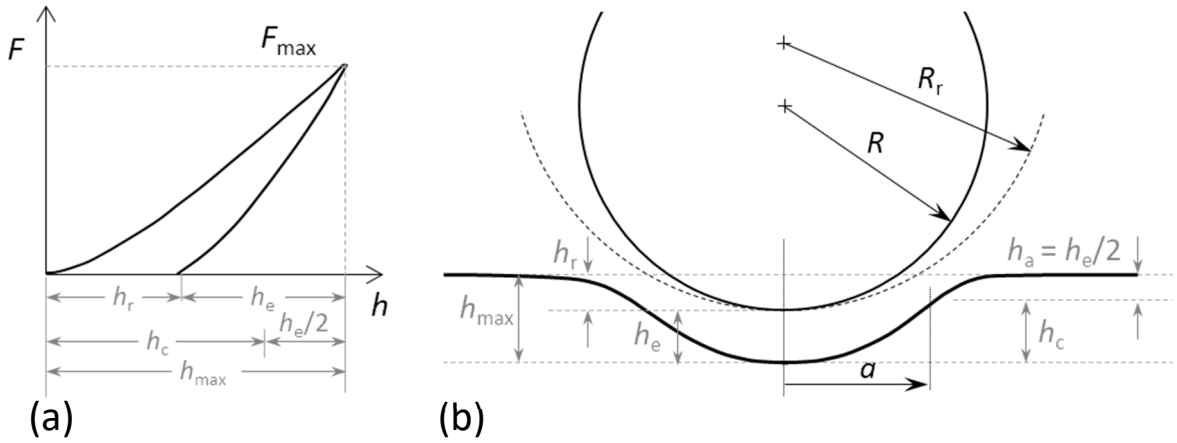

Fig. 3.5. Example nanoindentation curve upon loading to a maximum load F_{max} and maximum indentation displacement h_{max} and complete unloading (a). If plastic deformation occurred during loading, a residual impression is left on the sample surface after complete unloading. This impression has a depth of h_r and a radius of curvature of R_r (b). h_e is the elastic displacement and h_c is the contact depth. If considering the unloading from h_{max} to h_r to be fully elastic, then the depth of the circle of contact h_a is half of h_e according to the Hertzian equations [124]. Schematic was adapted from [124].

because a could be calculated from the relation $a = \sqrt{2Rh_c - {h_c}^2}$ or $a = \sqrt{2R_r h_r - {h_r}^2}$.

3.2.4 Sample requirements and preparation

A good sample surface condition is crucial to obtain reliable measurements in nanoindentation. Besides the need to be clean (i.e. free of contaminants), the surface also has to have a low enough roughness, because the calculations used to determine the contact area from the indentation depth are based on the assumption that the surface is perfectly flat. The surface finish should be at least comparable to the depth of indentation, if not better.

Correct sample mounting is also important. The sample surface to be tested should be parallel to the axis of translation of the sample stage. Furthermore, the sample needs to be securely mounted to the sample holder in order for the compliance of the mounting medium not to affect the measurements significantly. Therefore, only the thinnest possible layer of mounting medium should be used.

In this thesis, nanoindentation was performed on a CuZr-based bulk metallic glass (Chapter 5, §6.2), on Fe-based ribbons (§6.4) and on Au-based ribbons (Chapter 7). The ribbons were mounted onto sample holders with either superglue or the mounting wax Crystalbond 555–HMP (which has a flow point of 66°C). The CuZr-based bulk sample was fixed in cold-mounting resin (QUICK-SET by MetPrep). This mounting resin dissolves in acetone, and the sample could therefore be safely de-mounted after nanoindentation and treated (e.g. annealed or subjected to thermal cycling). The samples were polished with SiC abrasive grinding papers down to the grit size P4000, followed by 1 µm and $^1/_4$ µm diamond paste, and finally with the 0.06 µm colloidal silica suspension SILCO.

Another important sample requirement is that the sample should be thick enough, relative to the indentation depth, to ensure that solely the properties of the sample are probed, and not those of the underlying sample holder. The general rule is that the maximum indentation depth should be smaller than 10% of the sample thickness.

3.2.5 Testing procedure

Before measuring the sample by nanoindentation, it is advisable to clean the indenter tip and to verify that it gives accurate results. The indenter tip can be cleaned by indenting for example an aluminium block to depths larger than the displacement expected during the indentation of the sample. In this work, a spherical tip of 8 µm radius was used, and it was cleaned by indenting several times to a depth of 2 µm. In order to verify that the indenter is not damaged and its measurements

are reliable, regular testing of a calibration standard should be performed. A typical calibration standard material is fused silica.

Once the sample has been loaded onto the sample stage, a “microscope-to-indenter calibration” needs to be carried out. This calibration corrects the relative positioning between the microscope and indenter tip. During the setting up of the experiments, the microscope is placed directly above the sample stage, in order to allow the sample surface to be observed and to define the position of the indentation. Before each indentation, the nanoindenter head moves until the indenter tip is located above the desired position; a precise microscope-to-indenter calibration ensures that the indents are indeed performed at the chosen sites.

To get a reliable average value of the properties measured by nanoindentation, it is of interest to perform a large number of indents on every sample. Variation in the measured values can be due to errors arising for example from surface irregularities (e.g. scratches or surface contamination at certain places on the sample surface) or changes in temperature. Another source of the variation can be the inhomogeneity of the sample’s properties. Metallic glasses have been found to show structural heterogeneities which cause the mechanical properties to vary locally [20, 22, 129, 130, 131, 132]. Therefore, in this work, between 40 and almost 100 indents were measured per sample in order to obtain not only a reliable average value, but also to characterize the spread in values which provides information on the heterogeneity of the sample’s properties.

The distance between indents needs to be large enough to avoid interference between measurements. The indents should be spaced by at least 20–30 times the maximum indentation depth (for Berkovich indenters) and 7–10 times the maximum contact radius (for other indenter geometries) [125].

The loading protocol of nanoindentation is usually programmed by the user, and any desired test sequence is in principle possible. This means that during indentation at one site, multiple loading, holding and unloading segments, with different loading rates and maximum loads, can be applied (unlike conventional hardness tests, where the only test parameters that can be modified are the loading time and applied force). A popular pre-programmed test method in nanoindentation (which was, however, not used for the work here) is called ‘continuous stiffness measurement’ (CSM). This method consists of a series of small load increments, each followed by a partial unloading, from which the stiffness can be measured. Thereby, the hardness and modulus can be measured as a function of indentation depth.

Once the loading parameters have been set-up and the indent locations chosen, the door of the isolation cabinet can be closed and the experiments can start. First, before indentation begins, the

nanoindenter measures the thermal drift of the indenter (i.e. the displacement of the indenter tip caused by thermal expansion or contraction of the machine and sample due to changes in temperature) and waits until the thermal drift is below a certain threshold, pre-defined by the user. If the thermal drift is large during indentation, errors will be introduced in the measurement of displacement, which will cause the determined hardness and modulus values to be also incorrect. The threshold for thermal drift is usually recommended to be set to around 0.05 nm/s. A low threshold will produce more reliable measurements, but the settling time until the threshold value is reached may be very long (sometimes several hours). For the measurements performed here, a thermal drift threshold of 0.07 nm/s was chosen, which was usually reached within an hour.

But even a thermal drift of < 0.05 nm/s can cause significant uncertainty in the measured values, depending on the length of the experiment and the indented depth. Therefore, often a correction for thermal drift is performed on the data (an example is shown in Fig. 3.6). This is done by adding a hold segment to the test sequence, typically at the end of the test before the load is completely removed. An average drift rate v_{drift} is calculated from the indenter displacement during this hold

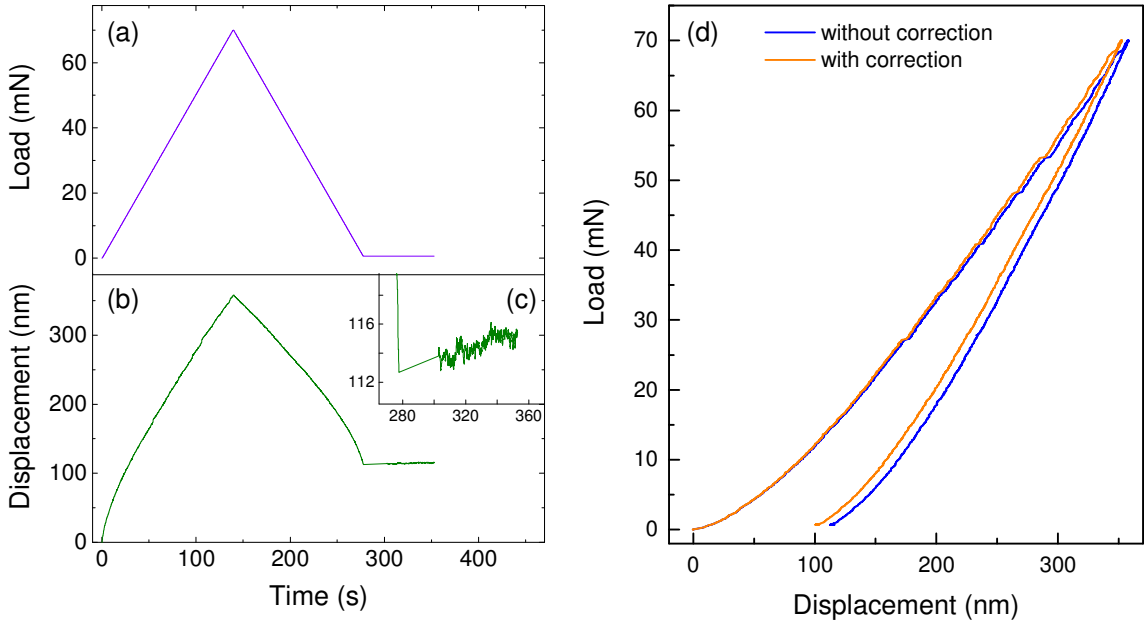

Fig. 3.6. Example load (a) and displacement (b) data recorded as a function of time during nanoindentation performed on the $Cu_{46}Zr_{46}Al_7Gd_1$ bulk-metallic-glass sample which was used in Chapter 5. A hold segment at a constant force of 0.7 mN was added at the end of unloading. Due to thermal drift, the measured indenter displacement increased during this hold segment (b); a zoom-in of this increase is shown in the inset (c). An average drift rate v_{drift} was calculated from this change in displacement, which was used to correct for the error of thermal drift of the entire load-displacement curve (d). For the example shown here, v_{drift} = 0.039 nm/s. If taking the correction into account, a hardness value of H = 6.40 GPa and indentation modulus of $E_{r,unloading}$ = 104.4 GPa is obtained (without correction, H = 6.16 GPa and $E_{r,unloading}$ = 104.8 GPa).

segment. The displacement data of the entire test is corrected by subtracting the value $v_{drift} \cdot t$, where t is the time, after the onset of loading, at which the displacement reading was taken.

3.3 Ultrafast differential scanning calorimetry (FDSC)

3.3.1 General information on differential scanning calorimetry

Differential scanning calorimetry (DSC) is a thermal analysis technique, which measures the change of heat flow (i.e. the energy going into and out of the sample) upon heating or cooling at a fixed rate. From the heat flow signal, temperature-dependent transitions occurring in a material can be measured. For metallic glasses, the most common transitions that are observed are melting, crystallization and the glass transition. Other events that can be detected are for example structural relaxations, chemical reactions, or even the Curie point of ferromagnetic materials [133]. From the heat-flow curve obtained by DSC, the temperature at which these transitions occur can be determined, as well as the energy associated with the transition and its kinetics. It should also be noted that besides studying transitions, DSC is also useful to measure the specific heat C_p of a material.

In DSC, the heat flow to the sample dQ/dt depends on the mass m and specific heat capacity C_p of the sample, as well as on the heating rate dT/dt according to the following heat flow equation:

$$\mathrm{d}Q/\mathrm{d}t = m \cdot C_p \cdot \mathrm{d}T/\mathrm{d}t \tag{3.14}$$

By integrating the heat flow dQ/dt, relative to a baseline, with respect to time from the beginning to the end of a transformation, the heat (or enthalpy) of the latter can be determined. From the above relation, it also follows that if the sample mass or the heating rate is increased, the DSC signal will be augmented (though the energy stays of course the same). Therefore, the sensitivity of the DSC trace is better at higher heating rates; however, results measured at lower rates have a better resolution [134].

Two types of DSC designs are typically used: the power-compensation DSC and the heat-flux DSC. Basic information regarding these designs can be found in ref.[134]. In the case of the power-compensation DSC, two separate furnaces are used. The sample, usually encapsulated in a small pan, is placed in one furnace, while a reference pan, which is typically empty, is placed in the other. Both furnaces are heated (or cooled) at the same rate, and the power required to maintain this rate is recorded. Once a transition occurs in the sample, it will either require heat to take place (meaning

it is an endothermic event) or will give out heat (i.e. exothermic event), and thus the power needed to keep up the specified heating or cooling rate will change. The DSC trace shows the difference in the required power of the two furnaces as a function of temperature or time.

The heat-flux DSC has only one furnace, in which both the sample and reference pans are placed in their designated positions. During heating and cooling of the furnace at a specified rate, the temperatures of both pans are measured separately. When a transition takes place, the temperature of the sample will either be lower or higher than the temperature of the reference pan (depending if the event is endothermic or exothermic). This temperature difference ΔT between pans is recorded, and converted into a heat-flow signal, which is considered to be linearly proportional to ΔT.

In this thesis, 'conventional' DSC (CDSC) is distinguished from 'ultrafast' DSC (FDSC). CDSC has been used since around 1960–1970. This technique is used for macroscopic samples with a weight in the range of mg, and the heating and cooling rates are limited to 'conventional' rates of normally around 1–200 K/min. On the other hand, FDSC is a relatively new technique, which was commercialized in around 2010. This method is used on samples with a weight in the ng–µg range, and can achieve very high heating rates. With the commercially available FDSC from Mettler Toledo, heating rates of up to 40,000 K/s (= 2,400,000 K/min) can officially be reached, though higher rates have been attained in other equipment [135, 136]. Since the rates applied in FDSC are very high, they are generally given in K/s, whereas the unit K/min is typically used for CDSC.

The following section (§3.3.2) gives the experimental details of the CDSC measurements made in this work. An introduction to FDSC in general, as well as some practical details, are given in §3.3.3 to §3.3.7.

3.3.2 Experimental details of conventional DSC measurements

CDSC was performed on a TA Instruments Q2000 DSC, which is a heat-flux type DSC. Liquid nitrogen was used as a cooling source. The furnace was purged with nitrogen gas at a flow rate of 50 ml/min. Temperatures ranging between −100°C and 600°C were applied. The measurements were performed using heating rates ranging from 5 to 180 K/min, and cooling rates of up to 100 K/min.

Details of the heating protocols applied for the different measurements can be found in the corresponding chapters (§6.4.2 and §7.2.2). In general, the sample was heated at the desired rate from room temperature or lower to a temperature above the last transition of interest (typically

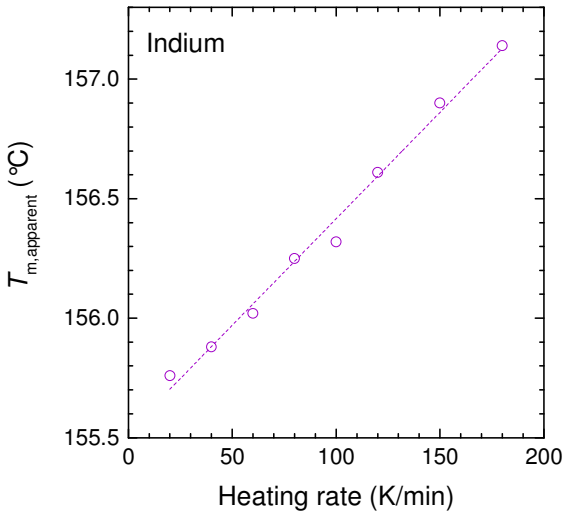

Fig. 3.7. Apparent melting onset temperature $T_{m,apparent}$ of indium (sample mass = 8.6 mg) measured by CDSC at different heating rates. The dashed line is a linear fitting of the points.

melting), then cooled back to the starting temperature. A second heating and cooling run, using the same rates as in the first run, was performed to obtain a baseline.

Aluminium pans with non-hermetic lids were used. Cleanliness is important for DSC, because contamination may lead to significant noise in the signal. Therefore, the samples were washed with acetone before being encapsulated in the pans.

A sample mass of between 5–20 mg is normally required to obtain a good signal. Since the heat flow is proportional to the sample mass, transitions may be more difficult to observe if the mass is too small; on the other hand, a too large sample may lead to significant errors in temperature due to thermal lag. In §6.4 and Chapter 7, CDSC was employed to study metallic-glass ribbons. In order to obtain the required mass, several ribbon pieces had to be stacked inside the pan.

As will be mentioned below in §3.3.7, significant thermal lag can also arise from fast heating rates. In §6.4, the CDSC measurements were performed at 20 and 60 K/min; at these rates temperature error due to fast heating is considered negligible (Fig. 3.7), and therefore no temperature correction of these measurements were performed. However, in Chapter 7, heating rates of up to 180 K/min were applied; a temperature correction was performed for these measurements as explained in §7.2.2.

3.3.3 Introduction to FDSC

Even before the commercialization of FDSC, attempts were made to increase the heating rates achievable in DSC. A key factor for increasing the scanning rate is to decrease the size of the system (smaller furnaces and samples). Thereby, by using sample masses in the µg–mg range, rates of up

to 750 K/min were achievable with the High Performance DSC (HPer DSC), which was commercialized by PerkinElmer [134, 137].

The possibility of reaching even higher rates is mainly attributed to the advancement of sensor technology, which allowed the development of chip-based calorimeters, such as the FDSC. These calorimeters consist only of a chip sensor, in which the heating elements and temperature sensors are integrated.

There are two main interests for using FDSC instead of CDSC. First, samples can be characterized which would have otherwise a too small mass for CDSC measurements, such as thin films. The second is of course the high heating and cooling rates as well as the large range of rates available, which make it possible to mimic the conditions in production processes that use high cooling rates (e.g. casting, blow moulding, injection moulding), and to study metastable materials as well as the kinetics of fast transformations. Fast heating is also useful to avoid sample degradation or reorganization phenomena (e.g. recrystallization, annealing) [134, 137].

3.3.4 FDSC instrument design

FDSC measurements were performed here on the FDSC1 from Mettler Toledo (Fig. 3.8a), which is a power-compensation type DSC. The following information on the set-up of the FDSC 1 was obtained from refs.[137, 138, 139].

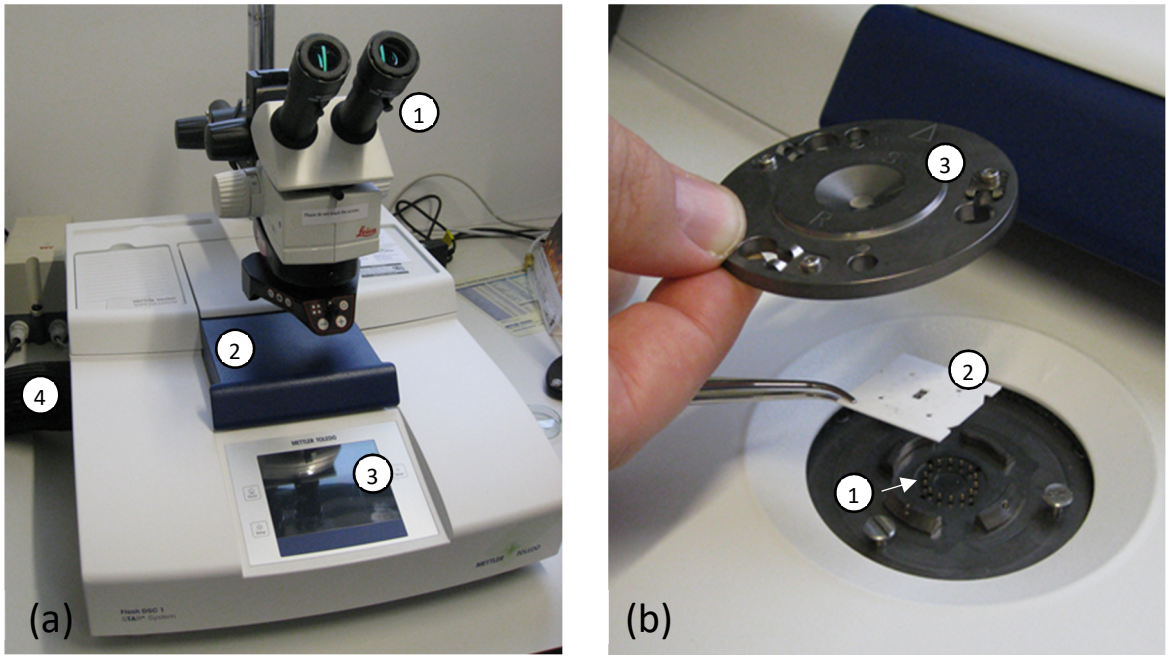

Fig. 3.8. Overview of the FDSC 1 equipment (a): optical microscope (1), insulation lid which covers the measuring cell (2), touchscreen for instrument control (3), connection to the intracooler (4). Measuring cell (b): electrical contact pins (1), sensor (2), sensor support clamp (3).

The main body of the equipment houses the electronic circuit boards (hidden out of reach of the user) and the measuring cell, which is accessed by sliding open the blue insulation lid. An optical microscope placed above the measuring cell facilitates insertion and removal of the sample. The instrument can be controlled directly via the touch screen at the front of the equipment, or through the operating software STARe.

By equipping the instrument with an intracooler, temperatures down to −105°C can be reached. When measuring at temperatures below room temperature, or when using an intracooler in general, the equipment has to be purged with a dry gas to prevent icing and condensation. Purge gases typically used in FDSC are nitrogen, argon and helium. The maximum heating and cooling rates at different temperatures depend on the type of gas [134, 137]. Here, nitrogen was used at a flow rate of around 25 ml/min.

The measuring cell consists of the sensor support and the electrical contact pins (Fig. 3.8b). The sensor is placed onto the contact pins, and held in place by closing the measuring cell with the sensor support clamp. The temperature of the sensor support (T_{ss}) is set by choosing between three states: 'power off', 'standby' and 'ready to run'. In the 'power off' mode, the connection between the FDSC and the intracooler is cut off, i.e. T_{ss} is not controlled. The temperature of the other two modes are defined by the user. The 'standby' mode is used for changing sensors or for inserting and removing samples, and is therefore normally set to around room temperature. In order to run experiments, the 'ready to run' mode has to be chosen. T_{ss} of this state has to be set to a value

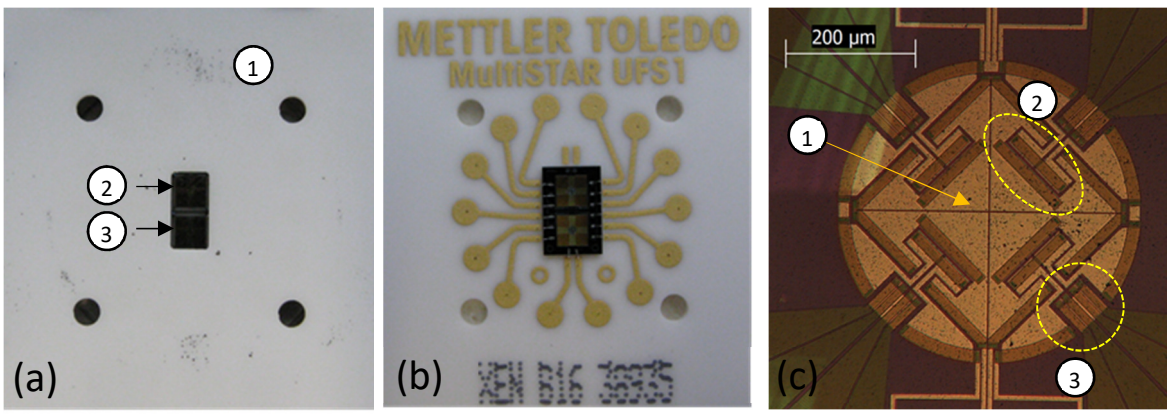

Fig. 3.9. View from above of the UFS 1 sensor (a): the ceramic plate (1) supports the microchip, which consists of a sample side (2) and a reference side (3), which are both around 1.6 mm × 1.6 mm. The membrane of the microchip is attached to the ceramic plate by a 300 µm-thick silicon frame. The sensor identification number is found on the underside of the sensor (b). Zoom-in on the microchip (c): measurement area coated with an aluminium layer (1), one of the heating resistors (2), hot junctions of 2 of the 8 thermocouples (3). The silicon frame around the chip acts as the cold junction of the thermocouples.

equal to or lower than the minimum temperature used in the experiments. For the measurements performed here, T_{ss} of the ready mode was set to either −105°C, −80°C or −40°C. A lower T_{ss} is desirable to achieve high cooling rates, however the disadvantage of a very low T_{ss} is that it takes longer to stabilize the system at that temperature.

The chip sensor used here is the UFS 1 sensor by Mettler Toledo, which is the current commercially available sensor for FDSC 1 (though in principle other sensors could be used). This sensor (Fig. 3.9a and b) consists of a microchip embedded in a ceramic plate. The microchip contains two identical parts, which act as two separate calorimeters: one for the sample, the other for the reference. Each part contains a membrane of silicon nitride and silicon oxide. At the centre of each membrane is the sample/reference area, coated with an aluminium layer to favour a uniform temperature distribution (Fig. 3.9c). This area is considered as the actual "furnace" of the calorimeter [138].

Each sensor has a unique identification number, which is found on the back of the ceramic plate (Fig. 3.9b). Before using a sensor for an experiment, its correction file, provided by the manufacturer, has to be imported into the STARe software.

During the experiment, the whole measuring cell (i.e. the sensor support and the surrounding gas) is cooled down to the sensor support temperature T_{ss} of the 'ready to run' mode. The sample area is heated with four heating elements (Fig. 3.9c). The temperature of the sample area is measured by eight thermocouples [138]. In principle the sample can be placed anywhere within the circular sample area, but to obtain an approximately correct temperature measurement it should lie between the heating elements, ideally in the centre.

Some specifications of the FDSC 1 equipment, according to Mettler Toledo, are mentioned below:

- Maximum temperature: 500°C when using the UFS 1 sensor (higher temperatures of up to 520°C can also be reached, as was used here, though this reduces the lifetime of the sensor [137].
- Minimum temperature: this depends on the cooling system used, and is −105°C for the intracooler used here.
- Heating rate range: 0.5 K/s to 40,000 K/s
- Cooling rate range: 0.1 K/s to 4000 K/s (though higher rates of up to 10,000 K/s can be reached if cooling from above 300°C and if using nitrogen or argon as purging gas [137])
- Temperature resolution: 0.01 K

- Temperature inaccuracy: < 5 K after sensor conditioning and correction procedure, §3.3.6. But by additional manual temperature calibration using e.g. the melting onset of known materials, the inaccuracy can be lower than 1 K.
- Sampling rate: max. 10 kHz

3.3.5 Information on samples for FDSC measurement

For fast heating and cooling rates, it is essential that the sample has a low heat capacity (implying that the sample mass must be small, around 10 ng to 10 µg [138, 139]) as well as a good thermal contact with the sensor; therefore ideally the sample should have a perfectly flat lower surface. In addition, the sample should be sufficiently thin to avoid a large temperature gradient within the sample. For an Au-based metallic glass, temperature gradients were found to be negligible for 20 µm-thick samples [140], therefore the sample thickness was kept below this value for the measurements performed here. There is also a limit on the other dimensions of the sample: as it should ideally be placed within the square formed by the four heating elements, its area should be smaller than 150 µm × 150 µm.

In order to obtain FDSC samples from metallic-glass ribbons, the ribbons were first gently ground using SiC grinding paper, of grit sizes P1200, P2500 and P4000, until the thickness was around 20 µm. In the case of metallic-glass rods, a 200–300 µm slice was first cut off, then ground to 20 µm. After grinding, the sample was cleaned with acetone. With the help of the optical microscope of the FDSC, a small rectangular piece was then cut with a scalpel on a glass slide. The desired size of the FDSC sample depends on the heating and cooling rates to be used. Bigger samples are advantageous for lower rates in order to get a signal that is distinguishable from the noise; but higher rates require smaller samples to avoid large thermal lag. By using a positioning tool tipped with a hair, the sample can be then picked up and gently placed onto the sensor.

Since FDSC samples are very small, their mass m cannot be measured by common balances. However, m can be estimated by comparing the enthalpy of melting ΔH_m obtained from a CDSC measurement, from which m is known, with ΔH_m of the FDSC curve. Since the specific enthalpy of melting (= $\Delta H_m/m$) is constant for the same material (crystallized to the same phase):

$$m_{FDSC} = \frac{\Delta H_{FDSC}}{\Delta H_{CDSC}} \cdot m_{CDSC} \tag{3.15}$$

where m_{CDSC} and ΔH_{CDSC} are the sample mass and enthalpy of melting of the CDSC measurement, and m_{FDSC} and ΔH_{FDSC} of the FDSC measurement.

3.3.6 Example of the procedure of a typical FDSC experiment

Before being used for a measurement, each chip sensor has to undergo a two-step treatment process. The first step is “conditioning”, during which the chip is heated according to a predefined protocol (which consists of heating from 45°C to 450°C at 27 K/s, holding for 15 s, cooling back to 45°C at 100 K/s, heating again to 450°C at 100 K/s and cooling again at the same rate). This step is repeated around 5 times. The second step is the “thermocouple correction”; here the sensor is held at −100°C for 0.1 s, then heated to 450°C at 550K/s. In this step, the signal of the thermocouples is compared with the thermal behaviour of the heating elements, and correspondingly corrected. The behaviour of the heating elements was determined by the supplier during production, and has to be imported into the software from the online database of the supplier by providing the identification number of the sensor.

The sample is placed on the chip in the ‘standby’ state. Before an experiment can be started, the FDSC is switched to the ‘ready to run’ state, and the sensor support is cooled down to the T_{ss} of this mode. The settling of the sensor support to this temperature can take up to 40 min if T_{ss} is set to −105°C.

The temperature programme of the FDSC measurement is set up with the STARe software. It can contain up to 200 segments, each no shorter than 1 ms, and is limited to a maximum total duration of 50 h. A segment can be either an isothermal step or a linear heating or cooling ramp. It is recommended [137] to add a short isothermal step, of around 0.1 s, between consecutive temperature ramps. It is also possible to add a loop, meaning that one can repeat a cycle of segments a large number of times, without surpassing the limit of 200 segments. A typical temperature protocol is for example: 1) isothermal step of 0.1 s at T_{ss} of the ready mode, 2) heating ramp to the maximum temperature, 3) isothermal step of 0.1 s, 4) cooling ramp back to T_{ss}, 5) repetition of steps 1–4 to obtain a baseline.

It should be noted that the entire measurement of one sample should be performed in a single programme, and not split up into separate consecutive programmes. The temperature of the sample is not measured during the switch from one programme to the other. Though it might seem logical to assume that the sample stays at T_{ss} during this switching time, previous experiments (not reported in this work) have shown that the sample seems to undergo some heating.

Since the sample mass is unknown, the heat flow curve has to be normalized in one way or another in order to be compared to other measurements. One way is to use the heat of melting as normalization factor, provided the complete melting peak is within the temperature limits of the FDSC. Another possibility is to normalize according to the glass-transition step height.

3.3.7 Temperature calibration of FDSC measurements

There are two main sources of error in the measurement of temperature. The first is the intrinsic error (or inaccuracy) of the chip sensor. This error is normally corrected for during the "thermocouple correction" process performed before the first use of the sensor (see §3.3.6), though this correction is not always accurate, especially when the sensor support temperature T_{ss} is below 0°C, as will be shown later. The second source of error arises from thermal lag, which is due to sample mass, fast heating or cooling rates, and to an imperfect contact of the sample with the sensor. It is therefore advisable to perform a temperature calibration for each sensor, and ideally also for every measurement.

In order to calibrate the temperature, one typically uses the melting onset T_m of a pure metal (e.g. indium), or the Curie temperature T_{Curie} of a known ferromagnetic material (e.g. nickel). The advantage of using the melting onset of a material is that a good contact between sample and sensor is established upon melting. In order to perform the temperature calibration, the metal has to be first pre-heated until it is melted and forms a perfect contact with the sensor. Upon a second heating run, T_m can be measured and used to determine the error (Fig. 3.10a). However, once a sample is melted, it may be difficult to remove it again from the sensor, meaning that the sensor may be useless for further measurements. This is however not the problem when using the Curie

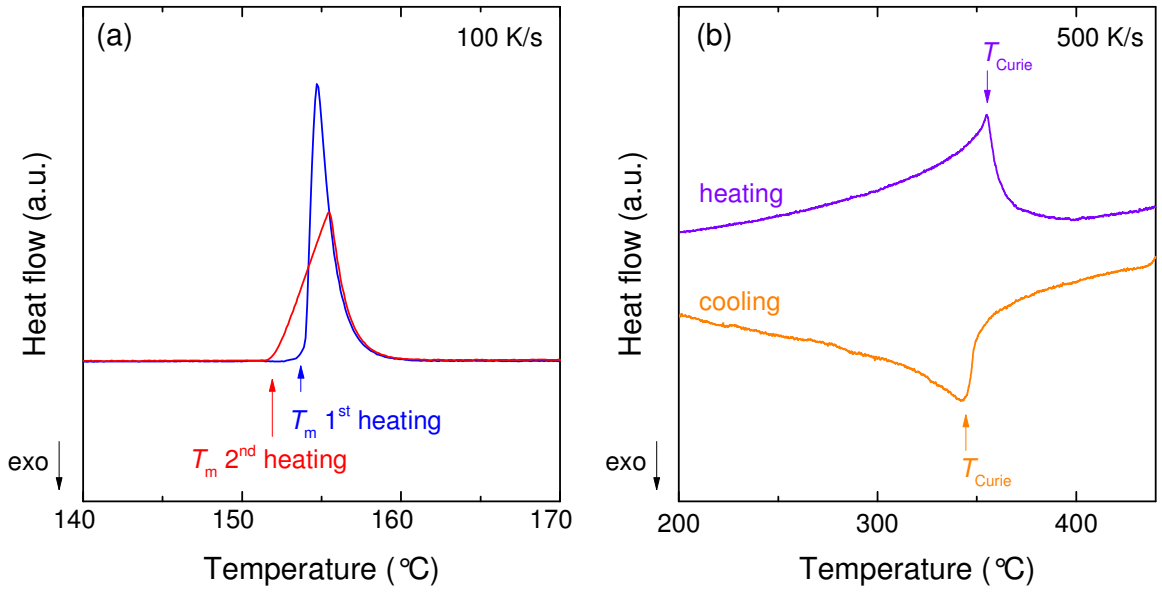

Fig. 3.10. Measurement of the melting onset T_m of indium by FDSC upon heating at 100 K/s (a). When the sample is melted for the first time (during the 1st heating run), it forms an almost perfect contact with the sensor. During the next heating run, the apparent onset of melting occurs at a lower temperature than during the 1st heating, since the contact between sample and sensor is better. The Curie temperature T_{Curie} of nickel can be measured upon heating as well as upon cooling (b).

transition for calibration, since the reference material does not have to be melted. Another advantage of using T_{Curie} is that it not only occurs upon heating (as is the case for melting), but also upon cooling (Fig. 3.10b), meaning that it can be used to calibrate the cooling as well as the heating curves of DSC measurements. It should be noted that freezing (e.g. of indium) is not suitable for calibrating the cooling curve because of supercooling.

Fig. 3.11 shows the apparent onset of melting $T_{m,apparent}$ of an indium sample (after pre-melting) and the apparent Curie temperature $T_{Curie,apparent}$ of a 10 µm-thick nickel foil measured by FDSC at different rates, using the same sensor.

It should be noted that the apparent temperatures $T_{apparent}$ deviate from the true values T_{true} due to thermal lag as well as other temperature deviations. $T_{apparent}$ can be described by the following equation [141]:

$$T_{\text{apparent}} = T_{\text{true}} + a_0 + a_1\alpha^{a2} + a_3\alpha m^{a4} \tag{3.16}$$

The coefficient a_0 takes into account temperature errors which are independent of the applied scanning rate α (e.g. inaccuracy of the sensor), and the last two terms in Eq. (3.16) represent the thermal lag. One part of the thermal lag, given by the term $a_1\alpha^{a2}$, is due to the thermal mass and resistance of the sample area of the sensor (i.e. it takes some time for the middle part of the sample area to heat up as the heating resistors are located at the edges of the sample area). The other part of the thermal lag, described by the term $a_3\alpha m^{a4}$, is caused by the thermal mass of the sample

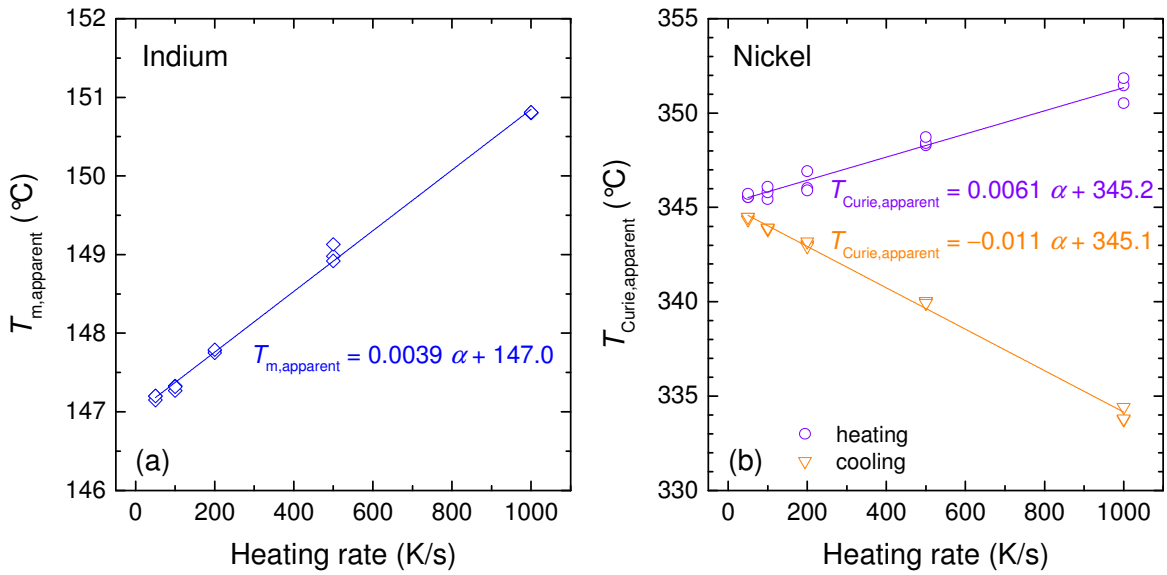

Fig. 3.11. The apparent onset of melting $T_{m,apparent}$ of a pre-melted indium sample (a) and apparent Curie temperature $T_{Curie,apparent}$ of nickel (b) as a function of heating rate α, measured by FDSC using the same sensor. Whereas T_{Curie} can be determined upon heating as well as cooling, melting only occurs upon heating. The time lag τ_{lag} and the inaccuracy of the sensor can be determined by fitting the data with a linear equation.

and the thermal resistance between heating element and sample. Assuming that the coefficient a_2 = 1 [141], Eq. (3.16) was here simplified to:

$$T_{\text{apparent}} = T_{\text{true}} + a_0 + \alpha \cdot (a_1 + a_3 m^{a4}) = T_{\text{true}} + a_0 + \alpha \cdot \tau_{\text{lag}} = T_0 + \alpha \cdot \tau_{\text{lag}} \qquad (3.17)$$

where τ_{lag} is a time lag with units of s (which, when multiplied by the scanning rate α, gives a temperature lag in the units of K) and T_0 (= T_{true}+ a_0) is the apparent temperature extrapolated to a heating rate of 0 K/s. Both contributions of thermal lag are here regrouped together as $\alpha \cdot \tau_{lag}$. In order to calibrate the temperature of the FDSC results in this work, a correction parameter ΔT_{corr} was considered as:

$$\Delta T_{corr} = \tau_{lag} \cdot \alpha + T_0 - T_{true} \qquad (3.18)$$

For the pre-melted indium sample, τ_{lag} = 0.0039 s and $T_{m,0}$ = 147.0°C (Fig. 3.11a). The inaccuracy of the sensor used for this measurement can be determined by calculating ΔT_{corr} for α = 0 K/s, and was found to be −9.6°C (if taking $T_{m,true}$ = 156.6°C). As can be seen in Fig. 3.11b, τ_{lag} of the nickel sample is different for heating and cooling (0.0061 s and −0.011 s, respectively), whereas $T_{Curie,0}$ is approximately the same (around 345°C). The difference in τ_{lag} between heating and cooling is due to the fact that they have different heat flow paths (the sample is heated by the heating resistors via the sample area on the chip membrane, whereas cooling occurs via the environment cooled to T_{ss}).

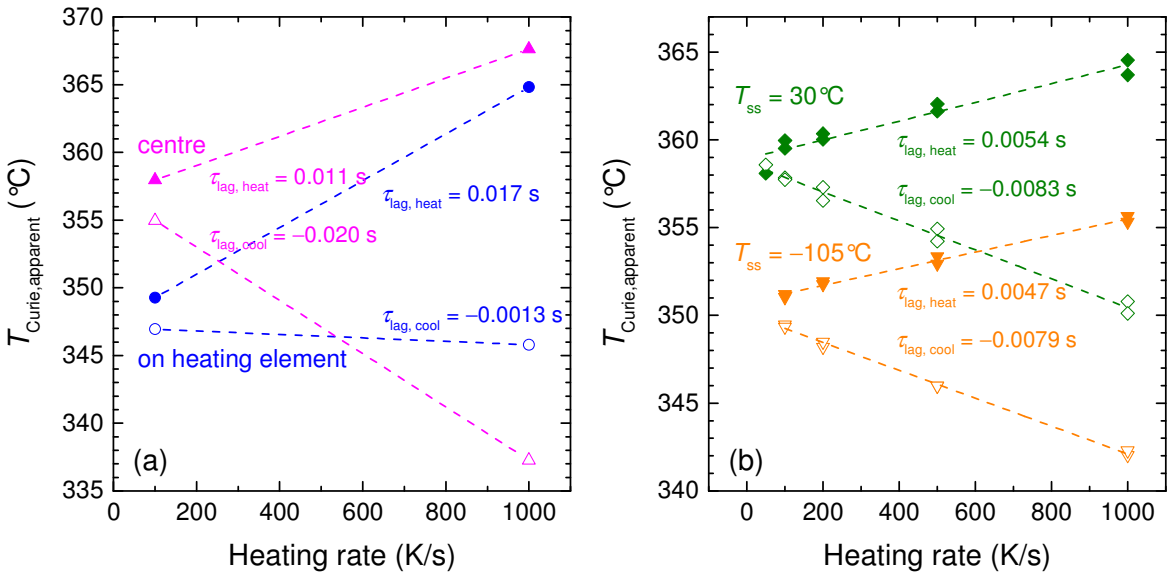

Fig. 3.12. The effect of sample position on the measured Curie temperature $T_{Curie,apparent}$ of nickel (a): when placing the sample on the heating element of the sensor, the Curie transition occurred earlier upon heating (i.e. at a lower apparent temperature) than when placing it in the centre. $T_{Curie,apparent}$ of nickel depends also on the sensor support temperature T_{ss} (b). The full and hollow symbols in (a) and (b) represent the values measured upon heating and cooling, respectively.

Considering the true value of T_{Curie} to be 358°C (determined from CDSC measurements), the error due to the sensor would be −12.9°C. One reason for the difference in sensor error determined from the indium and nickel calibrations may be because the temperature error of the sensor is not necessarily constant, but varies at different temperatures. A constant sensor error was however considered for all FDSC experiments performed in this thesis.

Another reason for the difference between the indium and nickel calibrations is that the sensor is not heated perfectly uniformly. If the sample is placed close to, or on top of, the heating element, its temperature will be higher than if it is placed in the exact centre of the heating area. Fig. 3.12a shows two measurements of T_{Curie} of the same nickel sample; for one it was positioned in the centre of the sensor, and for the other it was placed on a heating element.

Another important factor to consider is the sensor support temperature T_{ss} used for the measurements. For some sensors, the temperature error is much larger at lower T_{ss} (Fig. 3.12b). The reason for this is not entirely understood (though according to the suppliers of the FDSC equipment, some sensors were not correctly calibrated for low T_{ss} values during the manufacturing process).

Instead of using a reference material (e.g. indium, nickel) for temperature calibration, it is sometimes more convenient to use a known transition point of the actual sample being studied. In §7.2.2, for example, the melting onset of the crystallized Au-based ribbon was used to calibrate the temperature of each measurement. This takes into account not only the error due to sample placement, but also the error due to the thermal mass of the sample. But for the experiments done on the La-based samples in Chapter 4, no known transition point of the sample could be used for temperature calibration. Thermal lag is usually negligible for rates below 1000 K/s when measuring metallic glasses by FDSC, but this error has to be corrected for at higher rates. Therefore, a τ_{lag} for the La-based samples was roughly estimated in Chapter 4 by comparing it to the τ_{lag} measured for another sample. By considering the thermal lag due to the system (term $a_1\alpha^{a2}$ in Eq. (3.16), which was estimated by van Herwaarden to be 0.2 ms [141]) to be negligible compared to that due to the sample, it was here assumed that:

$$\text{thermal lag} = \alpha \cdot \tau_{\text{lag}} \propto \alpha \cdot m \cdot C_{\text{p}} \tag{3.19}$$

where m is the mass and C_p the heat capacity of the sample, and therefore:

$$\frac{\tau_{\text{lag}_{\text{sample1}}}}{m_{\text{sample1}} \cdot C_{\text{p, sample1}}} = \frac{\tau_{\text{lag}_{\text{sample2}}}}{m_{\text{sample2}} \cdot C_{\text{p, sample2}}} \tag{3.20}$$

4 Increasing the Energy through Plastic Deformation

4.1 Introduction

Plastic deformation of metallic glasses can lead to an increase in their energy, termed *rejuvenation*, with often the advantageous effect of improving their plasticity. As metallic glasses generally show negligible plasticity in tension, plastic deformation is introduced through processes where the glass is mechanically constrained and will not fracture during deformation, e.g. cold-rolling, high-pressure torsion (HPT), shot-peening etc. [5]. Besides the increase in energy, plastic deformation was also observed to lead to the development of shear bands, an increase in volume (i.e. decrease in density) and change in mechanical properties, such as reduction in hardness and elastic modulus [45, 46, 52, 142]. It should be noted that, depending on the initial sample state, relaxation instead of rejuvenation can be obtained. For example, shot-peening of an as-cast Pd-based BMG (which was initially relatively unrelaxed) was found to relax the sample, whereas after pre-annealing the sample it led to rejuvenation [57].

In the literature, the currently highest increase in energy through plastic deformation was obtained by tri-axial compression [62]. By introducing a circumferential notch in a (Zr-based) cylindrical bulk-metallic-glass sample and loading it under uniaxial compression, the notched region was subjected to tri-axial stresses; catastrophic shear-banding was thus constrained, and large strains within the notched area of up to 40% were achieved. The increase in energy was determined from the exothermic heat of relaxation ΔH_{rel} measured by heating the notched part up to T_g. After 40% strain, ΔH_{rel} increased from 0.49 kJ/mol to 1.13 kJ/mol (i.e. an increase of 131%). In addition, a ~20% reduction in hardness at the centre of the notched region was found. The induced rejuvenation of this notched specimen is considerably higher than what can be achieved by uniaxial loading of an un-notched sample, for which $\Delta H_{rel} \approx 0.65$ kJ/mol and a reduction in hardness of ≈ 6% was found.

In the present chapter, the aim is to equally achieve a high degree of rejuvenation through plastic deformation upon compression. Large plastic strains are here obtained by choosing the sample shape and size such that localized shear-banding and brittle failure are avoided. A $La_{55}Ni_{20}Al_{25}$ metallic-glass rod is cut into thin slices, creating samples of a low aspect ratio. Upon uniaxial compression, brittle failure is avoided because the sample is too thin for a shear band to form across the entire sample.

The same principle was previously explored in the literature (see §2.1), though less extensively than other methods [59, 60, 61]. For example, by using a specimen with a low aspect ratio and applying a low strain rate during compression, Bei et al. [59] achieved high plastic strains of up to 80% in a Zr-based BMG. They explained that if the sample aspect ratio (= height : diameter) is < 1, a single shear band cannot form through the entire sample, because shearing starts off at an angle of approximately 45° to the loading axis. Instead, many new shear bands have to be nucleated upon plastic deformation [59]. This prevents the stresses and strains being concentrated in a single shear plane, and brittle failure can be avoided (Fig. 4.1.). The strain rate is another important factor for achieving large strains. If the strain rate is low enough, the stresses built-up during plastic deformation have time to relax, and crack formation can be avoided [59]. After plastically deforming the sample, Bei et al. [59] observed a decrease in hardness, but they did not measure the increase in energy. On the other hand, Louzguine-Luzgin et al. [60] did measure ΔH_{rel} after compressing a low aspect-ratio sample of the composition $Zr_{61}Cu_{27}Fe_2Al_{10}$ to a plastic strain of 68%, and found an increase of 550 J/mol compared to the as-cast state.

The change in energy of the MG will be the main focus in the present work. After compressing the $La_{55}Ni_{20}Al_{25}$ samples to various degrees of plastic deformation, their heat flow curves were measured by ultra-fast differential scanning calorimetry (FDSC), and compared to the curves of the as-cast sample in order to determine the change in enthalpy of relaxation.

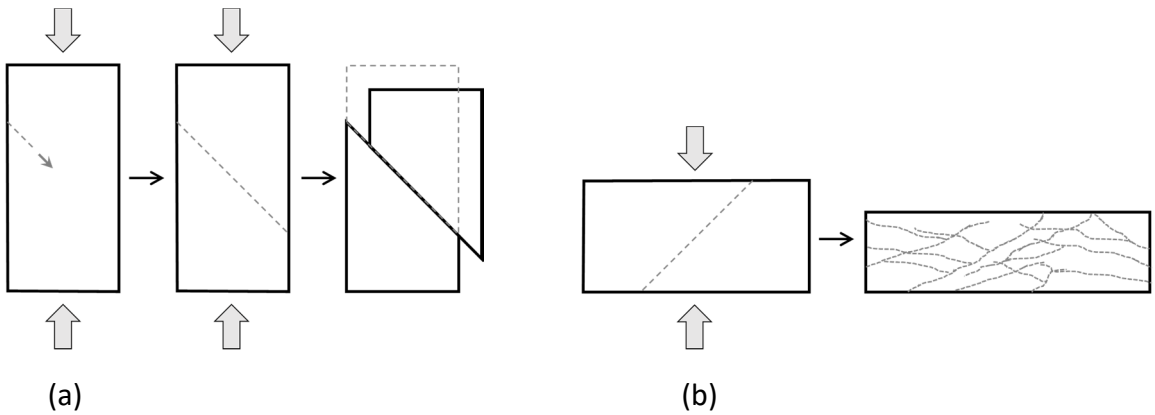

Fig. 4.1. Schematic diagrams of a large aspect-ratio sample (a) and a low aspect-ratio sample (b) loaded under compression. If the sample height : diameter ratio is large enough, a single shear band can propagate though the entire sample, leading to brittle failure (a). In the case of a low aspect-ratio sample, the compression plates block shear bands (which form at an angle of 45°C) from passing through the sample; instead new shear bands are nucleated to allow the flow of further plastic deformation (b).

4.2 Experiments

4.2.1 Compression

A 2-mm-diameter metallic-glass rod of the composition $La_{55}Ni_{20}Al_{25}$ was cut into 250 – 400 µm thick slices. The samples were uniaxially compressed at room temperature using a Tinius Olsen testing machine (H25K-S UTM) at a constant displacement rate of 0.015 mm/min. In order to achieve different degrees of deformation, three different maximum applied loads were used: 6, 8 and 20 kN (which deformed the samples by 30, 37 and 53%, respectively). As the practical limit of the utilized force cell was 20 kN, higher degrees of deformation (55, 63, 71, 83 and 85%) were achieved by cutting the 2 mm diameter slices lengthwise in order to reduce the area under compression and thus to increase the applied stress. The degree of deformation was defined as $(d_{\text{initial}} - d_{\text{deformed}})/d_{\text{initial}}$, where d_{initial} and d_{deformed} are the sample heights measured with a micrometer before and after compression, respectively. An example force–displacement compression curve is shown in Fig. 4.2. Brittle failure could be avoided and large strains obtained because of the low sample aspect ratio and strain rate. The aspect ratio (height : diameter) of the

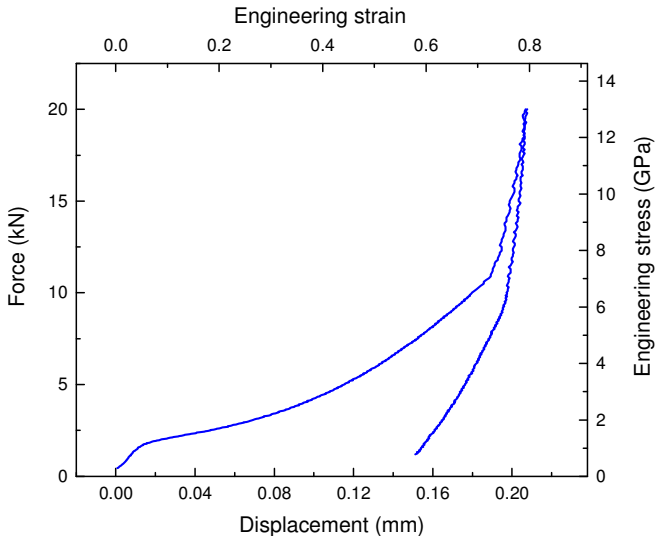

Fig. 4.2. Force–displacement curve upon compression of the sample deformed by 55%. As the initial sample height d_{initial} is known (to ± 1µm precision), the engineering strain $\varepsilon = (d_{\text{initial}} - d)/d_{\text{initial}}$ can be calculated. Only a rough estimate of the initial sample area A is known, and therefore the error in the determination of the engineering stress $\sigma = F/A$ is around ± 30%. From a force of around 11 kN on, the load-displacement curve turns upwards substantially. This may be because, since the initial sample height is relatively small (≈ 200–300 µm), after deforming the sample to a certain extent, the parts of the upper and lower compression anvils will come into contact with each other, enclosing the sample, and a larger total area (not anymore only the sample area but the entire anvil area) has to be compressed.

samples was below 0.4, and the strain rates ranged between $6.1 \cdot 10^{-4}$ s^{-1} and $1 \cdot 10^{-3}$ s^{-1}, depending on the initial sample height.

4.2.2 FDSC measurement

After compression, the change in thermal properties of the samples was characterized by DSC. Ultra-fast DSC (FDSC) instead of conventional DSC (CDSC) was mainly employed here because the samples used for compression were relatively small, and had a too low mass to get an acceptable heat flow signal by CDSC. In addition, the fast heating rates available in FDSC allow the observation of some calorimetric features (e.g. the endothermic sub-T_g, as will be shown in §4.3.3) which are not present at conventional rates. For FDSC measurement, the samples were polished down from both sides to a thickness of 20 µm, then cut with a scalpel into approximately 0.1 mm x 0.1 mm large pieces. These pieces have a mass of approximately 1 µg. This mass was determined by comparing the heat of crystallization ΔH_x of the as-cast sample measured by FDSC at 1 K/s with ΔH_x obtained from CDSC at the same heating rate. The FDSC sample pieces were heated to 793 K at 100K/s above the first melting peak, then cooled down to 303 K at the same rate. A second heating run was done to obtain a baseline. Between 4 and 10 samples were measured per sample condition. FDSC traces were also obtained for the metallic-glass ribbon of the same composition. The as-cast rod was also measured by conventional CDSC at 0.333 K/s (= 20 K/min) and 1 K/s (= 60 K/min).

4.3 Results and discussion

4.3.1 General features of CDSC and FDSC traces of the as-cast La-based rod

Example DSC heating traces of the as-cast rod measured at 1 K/s (by CDSC) and at 100 K/s (by FDSC) are shown in Fig. 4.3. A glass-transition step occurs at around 490 K, bringing the sample into the supercooled-liquid state, followed 50–100 K later by an exothermic crystallization peak, and finally the sample starts melting at around 700 K. The glass-transition onset temperature T_g and the crystallization temperature (onset $T_{x,onset}$ as well as peak T_x temperatures) depend on heating rate [143, 144]: at higher rates, these temperatures are shifted to higher values. The amount by which these temperatures shift upon a certain increase in heating rate is linked to the temperature dependence of the atomic mobility, which can be expressed in the form of an activation energy. The effective activation energy of the glass transition is generally higher than for crystallization, and therefore the shift of T_g is smaller than of T_x, as can be seen in Fig. 4.3. On the other hand, the

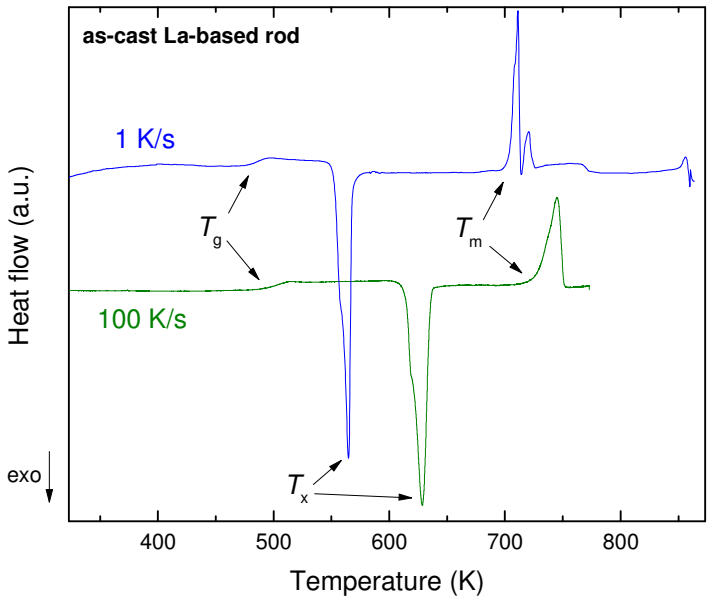

Fig. 4.3. DSC heating traces of the as-cast La-based rod measured at 1 K/s (by CDSC) and 100 K/s (by FDSC). The glass-transition onset, crystallization peak and onset of melting are denoted with T_g, T_x and T_m, respectively.

melting onset temperature T_m, of a given phase, is independent of the heating rate since it is thermodynamically defined. From our CDSC results, T_m was found to be ≈ 704 K, which is similar to the values found in the literature [145, 146]. However, when measuring at 100 K/s by FDSC, melting occurs at a significantly higher temperature of ≈ 733 K; the reason for this difference is not yet understood. It should also be noted that the melting observed in Fig. 4.3 is incomplete. According to the literature, melting finishes at around 940 K [147], whereas our CDSC and FDSC measurements are limited to 873 K and 793 K, respectively. It is furthermore interesting to note that, in the case of the curve measured at 1 K/s, the first melting peak is split, which indicates that some transition (though unknown) is taking place.

4.3.2 Increase in energy after plastic deformation

Crystallization is known to sometimes occur during mechanical deformation of metallic glasses. Depending mainly on sample composition and stress state, nano-crystals can form within shear bands, which was often observed to improve the plastic deformability of the metallic glass [33]. Signs that crystallization had taken place would be visible in DSC measurements as a decrease in $T_{x,onset}$ and in ΔH_x. No obvious crystallization induced by compression was observed here (Fig. 4.4). But due to the relatively large spread in the measured values of $T_{x,onset}$ (of around 5–20 K) and ΔH_x, it is difficult to conclude this for certain.

If a metallic glass is initially unrelaxed (i.e. contains a large amount of excess free energy), it will relax towards a lower energy state when heated up to the glass transition in DSC (provided the heating rate is not too fast). This relaxation is apparent as an exothermic peak just below T_g, which corresponds to the heat of structural relaxation ΔH_{rel}. The larger the measured ΔH_{rel} is, the more unrelaxed the metallic glass was before DSC measurement.

The as-cast rod showed no structural relaxation when measured at 100 K/s (Fig. 4.5a). After plastic deformation, an exothermic peak below T_g becomes visible and increases with higher degrees of plastic deformation, a sign that the glass is rejuvenated. But it should be kept in mind that the size (or occurrence) of the peak depends on the heating rate during the DSC measurement, and how it compares to the effective cooling rate α_{eff}, which is the rate needed to form a glass of the same energy by quenching from the melt [149]. An exothermic structural relaxation peak can only be observed if the heating rate is lower than α_{eff} (Appendix A, Fig. A.1). If the glass is heated at the same rate as α_{eff}, a simple step should be observed. But if the heating rate is faster, then an endothermic overshoot is observed at T_g. In the case of a freshly as-cast glass, α_{eff} corresponds to the actual cooling rate used during fabrication (though it should be noted that the as-cast samples

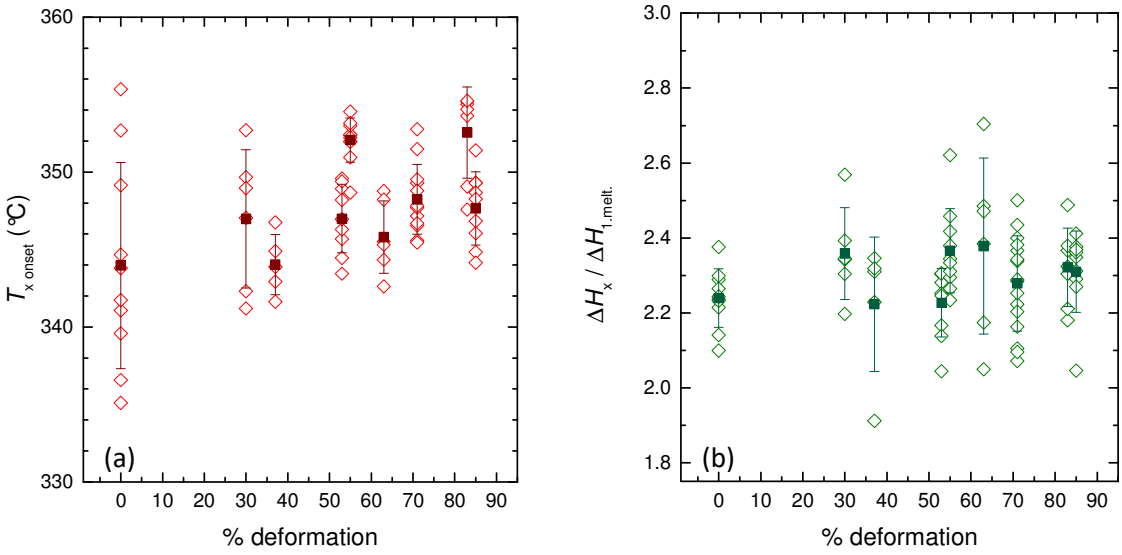

Fig. 4.4. Crystallization onset temperatures $T_{x,onset}$ (a) and the heat of crystallization ΔH_x (b) of the La-based rod as-cast and after deformation. As the mass of the FDSC samples are not known, the absolute value of ΔH_x is not directly measurable; instead the crystallization peak area is normalized by the first melting peak area $\Delta H_{1.melt}$ and $\Delta H_x/\Delta H_{1.melt}$ is determined. It should be noted that $\Delta H_{1.melt}$ is not the complete melting peak (ΔH_m should be bigger than ΔH_x, which is not the case here); further melting should occur at higher temperatures, which are above the temperature limit of the FDSC). The solid symbols and error bars correspond to the mean ± 1× standard deviation.

used here are not fresh, but have been stored for around 1 year at room temperature). As the plastically deformed samples are rejuvenated, their α_{eff} is higher than of the as-cast sample and also higher than the heating rate of 100 K/s applied here (as will be shown below), explaining why a structural relaxation peak can be observed for them but not for the as-cast samples.

Instead of considering ΔH_{rel} as a measure for the degree of rejuvenation induced upon compression, the difference in enthalpy ΔH_{diff} between the as-cast and the compressed samples was considered here, because it takes into account not only the heat of structural relaxation but also of the heat of the overshoot. ΔH_{diff} was calculated as:

$$\Delta H_{\mathrm{diff}} = \Delta H_{\text{as-cast}} - \Delta H_{\mathrm{deformed}} \tag{4.1}$$

$$\Delta H_{\mathrm{diff}} = \int_{T_1}^{T_2} C_{\mathrm{p,as\text{-}cast}}(T)\mathrm{d}T - \int_{T_1}^{T_2} C_{\mathrm{p,deformed}}(T)\mathrm{d}T \tag{4.2}$$

where $C_{p,as\text{-}cast}(T)$ and $C_{p,deformed}(T)$ are the specific heat as a function of temperature of the as-cast and deformed samples; T_1 (= 360 K) is below the onset of structural relaxation, and T_2 (= 540 K) is in the supercooled-liquid region. The values for T_1 and T_2 were chosen such that T_1 is before any structural relaxation starts and T_2 is after the glass transition, and where the curves overlap. The specific heat curves were estimated here by first subtracting a baseline, then scaling the FDSC heat flow traces so that the specific heat values of the glassy state $C_{p,glass}$ and of the supercooled-liquid state $C_{p,SCL}$ matched those found in the literature. $C_{p,SCL} \approx 37.6$ J/mol K at 550 K; $C_{p,glass}$ was considered to be similar to the specific heat of the crystal $C_{p,crystalline} \approx 22.7$ J/mol K at 350 K [148]. A

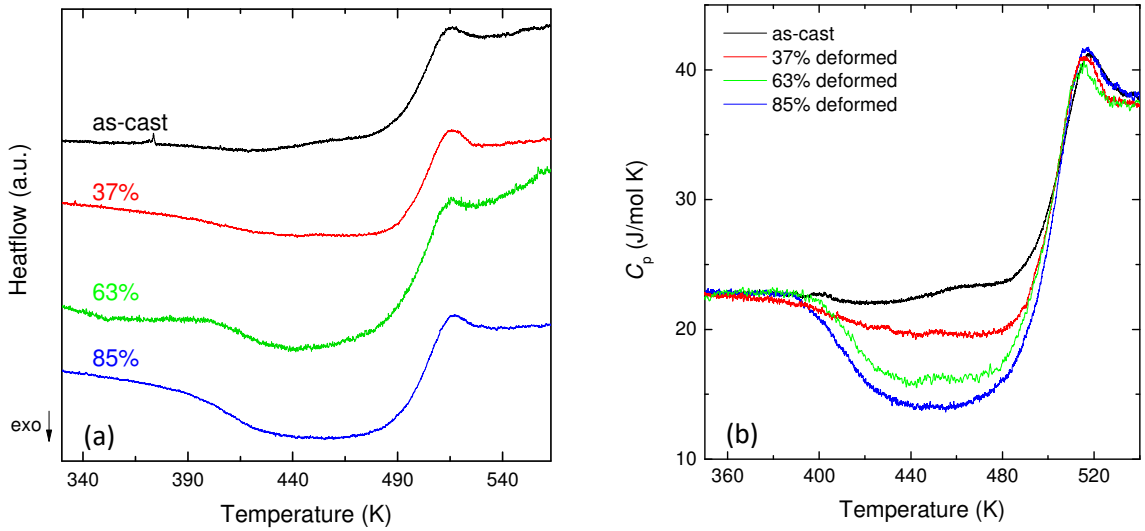

Fig. 4.5. Example heat flow curves measured at 100 K/s by FDSC of the La-based rod sample as-cast and after compression (a), focused on the glass transition. Specific heat flow curves (b) were obtained by appropriate scaling of the heat flow curves.

selection of the obtained C_p curves, zoomed-in on the structural relaxation event below T_g, are shown in Fig. 4.5b; the curves for all measured samples can be found in Appendix A (Fig. A.2).

No obvious change in enthalpy ΔH_{diff} was observed upon 30% deformation (Fig. 4.6a). But from 37% on, ΔH_{diff} started increasing, and reached on average ≈ 667 J/mol after 85% deformation, which

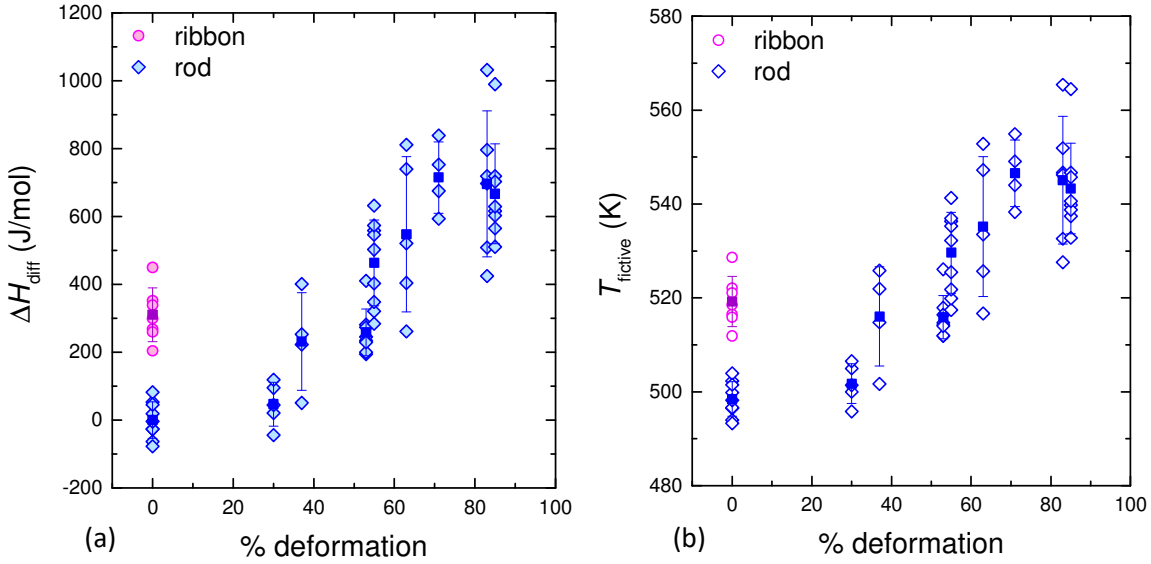

Fig. 4.6. The increase in energy ΔH_{diff} (a) and of the fictive temperature $T_{fictive}$ (b) of the rod after compression to different degrees of deformation (blue symbols) and of the as-cast ribbon (pink symbols). The zero point in (a) was taken as the average value of $\int_{T_1}^{T_2} C_{p,as\text{-}cast}(T)\mathrm{d}T$ for the as-cast rod. The solid symbols and error bars correspond to the mean ± 1× standard deviation.

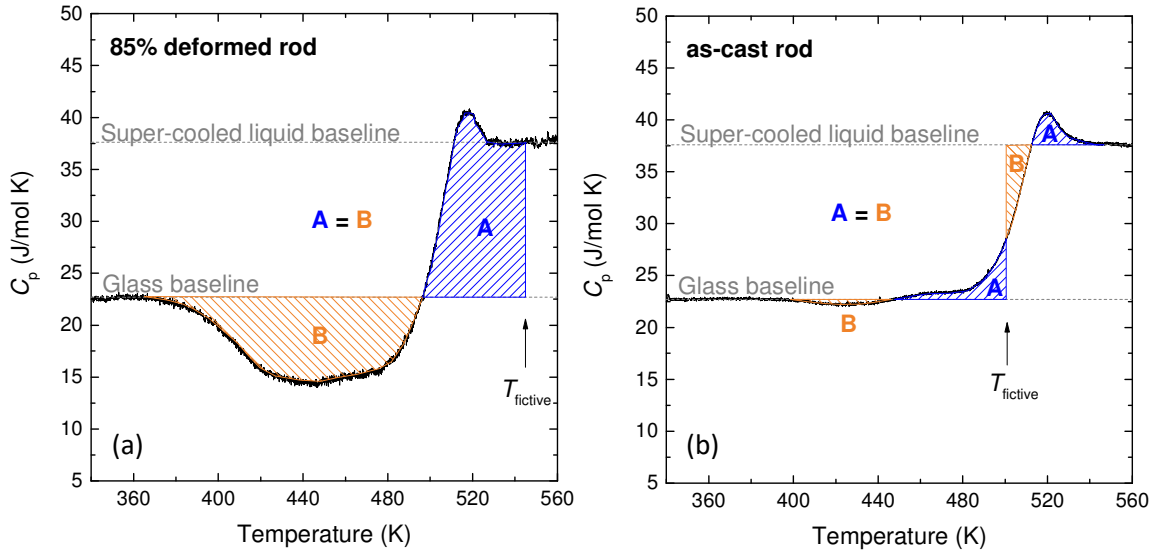

Fig. 4.7. Examples of the equal-area construction used for determining the fictive temperature $T_{fictive}$, in the case of an 85% deformed sample (a) and an as-cast rod sample (b). $T_{fictive}$ is placed so that when considering the glass transition to occur as a simple step at $T_{fictive}$, the area contained below the measured curve but above the horizontal line (area A) is equal to the area below the horizontal line but above the measured curve (area B).

corresponds to 9% of the heat of melting ΔH_m (ΔH_m = 7.5 kJ/mol [148]). ΔH_{diff} seems to increase linearly with the degree of plastic strain, and there is no clear saturation of the effect. The spread in ΔH_{diff} of the as-cast rod is around 160 J/mol, which is similar to the measurement error of ΔH_{diff}, as was estimated in Appendix A. The spread of values is higher for the deformed samples, ranging up to 600 J/mol, and is considerably larger than the estimated measurement error. A reason for the large spread may be because more unrelaxed samples are generally more heterogeneous [21, 150, 151, 152]. However, the length-scales of these heterogeneities are in the order of nm–µm, which is smaller than the size of the sample pieces measured in FDSC. A more likely reason is that the degree of plastic deformation was not uniform across the entire sample. Because the top and bottom sample surfaces are not perfectly even, nor are they perfectly parallel to each other, different areas of the sample will be affected differently during compression. The spread in the measured ΔH_{diff} values may also be due to the fact that the induced deformation is inhomogeneous, i.e. plastic strain occurred via shear banding. However, the FDSC sample pieces are most likely larger than the shear band spacing. The latter is in general expected to be roughly a tenth of the sample

Table 4.1. Values of the increase in energy upon plastic deformation induced by various treatments, according to literature, as well as the percentage of mechanical work done the stored energy corresponds to.

Process	Details	Energy increase ΔH_{diff} (J/mol)	% of work done
Cold-rolling	36% thickness reduction of a Pd-based ribbon [42]	200	4%
	90% thickness reduction of a Cu-based BMG [41]	820 (rolled at RT) 1350 (rolled at 150 K)	
High-pressure torsion	925 strain applied to a Zr-based rod [52]	1770	4%
Shot-peening	Pd-based BMG [57]	85	6%
Uniaxial compression	40% strain of a Zr-based rod [62]	160	1.5%
Tri-axial compression	40% strain of a notched Zr-based rod [62]	640 (notched region) 2930 (edge of notched region)	4.5%
Present work: Compression of low aspect ratio samples	37%	230	-
	55%	500	3%
	85% sample height reduction	670	-

thickness after deformation [153]. As in our case the samples after compression had a thickness of around 100 µm, the shear band spacing is probably one order of magnitude smaller than the FDSC sample pieces, and it is thus unlikely that the presence of shear bands play a large role in the spread of measured values.

The energy of a glass can also be described in terms of its fictive temperature $T_{fictive}$, which corresponds to the T_g measured at the same rate as the glass was cooled upon glass formation. $T_{fictive}$ can be determined through the equal-area construction at the glass-transition step [154], examples of this construction are given in Fig. 4.7. As $T_{fictive}$ is directly linked to the enthalpy, it shows the same trend upon deformation and has a similar spread in values as ΔH_{diff} (Fig. 4.6b). After 85% deformation, $T_{fictive}$ is on average ≈ 543 K, whereas the average $T_{fictive}$ value of the as-cast sample is ≈ 498 K; this is an increase of > 40 K.

For comparison, FDSC traces of an as-cast ribbon of the same composition were also measured. The internal energy of the ribbon was on average 310 J/mol higher than of the as-cast rod (Fig. 4.6), and $T_{fictive}$ ≈ 519 K. Ribbons are expected to have states of higher energy than rods, since higher cooling rates are applied during ribbon fabrication than during the casting of rods. But after compressing the rod by around 53–55%, an equivalent energy state as the ribbon could be reached.

The rejuvenation effect upon plastic compression observed here is similar to the energy increase induced by other plastic deformation methods found in the literature; some examples are shown in Table 4.1. In order to compare the efficiency of different methods, the induced energy (i.e. stored energy), is compared to the total mechanical energy needed during the process (i.e. work done). By estimating the work done in the present results from the stress–strain curve, we find that, in the case of the sample deformed by 55%, the stored energy is ≈ 3% of the work done (see Appendix A).

4.3.3 Ageing and the appearance of an endothermic sub-T_g peak

The temperature at which plastic deformation takes place is an important parameter for the achievable rejuvenation. Cold-rolling of a Cu-based bulk metallic glass at 150 K led to a significantly higher energy increase (1350 J/mol) than at room temperature (820 J/mol) [41]. Another example was shown for shot-peening [58]. The change in energy induced by shot-peening of a Pd-based metallic glass was larger at 77 K than at 298 K, whether considering the relaxation of the as-cast sample or the rejuvenation of the pre-annealed sample. During processing, there is always a competition between the damage created upon deformation and the repair of this damage through thermal relaxation [58]. At lower temperatures, thermal relaxation is diminished, and more damage is retained.

If the induced damage can be partially repaired during the deformation process at room temperature (RT), then repair may also be non-negligible after deformation, i.e. when the sample is simply sitting at RT.

For the present composition, RT (= 298 K) is around 66% of T_g (= 471 K). This is a considerable fraction, at which relaxations may occur. Structural relaxations are a universal feature of amorphous materials, and can be measured, among other methods, by dynamic mechanical analysis. The main relaxation mode, the α-relaxation, is linked to the glass transition and is only activated around T_g. On the other hand, the secondary β-relaxation, correlated to the localized motion and connected to shear-banding and deformation mechanisms, can occur well below T_g [26, 155]. In any case, RT ageing can be non-negligible for metallic glasses, especially for the La-based composition studied here [156]. It should be noted that samples termed here as "as-cast" were not fresh from fabrication, but were used after being stored for around 1 year at RT.

The effect of RT annealing was investigated here on the La-based rod deformed by 71%. Upon ageing, the area of the exothermic structural relaxation peak seems to decrease (Fig. 4.8), which is expected during thermal relaxation. After 42 days at RT, a small endothermic peak appears at the onset of the exothermic peak, which becomes more evident after 166 days. The appearance of such an endothermic sub-T_g peak after annealing below T_g has been frequently reported in literature, not only for metallic [157, 158, 159, 160, 161], but also for other glass systems [162, 149]. For some liquids, upon cooling from the melt, a glass can be produced which is heterogeneous and contains different zones of a wide range of relaxation times. Upon annealing at a certain temperature and

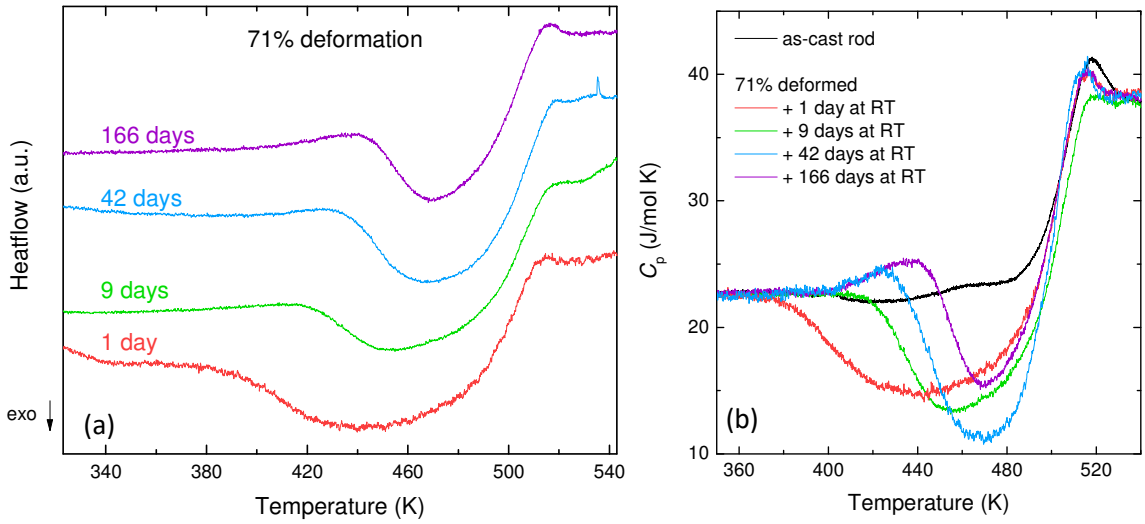

Fig. 4.8. Example heat flow curves measured at 100 K/s by FDSC of the La-based rod sample compressed by 71% and annealed at RT for up to 166 days, focused on the structural relaxation event below the glass-transition step (a). Specific heat flow curves C_p (b) were obtained by appropriate scaling of the heat flow curves.

time, zones with the appropriate relaxation times will relax. When heated up in a DSC scan, these relaxed zones disorder again and return to a higher-energy state, visible as an endothermic peak in the DSC trace. The peak size and the temperature at which it occurs depends on the annealing treatment.

The effect of RT annealing on the energy of the 71% deformed samples is shown in Fig. 4.9. The compression-induced rejuvenation relaxes away with time: after 166 days at RT, ΔH_{diff} decreased on average from 715 to 183 J/mol and $T_{fictive}$ decreased from 547 to 510 K. The sample is still slightly rejuvenated compared to the as-cast rod, but has now a lower energy than the as-cast ribbon. The energy decays exponentially with time. From the measured data in Fig. 4.9, it is difficult to say if the energy will further decrease or if saturation has been reached. In any case, the relaxation is substantial. This puts into question the usefulness of rejuvenation by deformation of metallic glasses that have a relatively low T_g, especially for practical applications.

The change in enthalpy upon heating is not the only information that can be extracted from a DSC trace. The shape of the heat flow (or C_p) curve below and around T_g depends on the relaxation events that occur upon heating, and thereby provides more detail on the structure and properties of the glass. For example, in the 71% deformed rod subjected to ageing, the decrease in energy is manifested by the appearance of an endothermic sub-T_g peak, which overlaps onto the exothermic structural relaxation peak; this results in a decrease in size of the latter. RT annealing does not seem to reverse the deformation-induced rejuvenation, in the sense that annealing is not simply a

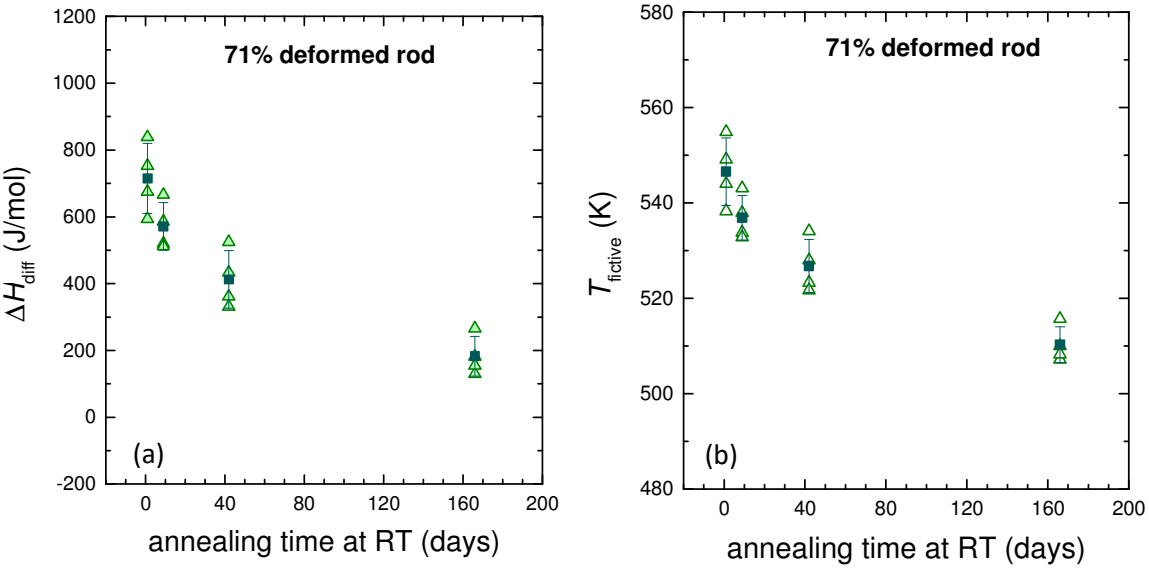

Fig. 4.9. Effect of room temperature (RT) annealing on the increase in energy ΔH_{diff} (a) and on the fictive temperature $T_{fictive}$ (b) of the La-based rod after 71% deformation. The solid symbols and error bars correspond to the mean ± 1× standard deviation. As for Fig. 4.6a, the zero point in (a) was taken as the average value of the as-cast rod.

backwards process of the rejuvenation, but instead adds an additional effect to the sample. As seen in the DSC traces (Fig. 4.8), the exothermic peak does not flatten with time, instead it keeps its depth but becomes narrower due to the superposition of the endothermic peak. This can be understood as the following: plastic deformation introduces several "soft" zones (which are more disordered than the rest of the glass) of a wide range of relaxation times. Upon annealing of the glass, some soft zones relax, whereas others stay soft. During heating in DSC, the relaxed zones become disordered again (endothermic event) whereas the zones which are still soft will relax (exothermic event).

4.3.4 Effect of heating rate on the observed sub-T_g peak

The position of the endothermic sub-T_g peak depends not only on the annealing treatment, but also on the heating rate at which the DSC trace was measured. At higher heating rates, the peak moves to higher temperatures [157], as was seen for the 71% deformed rod after 42 days at RT (Fig. 4.10a). Meanwhile, the exothermic structural relaxation became smaller, until it disappeared when the heating rate was faster than 2000 K/s.

In the case of the La-based ribbon, an endothermic sub-T_g peak also occurred when heated at rates above 100 K/s (Fig. 4.10b). As mentioned above, this ribbon was not measured directly after production, but after ageing for 1 year at RT. Due to the high cooling rates during melt-spinning, soft (high-energy) zones were probably introduced in the ribbon upon glass formation. Some of these soft zones relaxed during RT annealing, therefore causing an endothermic sub-T_g peak to appear upon heating in DSC. When measuring the ribbon at 7000 K/s, the sub-T_g peak overlapped onto the glass transition, and was not visible anymore at 10,000 K/s. In the work of Hu et al. [163], a ribbon of the same composition as here was pre-annealed at different temperatures before the C_p curve was measured in DSC. Hu et al. did not observe any endothermic sub-T_g peak upon annealing. This might be due to the fact that their DSC measurements were only performed at a relatively low heating rate of 20 K/min (= 0.333 K/s).

Heat flow traces of the as-cast rod measured at different heating rates are shown in Fig. 4.10c. For this sample, no distinct endothermic sub-T_g peak was observed for the entire range of rates applied. At 0.333 K/s, a small exothermic structural relaxation peak was observed below T_g, which shrinks at 20 K/s and is absent at 100 K/s. The rod was produced by casting; cooling rates upon casting of rods are typically orders of magnitude lower than upon melt-spinning of ribbons. Consequently, the produced rod is probably less heterogeneous than the ribbon, i.e. there are less

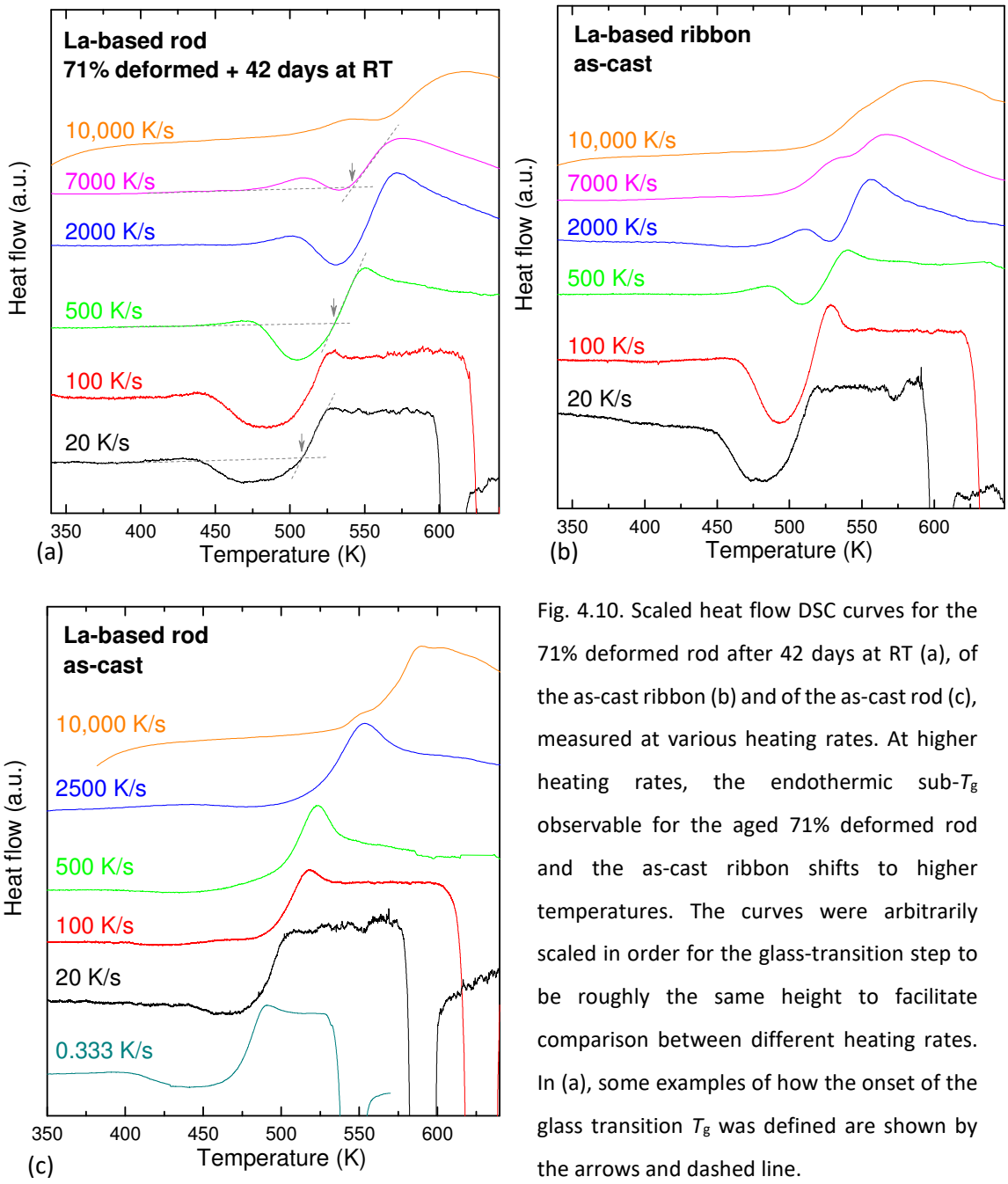

Fig. 4.10. Scaled heat flow DSC curves for the 71% deformed rod after 42 days at RT (a), of the as-cast ribbon (b) and of the as-cast rod (c), measured at various heating rates. At higher heating rates, the endothermic sub-T_g observable for the aged 71% deformed rod and the as-cast ribbon shifts to higher temperatures. The curves were arbitrarily scaled in order for the glass-transition step to be roughly the same height to facilitate comparison between different heating rates. In (a), some examples of how the onset of the glass transition T_g was defined are shown by the arrows and dashed line.

pronounced soft zones, which relax less during RT annealing, explaining the absence of an endothermic sub-T_g peak.

4.3.5 Activation energies of the sub-T_g peak, the glass transition and crystallization

The activation energy of the sub-T_g peak can be determined from the shift in peak temperature due to the increase in heating rate. According to the Kissinger analysis [143], the activation energy E is determined from:

$$\frac{\mathrm{d}\ln\left(\alpha/T_\mathrm{p}^2\right)}{\mathrm{d}\left(1/T_\mathrm{p}\right)} = -\frac{E}{R} \tag{4.3}$$

where α is the heating rate, T_p the peak temperature and R the gas constant. The sub-T_g peak temperatures (T_p) measured here were plotted in the form of $\ln(\alpha/T_\mathrm{p}^2)$ as a function of $1/T_\mathrm{p}$ (Fig. 4.11). These points were then fitted with a linear equation, from whose slope the activation energy $E_{\text{sub-Tg}}$ was deduced. $E_{\text{sub-Tg}}$ was found to be around 100 ± 20 kJ/mol for the as-cast ribbon as well as for the rod deformed by 71% and aged (Table 4.2). This value is practically equal to the activation energy found for the β-relaxation in this metallic-glass composition [156, 163].

The activation energies for crystallization (E_{Tx}) and for the onset of the glass transition (E_{Tg}) were also calculated, and are summarized in Table 4.2 (examples of how T_g was defined are shown in Fig. 4.10a). The shifts of these characteristic temperatures with heating rate are shown alongside the values of the endothermic sub-T_g peak in Fig. 4.12. More detailed Kissinger plots (i.e. $\ln(\alpha/T^2)$ as a function of $1/T$) for T_x and T_g can be found in Appendix A (Fig. A.3). The data for the as-cast ribbon and the deformed rod seem to lie on a straight line. On the other hand, a linear fitting of the data points is questionable for the as-cast rod, which was measured not only in FDSC, but also at lower heating rates in CDSC. Instead, the data points seem to lie rather on a slightly curved line, with a steeper slope at low heating rates than at high rates, therefore E_{Tg} and E_{Tx} are higher at lower rates (Table 4.2). Curving at high heating rates of the Kissinger plot for crystallization has been encountered in the literature [164, 165], and was correlated to the change in temperature dependence of the liquid viscosity [164].

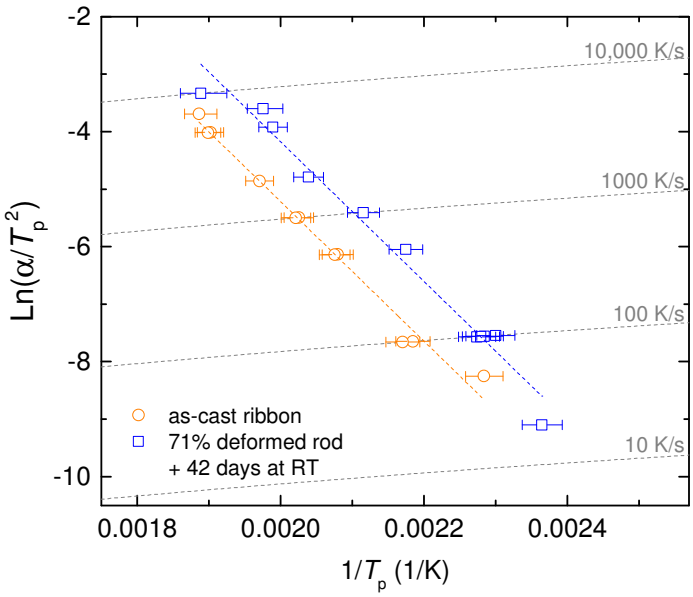

Fig. 4.11. Kissinger plot showing the peak temperature T_p of the endothermic sub-T_g event at different heating rates for the as-cast ribbon and for the 71% deformed rod aged at RT. The dashed blue and orange lines show the linear fitting of the data points.

Table 4.2. Activation energies of the endothermic sub-T_g event, of crystallization and of the onset of the glass transition. The energies of the β-relaxation, crystallization and glass transition from the literature of the same glass composition $La_{55}Ni_{20}Al_{25}$ are also shown here.

		Sample	Heating rate range (K/s)	Activation energy (kJ/mol)
Present work	Sub-T_g peak	As-cast ribbon	20–10,000	101 ± 21
		71% rod + 42 days RT	20–10,000	101 ± 17
	T_x peak	As-cast ribbon	20–1000	113 ± 28
		As-cast rod	20–1000	112 ± 36
		As-cast rod	0.333–100	185 ± 34
		71% deformed rod + 42 days RT	20–2000	112 ± 30
	T_g onset	As-cast ribbon	20–2000	351 ± 88
		As-cast rod	20–10,000	274 ± 58
		As-cast rod	0.333–100	357 ± 89
		71% deformed rod + 42 days RT	20–10,000	272 ± 48
Literature	β-relaxation	Ribbon [163]	-	109.9 ± 8
		Ribbon [156]	-	100
	T_x peak	As-cast rod [146]	0.042–0.67	161 ± 7
	T_g inflection	As-cast ribbon [148]	0.0167–0.67	376.9
	T_g onset	As-cast rod [146]	0.042–0.67	285 ± 20

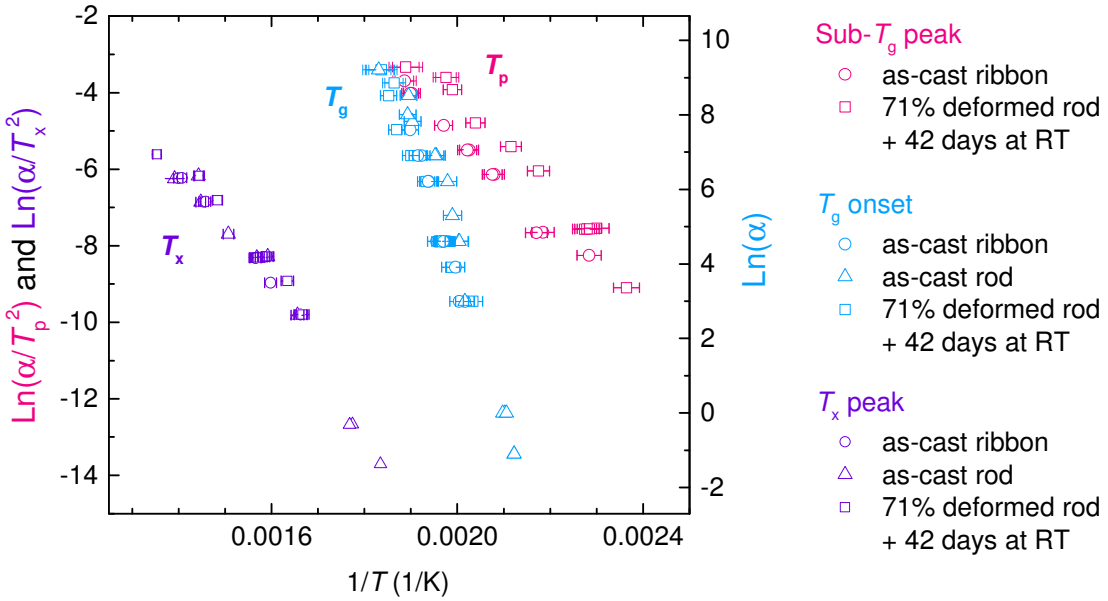

Fig. 4.12. Kissinger plots of the endothermic sub-T_g peak T_p, glass transition onset T_g and crystallization peak T_x measured for the as-cast ribbon, as-cast rod, and rod after deformation and ageing.

In any case, the obtained values from linear fittings for E_{Tg} (270–360 kJ/mol) and for E_{Tx} (110–185 kJ/mol) calculated here are in a similar range as was determined in the literature (E_{Tg} ≈ 280–380 kJ/mol [146, 148]; E_{Tx} ≈ 160 kJ/mol [146]). Although the errors are quite large, E_{Tg} is clearly higher than $E_{sub\text{-}Tg}$, indicating that it is easier to activate the sub-T_g peak than the glass transition. This is explained by the fact that the glass transition is a reordering process of the global atomic structure [155], whereas the endothermic sub-T_g event is due to short-range disordering of localized zones [163, 166].

4.3.6 Calculation of the fragility and estimation of the effective cooling rates

T_g is determined upon glass formation, and is therefore related to the viscosity of the supercooled liquid; crystallization also occurs in the supercooled liquid state, therefore its transformation rate should also scale with the viscosity of the liquid. Indeed, the activation energies of T_g and T_x were found to match that of viscous flow [167], and it is consequently possible to estimate the temperature dependence of the liquid viscosity from T_g and T_x. According to Angell [168], glass-forming systems can be classified as *strong*, having a near-Arrhenius temperature dependence of viscosity, or as *fragile*, with a non-Arrhenius dependency. Covalent glasses (e.g. SiO_2) tend to be *strong*, whereas organic liquids (e.g. o-terphenyl) are rather *fragile*; metallic glasses lie in between. The temperature dependence of viscosity $\eta(T)$ is generally displayed as an "Angell plot", which shows $\log(\eta)$ as a function of T_g/T. An Angell plot for the present metallic glass sample was determined from the heating-rate dependence data of T_g and T_x, since the plots of $\log(1/\alpha)$ as a function of $(1/T_g)$ and of $\log(T_x^2/\alpha)$ as a function of $(1/T_x)$ should be equal to the plot of $\log(\eta)$ as a function of $(1/T)$, apart from a shifting constant (Fig. 4.13). The temperature dependence of viscosity $\eta(T)$ between melting and T_g can usually be well described by the Vogel–Fulcher–Tammann (VFT) equation (as can be found in ref.[169])

$$\eta(T) = \eta_0 \exp\left(\frac{D^* T_0}{T - T_0}\right) \tag{4.4}$$

where η_0, D^* and T_0 are fitting parameters.

The fragility m is defined as the slope of the Angell plot at $T=T_g$ [169], with high m corresponding to a more fragile liquid. By fitting the data in Fig. 4.13 with the VFT equation, a fragility m ≈ 47 was obtained, which is relatively close to that found in literature for the studied composition $La_{55}Ni_{20}Al_{25}$ [148]. The fitting parameters of our data are given in Appendix A (Table A.1).

By knowing the fragility as well as the fictive temperature $T_{fictive}$ of a glass, its effective cooling rate (i.e. the cooling rate applied during glass formation) can be estimated. According to definition,

a glass cooled at 20 K/min should have a viscosity of $\eta = 10^{12}$ Pa s at T_g [168]. The viscosity at the glass transition is inversely proportional to the effective cooling rate, and thereby by knowing the viscosity at a specific temperature $T_{fictive}$, the cooling rate can be estimated. The effective cooling rate was defined in this manner for the La-based as-cast ribbon and rod, as well as for the rods compressed, and thereby rejuvenated, to different degrees; the values are displayed in Table 4.3. The effective cooling rates of the as-cast ribbon and rod were calculated to be 690 K/s and 40 K/s; these values are obviously lower (and, in the case of the ribbon, much lower) than the cooling rates that were applied during their fabrication. These low values reflect the fact that the samples called here "as-cast" are not fresh but have been aged at room temperature.

Upon 85% deformation of the rod, the energy was found to increase in average by ≈ 667 J/mol, and $T_{fictive}$ by > 45 K, as mentioned above. The effective cooling rate increased from 40 to 9300 K/s, an increase of almost 3 orders of magnitude. This means that to obtain a rod with an equivalent energy state upon quenching from the melt, it would have to be cast with a cooling rate of 9300 K/s.

As shown in Table 4.3, the effective cooling rate of the sample deformed to 71% thickness reduction was estimated to be 13,000 K/s, which is higher than for the 85% deformed sample. This

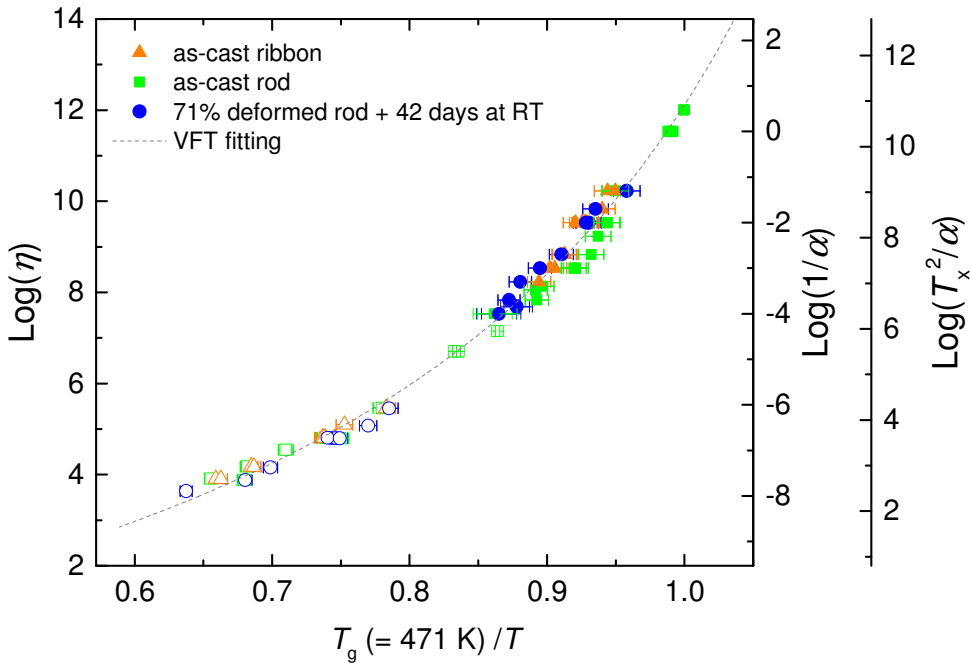

Fig. 4.13. Angell plot determined from the temperatures of glass-transition onset, T_g, and crystallization peak, T_x, measured at different heating rates α, thereby giving the temperature dependence of viscosity η. By definition, a viscosity of 10^{12} Pa s is expected at a temperature equal to the T_g measured at 20 K/min [168], which for the present sample is 471 K. The log(1/α) (corresponding to the T_g data points) and the log(T_x^2/ α) (corresponding to the T_x points) axes were accordingly shifted vertically to satisfy this convention.

Table 4.3. Summary of the average fictive temperature $T_{fictive}$, the viscosity η at $T_{fictive}$ determined from the Angell plot, and the corresponding effective cooling rate for the as-cast ribbon, as-cast rod, as well as for rods compressed by 37, 63, 71 and 85%.

Sample	$T_{fictive}$ (K)	Log(η)	effective cooling rate (K/s)
As-cast ribbon	519	8.7	690
As-cast rod	498	9.9	40
37% deformed rod	521	8.6	890
63% deformed rod	535	7.9	4200
85% deformed rod	543	7.6	9300
71% deformed rod + 1 day at RT	547	7.4	13,000
+ 9 days at RT	537	7.8	5000
+ 42 days at RT	527	8.3	1700
+ 166 days at RT	510	9.2	230

is because the average $T_{fictive}$, on which the determination of the effective cooling rate is based here, is slightly higher for the 71% (547 K) than for the 85% deformed sample (543 K), even though the degree of achievable rejuvenation seems to be lower for the 71% deformed sample according to the trend given by the ΔH_{diff} and $T_{fictive}$ data in Fig. 4.6.

4.4 Conclusions

Introduction of damage through plastic deformation is a well-known approach to increase the energy of metallic glasses and change their properties, and has been explored for more than 40 years, by typically using methods such as cold-rolling to apply large deformation while avoiding fracture. In the present work, an infrequently used approach to reach large plastic strains was explored, in which brittle fracture is avoided by deforming samples with a low aspect ratio through uniaxial compression. Large plastic strains leading to a reduction of up to 85% in sample height were thereby achieved in $La_{55}Ni_{20}Al_{25}$ rods. The resulting increase in internal energy of the metallic glass was determined here, which has not yet been frequently measured in literature for this approach of inducing rejuvenation. FDSC was employed here, which allowed several measurements of the same sample to be performed. For a certain amount of deformation, a large spread in the

degree of rejuvenation was observed, indicating that damage was probably not introduced homogeneously in the sample. After 85% deformation, the average increase in energy was around 670 J/mol, which is in the range of values obtained through other plastic deformation-inducing methods such as cold-rolling or high-pressure torsion.

By determining the fragility of this glass composition through the measurement of the onset of glass transition T_g as well as the crystallization peak T_x at different heating rates, effective cooling rates of the rejuvenated samples were estimated. The energy states of these samples were found to correspond to effective cooling rates of up to approximately 10,000 K/s.

For the studied metallic glass composition $La_{55}Ni_{20}Al_{25}$, room temperature (RT) is a relatively high fraction of T_g, and consequently thermal relaxation at RT can be significant. The effect of RT ageing was investigated here on a rod deformed by 71%. The deformation-introduced increase in energy was found to relax away with time, and disappeared almost entirely after 166 days. This relaxation was manifested by the appearance of an endothermic sub-T_g peak in the DSC trace, which is a signature of relaxed soft regions disordering again upon heating. This indicates that plastic deformation increased the heterogeneity of the glass, inducing zones of a wide spectrum of relaxation times, some of which re-order again upon storage at RT. This is similar to what is expected, and what was found, for melt-spun ribbons. Whereas no sub-T_g peak was detected for a pre-annealed La-based ribbon in literature [163], this peak was observed here for ribbons, by heating at high rates only achievable by FDSC.

To conclude, a La-based rod could be rejuvenated by plastic deformation, and even though the increase in energy relaxed away upon storage at RT, the deformed rod showed similar characteristics as the RT-aged melt-spun ribbon.

5 Elastic Cycling

5.1 Introduction

The previous chapter dealt with the possibility of changing the properties of a metallic glass through plastic deformation. In the case of crystalline alloys, the use of plastic strains is a well-known technique to change properties and one of the basic procedures for mechanical processing. By definition, 'plastic deformation' corresponds to a permanent change in shape. Plastic flow in crystalline alloys occurs through the glide of dislocations and can cause their multiplication, which can lead to a change in properties. In contrast, 'elastic' is defined as reversible, meaning the material returns to its original state after the stress is removed. Nevertheless, it was found that even before the apparent macroscopic yielding of glasses, local strains can be high enough to rearrange the atomic configuration [36]. These rearrangements are not completely recovered upon stress removal, leading to a different final structure. This is because glasses are heterogeneous and show non-affine strains. In a simple crystal, all atoms have an identical surrounding, and displacements are affine. But in a glass, each atom has a unique surrounding; the displacements can have, apart from an affine component, also non-affine contributions [35], which can lead to a partly irreversible change in structure.

By thermomechanical processing of metallic glasses in the macroscopic elastic regime, a range of energy states could be reached, with improvements in mechanical properties. For example, rejuvenation of bulk metallic glasses was obtained through elastostatic loading (§2.1), where a static compressive load in the elastic regime was applied for several hours, which led to creep and viscous flow [64, 65, 66, 67]. Another example which exploits strains within the elastic limit is thermal cycling [99]. By cycling a metallic glass between room and liquid-nitrogen temperature, thermal strains within the elastic limit were introduced. Both methods led to an increase in compressive plasticity of the sample, as well as an increase in energy of 100–300 J/mol.

Although rejuvenation of metallic glasses is often desired with the aim of reducing their brittleness, relaxation has also many advantages, for example increases in thermal stability and resistance to crystallization, higher corrosion resistance, and higher hardness. Relaxation through elastostatic loading was observed for Zr-based metallic-glass rods [70]. After compressive loading at 90% of the yield stress for 5 days, an increase in density, hardness and yield strength as well as a decrease in energy was observed. Relaxation was also achieved by subjecting a bulk metallic glass

to ultrasonic waves at room temperature for 48 h [87], after which the glass apparently showed an increase in hardness, elastic modulus, and a higher thermal stability.

Strengthening of metallic glasses was also observed upon elastic cycling with a nanoindenter [74, 75, 76]. Yielding of metallic glasses can be detected by nanoindentation using a spherical tip as the first displacement burst in the load–displacement curve when indenting at a constant loading rate. Discrete displacement bursts, named 'pop-ins', correspond in metallic glasses to the activation of shear events, and represent the initiation and propagation of shear bands [128, 170]. Upon cyclic loading with a spherical indenter in the nominal elastic range, the yield load (i.e. the load at which the first pop-in appears), was found to increase in the case of several metallic-glass compositions. The cycling was understood to lead to the accumulation of small and permanent structural changes, and the induced hardening was interpreted as a gradual 'shaking down' of the glass to an ideal state with higher structural order [74].

It was often attempted to demonstrate a correlation between the mechanically induced structural ordering and the more 'conventional' relaxation caused by annealing [74, 81, 131]. It would be interesting if an equivalent or even superior relaxation effect through mechanical means could be obtained than by thermal annealing. The hope would be to reach highly ordered states by reducing the risks of annealing such as crystallization or oxidation, or even to achieve ultrastable states which might not be accessible through thermal relaxation. But the hardening effect of elastic cycling was sometimes observed to dissipate with time once the load was removed [76, 80, 81]; the viability of obtaining highly stable states via elastic cycling, which are durable, is therefore questionable.

In the present work, the effect of elastic cycling was tested on a CuZr-based bulk metallic glass, with the major aim of comparing it to the relaxation induced by annealing. Nanoindentation was employed here to apply the elastic cycles as well as to measure the change of sample properties. One advantage of nanoindentation is that it is a non-destructive method, therefore the effect of elastic cycling and annealing could be tested on the same sample, and errors arising from the variation between samples could be avoided. Furthermore, the influence of the initial sample structure on the cycling effect was also explored. The sample was subjected to elastic cycling not only in the as-cast state, but also after rejuvenation induced by thermal cycling, and after thermal annealing.

5.2 Experiments

5.2.1 Sample preparation

A sample with the dimensions of around 2.5 mm × 2 mm × 0.5 mm was cut from a metallic-glass plate of the composition $Cu_{46}Zr_{46}Al_7Gd_1$. A good surface finish of the sample is critical to achieve correct results by nanoindentation; the polish finish should be comparable to the depth of indentation, if not better, and surface damage during polishing, such as hardening, should ideally be avoided. To achieve an adequate surface finish, the sample was polished with SiC abrasive grinding papers down to the grit size P4000, followed by 1 µm and $^1/_4$ µm diamond paste, and finally with a 0.06 µm colloidal silica suspension.

5.2.2 Sample treatments

As mentioned above, the effect of elastic cycling was tested on three different initial structural states: 1) as-cast, 2) in a less relaxed state, which was attempted to be obtained through thermal cycling, and 3) in a more relaxed state, achieved through thermal annealing.

Thermal cycling was carried out according to the work of Ketov et al. [99], and as described in §3.1.2. 10 cycles were carried out here, because in the literature, 10 thermal cycles were found to significantly increase plasticity in compression [99]. After thermal cycling, the sample surface was repolished with colloidal silica suspension.

Annealing was performed for 24 h at 630 K, which corresponds to 90% of T_g (≈ 700 K [171]. To prevent oxidation as much as possible, the sample was enclosed along with titanium beads in a silica-glass tube under vacuum before being placed in the furnace. After annealing, the sample was repolished with diamond paste and colloidal silica suspension to remove the oxide layer. No crystallization after annealing was detected by X-ray diffraction (Appendix B, Fig. B.1).

5.2.3 Nanoindentation measurements and elastic cycling

Sample characterization and elastic cycling were performed by nanoindentation, which was carried out at room temperature on a MTS Nanoindenter XP with a diamond spherical indenter of tip radius 8 µm. For all tests, the maximum allowable thermal drift was set to 0.07 nm/s. Indentation was performed under load control, with a loading and unloading rate of 0.5 mN/s. Details of the procedure for determining the mechanical properties from the nanoindentation curves are given in §3.2.3. An advantage of nanoindentation is that a large number of

measurements can be made on the same sample, allowing a reliable average value to be determined. Here, between 40 and 95 indents were made per test. The indents were taken within an area of approximately 500 µm x 500 µm, and the spacing between neighbouring indents was at least 20 µm. Two types of indentation tests were carried out:

1) *Simple indentation*: This test was used to measure the initial mechanical properties of the sample. The sample was indented to a maximum load F_{max}, then unloaded (Fig. 5.1a and b). F_{max} was chosen so that it was above the initial yield load F_y, defined as the load at which the first pop-in appeared. F_{max} was accordingly set to 70 mN for the sample as cast and after

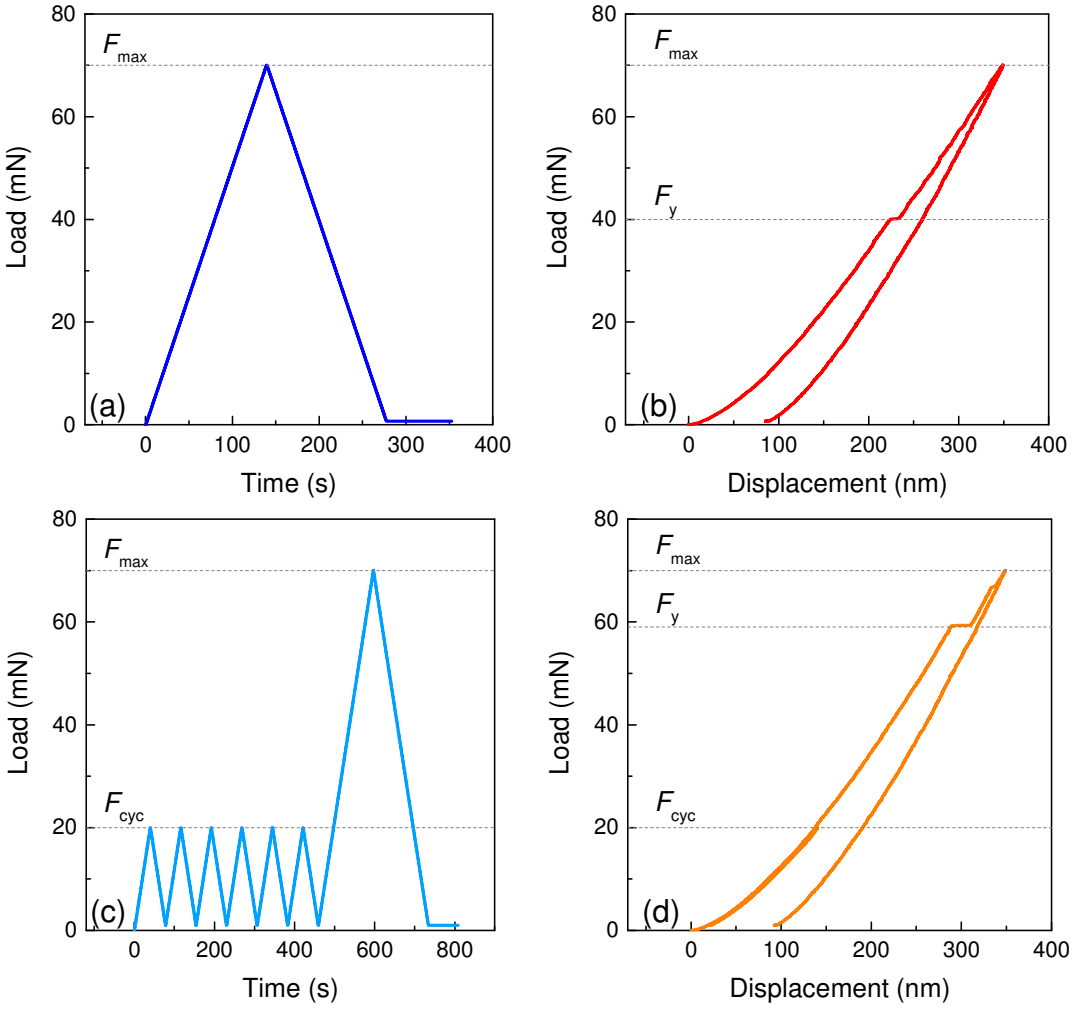

Fig. 5.1. In a 'simple' indentation measurement (a and b), the sample is indented monotonically to a maximum load F_{max}, during which the sample yields. The activation of shear events are visible as 'pop-ins' in the load–displacement curve; the load at which the first pop-in occurs is defined as the initial yield load F_y. During a 'cyclic' indentation test (c and d), the sample is cycled in the nominally elastic regime, i.e. to a load F_{cyc} which is well below F_y, before being indented up to F_{max}.

thermal cycling, though this had to be increased to 120 mN for the annealed sample as it had a higher F_y.

2) *Cyclic indentation*: In this test, the sample was subjected to elastic cycling. Six cycles of loading and unloading were applied to the sample. The maximum load of these cycles, F_{cyc}, was set to approximately 50% of the average F_y, previously determined by the "simple indentation" tests, in order to stay in the elastic regime. For the sample in its as-cast, thermally cycled and annealed states, F_{cyc} was chosen as 20 mN, 15 mN and 20 mN, respectively. Immediately after these elastic cycles, a final load of F_{max} was applied which led to yielding of the sample (Fig. 5.1c and d) and from which the effect of elastic cycling on the mechanical properties was determined.

As mentioned above, all treatments were applied on the same sample in order to maximize comparability between the different effects. The order of sample treatments and nanoindentation measurements is summarized in Fig. 5.2. The as-cast sample was first characterized by nanoindentation (simple as well as cyclic indentation) before being subjected to thermal cycling, followed by further nanoindentation. Finally, the sample was annealed, and indentation was performed once again.

Since many indents were performed per sample state, the results from all indentation load–displacement curves are presented in the form of a cumulative distribution curve, with an average value characterized by the median point at 50%. Cumulative distribution curves also help to characterize the spread of values obtained for each sample state. It was observed in the literature [131] that the variability in yield behaviour of metallic glasses, when measured at temperatures

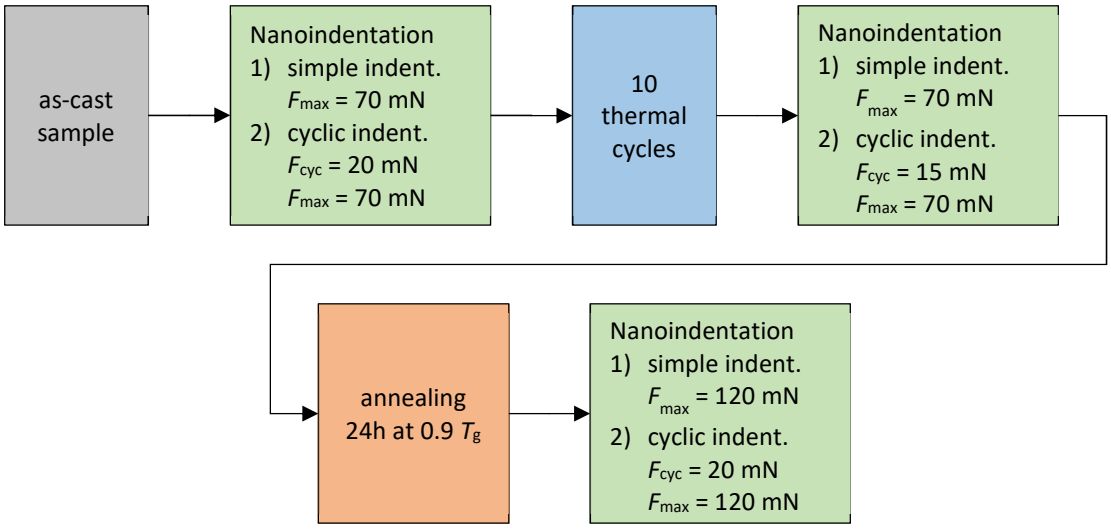

Fig. 5.2. Flow-chart showing the order of treatments and nanoindentation tests applied to the CuZr-based metallic-glass sample.

well below the glass transition, is mainly due to the structural heterogeneity of the glass (whereas in the case of single crystals, thermal fluctuations are the dominating reason for variation in the measured yield values).

5.3 Results and discussion

5.3.1 Behaviour at the first yield event

The mechanical properties determined by nanoindentation are displayed in the form of cumulative distribution curves in Fig. 5.3. Apart from the typical indentation results of hardness and elastic modulus, information on the beginning of yielding could also be obtained, since a spherical indenter tip was used (see §3.2.1). The appearance of the first pop-in during spherical indentation corresponds to the first shear event (i.e. first activation of shear transformation zones); the load at which this occurred is defined as the *initial yield load* F_y, and the stress at this point is the *initial yield pressure* P_y.

After thermal cycling the as-cast CuZr-based metallic-glass sample, the F_y values were lower by around 28%, meaning that the onset of shear banding was facilitated. Subsequent annealing increased F_y again, to a similar median value as that of the as-cast sample. Annealing relaxes metallic glasses, and is known to bring them to more ordered states with typically higher yield loads and lower plasticity.

Elastic cycling on the as-cast sample was found to increase the median F_y value by around 39% (Fig. 5.3a); this is a similar 'strengthening' effect as was observed in the literature upon elastic nanoindentation cycling of Fe- and Pd-based metallic glasses [74, 75, 76].

The effect of elastic cycling was also explored on the sample after being thermally cycled and after annealing. When applied to the annealed sample, the median value of F_y increased by 42%, which is similar to what was observed for the as-cast state. But when applied to the sample after thermal cycling, the strengthening effect was smaller; the median of F_y increased by only 19%. It is interesting to note that the annealed sample, which should already have been significantly relaxed, could be further strengthened, whereas the thermally cycled sample, which should be rejuvenated, was less affected. One may argue that this is because the cycling amplitude F_{cyc} was smaller for the thermally cycled sample than for the as-cast and annealed sample (the absolute load F_{cyc} was 15 mN instead of 20 mN), but the relative load applied F_{cyc}/F_y was approximately the same for all sample states, i.e. F_{cyc} was chosen as 50% of the median F_y. In any case, it is difficult to explain this result if

elastic cycling induces relaxation, since rejuvenated samples should be in principle more affected than already very relaxed ones. The current findings are however better understandable if the "strengthening" by elastic cycling is considered to be due to the build-up of anelastic strains [79]. In an average metallic-glass sample, the cyclic stress introduces anelastic strains, which build up and lead to apparent hardening. But in a rejuvenated sample, e.g. after thermal cycling, more

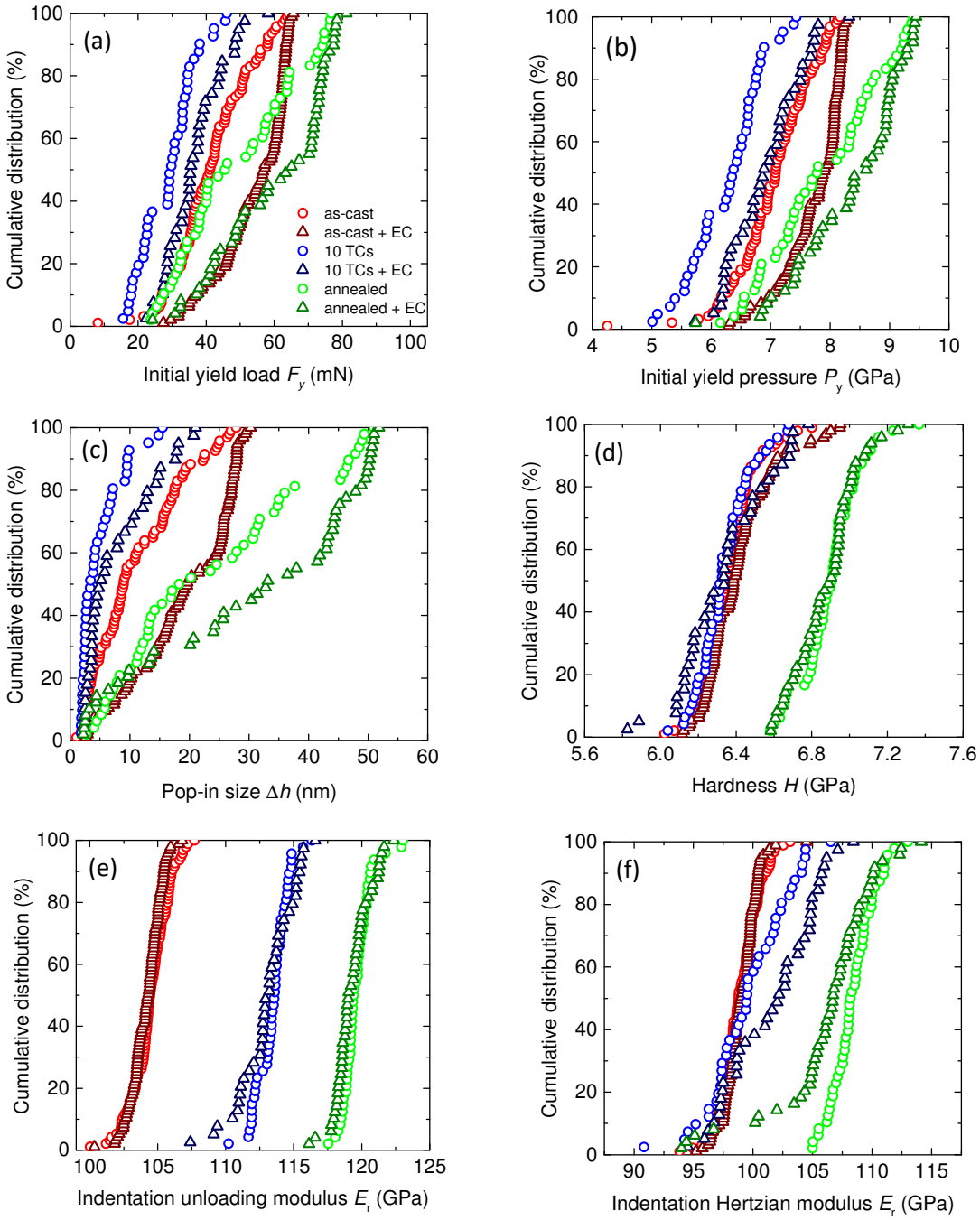

Fig. 5.3. Cumulative distribution curves of mechanical properties, measured by spherical nanoindentation, of the CuZr-based bulk metallic glass sample as cast, after thermal cycling, after annealing, and upon elastic cycling.

mobile regions are present in the glass. The strains introduced during elastic cycling may partially relax away (faster than in a not-rejuvenated sample) due to this increased mobility, and cannot fully build up, leading to a smaller hardening effect.

Similar trends as for F_y were found for the initial yield stress P_y (Fig. 5.3b) and for the 'size' Δh (Fig. 5.3c) of the initial pop-in, i.e. the displacement traversed by the indenter during the first shear event. The median values of these properties were both lowered by thermal cycling (by a similar amount as observed for thermal cycling of a La-based ribbon [99]), and increased by elastic cycling and annealing. It is interesting to note the relationship between the size of the first pop-in Δh and the stress P_y at which it occurred. Δh tends to increase with P_y, as is shown in Fig. 5.4. The data points of P_y vs. Δh from all measured indents seem to lie on a master curve. This is because Δh is approximately linear to the displacement h_y at which the first pop-in appears (as is shown in ref. [170]), since upon increase of the indentation depth, the length scale of the indentation geometry also becomes larger. Thermal cycling reduced the spread in Δh and P_y values and shifted the median point to the lower end of the curve. In contrast, annealing increased the range of values; Δh and P_y of the annealed sample spread from the lower end of the curve up to values higher than of the as-

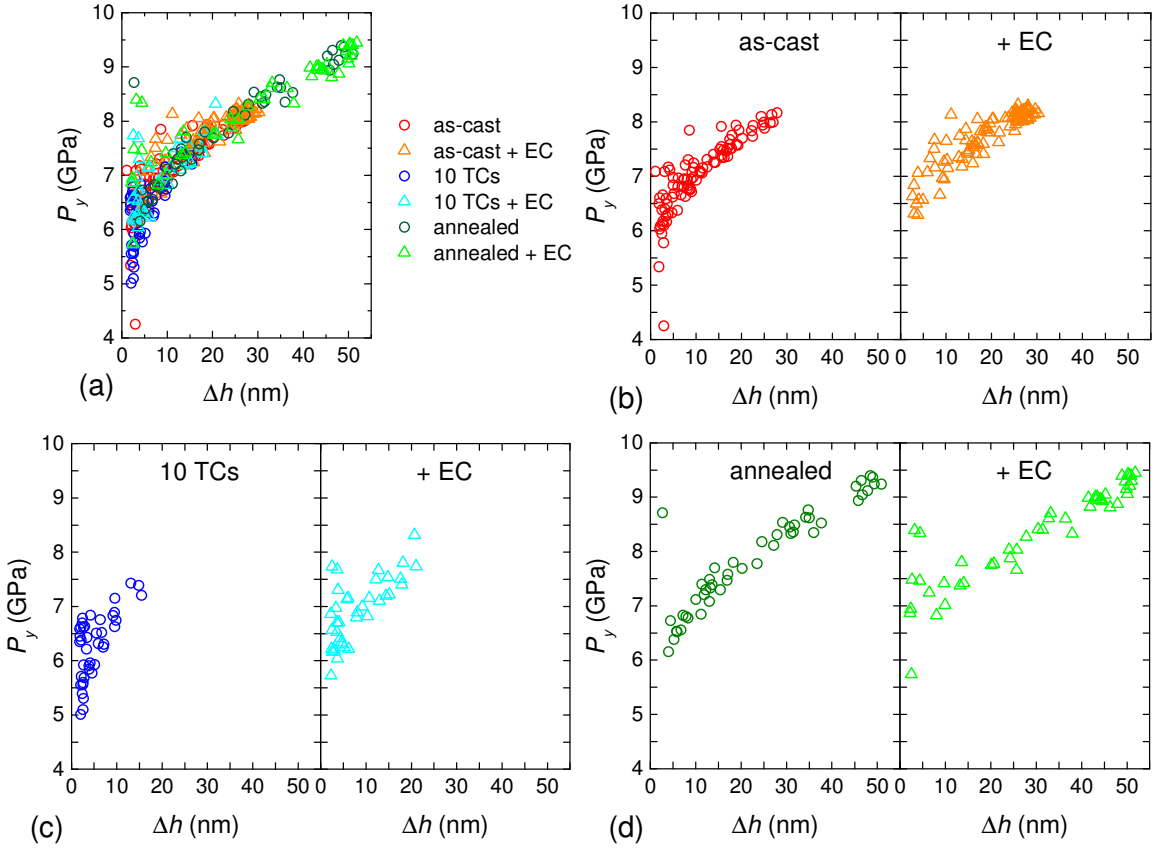

Fig. 5.4. Relationship between the stress P_y and the size Δh of the first occurring pop-in for all samples (a). The P_y and Δh relationships for the different sample states with and without elastic cycling are shown separately in (b), (c) and (d) for the as-cast, thermally cycled and annealed samples, respectively.

cast sample. Elastic cycling, on the other hand, did not seem to impact much the position of these points on the curve.

Although elastic cycling and annealing both increased the median values of F_y, P_y and Δh, they had different effects on the shape and spread of their distribution curves. It was concluded by Packard et al. [131] that, in the case of metallic glasses, the structural variability of the sample is the dominating cause for the spread of F_y-values measured by nanoindentation. Interestingly, elastic cycling of the sample in the as-cast and annealed states only slightly increased the lower tail of the cumulative distributions of F_y, P_y and Δh, and did not affect at all the upper end. In other words, elastic cycling did not change much the range of values obtainable, but rather increased the probability of measuring a value at the higher end of the range. If considering the spread of the distribution curve to be mainly due to the structural heterogeneity of the glassy sample, this may imply that elastic cycling had the biggest effect on the regions of average strength, only marginally affected the weaker regions and did not affect the stronger regions. This may be explained by considering several observations from the literature: 1) during cycling in the nominally elastic range, shear transformation zones (STZs) are activated back and forth, leading to 'hardening' [74], 2) there exists a stress threshold value, below which cycling does not seem to have an effect [74], and 3) that the hardening is due to the build-up of anelastic strains [79], and fades away with time [76, 80]. Upon cyclic indentation of an average region, the cyclic stress could activate STZs back and forth, which led to strengthening of that part of the sample. But when testing a stronger region, the cyclic stress was maybe below the threshold value for this region, and could not fully activate the STZs, and the yield behaviour was therefore only slightly, if at all, affected. On the other hand, the stress applied during cycling was probably high enough to activate the STZs in the weaker regions. But these weak regions are probably also easily able to undergo internal atomic rearrangements; therefore anelastic strains may have started relaxing away during cycling and could not entirely build up, which may explain why no significant strengthening occurred.

When applying elastic cycling to the sample after being subjected to thermal cycling, the entire distribution curves of F_y and P_y were shifted to higher values. This may imply that all indented regions were probably affected by elastic cycling to a similar degree, keeping the size of the spread approximately the same. Upon thermal cycling, the median of Δh and its range of distribution decreased (as well as the indenter velocity during pop-ins, as will be shown below), implying that shearing probably progresses more uniformly and that there is less variability of yield behaviour from one indented area to the other than in the as-cast state, and accordingly the effect of elastic cycling may be similar across the entire sample.

In contrast to elastic cycling, annealing was found here to considerably extend the range of F_y, P_y and Δh by increasing the maximum values measured, while keeping some parts of the sample at lower yield values. The fact that annealing increases the spread of measured values may seem at first contradictory to the common way of thinking, which is that annealing relaxes the sample and brings it to a more stable state with lower energy and higher density with less free volume. In this picture, the sample should have a more uniform structure and be less heterogeneous. But annealing was in some cases found to increase the heterogeneity. For example, fluctuation electron microscopy measurements of an Al-based metallic glass showed that while annealing at 200°C did make the sample more structurally homogeneous, annealing at 230°C led to an even greater heterogeneity than of the as-cast sample [172]. Upon glass formation by cooling from the melt, zones with different atomic mobilities and relaxation times are frozen in [129], and upon annealing, it may be expected that these different zones behave differently upon annealing. For example, annealing of a Zr-Ni amorphous thin film was found to proceed non-uniformly over the whole sample [173]. From energy dissipation maps obtained by dynamic atomic force microscopy before and after annealing, it was observed that annealing broadened the energy spectrum within the film and thus increased the degree of structural heterogeneity.

In the present results, annealing had a stronger effect than the elastic cycling treatment; it increased the median values and the range of F_y, P_y and Δh by a higher amount (Appendix B, Table B.1). This is opposite to what was found by Packard et al. [74], who reported that annealing of two metallic glasses had only an 'extremely subtle' effect on the yield strength measured by nanoindentation, whereas elastic cycling affected the samples 'far more drastically'. It may be difficult to affirm which method has effectively a bigger impact, since the effect of both depends on many parameters (e.g. annealing temperature and time, initial sample state, number and amplitude of elastic cycles…), and only one set of annealing parameters was employed here, as well as in the work of Packard et al. [74].

In any case, the present results show that the underlying strengthening mechanisms of elastic cycling and annealing are not equivalent, as can be further seen from the measurements of the indentation modulus E_r and the hardness H, discussed next.

5.3.2 Hardness and elastic modulus

The effects of thermal cycling, annealing and elastic cycling on the indentation modulus E_r and the hardness H measured are shown in Fig. 5.3 d–f. E_r was calculated here by two alternative approaches, as was mentioned in §3.2.3: the 'unloading' modulus $E_{r,unloading}$ was determined from

the unloading curve, whereas the 'Hertzian' modulus $E_{r,Hertzian}$ was extracted from the loading curve. Elastic cycling barely, if at all, affected H or $E_{r,unloading}$ of the sample in all three states. The effect on $E_{r,Hertzian}$ is less straightforward: there is clearly no significant effect on the as-cast state; but, for the thermally cycled sample, subsequent elastic cycling slightly shifted the upper part of the $E_{r,Hertzian}$ distribution curve to higher values; and, for the annealed sample, shifted the lower part of the curve to lower values.

Both indentation moduli $E_{r,Hertzian}$ and $E_{r,unloading}$ were however significantly increased upon annealing. It should be pointed out that $E_{r,unloading}$ gave systematically higher values than $E_{r,Hertzian}$, and it is not yet understood why this is the case. The median values of the moduli of the as-cast sample are $E_{r,unloading}$ = 105 GPa and $E_{r,Hertzian}$ = 99 GPa. These indentation modulus values correspond to an elastic modulus of 96 and 90 GPa, respectively, with the latter being closer to the value of 90.6 GPa obtained in the literature from ultrasonic measurements [171].

It was not possible to deduce here the effect of annealing on H since this property depends on the maximum load F_{max} applied during indentation. F_{max} had to be increased from 70 mN to 120 mN when measuring the sample in the annealed state in order to assure that yield could occur, and therefore the H values measured for the annealed state are not comparable to those of the other states. Still, hardness of metallic glasses is expected to increase upon annealing, as was often observed in the literature [174, 175].

5.3.3 Pop-in velocity

Another property which could be extracted from the nanoindentation results is the pop-in velocity $v_{pop\text{-}in}$, i.e. the speed at which the tip indents the sample during the pop-in. Instead of measuring the velocity at each individual pop-in, Denis et al. [176] determined an average pop-in velocity $v_{average}$. This average was calculated by first subtracting a constant value (corresponding to

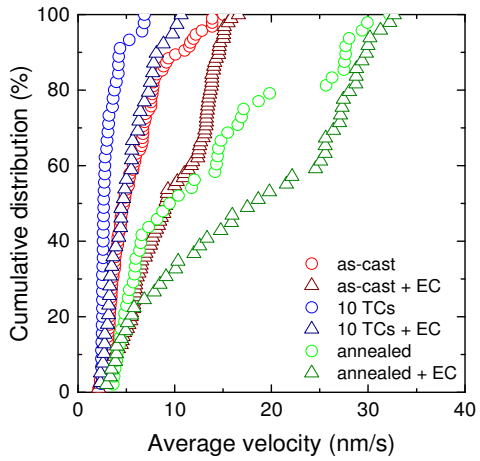

Fig. 5.5. Cumulative distribution curves of the average indenter velocity during pop-ins.

the velocity if no pop-ins would have occurred) from the indenter velocity, then integrating it as a function of displacement, and finally dividing this by the maximum indented depth. An equivalent average value was determined for the present sample, and is shown in Fig. 5.5. $v_{average}$ was affected by elastic cycling, annealing and thermal cycling in a similar manner as F_y, P_y and Δh. But the value $v_{average}$ does not provide information on how the average shearing speed is distributed among the individual pop-ins occurring during an indent, i.e. if the entire velocity is concentrated within one very big and fast pop-in, or if it is split among many small and slower pop-ins. In order to gain a better insight on how $v_{average}$ is spread among pop-ins, the individual velocities $v_{pop\text{-}in}$ of all pop-ins were determined for each indentation curve measured here. Fig. 5.6d–f shows the range of $v_{pop\text{-}in}$ of all pop-ins from all curves, in the order of occurrence within each indent. It can be observed that the fastest pop-ins tended to take place during the first few shear events. In addition, the range of $v_{pop\text{-}in}$ at the beginning of yield was quite large, and upon further shearing the maximum $v_{pop\text{-}in}$ decreased. The mean values of $v_{pop\text{-}in}$ for each indent are shown in the form of cumulative distribution curves in Fig. 5.6a–c, with the error bars corresponding to the minimum and maximum values found within each indentation curve. The spread in $v_{pop\text{-}in}$ within a single indent, as well as among all indents per sample state, was greatly reduced upon thermal cycling and increased upon annealing. As pop-ins are related to the operation of individual shear bands [177], $v_{pop\text{-}in}$ is linked to the shear band propagation speed. Hence, thermal cycling seemed to reduce the speed of shear bands, and made shearing occur less abruptly, as was also observed after rejuvenation of a Pt-based metallic glass upon high-pressure torsion [176], whereas annealing introduced a large variety of shear band speeds. Elastic cycling increased the average $v_{pop\text{-}in}$ for the as-cast, thermally cycled and annealed sample states, but its effect was less pronounced than annealing, and did not affect much the spread of $v_{pop\text{-}in}$. The observations concerning $v_{pop\text{-}in}$ are equivalent to what was found for the other parameters F_y, P_y and Δh concerning yielding.

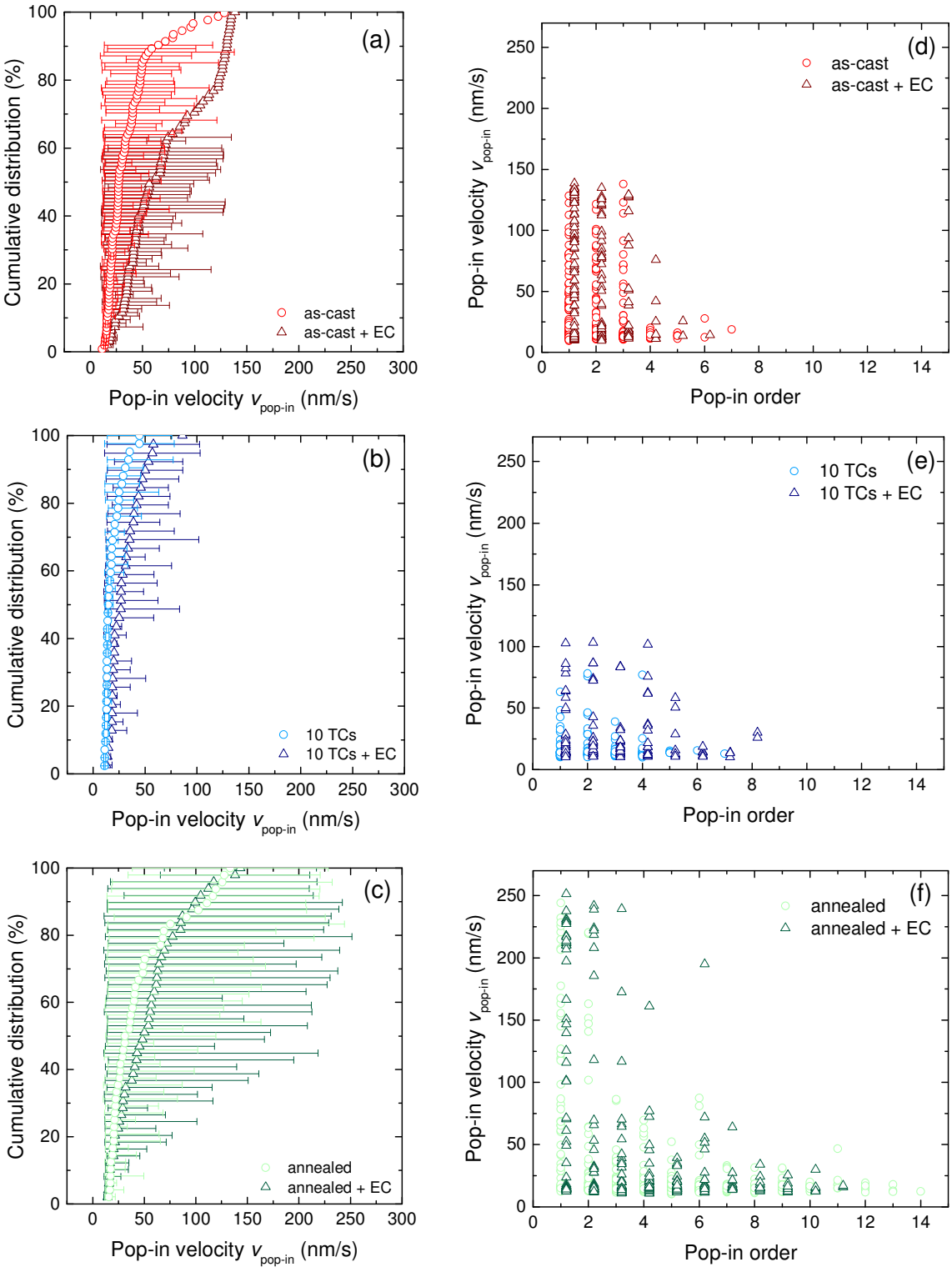

Fig. 5.6. The velocity $v_{pop\text{-}in}$ of every individual pop-in was calculated, and is presented in the form of cumulative distribution curves (a–c), where every point is the mean $v_{pop\text{-}in}$ of a single indentation curve, with the error bars corresponding to the minimum and maximum $v_{pop\text{-}in}$ occurring during that indent. The velocities of all pop-ins are also shown in their order of appearance during indentation (d–f); to better distinguish the data points obtained from the uncycled and elastic-cycled indentation curves, the values from the latter are slightly shifted to higher 'pop-in order' values.

5.4 Conclusions

The effect of elastic cycling was explored on a CuZr-based metallic glass using nanoindentation. Elastic cycling by nanoindentation (i.e. not macroscopic loading) was found to increase the stress required to initiate shearing (i.e. for the first pop-in to occur); the degree of this strengthening was similar as to what was previously found for other metallic-glass compositions in the literature. In addition, elastic cycling increased the average pop-in velocity, which is correlated to the speed of propagation of shear bands. But elastic cycling did not change the hardness, nor affect significantly the elastic modulus, both properties which are normally affected upon relaxation.

In the literature [74], the strengthening effect of elastic cycling was interpreted as a gradual 'shaking down' of the metallic glass to a more stable state of lower energy, and that therefore the glass should become more relaxed. The present findings show that this is probably not the case, for several reasons. For example, elastic cycling affected the metallic glass in a different way than annealing, which is the conventional method for inducing relaxation. Annealing had a stronger strengthening effect than elastic cycling, and furthermore also increased the width of the distribution curves of the yield stress and pop-in velocities, whereas elastic cycling only increased the median values. In addition, annealing was found to significantly increase the elastic modulus, which was hardly affected by elastic cycling. Another reason is that elastic cycling strengthened the sample in the rejuvenated state to a lesser degree than the annealed one, which should not be the case if elastic cycling really is a mechanical relaxation method, but is more consistent with the picture that the apparent strengthening is due to the build-up of anelastic strains.

6 Thermal Cycling

6.1 Introduction

Many mechanical treatments which were found to induce relaxation or rejuvenation of metallic glasses require the sample to have a specific shape. For example, a flat disk is necessary for high-pressure torsion, whereas a ribbon or plate is needed for cold-rolling; furthermore, the high rejuvenation achieved by Pan et al. [62] upon large deformation under compression was only possible due to the notch machined into the rod. Several other mechanical treatments affect only the surface of the sample, as is the case of shot-peening and ion or electron irradiation.

Thermal treatments, on the other hand, affect the entire sample and can be applied to any sample shape. Metallic glasses can be relaxed by 'conventional' annealing at temperatures below (but close to) the glass-transition temperature T_g, and rejuvenated again by 'recovery annealing' (§2.3) [94, 95]. The latter consists of heating the glass into the supercooled-liquid region, followed by cooling at high rates back to lower temperatures, so that a glassy state is reached again. The internal energy of the glass depends on the quench rate; to rejuvenate the sample, the quench rate has to be higher than the effective cooling rate of the glass before treatment. The effective cooling rate is the rate at which the liquid has to be cooled in order to form a glass with the same energy. This means to rejuvenate an as-cast glass by recovery annealing, the cooling rate has to be higher than the quench rate used to produce the initial glass, which is difficult to achieve for many metallic-glass compositions. But when the glass relaxes, its effective cooling rate is lowered, and recovery annealing may be a useful method to bring it back towards a more unrelaxed state.

A thermal method which was found to rejuvenate even as-cast metallic glasses is thermal cycling (§2.3). By applying cycles between cryogenic temperatures (e.g. liquid-nitrogen temperature) and room temperature, several metallic-glass compositions were rejuvenated; their heat of relaxation and their plasticity in compression were found to increase [99, 101, 102]. The rejuvenation is thought to be due to non-affine thermal strains, which occur during thermal cycling because of the heterogeneity of metallic glasses [35, 99].

In the present chapter, the effect of thermal cycling on metallic glasses will be further investigated. Different aspects were explored, and are presented in the three sections below. The first aspect was to compare thermal cycling with annealing (§6.2). If thermal cycling induces rejuvenation, and annealing relaxation, one may expect them to have opposing effects on the

properties of metallic glasses, and it would interesting to find out to what extent thermal cycling may reverse the relaxation of annealing. In §6.3, the effect of thermal cycling on stress and strain relaxation will be explored by mandrel bending experiments. Finally, in §6.4, thermal cycling will be performed on a Fe-based metallic-glass ribbon, which is commercially available due to its good soft magnetic properties. The disadvantage of such Fe-based glasses is that after annealing they are especially brittle, and therefore the possibility of increasing their plasticity, for example through rejuvenation induced by thermal cycling, would be of great interest.

6.2 Thermal cycling vs. annealing

6.2.1 Recovery of relaxed metallic glasses

The typical disadvantage of ageing is that it increases the brittleness of metallic glasses. Therefore there is a great interest in being able to rejuvenate a relaxed glass, i.e. to bring the sample back to its original state and recover (or maybe even improve) its initial properties. Examples in the literature where this has been achieved are not very common, but do exist. For example, high-temperature creep was found to recover the plasticity of a pre-annealed Zr-based bulk metallic glass [111]. Another example is by shot-peening: the relaxation enthalpy of a Pd-based glass, which was first reduced upon annealing, could be increased again by peening at 77 K, and even exceeded the relaxation enthalpy of the as-cast state [58]. As mentioned above in §6.1, recovery annealing was found to rejuvenate a relaxed sample, though a full recovery to its pre-annealed state was not (yet) obtained experimentally.

Can thermal cycling also recover the as-cast properties of an aged metallic glass? In the initial work on thermal cycling by Ketov et al. [99], it was shown that although thermal cycling could increase the plastic strain of a partially relaxed metallic glass, no effect was observed on a fully relaxed sample. This was explained with the fact that an initial heterogeneity in the glass is necessary for thermal cycling to induce rejuvenation [99]. Upon annealing, the glass was assumed

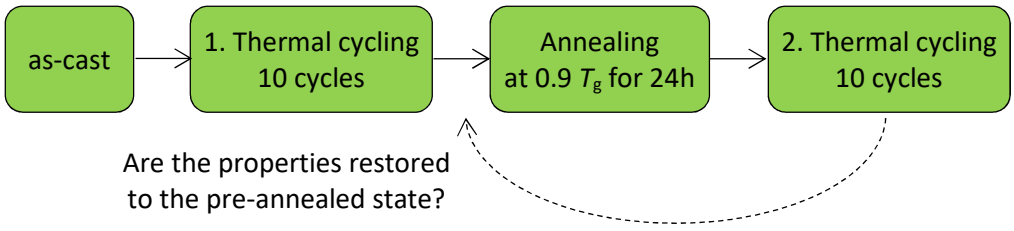

Fig. 6.1. Diagram showing the sequence of treatments applied to the $Cu_{46}Zr_{46}Al_7Gd_1$ bulk-metallic-glass sample.

to become more homogeneous, and thus the fully relaxed sample may not have had a high enough heterogeneity to be significantly affected by thermal cycling.

The effect of thermal cycling an annealed metallic glass is also briefly explored here, by measuring the change in properties by nanoindentation. The change in mechanical properties upon thermal cycling followed by annealing of a $Cu_{46}Zr_{46}Al_7Gd_1$ sample, which is the same composition as was tested in ref.[99], was already shown in Chapter 5. Thermal cycling was found to decrease the initial yield stress and the propagation speed of individual shear events, both property changes which are linked to rejuvenation. Subsequent annealing increased these properties again, as is expected after relaxation. In order to see if this annealing-induced relaxation can be reversed again, the same sample was treated to further thermal cycling (Fig. 6.1), and the results are presented here.

6.2.2 Experiments

The same experimental procedures as in §5.2 were applied here. The $Cu_{46}Zr_{46}Al_7Gd_1$ bulk metallic glass, which was treated to 10 thermal cycles, followed by annealing at 0.9 T_g (≈ 630 K) for 24 h in Chapter 5, was treated here to a further 10 thermal cycles (Fig. 6.1). The change in mechanical properties due to this additional treatment was determined by nanoindentation using the same parameters as in §5.2.3: a spherical tip of radius 8 µm was used to indent the sample to a maximum load F_{max} of 120 mN, with loading and unloading rates of 0.5 mN/s. 54 indents were performed, with a minimum spacing between indents of 20 µm.

6.2.3 Results and discussion

The following mechanical properties were measured for this sample by nanoindentation: the initial yield load F_y and stress P_y, corresponding to the load and stress needed to activate the first pop-in (i.e. displacement burst), the size of the first pop-in Δh, the hardness H and the indentation moduli $E_{r,unloading}$ and $E_{r,Hertzian}$, which were defined from the unloading and loading curves, respectively (Fig. 6.2). The average pop-in velocity $v_{average}$ and the distribution of the velocities of individual pop-ins $v_{pop\text{-}in}$, which provide information on the propagation speed of shearing, were also determined and are shown in Fig. 6.3 and in Appendix C (Fig. C.1). The mechanical properties of the sample in its as-cast state, after the first thermal cycling treatment as well as after annealing were already shown and discussed in Chapter 5, but are displayed here again, in order to compare with the properties measured after additional thermal cycling.

As was seen before in §5.3, the first thermal cycling treatment, applied to the sample in its as-cast state, decreased the median values of F_y, P_y, Δh, $v_{average}$ and $v_{pop\text{-}in}$, and decreased also the width of distribution of these properties (apart from P_y, which showed a negligible change in distribution width after thermal cycling). Subsequent annealing increased the median values of these properties

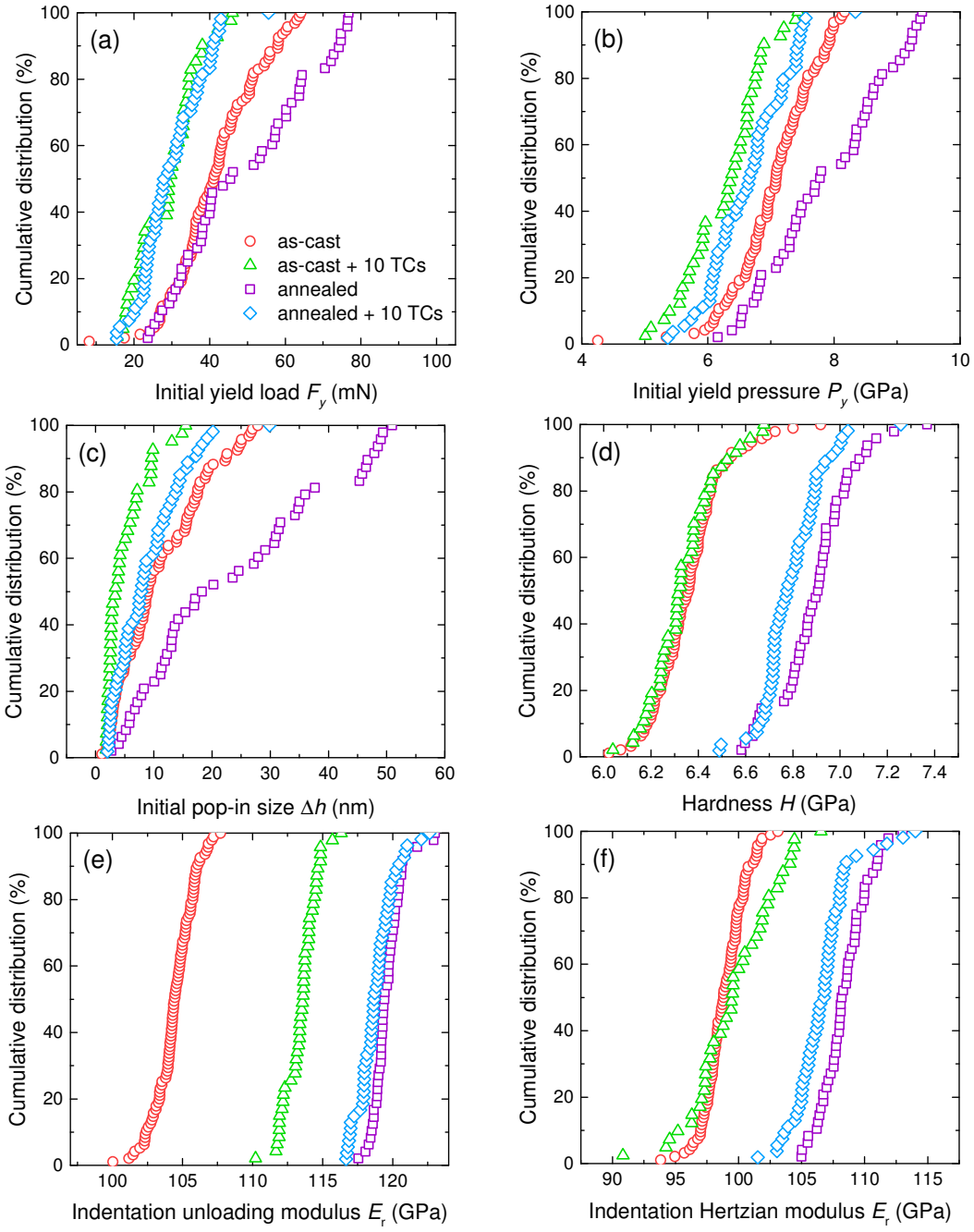

Fig. 6.2. Cumulative distribution curves of the initial yield load F_y (a), the initial yield stress P_y (b), the size Δh of the first pop-in (c), the hardness H (d), and the indentation moduli $E_{r,unloading}$ (e) determined from the unloading curve and $E_{r,Hertzian}$ (f) obtained from fitting the loading curve with the Hertzian equation, measured by spherical nanoindentation of the $Cu_{46}Zr_{46}Al_7Gd_1$ bulk-metallic-glass sample in the as-cast state, after thermal cycling, after annealing, and after further thermal cycling.

again, and also expanded the range of values measured, i.e. some parts of the annealed sample had values as low as after thermal cycling, whereas other parts showed values which were even larger than for the as-cast state (§5.3.1). If considering the width of the F_y distribution to be mainly due to the heterogeneous structure of the glass [74], this would imply that thermal cycling decreased the heterogeneity of the sample, and annealing increased it again, which is contradictory to what is typically expected. Upon rejuvenation, metallic glasses were sometimes found to become more heterogeneous (e.g. ref.[21]). Relaxation, on the other hand, is commonly thought to lead to a more homogeneous structure, though examples showing the opposite do also exist (e.g. refs.[172, 173]).

Thermal cycling of the annealed sample affected the mechanical properties in a similar fashion as thermal cycling of the as-cast state. The properties linked to pop-ins (F_y, P_y, Δh, $v_{average}$ and $v_{pop\text{-}in}$), which are believed to represent the initiation and propagation of individual shear events, were significantly affected. The median values of these properties, as well as the widths of their distributions, were again lowered upon cycling. The distribution of F_y was returned completely to the sample's pre-annealed state, i.e. it overlaps almost entirely the distribution curve of the initially thermal-cycled state. The distribution curves of the other pop-in related properties (P_y, Δh, $v_{average}$ and $v_{pop\text{-}in}$) were also reduced, to values that are slightly lower than of the as-cast sample, but higher than after the first thermal cycling treatment. From these results, thermal cycling seemed to have successfully reversed the relaxation induced by annealing, i.e. rejuvenated the sample back to its pre-annealed state.

However, a different conclusion is obtained when considering the results on hardness H and elastic modulus ($E_{r,unloading}$ and $E_{r,Hertzian}$). These properties, which depend rather on the overall structure of the sample, were affected to a much lesser degree (if at all) by thermal cycling than the properties linked to pop-ins. Thermal cycling of the annealed sample shifted the distribution curves

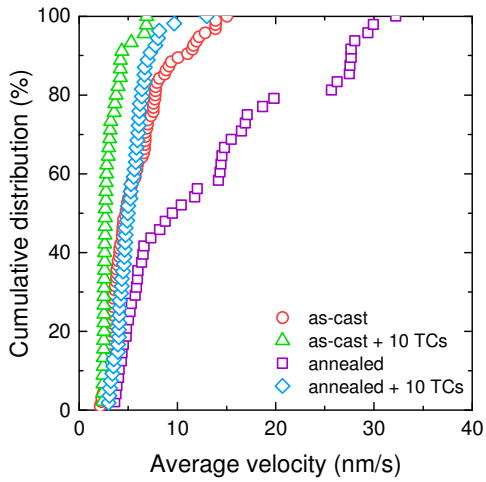

Fig. 6.3. Average indenter velocity due to pop-ins of the as-cast sample and after different treatments.

of H, $E_{r,unloading}$ and $E_{r,Hertzian}$ to slightly lower values, but by far did not return these values to those of the pre-annealed state (Fig. 6.2d–f). It should once again be noted that the hardness values H given in Fig. 6.2d depend on the maximum load F_{max} applied during indentation. The H results of the annealed and subsequently thermal cycled states were indented to an F_{max} of 120 mN, and can be compared with one another, but cannot be compared to the H values of the as-cast state and after the first thermal cycling treatment, for which F_{max} was 70 mN. Therefore, one does not know in principle if thermal cycling did or did not reverse the effect of annealing on H. But since H and the elastic modulus are known to scale with each other [178], one may expect H to be affected by treatments in a similar way as E_r, and it is clear that thermal cycling did not decrease the elastic modulus E_r back to its pre-annealed value.

It is interesting to note the difference in the effects of thermal-cycling on the as-cast and annealed sample states. While the relative change of properties upon thermal cycling is approximately the same (i.e. the change of the median value, as a percentage of the median value before thermal cycling), the change in absolute values is much larger when thermal cycling the annealed sample than the as-cast sample. The work by Ketov et al. [99] proposed that heterogeneities are necessary for thermal cycling to have an effect. If considering the observed increase in the width of the F_y distribution after annealing to be correlated to the structure becoming more heterogeneous, this may explain why the effect of thermal cycling is more effective on the annealed than on the as-cast state.

It is not well understood why thermal cycling of the as-cast sample increased the indentation modulus $E_{r,unloading}$ measured from the unloading curve by around 10%. One may expect the elastic modulus to decrease upon rejuvenation, and Ketov et al. [99] indeed found that thermal cycling decreased the indentation modulus of a La-based ribbon. But no change in elastic moduli measured by resonant ultrasound spectroscopy was found after thermal cycling a $Cu_{46}Zr_{46}Al_7Gd_1$ bulk sample (which is the same composition as was used here) [99]. In further work by Ketov et al. [105], the effect of thermal cycling on the local apparent elastic modulus of the surface of three Zr-based metallic-glass compositions was measured by atomic force microscopy; for two of the compositions, the average modulus increased after cycling, though this increase was only temporary. The increase in modulus was concluded to be limited to the surface region, and might be due to stresses introduced at the surface. But it is not very likely for the increase in $E_{r,unloading}$ observed here to be due to surface stresses, because otherwise an increase in H and $E_{r,Hertzian}$ should also have been observed. Furthermore, no increase in $E_{r,unloading}$ after thermal cycling of the annealed sample was observed (instead it decreased slightly, as expected upon rejuvenation). It is therefore suspected that the observed increase $E_{r,unloading}$ after cycling of the as-cast sample is due

to some systematic error in the measurement of this value, though the reason for such an error is not yet understood.

In any case, the present results show that the effect of thermal cycling is not the pure opposite to relaxation through annealing. Whereas annealing increased all of the mechanical properties measured here by nanoindentation, thermal cycling only affected those properties which depend on local shear events. As a consequence, once the $Cu_{46}Zr_{46}Al_7Gd_1$ sample was annealed, it could not be fully restored back to its as-cast state through thermal cycling. Although this may seem at first disappointing, promising properties were achieved by combining these two treatments. By first annealing, then thermal cycling the $Cu_{46}Zr_{46}Al_7Gd_1$ sample, a lower initial yield stress and pop-in velocity, but higher hardness and elastic modulus were obtained compared to the as-cast state. Usually, the yield stress tends to scale with hardness and elastic modulus, and an increase in the latter two properties often occurs alongside a decrease in plastic strain (as is typically observed upon annealing of metallic glasses). In the current results, a lower initial yield stress and pop-in velocity was observed, meaning that shear events were more easily activated [128, 177], and that shearing progressed less abruptly [176]. These are signs that plastic flow is facilitated and may be less likely to end in a catastrophic (i.e. brittle) failure, even though the hardness and modulus increased.

However, it should be kept in mind that this behaviour determined by nanoindentation does not necessarily imply that the actual plastic strain upon macroscopic loading will be increased. But the fact that thermal cycling seemed to affect dominantly the pop-in behaviour (i.e. local soft spots responsible for activation of shear banding) and less the global material raises the hope that it may be possible to tune the properties of metallic glasses by careful combination of different treatments.

6.3 The effect of thermal cycling on anelastic strain recovery

6.3.1 Introduction

Several studies so far have shown that thermal cycling can affect the yield behaviour and plasticity of metallic glasses [97, 99, 102, 101]. But the effect of thermal cycling on the mechanical behaviour before yielding has not yet been frequently explored.

When applying a stress within the elastic regime, elastic, anelastic and viscoplastic strains can occur within a material. Elastic and anelastic strains are both fully recoverable, but while elastic

strains recover instantaneously upon stress removal (as well as develop instantaneously upon stress application), anelastic strains are time-dependent i.e. they need time to develop as well as to recover. Viscoplastic strains are also time-dependent, but not recoverable. In crystalline alloys, anelastic strains are usually minor, and viscoplastic strains typically become important during creep at temperatures above 0.5 T_m (where T_m is the melting point). But metallic glasses can develop viscoplastic strains even at lower temperatures, and they show in general much higher anelastic strains than crystalline alloys [132, 179]. For example, the appearance of anelastic and viscoplastic strains, of almost 0.5% and 0.4%, respectively, was observed in a Ni-based bulk metallic glass after applying a constant compressive load within the elastic range for 30 h at room temperature, which corresponds to 0.33 T_g or 0.2 T_m [67]. Since these strains play an important role during loading of metallic glasses, it is of interest to see if their behaviour is affected by thermal cycling.

Furthermore, it would be interesting to know if thermal cycling can affect internal stresses. Annealing is the typical method applied to relax away stresses which are introduced during shaping and bending or even during the production of metallic glasses. For example, during the winding up or cutting of some metallic-glass ribbons, used as transformer cores due to their excellent soft magnetic properties, internal stresses are introduced. These stresses can have a negative effect on the magnetic properties, and therefore after winding, the cores are typically annealed to get rid of these stresses. But the disadvantage of annealing is that it also renders metallic glasses brittle.

More unrelaxed metallic glasses are expected to have more free volume and a higher atomic mobility [41, 180, 181]. Could the increase in atomic mobility introduced during rejuvenation, e.g. by thermal cycling, be used to relax stresses? This possibility is explored here on a La-based metallic-glass ribbon by a mandrel winding method [182, 183, 184], a simple technique used to determine stress and strain relaxation. By winding the ribbon around a mandrel (i.e. a rod), a fixed deformation

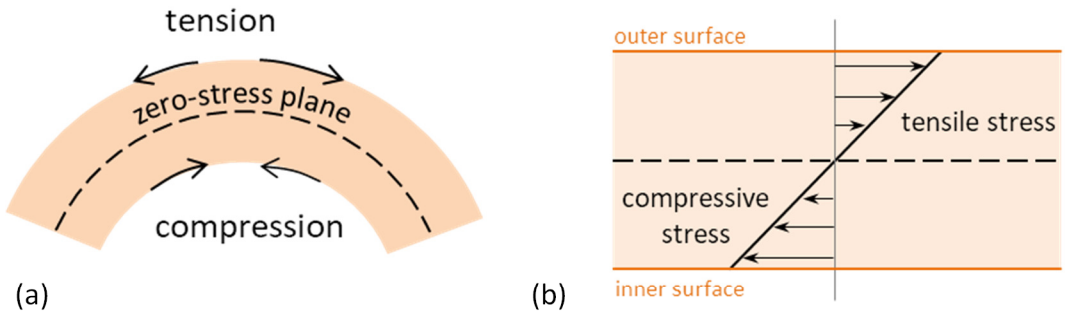

Fig. 6.4. Upon bending of a ribbon, the outer surface is under tension, while the inner surface is under compression (a). A zero-stress plane is situated at the middle of the ribbon. The stress varies linearly along the thickness of the ribbon, with a maximum tensile stress at the outer surface and a maximum compressive stress at the inner surface (b).

is applied, and stresses are introduced in the ribbon. The outer surface of the ribbon is in tension, the inner in compression, and the middle of the ribbon is free of stresses and strains (Fig. 6.4). When the ribbon is released from the mandrel, it will spring back to regain its initial shape (or not, depending on the type of strain introduced during bending). By measuring this change in shape upon unwinding as a function of time, the kinetics of strain relaxation can be determined, since the curvature of the ribbon is directly related to the strain. If the deformation applied to the ribbon

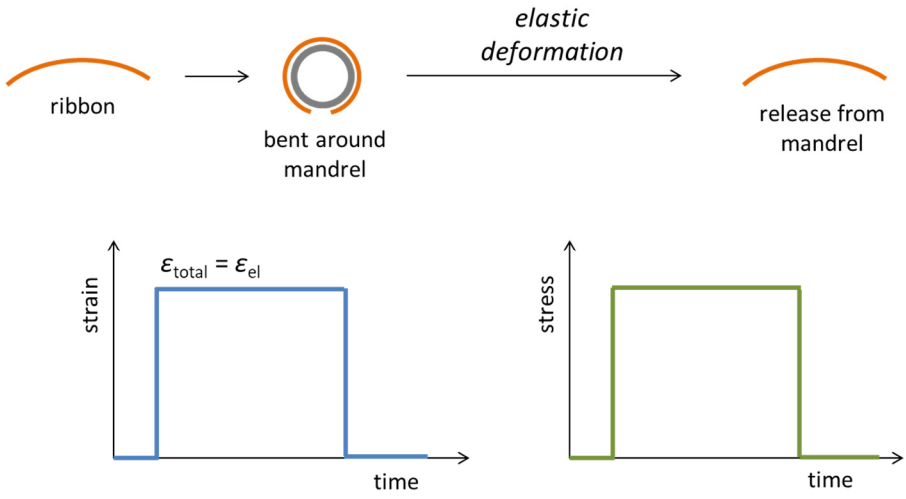

Fig. 6.5. If only elastic deformation occurs during bending of a ribbon around a mandrel, the stress will stay constant during bending, and both stress and strain will recover instantaneously once the ribbon is released. The curvatures of the ribbon before and after bending will be identical.

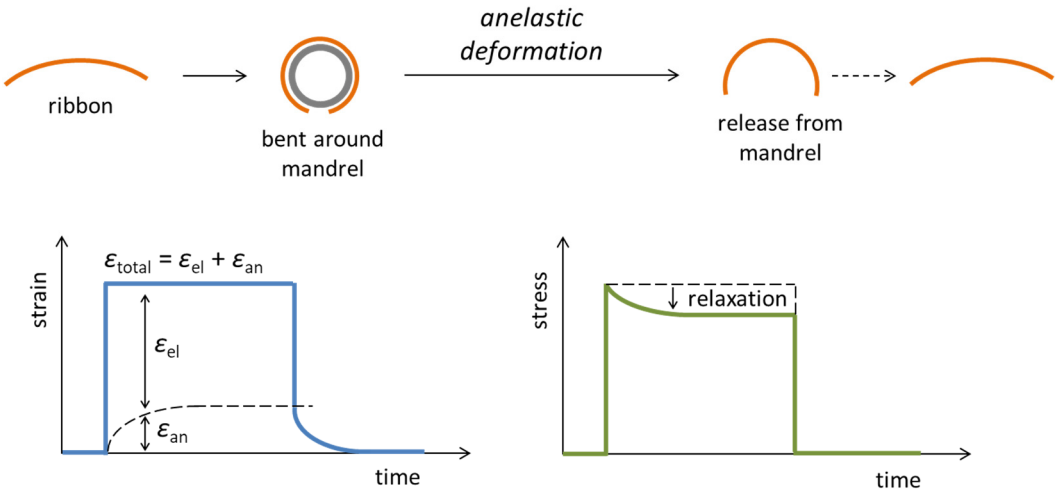

Fig. 6.6. If part of the deformation upon bending of a ribbon is anelastic, the stress will partially relax during bending, and once the ribbon is removed from the mandrel, the anelastic portion of the strain ε_{an} will recover upon time. This implies that the curvature of the ribbon will change with time after bending, until it reaches the same curvature as initially.

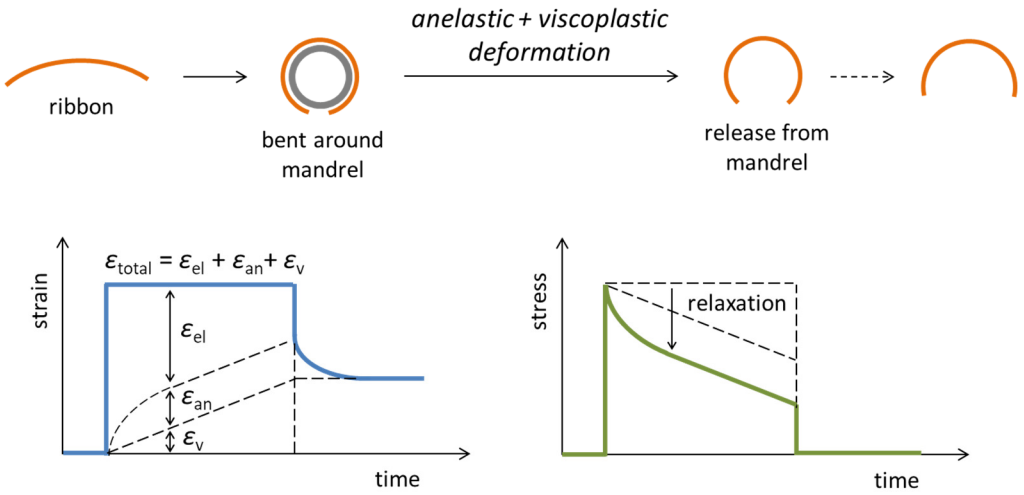

Fig. 6.7. Besides elastic and anelastic deformation, it is also possible for viscoplastic flow to take place during bending (for example as would be expected upon annealing). Once the ribbon is released, the elastic part of the strain ε_{el} recovers instantaneously, while the anelastic part ε_{an} recovers after some time, but there will also be a residual strain due to the viscoplastic flow ε_v, corresponding to a permanent deformation of the ribbon.

upon bending is purely elastic, the introduced stress will stay constant during the bending time, and will disappear, along with the strain, instantaneously once the ribbon is released from the mandrel, and the final curvature of the ribbon will be the same as before bending (Fig. 6.5). If anelastic deformation occurs during bending, the total strain will stay constant (since it is fixed and given by the radius of the mandrel), but the stress will partially relax. When the ribbon is taken off the mandrel, the internal stress will be lower than at the beginning of the bending, therefore one portion of the strain, i.e. the elastic part, will disappear instantaneously, whereas the rest, which corresponds to the anelastic part, will need time to recover (Fig. 6.6). Once the entire strain has recovered, the ribbon will, again, present the same curvature as before the mandrel experiment. If viscoplastic flow took place as well during bending, as would typically be observed if the ribbon were annealed while it was bent, a residual strain would remain upon release from the mandrel, which would be visible as a permanent curvature change of the ribbon (Fig. 6.7).

6.3.2 Experiments

The possible influences of thermal cycling on viscoplastic stress relief and anelastic strain recovery were explored with the mandrel method on a $La_{55}Ni_{20}Al_{25}$ metallic-glass ribbon of an average thickness of 30 µm. For each test, 5-cm lengths of ribbon were wound around cylindrical mandrels of 6.3 mm diameter. Due to this bending, a strain ε_B is imposed, with a maximum value

at the ribbon surface given by $\varepsilon_B = (d/2)[\,(1/R) - (1/r_0)]$ [182], where *d* is the ribbon thickness, *R* the mandrel radius and r_0 the initial radius of curvature of the ribbon (since the as-cast samples are not perfectly flat). As shown in Fig. 6.4, the outer (convex) surface is under tension, while the inner (concave) surface is under compression. Three different conditions were applied during mandrel bending, and are schematized in Fig. 6.8. Sample A was wound around the mandrel at room temperature (RT) for 10 min. Sample B was subjected to 5 thermal cycles (TCs), while being wound around the mandrel. Thermal cycling was performed as in ref.[99], and as described in §3.1.2. In the case of sample C, the ribbon was first treated to 5 TCs, and then wound around the mandrel at RT for 10 min.

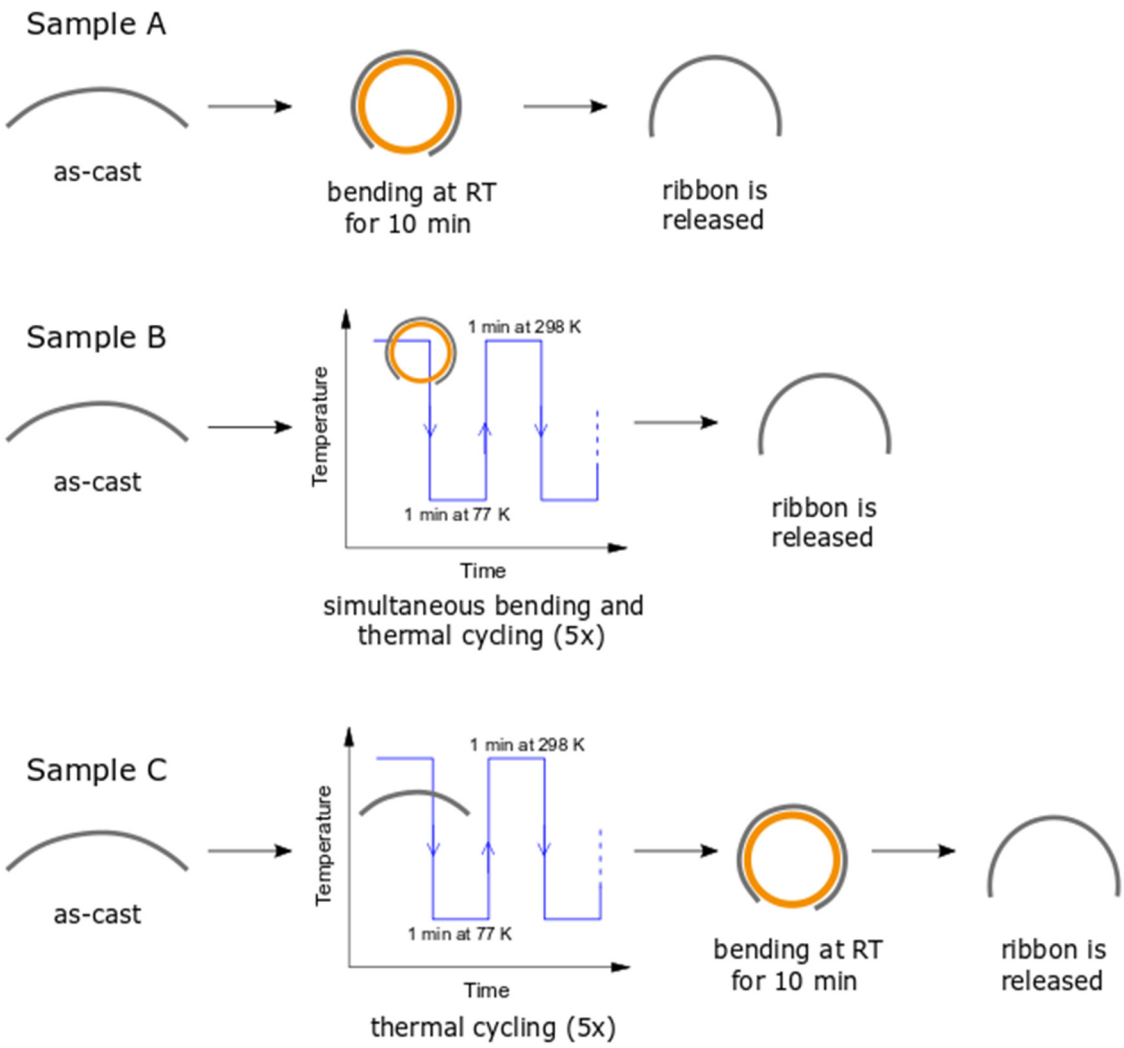

Fig. 6.8. Schematic representation of mandrel treatments. Sample A is held on the mandrel at room temperature (RT), sample B is subjected to five thermal cycles while being held on the mandrel, and sample C is first subjected to five thermal cycles and then wound and held on the mandrel at RT. The total time on the mandrel is the same (10 min) in each case. After that time, the samples are released from the mandrels and their curvatures are measured as a function of time.

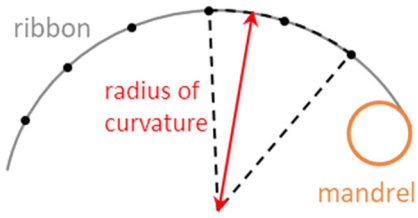

Fig. 6.9. Schematic of the determination of the radius of curvature. After bending on the mandrel, the ribbon is released from one end (but the other end is left attached to the mandrel, this speeds up the process of unwinding, and allows the ribbon to relax in air, and any friction with the surface on which the mandrel stands is avoided) and a photograph is taken. Points (shown in black) are placed along the ribbon, and a radius of curvature for each 3 consecutive points is calculated. The average of these radii is used to determine the strain.

Once unwound from the mandrel, each sample's radius of curvature $r(t)$ was measured as a function of time, by taking digital photographs every 10–60 s. Along the ribbon length, 5 to 7 virtual points were placed in each photograph. For every 3 consecutive points, a radius of curvature was calculated (Fig. 6.9). The average of these radii gave the radius of curvature of the ribbon r. The error in the measurement of r is approximately 2%. The elastic strain is given by $\varepsilon_e(0) = (d/2)[\,(1/R) - (1/r\,(0))]$, where $r(0)$ is the radius of curvature at the moment of unwinding ($t = 0$), and the anelastic strain, which evolves over time, is determined as $\varepsilon_a(t) = (d/2)\,[(1/r(t)) - (1/r_0)]$ [182].

6.3.3 Results and discussion

The strain ε_B imposed upon winding the ribbons around the mandrels, as well as the elastic ε_{el} and anelastic ε_{an} portions of that strain, are summarized in Table 6.1 for the various conditions during bending. The bending strain ε_B depends not only on the mandrel radius and ribbon thickness, but also on the initial ribbon curvature. For better comparison between the three treatments, ribbon pieces of similar initial curvatures were chosen, resulting in an imposed strain ε_B of roughly 0.6% for all samples. This strain is well within the elastic limit, which is around 2% for metallic glasses in general [185]. Directly upon unwinding (i.e. at $t = 0$), the majority of the imposed strain was recovered instantaneously as elastic strain, and only a small percentage, though non-negligible, was left as anelastic strain ε_{an} in the ribbons. Sample B, which was thermally cycled while bent, showed the smallest anelastic strain component of $\varepsilon_{an}(0)/\varepsilon_B = 0.037$, compared to values of 0.048 and 0.050 for the ribbons bent at RT. This is probably due to the fact that the average temperature

Table 6.1. Bending strain ε_B imposed upon winding of the samples A, B and C around mandrels of 6.3 mm diameter under different conditions, as well as the elastic (ε_{el}) and anelastic (ε_{an}) portions of this strain measured upon unwinding at time $t = 0$. Error of ε_B is around ± 0.015%, of ε_{el} ± 0.014%, ε_{an} ± 0.001% and $\varepsilon_{an}/\varepsilon_B$ ± 0.002.

Sample	Initial state	Time on mandrel	Treatment during bending	ε_B (%)	$\varepsilon_{el}(t=0)$ (%)	$\varepsilon_{an}(t=0)$ (%)	$\varepsilon_{an}(t=0)/\varepsilon_B$
A	as-cast	10 min	RT	0.57	0.55	0.026	0.046
B	as-cast	10 min	5 TCs	0.58	0.56	0.021	0.036
C	5 TCs	10 min	RT	0.60	0.57	0.029	0.048

in the case of sample B is considerably lower than room temperature, and anelastic strain is known to develop faster, and to a larger extent, at higher temperatures [184, 186].

The recovery of the anelastic strain with time after release from the mandrel is shown in Fig. 6.10. An obvious observation from these results is that thermal cycling did not enhance viscoplastic flow during bending, which would otherwise be apparent as a permanent change in ribbon curvature, and a permanent residual strain (as shown in the example in Fig. 6.7). Instead, the residual strain in samples B and C fully recovered after around 300–400 s after unwinding. On the contrary, sample A, which was bent at room temperature and was not subjected to any thermal cycling, did not fully recover its anelastic strain. Even after 600 s, which is equal to the loading time, around a third of $\varepsilon_{an}(t = 0)$ was still present. From these strain measurements it is not clear if strain relaxation of sample A has saturated at 600 s, or if the strain would continue to relax at longer times. But the latter possibility is more likely, since it is known from the literature that the relaxation times of anelastic strains in metallic glasses can be much longer than the time needed to build them up [182]. In the work of Ju et al. [182], an Al-based amorphous ribbon was wound around a mandrel for $2 \cdot 10^6$ s before being released. After a relaxation time equal to the winding time, around a third of the introduced anelastic strain was still remaining (which is a similar result as seen here for sample A), and even after a relaxation time of $2 \cdot 10^7$ s, an order of magnitude larger than the loading time, the residual strain had not fully recovered, and continued to relax.

The fact that a full recovery of ε_{an} could be observed for samples B and C within 400 s demonstrates that thermal cycling clearly accelerated the rate of anelastic strain relaxation. Interestingly, applying the 5 thermal cycles during or before mandrel bending had the same effect.

In the literature, metallic glasses are often modelled as an elastic solid-like matrix containing liquid-like soft spots [23, 24]. These soft spots have a lower viscosity than the solid-like matrix and

more free volume, and act as flow units which are considered responsible for inelastic deformation upon loading within the nominally elastic regime. Once the load is removed, the elastic matrix applies back-stresses on these soft spots, and thereby restores the initial shape. Flow units have a large range of relaxation times τ and activation energies E_a [182, 183]. The probability of a flow unit being activated depends on how its E_a and τ relate to the available driving force (i.e. local stresses applied to the atomic configuration), as well as to the temperature and time. During a stress relaxation experiment, only those flow units will be activated which have low enough activation energy barrier (i.e. one that can be overcome by the given driving force at the current temperature). If the loading time is long, temperature high and driving force large enough, a high density of flow units can be are activated which may lead to percolation, and homogeneous plastic flow can occur [183].

Mandrel stress relaxation experiments in the literature [183, 184] found that the stress relaxation rate is decreased by pre-annealing metallic-glass ribbons, but increased when deforming the ribbons (e.g. by cold-rolling) before winding them around the mandrel. This was understood by the fact that flow units are annihilated during annealing, and created upon deformation. The anelastic strain recovery measurements presented here may provide information on how thermal cycling affects these flow units. Strain recovery was clearly accelerated by thermal cycling. This suggests that flow units were softened, meaning that their τ and E_a were reduced and thereby they were more easily activated. It should be noted that the activation of flow units, i.e. the development of anelastic strain, was not directly observed, but it is assumed that the rate of its development is

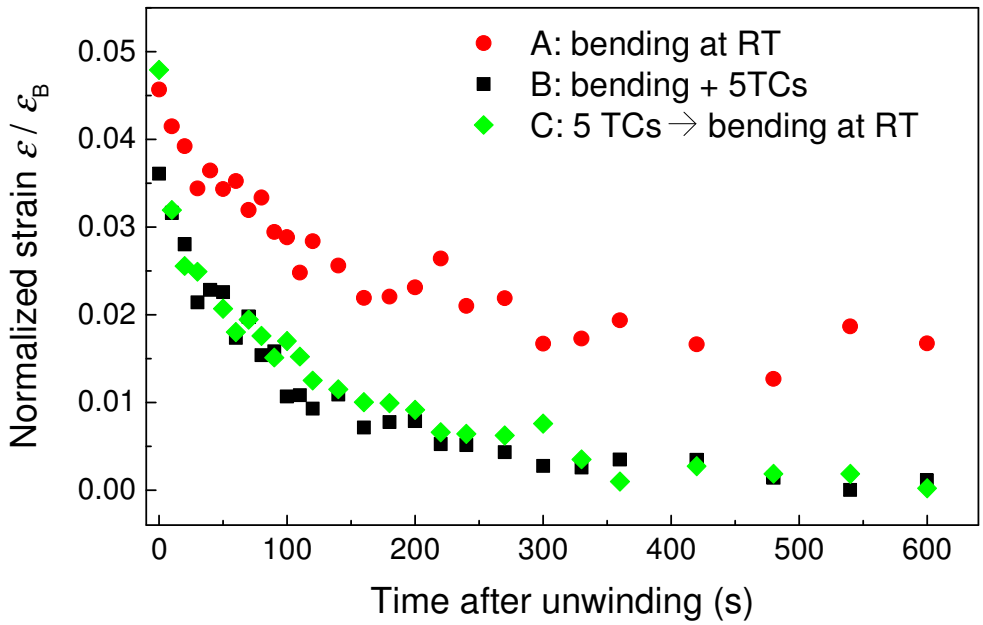

Fig. 6.10. Evolution of the strain upon unwinding the ribbons from the mandrels, normalized to the strain ε_B imposed during bending.

probably affected in the same manner as the rate of its recovery. The amount of anelastic strain built-up during bending should however be given by $\varepsilon_{an}(0)$, and as seen in Table 6.1, this value is not larger for the thermally cycled samples B and C. From this result, thermal cycling did not seem to increase the number of activated flow units. This may seem inconsistent with the observation above that thermal cycling shortens τ, which should imply that more flow units have a τ below the loading time and can be activated. The time defined here as $t = 0$ is physically not possible to be the instantaneous moment of unloading. During the process of unwinding the ribbon and taking the first photograph from which $\varepsilon_{an}(0)$ is calculated, the ribbon will have already started relaxing. In the case of samples B and C, the strain recovery rate is much faster than for sample A, and any difference between the defined time $t = 0$ and the real moment of unwinding will have led to a bigger underestimation of $\varepsilon_{an}(0)$. In any case, even if thermal cycling had increased the amount of flow units activated, this increase would not have been very substantial, since it did not lead to the percolation of flow units (i.e. viscoplastic flow).

In summary, thermal cycling, applied during or before mandrel bending, seems to have mainly softened the soft spots, thereby speeding up anelastic strain recovery, but did not affect viscoplastic flow.

6.4 Thermal cycling of Fe-based ribbons

6.4.1 Introduction

Metallic glasses do not have many industrial applications yet; the main current commercial interest for these materials still lies in their magnetic properties. Several Fe- and Co-based metallic glasses have excellent soft magnetic properties, but are also very brittle, especially after annealing. It would therefore be of interest to improve their plasticity, for example through rejuvenation. The plasticity of several metallic-glass compositions (La-, Cu- and Zr-based) could successfully be increased by thermal cycling [99, 101, 103], and it would be nice to explore if this treatment can also have beneficial effects on Fe-based glasses.

It is not yet entirely clear what characteristics a glassy sample has to have in order to be affected by thermal cycling. A certain degree of heterogeneity is assumed to be required, in order for non-affine strains to be able to form during cycling [99, 106]. Furthermore, the outcome of thermal cycling can be diverse, and seems to depend on the atomic bonds [105]. The initial energy of the metallic glass is also assumed important: a glass which is already very unrelaxed may become more

structurally ordered (instead of disordered) upon processing [5]. Furthermore, the temperature difference applied during cycling, as well as the lower and upper temperature limits relative to the T_g of the metallic glass, must play a role, though such effects have not yet been explored in the literature.

In the following, the effect of thermal cycling on amorphous ribbons of $Fe_{73.5}Cu_1Nb_3Si_{15.5}B_7$ is investigated. This composition is a commercially available metallic glass, and is the precursor of the partially nanocrystalline metallic-glass ribbon VITROPERM made by Vacuumschmelze GmbH (Germany), which is used as transformer cores. The effect of thermal cycling on these ribbons was explored here by determining the change in mechanical and magnetic properties after cycling.

6.4.2 Experiments

Up to 180 thermal cycles (TCs) were applied to the amorphous $Fe_{73.5}Cu_1Nb_3Si_{15.5}B_7$ ribbons. Thermal cycling was carried out as described in §3.1.2. Thermal cycling did not induce crystallization, as observed from X-ray diffraction (Appendix C, Fig. C.2).

The mechanical properties, before and after cycling, were determined by nanoindentation using a spherical 8 µm-radius tip. The maximum load was 100 mN, and a loading and unloading rate of 0.5 mN/s was applied. Four batches of 20 indents each were performed in order to achieve 80 indents in total per sample state. The properties of the ribbon were found to vary substantially between batches, e.g. the average initial yield load F_Y of the as-cast ribbon varied by more than 15%. Therefore, indents measured after thermal cycling were placed between the indents already made on the as-cast sample, as schematically shown in Fig. 6.11, with an approximate spacing between indents of 30 µm.

The magnetic properties examined were the magnetic coercivity H_c and saturation magnetization M_s, which were determined from hysteresis loops measured with a magnetic loop

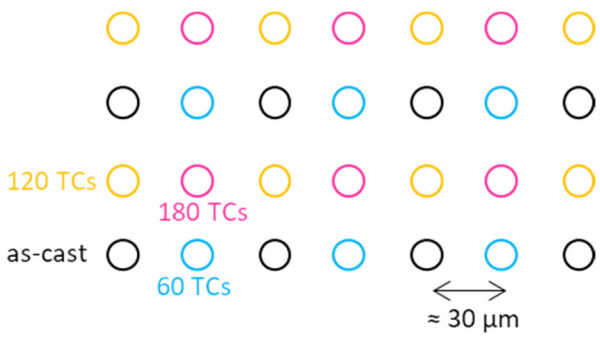

Fig. 6.11. Schematic of 'chequerboard'-like placement of indents. In order to avoid measuring a difference in mechanical properties by nanoindentation which is only due to location within the sample, the same area is tested after 60, 120 and 180 thermal cycles (TCs) as of the as-cast state.

tracer at room temperature. Hysteresis loops were measured up to two maximum applied fields H_{max}: 0.66 kA/m, from which H_c was measured, and 4.25 kA/m, which was used to determine M_s. The effects of 10, 60, 120 and 180 TCs on H_c and M_s were measured for three ribbon samples.

Mössbauer spectroscopy was also performed on the ribbons, with the hope of being able to identify some structural changes after thermal cycling. These measurement were kindly carried out by Prof. M. Miglierini from the Slovak University of Technology in Bratislava (Slovakia). Brief experimental details are given in Appendix C.

The effect of thermal cycling on the Curie temperature T_{Curie} was also measured. T_{Curie} can be used as a measure for structural relaxation in metallic glasses, and can be determined by differential scanning calorimetry (DSC) [133]. It appears as a small but sharp endothermic peak in the heat flow curve. T_{Curie} of the Fe-based ribbon in its as-cast state as well as after thermal cycling was measured here by heating from room temperature to 600°C at 20 K/min with a Q2000 DSC (TA Instruments). DSC traces using other heating rates, ranging between 5 and 100 K/min were also measured for the as-cast sample in order to demonstrate the effect of heating rate on the measured value of T_{Curie}.

6.4.3 Results and discussion

From the literature [99] and from previous results (§6.2), it is known that thermal cycling can have a significant rejuvenation effect on the mechanical properties measured by nanoindentation of La- and CuZr-based metallic glasses. Especially the pop-ins were found to be affected: after 10 thermal cycles (TCs), the initial yield load F_y (i.e. load at which the first pop-in occurred) decreased on average by around 30%, and the size of the first pop-in Δh by 40–60%. But in the case of the Fe-based ribbon explored here, 10 TCs did not affect the properties to such an extent. The median values of the initial yield load F_y and pressure P_y did not change upon 10 TCs, however the lower ends of these distribution curves were shifted to slightly higher values (meaning that the softer regions of the sample were strengthened), which may indicate a slight relaxation of the glassy sample (Appendix C, Fig. C.3). The hardness H, indentation moduli $E_{r,unloading}$ and $E_{r,Hertzian}$, and Δh were barely, if at all, affected. But by increasing the number of TCs to 60, 120 and 180, a decrease in all measured properties was observed (Fig. 6.12). As was the case for the La- and CuZr-based metallic glasses, the pop-in-related properties F_y, P_y and Δh were affected to a greater extent than H, $E_{r,unloading}$ and $E_{r,Hertzian}$, which rather depend on the global structure. After 180 TCs, the median of F_y was found to decrease by around 24%, and of Δh by 31%.

Interestingly, the rejuvenation effect of thermal cycling on the mechanical properties did not seem to be permanent. Three months after thermal cycling was carried out, nanoindentation was performed once more, and the property values were found to increase again. Whereas F_y and Δh did not fully recover to the initial state, H, $E_{r,unloading}$ and $E_{r,Hertzian}$ increased to even higher values

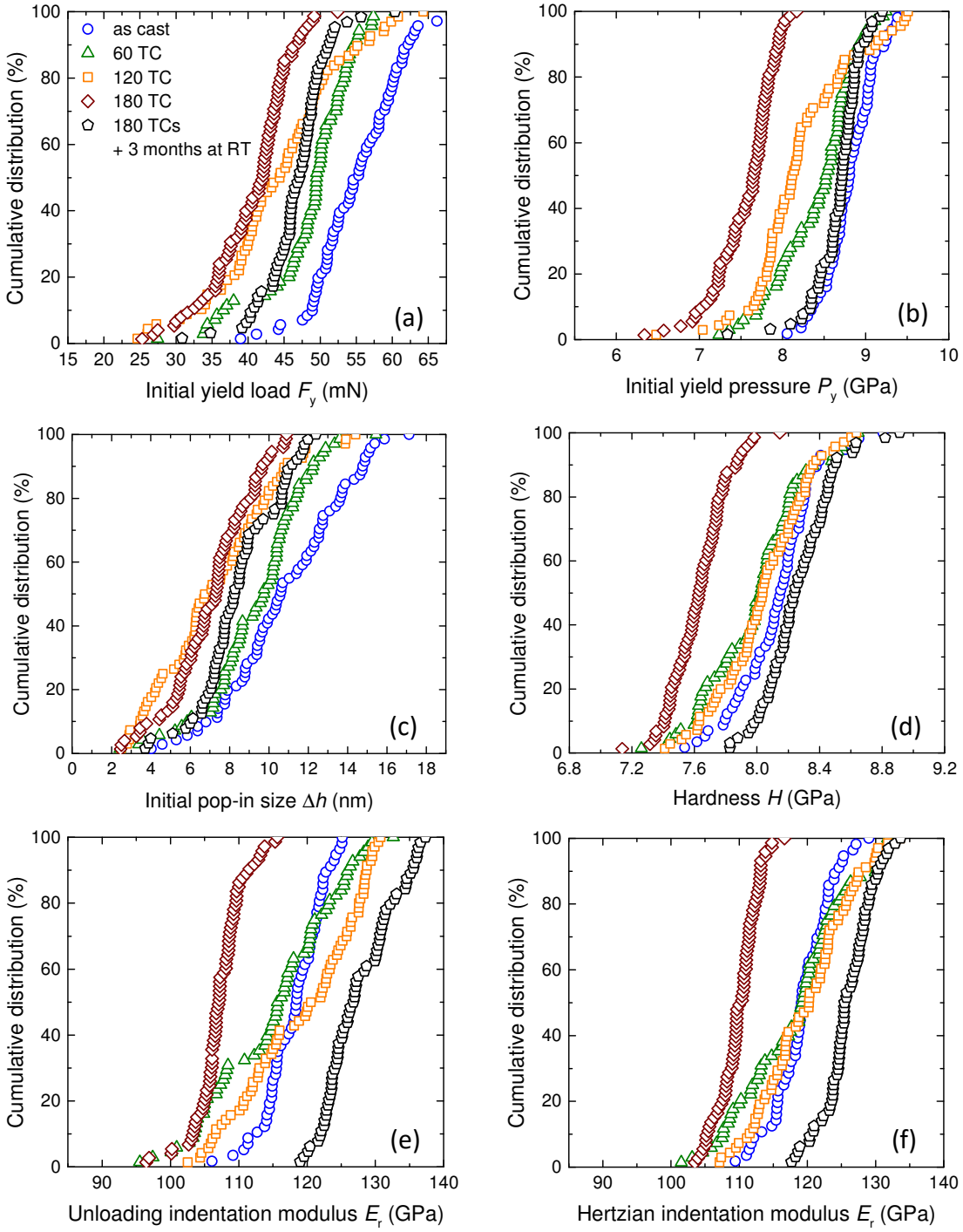

Fig. 6.12. Cumulative distribution curves of several mechanical properties determined by nanoindentation for the amorphous as-cast Fe-based ribbon, after 60, 120 and 180 thermal cycles (TCs), and after storage of the sample at room temperature for 3 months after the cycling was performed.

than of the as-cast sample. Relaxation at room temperature can be significant for metallic glasses with relatively low glass-transition temperatures T_g (as was observed for the La-based glass studied in Chapter 4), but Fe-based glasses have a relatively high T_g and room-temperature ageing is unlikely to be significant. For the amorphous ribbon studied here, no glass-transition step could be distinguished by DSC (Fig. 6.13). The onset of crystallization T_x probably overlapped with or occurred before T_g. This means that room temperature is certainly less than 40% of T_g. If it is assumed that the recovery in mechanical properties is not due to ageing of the sample, then the effect of thermal cycling itself is probably recoverable. The non-affine thermal strains introduced during thermal cycling [35, 99], which should be well within the elastic regime [122], may be in this case anelastic. The reversal of one of the effects of thermal cycling after room-temperature ageing was seen also in ref.[105]. Ketov et al. observed an increase in Young's modulus of the surface of two Zr-based metallic glasses after thermal cycling, which disappeared after relaxation at room temperature for 3 days [105]. But how room-temperature relaxation affected the other, maybe more important, changes (e.g. increase in plasticity) was not shown.

Many Fe-based metallic-glass compositions are ferromagnetic, and present a Curie temperature T_{Curie}. The T_{Curie} of metallic glasses is known to increase upon structural relaxation [88] and is a simple way to monitor the degree of relaxation. The amorphous $Fe_{73.5}Cu_1Nb_3Si_{15.5}B_7$ ribbon studied here was found to have a T_{Curie} of around 323°C, measured by DSC with a heating rate of 20 K/min (Fig.

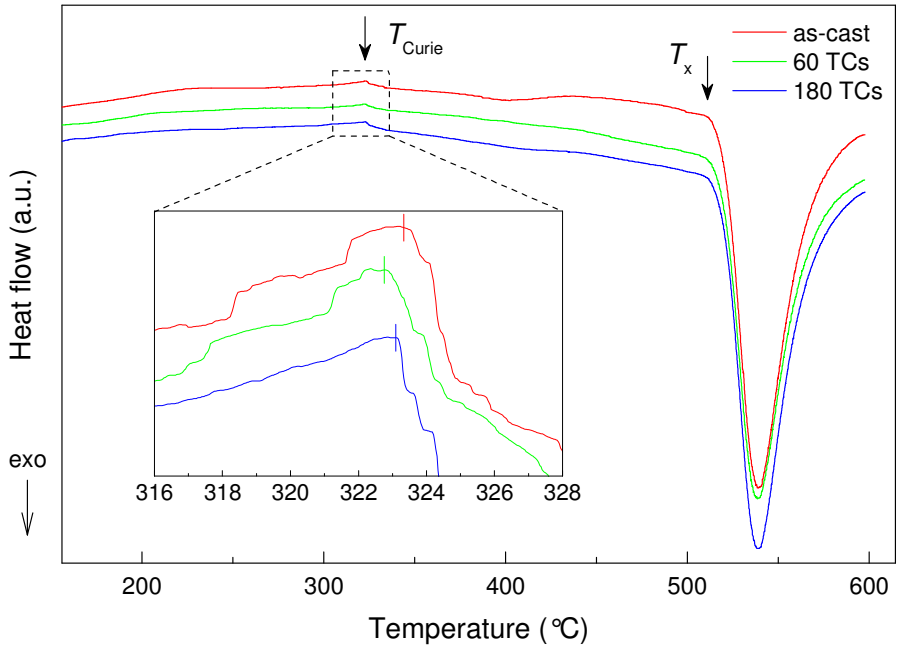

Fig. 6.13. DSC heat flow curves, measured at 20 K/min, of the as-cast Fe-based ribbon, and after 60 and 180 thermal cycles (TCs). The onset of crystallization T_x is at around 520°C. At around 323°C, a small endothermic peak is visible, which corresponds to the Curie temperature T_{Curie}. The inset shows a zoom-in on T_{Curie}.

6.13). As expected, T_{Curie} increased significantly upon annealing (Fig. 6.14a): 15 min annealing at 400°C led to an increase of over 10°C. On the other hand, thermal cycling did not induce much change (Fig. 6.14b). Cycling of up to 30 TCs did not seem to affect T_{Curie}, but after 60 TCs, a decrease of around 0.75°C was observed. Further cycling increased T_{Curie} again. This decrease of less than 1°C after 60 TCs seems minimal, especially when comparing to the change that annealing can achieve. However, Ri et al. [107] found similarly a decrease of 1 K after applying 120 TCs to $Fe_{78}Si_9B_{13}$ ribbons, and claimed this to be a sign of rejuvenation.

An important fact to take into consideration concerning the measurement of T_{Curie} is that metallic-glass samples relax during heating up. If low heating rates are used during the DSC measurement, the sample will relax more, and the measured T_{Curie} will be higher [187]. This was also observed in the present case, as can be seen in Fig. 6.15a. T_{Curie} was above 326°C when measured at 5 K/min, and around 320°C at 100 K/min. If thermal cycling of the Fe-based ribbon really did induce some disorder, it is likely that heating during DSC measurement partially relaxed out this rejuvenation. In addition, more unrelaxed glasses relax faster than already relaxed ones [187]. In order to lower the relaxation during DSC measurement, T_{Curie} of the thermally cycled Fe-

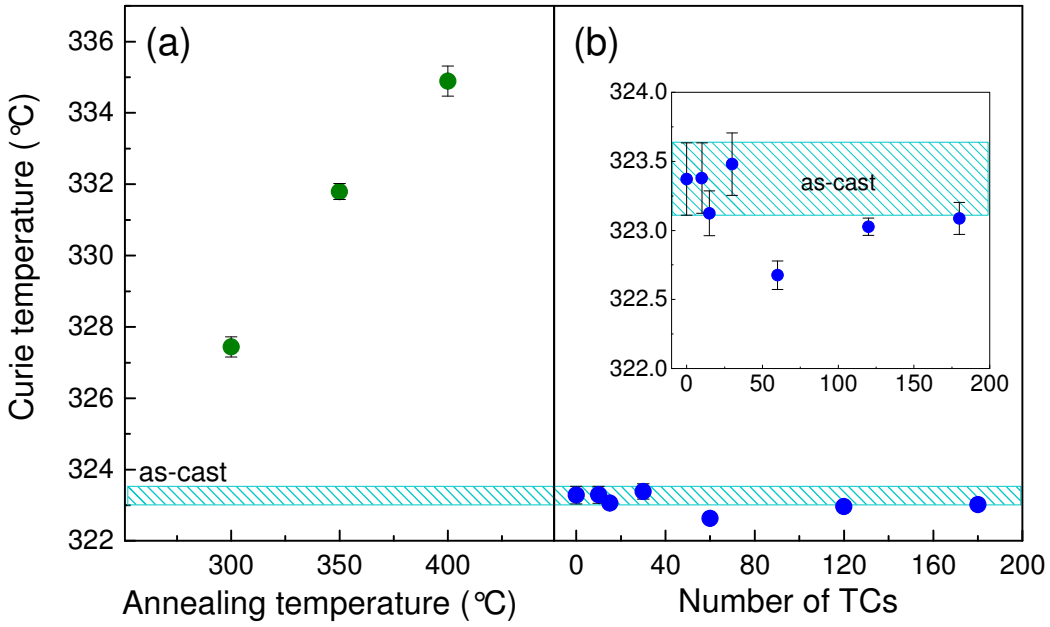

Fig. 6.14. The Curie temperature T_{Curie} of the amorphous $Fe_{73.5}Cu_1Nb_3Si_{15.5}B_7$ ribbon measured by DSC at 20 K/min. The shaded blue band gives the range of T_{Curie} values determined for the ribbon in its as-cast state, with the width of the band corresponding to ±1 standard deviation measured over more than 20 samples. After 15-min anneals at 300, 350 and 400°C, T_{Curie} increased by several °C (a). Thermal cycling led to a small decrease of almost 1°C after 60 TCs (b). A more detailed view of the effect of thermal cycling on T_{Curie} is shown in the inset. The error bars represent the standard deviation. T_{Curie} of the annealed and thermally cycled samples were determined from 2 to 6 DSC measurements per treatment condition.

based glass (up to 60 TCs) was also measured at a higher heating rate of 100 K/min (Fig. 6.15b). But even for this heating rate, there is no clear decrease of T_{Curie} upon cycling.

Magnetic properties are sensitive to the structure as well as to internal stresses. Annealing of ferromagnetic metallic glasses typically leads to a decrease in magnetic coercivity H_c, which is mainly due to the relief of internal stresses present in the as-cast glasses [188]. The saturation magnetization M_s is also sensitive to structural relaxation; M_s of Fe-based metallic glasses was found to decrease [189] or increase [190] upon annealing. H_c and M_s of the present amorphous $Fe_{73.5}Cu_1Nb_3Si_{15.5}B_7$ ribbon were determined here by measuring the magnetic hysteresis loops. As can be seen in Figs. 6.16 and 6.17, thermal cycling did not change the shape of the loop, nor did it affect H_c or M_s. The advantageous side of this result is that thermal cycling did not degrade the relatively good soft magnetic properties of this metallic glass; but from a more negative point of view, this result did not provide any evidence that thermal cycling may have induced rejuvenation (or relaxation).

Changes in the structure of magnetic metallic glasses may also be detected by Mössbauer spectroscopy. The isomer shift *IS* and hyperfine magnetic field B_{hf}, which are determined by fitting of the Mössbauer spectra [191], are sensitive to the short-range order of metallic glasses, and depend on the chemical environment around Fe atoms. For example, atomic rearrangements in the

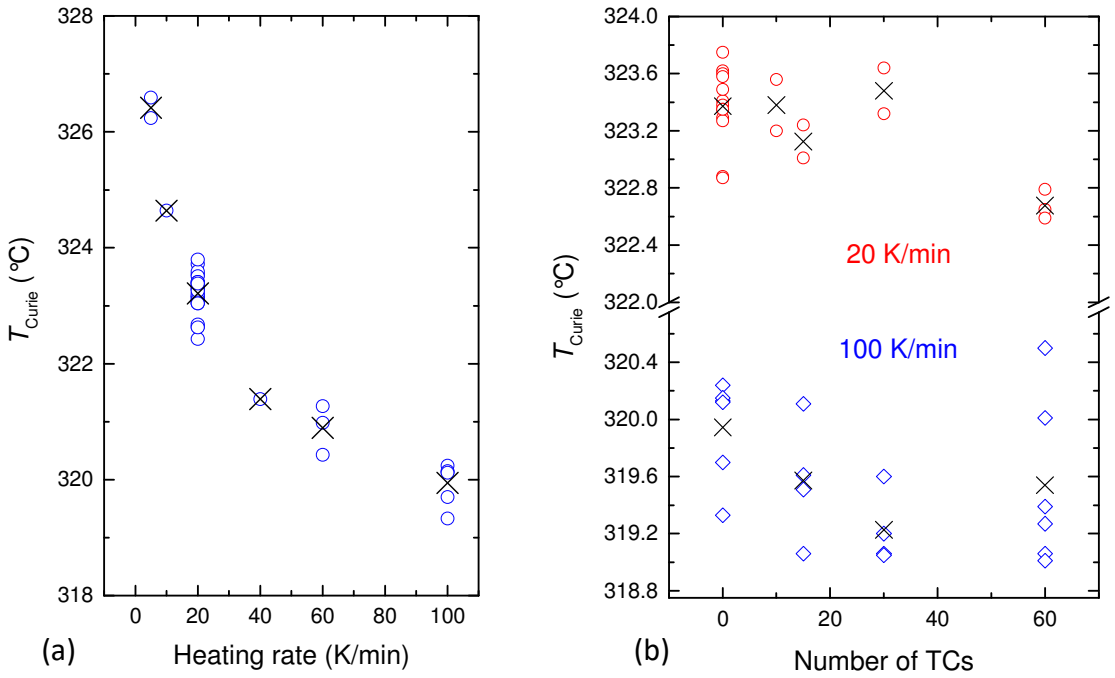

Fig. 6.15. Effect of heating rate during DSC measurement on the measured Curie temperature T_{Curie} of an as-cast ribbon (a). Curie temperature T_{Curie} as a function of thermal cycles (TCs), measured at 20 and 100 K/min (b). The circles represent individual measurements, and the crosses correspond to the average values.

amorphous phase caused by annealing of a similar Fe-based composition to the one studied here were detected from changes in the hyperfine magnetic-field distributions measured by Mössbauer spectroscopy [191]. Mössbauer spectra were obtained here for the $Fe_{73.5}Cu_1Nb_3Si_{15.5}B_7$ ribbon in its as-cast state and after 60 and 180 TCs (Appendix C, Fig. C.4). *IS* and B_{hf} seemed to increase slightly after 180 TCs (Fig. 6.18), but the changes are within the experimental errors.

According to the results on magnetic properties (T_{Curie}, H_c, M_s, *IS* and B_{hf}), thermal cycling of the Fe-based ribbon barely induced any structural changes. Yet thermal cycling did affect the mechanical properties determined by nanoindentation; especially properties related to pop-ins

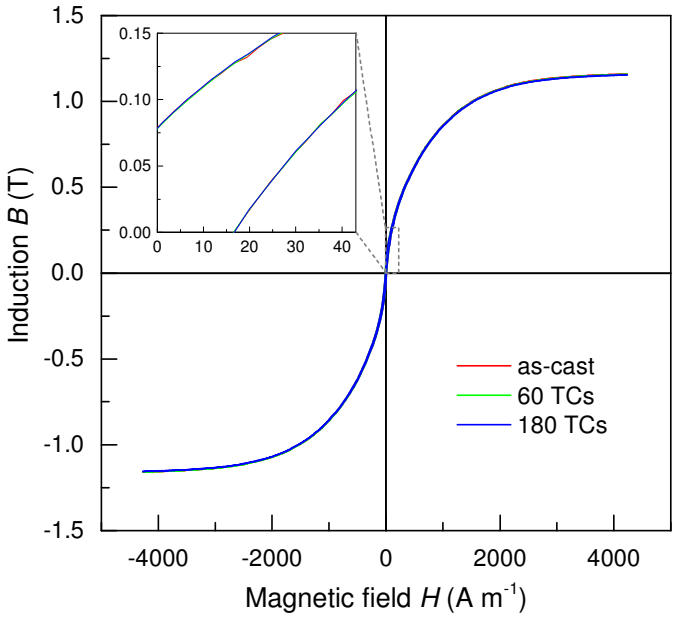

Fig. 6.16. Magnetic hysteresis curve of the ribbon as-cast and after thermal cycling.

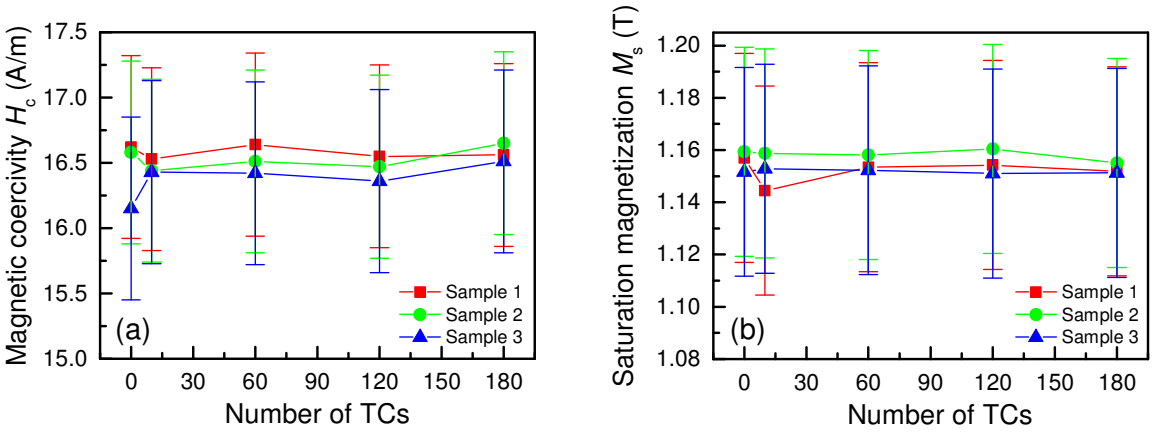

Fig. 6.17. Magnetic coercivity H_c (a) and saturation magnetization M_s (b) as a function of the application of thermal cycles (TCs) on the amorphous $Fe_{73.5}Cu_1Nb_3Si_{15.5}B_7$ ribbon. Three samples were measured. The slight variations of H_c and M_s observed are well within the experimental error, which is given by the error bars.

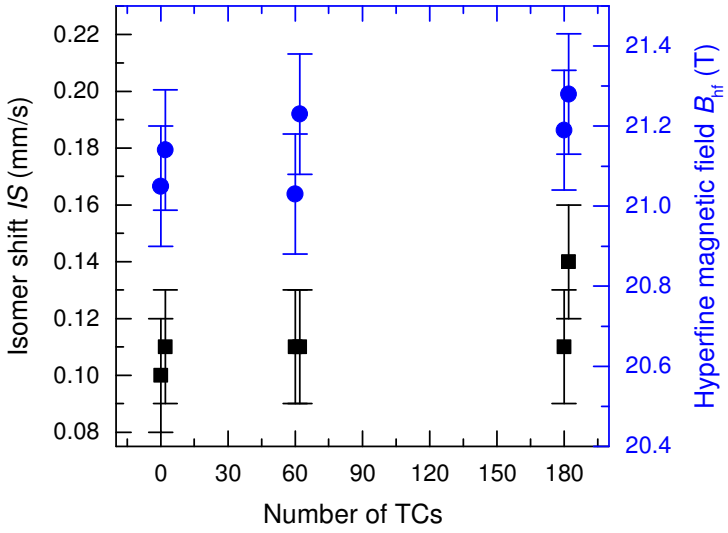

Fig. 6.18. Effect of 60 and 180 thermal cycles (TCs) on the isomer shift *IS* and hyperfine magnetic field B_{hf} of the Fe-based metallic-glass ribbon, determined by Mössbauer spectroscopy. Two ribbon samples were measured per sample state. The error bars correspond to errors from the fitting procedure.

showed rejuvenation. But it seems to be less effective for this glass than for other metallic-glass compositions (such as La- or CuZr-based systems), since a much higher number of TCs were needed to achieve a similar decrease in initial yield stress. In the work of Ri et al. [107], thermal cycling of another Fe-based glass was found to have an alternating effect between relaxation and rejuvenation, although the global effect tended towards the latter. A similar process may be taking place for the ribbon tested here, and may be an explanation why more cycles are required than for other glass systems. Furthermore, it may be that the cycling parameters (e.g. upper and lower temperature limits) are not appropriate, i.e. a greater temperature change during cycling may be necessary to induce the same thermal strains as in metallic glasses with lower T_g.

6.5 General conclusions on the results of thermal cycling

The main findings of the above three sections are as follows: Nanoindentation measurements of a $Cu_{46}Zr_{46}Al_7Gd_1$ bulk metallic glass showed that thermal cycling significantly reduced the median values of initial yield load F_y and stress P_y and the size of the first pop-in Δh, but barely affected the hardness or indentation modulus. Consequently, thermal cycling could only partially reverse the effect of annealing. From elastic-bending experiments on a $La_{25}Ni_{20}Al_{25}$ ribbon, it was observed that thermal cycling sped up the recovery rate of anelastic strain, which depends mainly on the 'flow units' within the glassy sample. Finally, thermal cycling on a $Fe_{73.5}Cu_1Nb_3Si_{15.5}B_7$ metallic-glass ribbon clearly affected F_y, P_y and Δh (though many more cycles are necessary than for other

metallic-glass compositions), but barely any variation was observed in the magnetic properties, which are sensitive to structural changes of the material. Furthermore, the effect of cycling on the nanoindentation-measured properties of the Fe-based ribbon was not permanent, and partially relaxed away with time.

From the nanoindentation measurements, it is clear that thermal cycling affects mainly the pop-ins. The structure of metallic glasses is often schematized as a relatively stiff, solid-like matrix containing liquid-like soft spots [23, 24]. These soft spots are the regions where shearing is initiated, and where pop-ins take place. They are also responsible for anelastic flow. From the above results, thermal cycling seemed to target mainly the soft spots, without affecting much the global structure. One may argue that any change in properties must be linked to a change in structure, though often a small modification of the structure can lead to significant changes in the properties of metallic glasses [2]. The fact that thermal cycling targets specifically some properties while leaving others unaffected is highly motivating, and provides the hope that by careful selection and combination of thermal cycling with other treatments, it may be possible to tailor metallic glasses in order to achieve remarkable properties.

7 Characterization of an Aged Au-based Metallic Glass by FDSC

7.1 Introduction

The possibility of obtaining a metallic alloy with a glassy structure by rapid solidification was first demonstrated on the composition $Au_{75}Si_{25}$ [1]. This metallic glass was however a relatively bad glass-former with a low thermal stability, and crystallized after 24 h at room temperature. In the following years, metallic glasses of other compositions were discovered with better glass-forming ability and higher stability, and research tended to focus on such systems (e.g. Zr- or Pd-based) rather than on Au-based glasses. But the interest for the latter increased once Au-based compositions were found with not only a good enough glass-forming ability to form bulk samples but also high stability and a large supercooled-liquid region, which allows for thermoplastic forming [192].

Gold alloys have many applications, for example in electronics or in the medical sector, but they are best known and most cherished as jewellery. Metallic glasses based on gold have several advantages over their crystalline counterparts in this sector: they have a significantly higher hardness [192], scratch resistance and a better surface finish due to the lack of grain boundaries.

The interest in studying Au-based metallic glasses lies not only in the vast range of potential applications, but also in their experimental advantages. These glasses have a good resistance to oxidation and have relatively low characteristic temperatures (i.e. glass-transition temperature T_g, crystallization temperature T_x, onset of melting T_m). These temperatures, as well as the structural relaxation behaviour and other calorimetric properties of these systems are therefore easily characterized by conventional differential scanning calorimetry (CDSC), i.e. high-temperature calorimeters are not necessary. These metallic glasses are also ideal for ultra-fast DSC (FDSC) measurements, especially if using the FDSC 1 by Mettler Toledo, which is limited to around 773 K (500°C). Furthermore, the melting temperature and the critical cooling rate of many Au-based glasses are well within the limits of the FDSC 1, meaning that a sample can be vitrified in the FDSC again after being melted.

In the case of Au-based metallic glasses, room temperature (RT) is quite high relative to their T_g (above 70% of T_g), and storage at RT can lead to significant structural relaxation. A signature of this ageing is the presence of an endothermic peak below T_g in the heat capacity curve measured by DSC, for example as shown in Fig. 7.1 for the composition $Au_{49}Cu_{26.9}Si_{16.3}Ag_{5.5}Pd_{2.3}$. This sub-$T_g$ peak

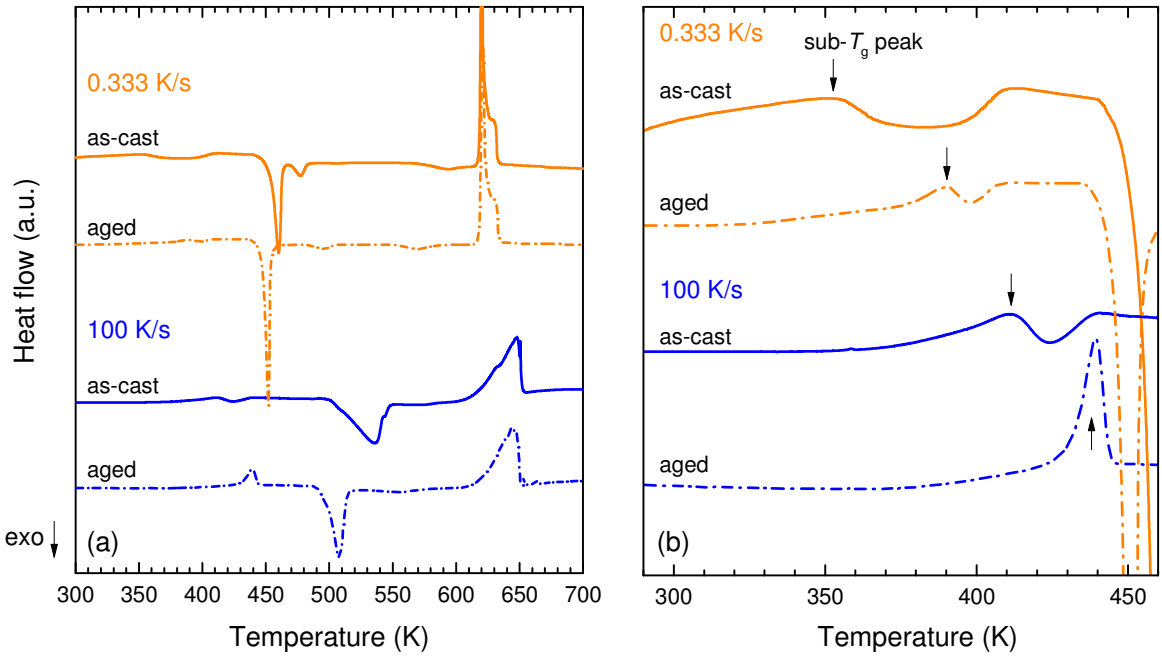

Fig. 7.1. Scaled DSC traces of the as-cast and aged Au-based ribbons measured at 20 K/min (= 0.333 K/s) by CDSC and at 100 K/s by FDSC (a). A zoom-in on the endothermic sub-T_g peak is shown in (b).

corresponds to the disordering of highly ordered zones in the glass during heating up in the DSC [163, 166], and has been observed upon annealing of many glasses (not only metallic) [157, 158, 159, 160, 161, 162, 149]. Such a sub-T_g peak was also observed in §4.3.3 for a La-based metallic-glass ribbon.

In the present chapter, the composition $Au_{49}Cu_{26.9}Si_{16.3}Ag_{5.5}Pd_{2.3}$ will be studied by DSC, with the main focus on the endothermic sub-T_g peak. The kinetics of this disordering event was characterized by heating at a wide range of different rates through the use of conventional DSC as well as FDSC.

Furthermore, the possibility of rejuvenating a ribbon, which was aged for several years at RT, was explored through a form of *recovery annealing* [94, 95]. By annealing above the fictive temperature (i.e. the crossing point of the glass enthalpy with the supercooled-liquid enthalpy), followed by fast cooling, the magnitude of the endothermic peak could be decreased. The effect of this annealing treatment on the mechanical properties was explored using nanoindentation.

7.2 Experiments

7.2.1 Samples

Two metallic-glass ribbons of the composition $Au_{49}Cu_{26.9}Si_{16.3}Ag_{5.5}Pd_{2.3}$ with different thermal histories were studied. The first, which was provided by Prof. J. Löffler's group (ETH, Switzerland), was melt-spun in 2013, and since then kept in a freezer at around 251 K (−22°C). The second ribbon was provided by K. Georgarakis (EURONANO SIMaP Grenoble INP, France). It was melt-spun in 2010 and then stored at RT. All the experiments reported here were performed in the years 2017 and 2018.

The second ribbon, after spending around 7–8 years at RT, is very relaxed (as will be seen in the next section §7.3), and is therefore referred to in the following as "aged". In comparison, the first ribbon is still relatively unrelaxed, and is called here "as-cast", even though it went through some relaxation since it was spun.

7.2.2 DSC measurements

The Au-based ribbons were characterized by CDSC and FDSC. The aged ribbon contained some crystals at its surface (which were already present in its as-cast state), and was therefore ground (with SiC grinding papers of grit sizes between P1200 and P4000) on both sides in order to remove these crystals, before being measured by CDSC and FDSC. Grinding was also performed to reduce the ribbon thickness from around 40 to below 20 µm, in order to reduce thermal-lag errors when measuring at high heating rates by FDSC. The as-cast ribbon was completely amorphous in its initial state (according to X-ray diffraction measurements), and had a thickness of around 16 µm (i.e. thin enough for FDSC measurement), and could therefore be directly used without prior grinding.

In the case of CDSC, the samples (of around 10–15 mg) were heated from 173 K (−100°C) to 773 K (500°C), which is well above the melting peak, before being cooled back to 173 K, followed by a second heating run (on the now-crystallized sample) in order to obtain the baseline. Heating rates between 0.833 K/s (= 5 K/min) and 3 K/s (= 180 K/min) were used. In order to take into account temperature errors arising from thermal lag due to heating at the high rates, the melting onset T_m (= 618 K) measured upon the first heating run was used as a calibration point. The apparent T_m measured at different heating rates by CDSC is shown in Appendix D, Fig. D.1.

For the FDSC measurements, samples of a maximum size of 150 µm × 150 µm were first cut with a scalpel from the ribbons. The sample mass was estimated to be around 1–2 µg. They were then

heated from either 173, 193 or 233 K (−100°C, −80°C or −40°C) to 773 K (500°C) at heating rates ranging between 2 and 10,000 K/s, held at 773 K for 0.1 s and then cooled at 100 K/s, during which the samples crystallized. A second heating run was performed at the same heating rate as the first, in order to measure the baseline as well as to obtain the onset temperature of melting $T_{m(cryst.)}$ of the crystallized sample. $T_{m(cryst.)}$ was used as a temperature calibration point. More information on the temperature-calibration procedure is given in Appendix D, alongside example heat-flow curves of the different heating and cooling runs.

7.2.3 Recovery annealing heat treatment

The possibility of rejuvenating the aged Au-based metallic-glass ribbon through annealing was explored by FDSC. The heating protocol is shown in Fig. 7.2. Samples were heated to T_a at 100 K/s (where T_a is above the fictive temperature $T_{fictive}$ ≈ 373 K), kept at T_a for a certain time t_a, then cooled again at 100 K/s. The DSC heat flow curve of the sample was measured at 100 K/s directly after annealing. As for the other FDSC measurements mentioned in §7.2.2, the sample was then cooled at 100 K/s in order to crystallize the sample, followed by a second heating run in order to obtain the baseline. Two other cooling rates, 2 K/s and 5000 K/s, were tested for T_a = 423 K and t_a = 10 s.

In order to determine the effect of this annealing on the mechanical properties, annealing was also performed on a macroscopic sample (a piece of ribbon of 2 cm length), which was then

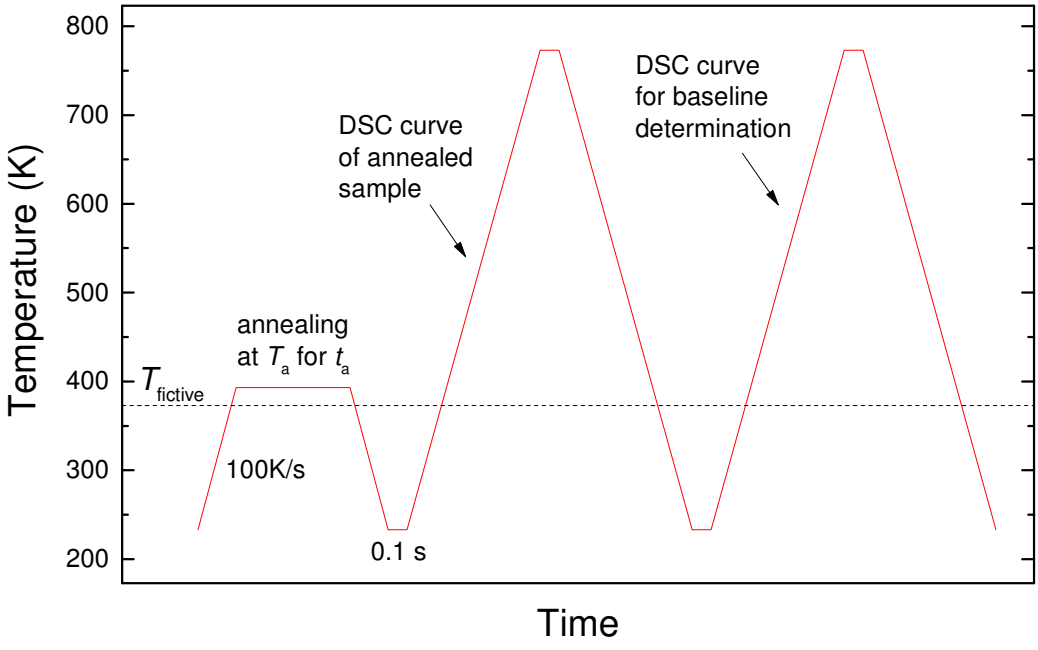

Fig. 7.2. Annealing treatment performed by FDSC on the aged Au-based metallic-glass ribbon. Heating and cooling rates were 100 K/s.

characterized by nanoindentation. This sample was dipped in 423 K hot sunflower oil (heated on a hot plate), then taken out after 10 s and quenched in water at around room temperature. The sample was then cleaned in an ultrasonic bath. One end of the sample was cut off, and measured by FDSC.

7.2.4 Nanoindentation

The effects of the recovery annealing heat treatment on the mechanical properties of the aged ribbon were determined by nanoindentation using a spherical indenter. Before indentation, a 2 cm-long sample was cut from the aged Au-based ribbon and ground in order to remove the surface crystals, then polished with 1 µm diamond paste and finally with a 0.06 µm colloidal silica suspension. Around 90 indents were performed with a spherical tip of 8 µm radius. A constant loading rate of 0.5 mN/s was used, and a maximum load of 50 mN was applied.

Nanoindentation was carried out again after the recovery annealing treatment. Around 40 indents were performed, placed between or next to the previous indents. The spacing between indents was larger than 20 µm.

7.3 Results and discussion

7.3.1 Relaxation kinetics determined by DSC measurements

DSC heat-flow curves of the as-cast and aged Au-based ribbons are shown in Fig. 7.1a. When measuring with a heating rate of 20 K/min (= 0.333 K/s), T_g occurred at around 400 K, the onset of crystallization $T_{x,onset}$ at around 450 K and of melting T_m at 620 K. As mentioned above, room-temperature ageing is quite significant for this composition, and consequently an endothermic sub-T_g peak is apparent (Fig. 7.1b). This peak was even present for the as-cast sample, which was stored at 251 K (−22°C). As expected, the sub-T_g peak was larger and occurred at a higher temperature for the aged ribbon. It also shifted to higher temperatures when measuring at a higher heating rate. In the case of the aged ribbon, it overlapped with T_g on heating at 100 K/s and formed a large overshoot.

Since the melting temperature is quite low and the critical cooling rate of this composition is within the capacity of the FDSC, crystallization can be avoided upon cooling at a high enough rate, and a new glass, called here “re-melted”, could be formed and characterized directly afterwards in

the FDSC (Appendix D, Fig. D.3). The critical cooling and heating rates to avoid crystallization have already been studied in the literature, and were found to be around 600 K/s and 6000 K/s, respectively [165]. The sub-T_g peak is not present in the freshly formed re-melted sample, but appeared quickly upon annealing even at temperatures below RT (Fig. 7.3). It should be noted that this re-melted glass, which is formed by cooling from 773 K (i.e. well above the melting temperature), is different to, and should not be confused with, the recovery-annealed samples discussed in §7.3.2 which are formed by cooling from 373 – 463 K (i.e. the supercooled liquid region).

The change of enthalpy with temperature can be determined by integrating the specific heat $C_p(T)$. The latter was estimated by scaling the measured heat flow curves in order for the specific-heat values of the glassy state $C_{p,glass}$ and of the supercooled-liquid state $C_{p,SCL}$ to match those found in the literature. $C_{p,glass}$ was taken as ≈25 J/mol K and $C_{p,SCL}$ as ≈45 J/mol K [193]. The heat-flow curves of the sample upon heating at 100 K/s are shown in Fig. 7.4a, and the enthalpy H vs. temperature T plot in Fig. 7.4b. From the enthalpy vs. temperature plot, one can observe that the enthalpy slope of the as-cast glass increases at around 400 K, then returns back to the initial slope, shortly before the supercooled-liquid state was reached. This increase in energy corresponds to the occurrence of the sub-T_g peak in the heat flow curve, during which certain relaxed zones in the glass

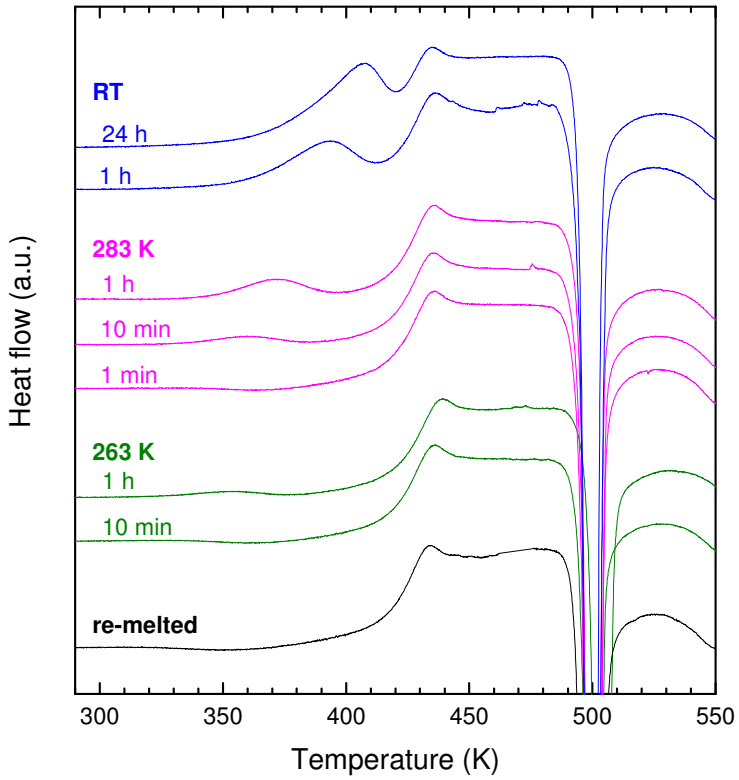

Fig. 7.3. FDSC curves measured at 100 K/s showing the appearance of the sub-T_g peak for the re-melted sample upon annealing at various temperatures and times.

become disordered. Upon relaxation through RT ageing, the enthalpy of the Au-based ribbon decreased, and the sub-T_g peak overlapped with T_g, forming an overshoot in the heat flow curve. This overshoot implies that in the H vs. T plot, the enthalpy slope of the glassy state is retained to well above the fictive temperature $T_{fictive}$, and disordering of the relaxed zones occurs at a higher temperature than for the as-cast sample (Fig. 7.4b).

The effective activation energy $E_{sub\text{-}Tg}$ of this disordering event can be defined by determining the shift of the sub-T_g (or overshoot) peak temperature T_p upon increasing the heating rate α, and using the Kissinger equation [143], given in §4.3.5. According to Evenson et al. [194], $E_{sub\text{-}Tg}$ of their as-cast $Au_{49}Cu_{26.9}Si_{16.3}Ag_{5.5}Pd_{2.3}$ glass was found to be 88.9 ±6 kJ/mol, which corresponds to ≈ 27 ±1.8 RT_g, and agrees well with the correlation $E_\beta \approx 26$ (±2) RT_g between the activation energy of the β-relaxation E_β and T_g proposed by Yu et al. [195]. But it should be noted that $E_{sub\text{-}Tg}$ depends on the thermal history of the glass [157, 194, 196]. A more recent study by Song et al. [196] measured the activation energies $E_{sub\text{-}Tg}$ for this glass composition treated to different anneals. $E_{sub\text{-}Tg}$ was found to increase with annealing temperature and time. This can be understood from the fact that the more relaxed the glass is, the lower is the atomic mobility, and therefore a higher energy is needed to activate the transition [157]. Furthermore, this large range of $E_{sub\text{-}Tg}$ measured

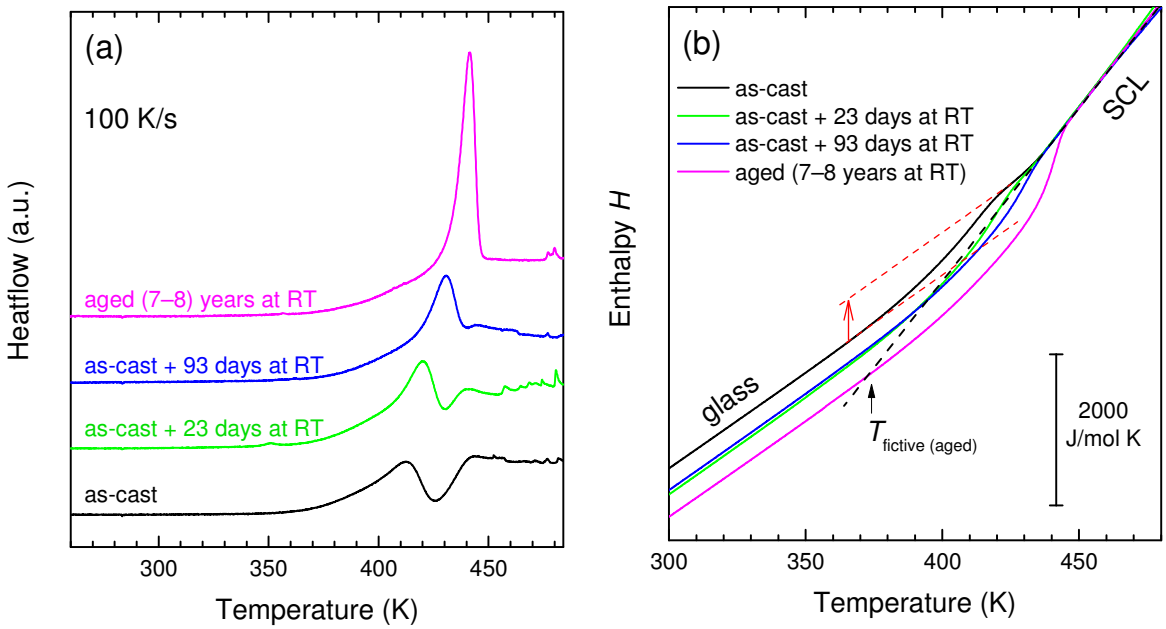

Fig. 7.4. Evolution of the endothermic sub-T_g peak upon room temperature annealing of the as-cast ribbon measured by FDSC at 100 K/s (a). Upon ageing, the ribbon relaxed and its enthalpy decreased (b). The fictive temperature $T_{fictive}$ (which corresponds to the crossing point of the enthalpy glass line with the supercooled-liquid (SCL) line) decreased upon ageing. The endothermic sub-T_g peak observed for the as-cast sample in (a) corresponds to the increase in enthalpy upon heating as seen in (b), given by the red arrow, before the supercooled-liquid region is reached.

by Song et al. implies that this disordering process has a spectrum of relaxation times and activation energies.

In addition, Song et al. found that $E_{\text{sub-Tg}}$ did not increase uniformly; instead it showed a step-like increase [196]. At the beginning of the annealing treatment, the increase was relatively small, with $E_{\text{sub-Tg}}$ ranging between 75–100 kJ/mol. Then after a time t_{trans}, $E_{\text{sub-Tg}}$ jumped to values between 150–175 kJ/mol and remained roughly constant. t_{trans} was shorter for higher annealing temperatures. Whereas $E_{\text{sub-}Tg}$ in the first stage is similar to E_{β}, $E_{\text{sub-Tg}}$ is closer to the activation energy of the α relaxation in the second stage.

In the present work, $E_{\text{sub-Tg}}$ was determined for the as-cast and aged Au-based metallic-glass ribbons, as well as for the re-melted sample annealed for 1 min at 303 K in the FDSC. Example DSC curves of these glasses at different heating rates are given in Fig. 7.5. The peak temperatures T_{p} were plotted in the Kissinger plot in the form of $ln(\alpha/T_{\text{p}}^2)$ vs. $1/T_{\text{p}}$ (Fig. 7.6); $E_{\text{sub-Tg}}$ was then found from the slope of the curve given by these points. The present results agree well with the findings in the literature. $E_{\text{sub-Tg}}$ was found to depend on the sample state, with the more relaxed sample having a higher $E_{\text{sub-Tg}}$ than the fresher one. Furthermore, the values of $E_{\text{sub-Tg}}$ were in the same range as those measured by Song et al. [196]. The data points of the as-cast sample lie on a straight line, and its $E_{\text{sub-Tg}}$ was easily defined. The same was the case for the re-melted (and slightly annealed) sample. In the case of the aged sample, the points show a slight curvature at high heating

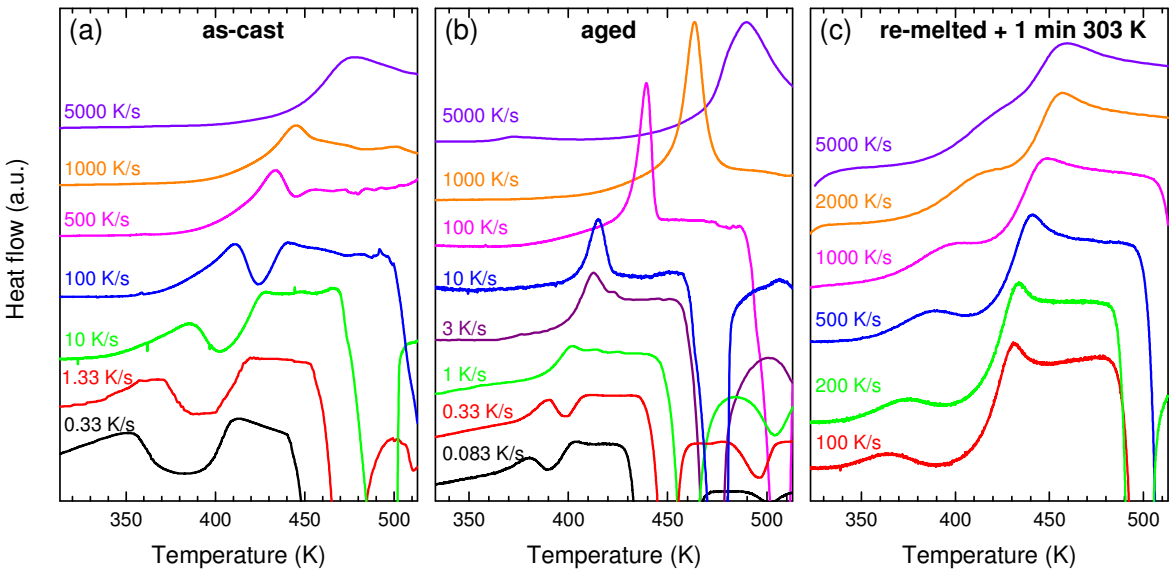

Fig. 7.5. DSC curves at various heating rates of the as-cast (a) and aged (b) samples, and of a re-melted sample after slight annealing at 303 K for 1 min (c), zoomed-in on the sub-T_g and glass-transition event. For visual purposes, the curves were scaled in order for the height of the glass-transition step to be approximately the same for all heating rates.

rates. $E_{sub\text{-}Tg}$ was therefore determined by a linear fit of the values measured up to a rate of 5000 K/s, and is given in Table 7.1, along with the values for the other samples.

As mentioned above, Song et al. observed a jump in activation energy after a certain annealing time t_{trans}, which was interpreted as a transition from a β to an α-relaxation-like behaviour of the disordering event [196]. Interestingly, this transition seemed to coincide with the sub-T_g peak

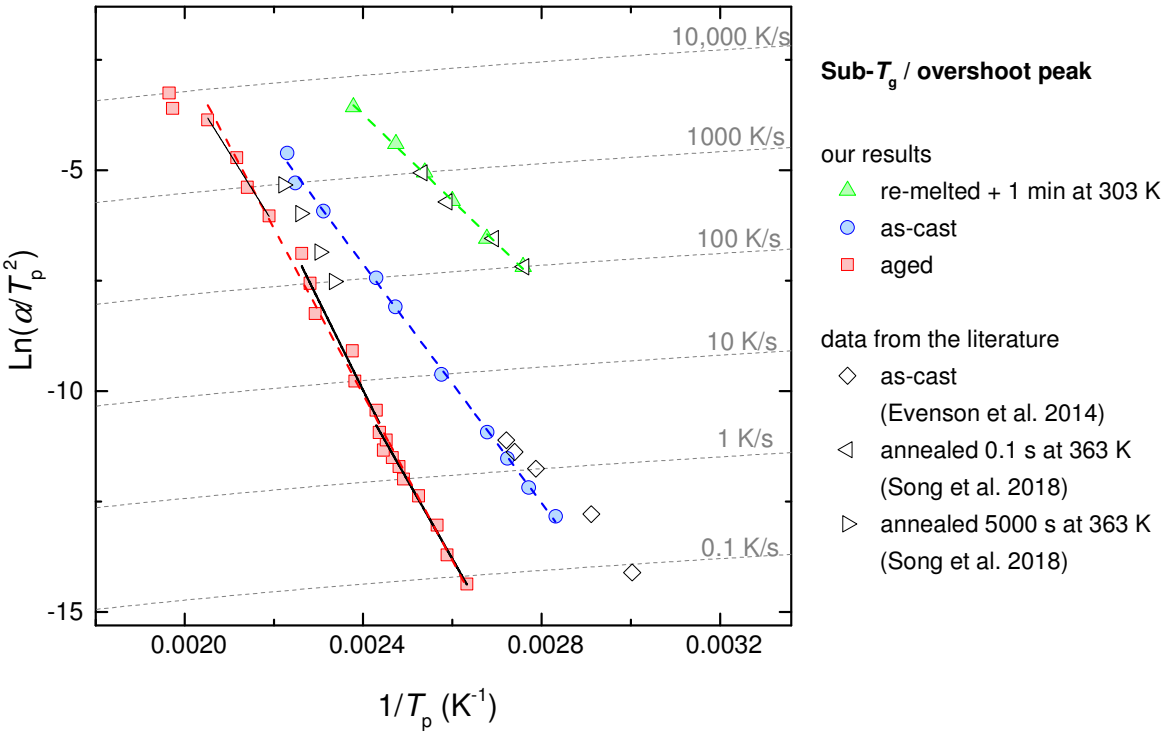

Fig. 7.6. Kissinger plot of the sub-T_g (and overshoot) peak for samples aged to different degrees, as well as some data from the literature [194, 196].

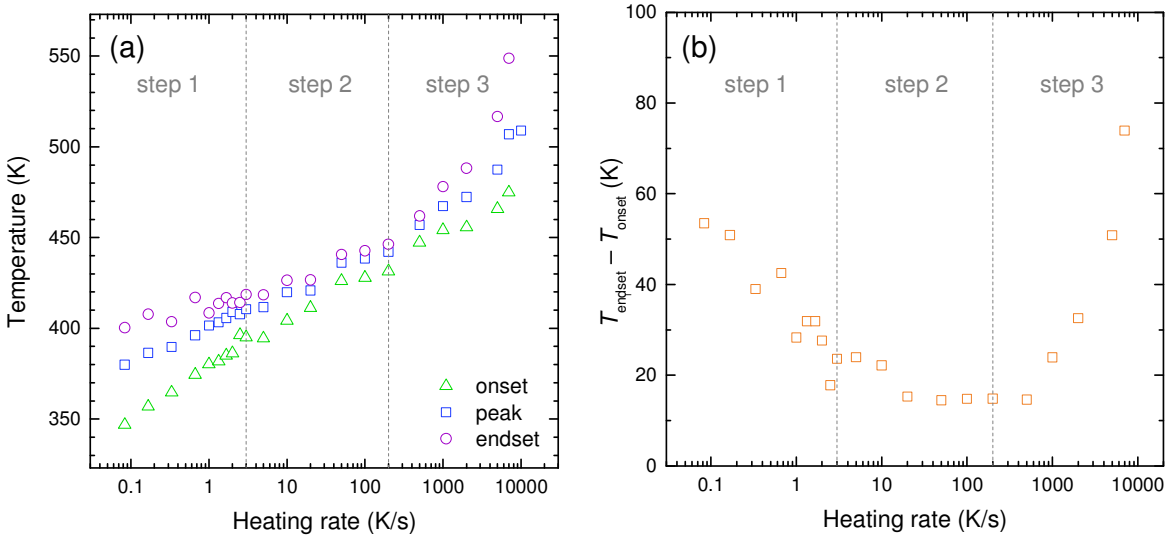

Fig. 7.7. Onset, peak maximum and endset temperatures of the endothermic sub-T_g (or overshoot) peak of the aged ribbon determined for various heating rates (a). The peak "width" was estimated as the temperature difference between peak onset and endset (b).

overtaking T_g. For an annealing time $t_a < t_{trans}$, their T_p is below T_g, though for $t_a > t_{trans}$, T_p is well above T_g.

In the case of our re-melted (and slightly annealed) sample, the endothermic disordering event was present as a sub-T_g peak for the entire range of heating rates applied. For the as-cast ribbon, the sub-T_g peak overlapped with T_g at 1000 K/s; at higher rates, the peak was not easily distinguishable anymore. Concerning the aged ribbon, the peak was below T_g up to 3 K/s, then surpassed T_g and was present as an overshoot at higher heating rates. Could this change from sub-T_g peak to overshoot be related to a change of activation energy, as was the case in the results of Song et al.?

Further information on the disordering peak of the aged sample could be obtained by considering not only the peak position (i.e. peak maximum), but also how the starting and end points of the peak varied as a function of heating rate (Fig. 7.7a). The onset T_{onset} and endset T_{endset} temperatures of the peak were defined as shown in Appendix D, Fig. D.4. From these temperatures, a peak "width" was determined, which corresponds to $T_{endset} - T_{onset}$. By looking at the peak width as a function of heating rate (Fig. 7.7b), the data for the aged ribbon could be divided into three steps:

Step 1) At low heating rates, the peak width decreased as the heating rate increased, until around 3 K/s. In this range of heating rates, the peak maximum is below T_g. The peak started out as a clear sub-T_g peak at 0.083 K/s, then overlapped with the glass-transition step at 1–3 K/s.

Step 2) Between 3 and 200 K/s, the peak width stayed roughly constant. The peak is now present as a clear overshoot above T_g.

Step 3) The peak width increased again with heating rate.

Besides defining $E_{sub\text{-}Tg}$ for the entire range of heating rates, activation energies were also measured for each of these steps separately, and are given in Table 7.1. $E_{sub\text{-}Tg}$ of the 1st step (147 ± 7 kJ/mol) is lower than of the 2nd step (170 ± 16 kJ/mol), though this change in activation energy is smaller than the jump in energies found by Song et al. [196]. In the 3rd step, $E_{sub\text{-}Tg}$ decreases again (to 134 ± 13 kJ/mol). However, the differences in $E_{sub\text{-}Tg}$ are not very large. In fact, considering the errors, the $E_{sub\text{-}Tg}$ values for all three steps are relatively close to the $E_{sub\text{-}Tg}$ obtained from the fitting of the entire data range from 0.083 to 5000 K/s (156 ± 3 kJ/mol). It is clear that we cannot distinguish any step-like transition from our measurements, which instead seem to suggest that a single disordering process is involved here, with a spectrum of activation energies.

The activation energies for the glass transition E_{Tg} and for crystallization E_{Tx} were also determined here for the as-cast and aged ribbons from the Kissinger plots in Fig. 7.8. For both ribbons, the crystallization peak data lie on a straight line up to around 100–200 K/s (Fig. 7.8a), after which there is a slight curving of the points to higher temperatures. This curving at high rates, observed also in the literature for this glass composition [165] as well as for other glasses [164], is related to the change of temperature dependence of the liquid viscosity [164]. E_{Tx} was determined by fitting the points up to 200 K/s, and is given in Table 7.1. For the as-cast ribbon, $E_{Tx} \approx 158$ kJ/mol, which is close to the values found in the literature [196, 197]. Interestingly, in the case of the aged ribbon, crystallization occurs at lower temperatures and has a slightly higher E_{Tx} (≈ 189 kJ/mol) than for the as-cast sample. During the long storage time at RT, pre-nucleation of the crystals may have

Table 7.1. Activation energies E of the sub-T_g peak, T_g and the crystallization peak T_x determined from the Kissinger plots shown in Figs. 7.6 and 7.8.

Transformation event	Sample	E (kJ/mol)
Sub-T_g / overshoot peak	re-melted + 1 min at 303 K	81 ± 2
	as-cast	112 ± 2
	aged – general (0.083–5000 K/s)	156 ± 3
	– step 1 (0.083–3 K/s)	147 ± 7
	– step 2 (3–200 K/s)	170 ± 16
	– step 3 (500–5000 K/s)	134 ± 13
Literature:	as-cast [194]	88.9 ± 6
	annealed 0.1 s at 363 K [196]	75
	annealed 5000 s at 363 K [196]	160
T_g	as-cast	357 ± 34
	aged	191 ± 6
T_x	as-cast	158 ± 4
	aged	189 ± 5
Literature:	as-cast ribbon [197]	162 ± 3
	freshly formed sample by cooling from the melt in the FDSC [165]	161

occurred, thereby facilitating the onset of crystallization and decreasing T_x. Although the obtained E_{Tx} of the aged ribbon is slightly higher than of the as-cast sample, this difference is probably not significant, because both data sets can be relatively well superimposed on one another when vertically shifting them, as will be shown below in Fig. 7.9.

In order to determine E_{Tg}, T_g was measured as the onset of the glass transition. An example of how this onset was defined is shown in Appendix D, Fig. D.4. Unfortunately, the onset of T_g could not be successfully determined for all heating rates, because for some rates (between 0.667–20 K/s for the aged and between 500–2000 K/s for the as-cast ribbon), the sub-T_g peak started overlapping with T_g. These points were therefore not considered for the calculation of E_{Tg} (Fig. 7.8b).

Interestingly, ageing did not seem to affect the T_g measured at low heating rates; up to 100 K/s, T_g of the as-cast and aged ribbons were quite similar. However at higher rates, there was a big difference in T_g between the two ribbons. By linear fitting of the data, E_{Tg} of the aged ribbon was found to be ≈ 191 kJ/mol, which is practically identical to E_{Tx} determined for this ribbon. The as-cast ribbon, on the other hand, had a much larger E_{Tg} of ≈ 357 kJ/mol (Table 7.1).

It should be noted that a linear fitting of these data may not be entirely correct, especially since they were measured over a large range of heating rates. It is known that the transformation rates

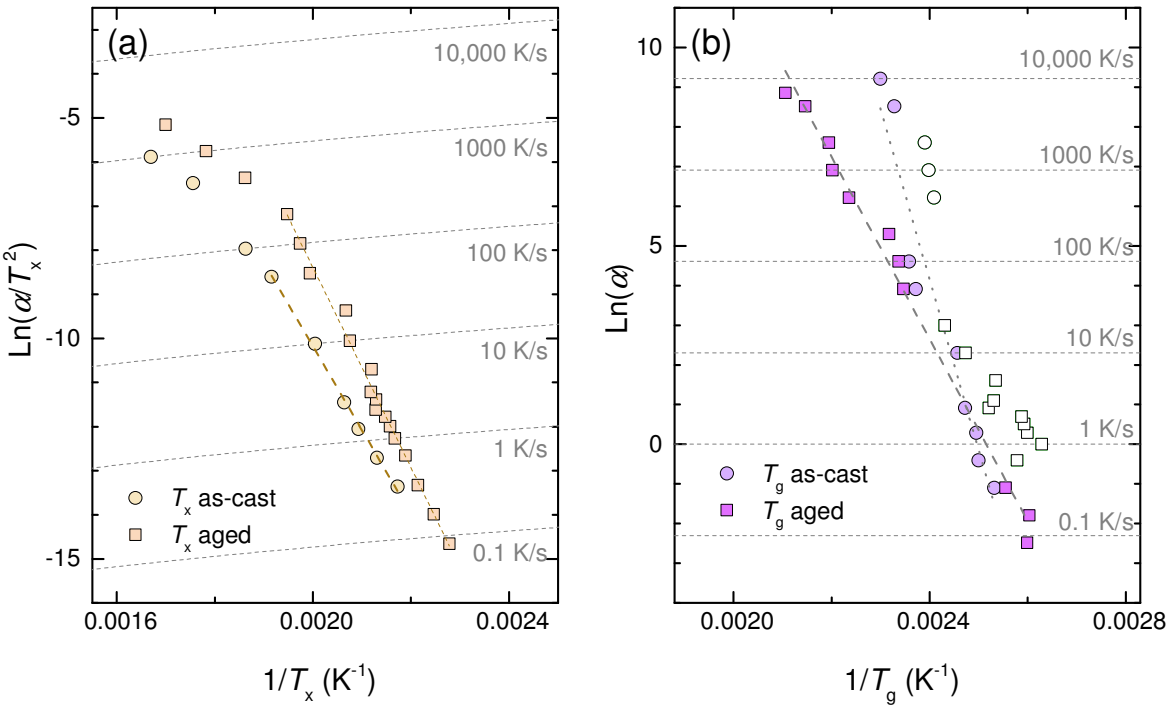

Fig. 7.8. Kissinger plot of the crystallization peak T_x (a) and the onset of T_g (b) of the as-cast and aged ribbons. At heating rates α of 0.667–20 K/s for the aged and 500–2000 K/s for the as-cast ribbon, the onset of T_g was influenced by the sub-T_g peak. These points were therefore not considered for calculating the activation energy E_{Tg}, and are shown with hollow symbols in (b).

of the glass transition and of crystallization scale with the viscosity [167]. How the viscosity changes with temperature depends however on the type of glass [168]. In the case of some glasses, such as SiO_2, the liquid viscosity shows an Arrhenius variation with temperature; these liquids are termed as "strong", and their viscosity can be fitted with a straight line in the "Angell" plot, which shows $\log(\eta)$ as a function of T_g/T (Fig. 7.9). On the other hand, the viscosity of "fragile" glass-forming liquids (e.g. o-terphenyl) changes with temperature in a strongly non-Arrhenius manner [168], and shows up as a curve in the Angell plot. Glass-forming metallic liquids typically lie in-between these two extreme cases. The simplest possible description of the viscosity as a function of temperature is given by the Vogel-Fulcher-Tammann (VFT) equation [168, 169]:

$$\eta(T) = \eta_0 \exp\left(\frac{D^* T_0}{T - T_0}\right) \tag{7.1}$$

where η_0, D^* and T_0 are fitting parameters, with D^* controlling the curvature on the Angell plot. In order to determine E_{Tg} of this Au-based metallic glass, Song et al. [198] applied a VFT fitting to their T_g, and obtained a E_{Tg} which depends on temperature. At higher temperatures (≈ 440 K), they found E_{Tg} = 170 kJ/mol, and at lower temperatures (≈ 410 K), E_{Tg} = 374 kJ/mol [198].

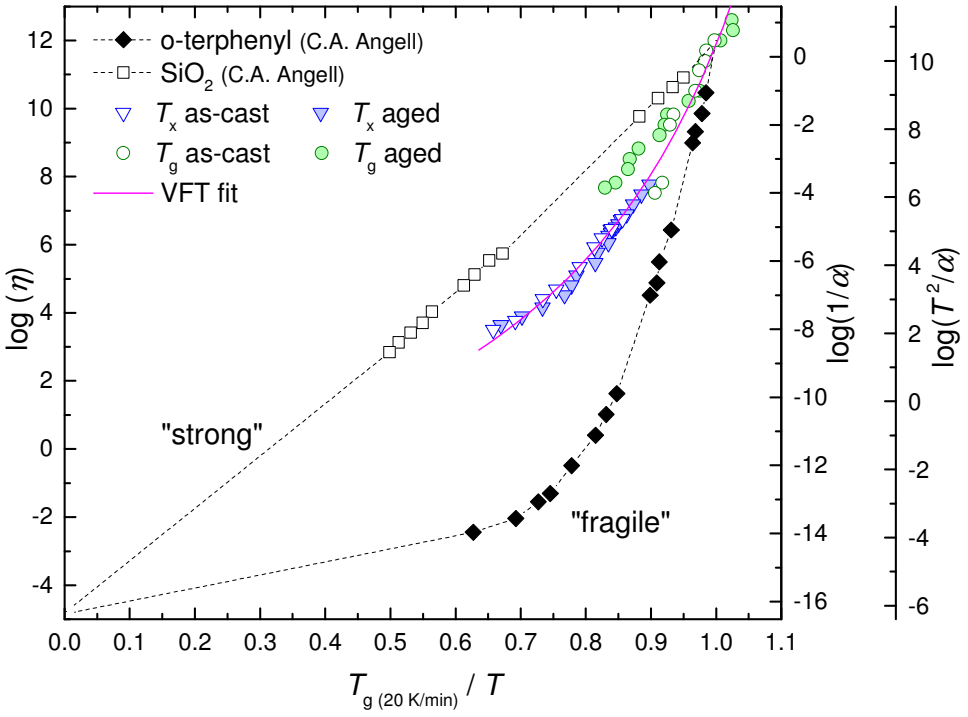

Fig. 7.9. Angell plot, showing the variation of viscosity η (in units of Pa s) as a function of temperature T. The x-axis is normalized by $T_{g(20\,K/min)}$, which is the value of T_g measured at a heating rate of 20 K/min (= 0.333 K/s). For the Au-based metallic glass, $T_{g(20\,K/min)}$ was considered here as 394 K. Examples of typically "strong" and "fragile" glasses were taken from ref.[168].

As the activation energies of T_g and T_x were found to match that of viscous flow [167], the T_g and T_x values measured here as a function of heating rate could be used to estimate the temperature dependence of viscosity of the liquid, and determine the fragility m, which corresponds to the slope of the Angell plot at $T = T_g$ [169].

In order to obtain the Angell plot, the T_g data were displayed as $\log(1/\alpha)$ vs. $T_{g(20\ K/min)}/T_g$, where α is the heating rate and $T_{g(20\ K/min)}$ the value of T_g determined at a heating rate of 20 K/min (= 0.333 K/s), then shifted vertically until the value at $T_{g(20\ K/min)}/T_g = 1$ corresponded to a viscosity of 10^{12} Pa s. The crystallization data was plotted as $\log(T_x^2/\alpha)$ vs. $T_{g(20\ K/min)}/T_x$, and shifted until they continued the trend given by T_g. The T_x data of the as-cast and aged ribbons had a similar curvature, and could therefore be overlapped acceptably well with each other. They also seemed to continue well the trend given by T_g of the as-cast sample. By fitting these data with the VFT equation ($D^* = 11.8$ and $T_0 = 284.5$ K), a fragility of $m = 47.9$ was obtained, which is similar to the m values found in the literature for this composition of 52.8 [199], 49 [200] and 47 ± 6 [197]. However, T_g of the aged ribbon followed a different trend, with higher values than expected according to the VFT fitting, especially at higher heating rates. This is probably due to the effect of how the glass transition occurs when heating a glass, especially if it is very relaxed, at high rates. If a glass is heated at a rate which is lower than its effective cooling rate (i.e. the cooling rate at which it was formed), it has time to relax to a state of lower energy, and thus goes through the glass transition at a lower temperature than T_g observed during glass formation. But if the heating rate is higher than the effective cooling rate of the glass, there is an overshoot, and T_g upon heating occurs at a higher temperature. The more relaxed a glass is, the lower is its effective cooling rate, which leads to a larger overshoot effect. In the case of the aged ribbon, the sample was not only very relaxed, but was also measured at quite high heating rates of up to 7000 K/s. The increase in T_g due to this overshoot effect was therefore quite large, and the measured T_g values diverged significantly from the prediction of the VFT fitting in Fig. 7.9.

The results obtained here seem to suggest that the as-cast ribbon indeed follows 'liquid-like' kinetics, meaning that the transformation rate of the glass transition and of crystallization scale with the viscosity of the liquid. At lower temperatures (i.e. where the glass-transition data measured here lie), the change in viscosity with temperature is larger than at higher temperatures (i.e. where the crystallization data lie); this corresponds to E_{Tg} being significantly larger than E_{Tx}. In contrast, T_g of the aged ribbon seems to rather follow 'glass-like' kinetics. As shown schematically in §1.1, Fig. 1.1b, the viscosity of the glass is expected to vary less with a change in temperature than that of the liquid at temperatures close to T_g.

7.3.2 Rejuvenating the aged ribbon by annealing above the fictive temperature

Once a glass has been formed from the liquid, its energy can be modified by reheating it above the T_g into the supercooled-liquid region and subsequently quenching at a lower or higher cooling rate than used during the initial glass formation. Using this principle, Wakeda et al. [94, 95] succeeded in rejuvenating a relaxed metallic glass experimentally as well as by simulation, and termed this method 'recovery annealing'.

This rejuvenation technique was applied here to the aged Au-based ribbon in the FDSC. It should be noted that the importance was here considered to be heating the glass above $T_{fictive}$, which is not always necessarily close to the T_g measured upon heating in the DSC, because the latter depends on the heating rate applied, whereas $T_{fictive}$ does not. In the case of Wakeda et al.'s experiments, T_g may well be close to $T_{fictive}$. But in the case of our aged Au-based ribbon, $T_{fictive}$ was lower than the apparent T_g measured by CDSC and FDSC, because the sample was very relaxed and the applied heating rates were relatively high compared to the sample's effective cooling rate (as is shown below). Through the equal-area construction, $T_{fictive}$ was determined to be around 373 K for the aged ribbon, which is 30 K lower than $T_{fictive}$ of the as-cast sample (Fig. 7.10).

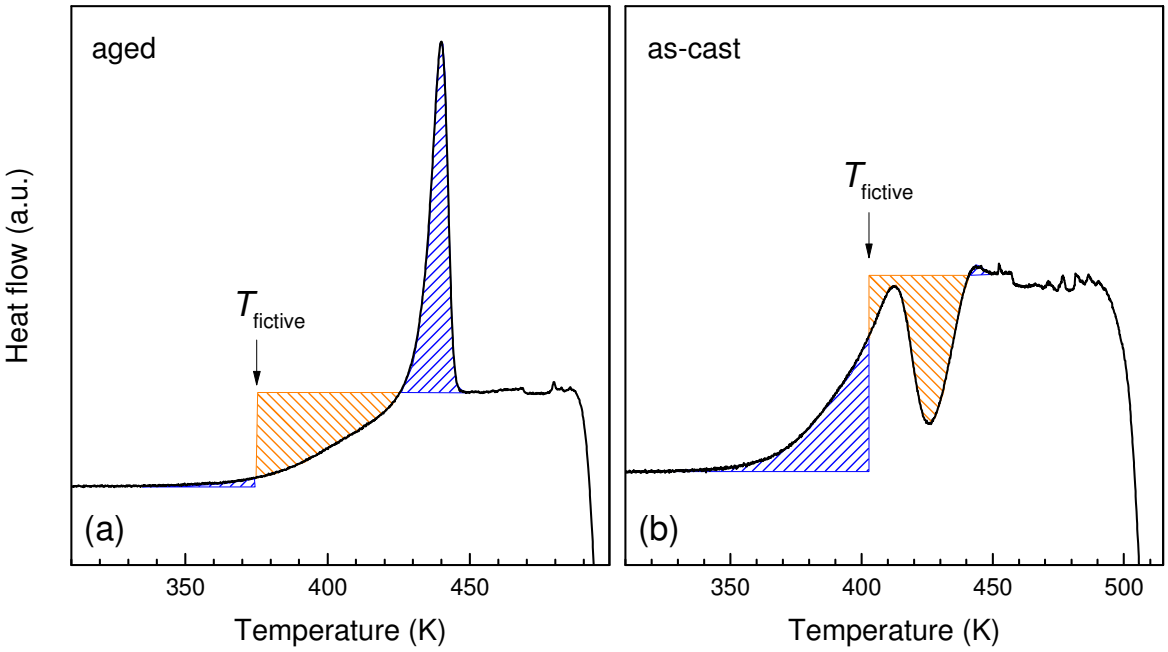

Fig. 7.10. Determination of the fictive temperature $T_{fictive}$ of the aged (a) and as-cast (b) ribbons through the equal-area construction of the heat flow curve measured at 100 K/s. $T_{fictive}$ is placed in order for the blue shaded area (i.e. the area below the curve and above the horizontal line) to be equal to the orange shaded area (i.e. area above the curve and below the horizontal line). On average, $T_{fictive}$ of the aged ribbon was ≈ 373 K, and of the as-cast ribbon ≈ 403 K.

This decrease of 30 K upon ageing is similar to the decrease in $T_{fictive}$ obtained in the literature for ultrastable glasses. Through vapour deposition at relatively low rates at high substrate temperatures, some glasses (non-metallic as well as metallic) could be formed which showed outstanding kinetic and thermodynamic stabilities [39, 40, 201]. For example, a molecular glass, which was deposited on a substrate heated to around 50 K below T_g at a rate of around 5 nm/s, had a 31 K lower $T_{fictive}$ and a 16 K higher T_g, measured upon heating by DSC, than the "ordinary" glass produced by cooling from the liquid [201]. Another example is of a Zr-based metallic glass: by depositing this glass at 0.19 nm/s at a substrate temperature of 0.8 T_g, $T_{fictive}$ was found to decrease by 38 K, and T_g and T_x increased by 51 K and 207 K, respectively, compared to the ordinary bulk metallic glass [40]. Furthermore, this ultrastable glass had an increased density and showed a 30% higher hardness and fracture strength than the ordinary glass.

Although the aged Au-based metallic glass studied here had a similar decreased $T_{fictive}$, its $T_{g(20\ K/min)}$ (i.e. the T_g measured at the conventional rate of 20 K/min) was practically equal to that of the as-cast ribbon. In addition, the degree of ultrastability is commonly expressed in the literature by the ratio $T_{fictive}/T_{g(20\ K/min)}$, which is around 0.8–0.85 for the ultrastable glasses formed by vapour deposition. For our aged Au-based ribbon, this ratio is much higher ($T_{fictive}/T_{g(20\ K/min)} \approx 0.95$). Furthermore, the interest of having a stable glass is not simply in having a low energy, but rather of having a better resistance to crystallization. This was not the case for the aged Au-based ribbon, because although it did have a significantly lower energy, it had also a lower T_x than the as-cast ribbon. Therefore, the present Au-based ribbon may be unusually well annealed, but it cannot be considered as ultrastable.

By knowing $T_{fictive}$ of the sample, the viscosity at this temperature can be defined from the Angell plot shown in Fig. 7.9, from which an effective cooling rate can be estimated. The effective cooling rate of a sample is the rate required to quench a liquid in order to form a glass with the same energy. By definition, a glass cooled at 20 K/min (= 0.333 K/s) is expected to have a viscosity at the glass transition of 10^{12} Pa s. According to the extrapolation of our Angell plot given by the VFT fitting, the viscosity of the present glass is roughly 10^{15} Pa s at $T_{fictive}$ = 373 K. Since a certain increase in viscosity at the glass transition corresponds to a proportional decrease in cooling rate, this implies that the effective cooling rate of the aged sample is around $3.33 \cdot 10^{-4}$ K/s. In contrast, the as-cast glass, with $T_{fictive}$ = 403 K, should have a viscosity of around 10^{11} Pa s at $T_{fictive}$, meaning that its effective cooling rate is around 3.33 K/s. This cooling rate is significantly lower than the quenching rate during melt-spinning of the ribbon, probably because even though this sample is called here "as-cast", it has gone through some relaxation since its fabrication.

With the aim of achieving rejuvenation, the aged ribbon was annealed at $T_{fictive}$ = 373 K and above, for times ranging between 0.1 s and 1 h, followed by cooling at 100 K/s. After annealing, the overshoot peak was found to decrease in height (Fig. 7.11a). This decrease in height corresponds to an increase in internal energy (Fig. 7.11b) and in $T_{fictive}$. The change in energy ΔH was determined

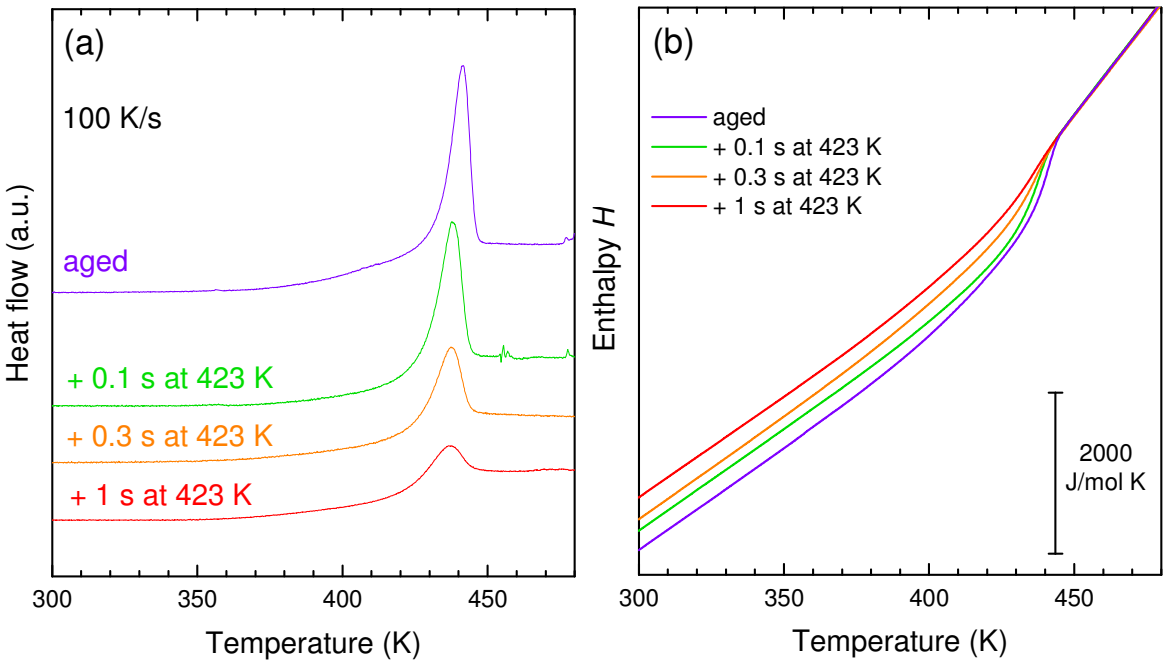

Fig. 7.11. Example of the effect of annealing at 423 K for different times on the FDSC heat flow curve measured at 100 K/s (a) and the enthalpy (b), which was determined by integration of the specific heat $C_p(T)$ estimated by adequate scaling of the heat flow curves.

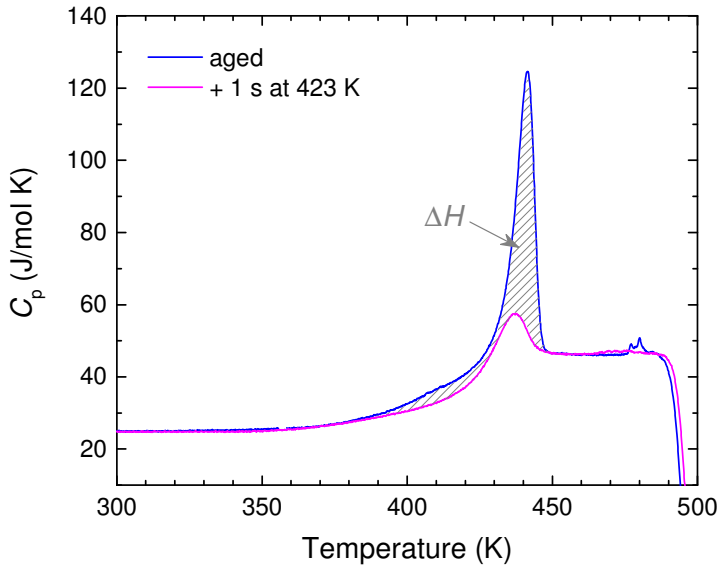

Fig. 7.12. The overshoot peak observed in the aged ribbon, measured at a heating rate of 100 K/s, decreased upon recovery annealing. The area between specific-heat curves $C_p(T)$ of the aged and annealed samples corresponds to the change in energy upon recovery annealing.

by calculating the area between the specific heat curves $C_p(T)$ of the aged and annealed samples (Fig. 7.12). The increase in energy and in $T_{fictive}$ for the different annealing conditions is shown in Figs. 7.13 and 7.14, respectively. It should be noted that when annealing at 443 K for more than 10 s (or more than 1 s, in the case of T_a = 463 K), the heat of crystallization ΔH_x relative to the heat of melting ΔH_m was found to decrease, which implied that crystallization occurred. In Figs. 7.13 and 7.14, only those points are shown for which no crystallization was observed.

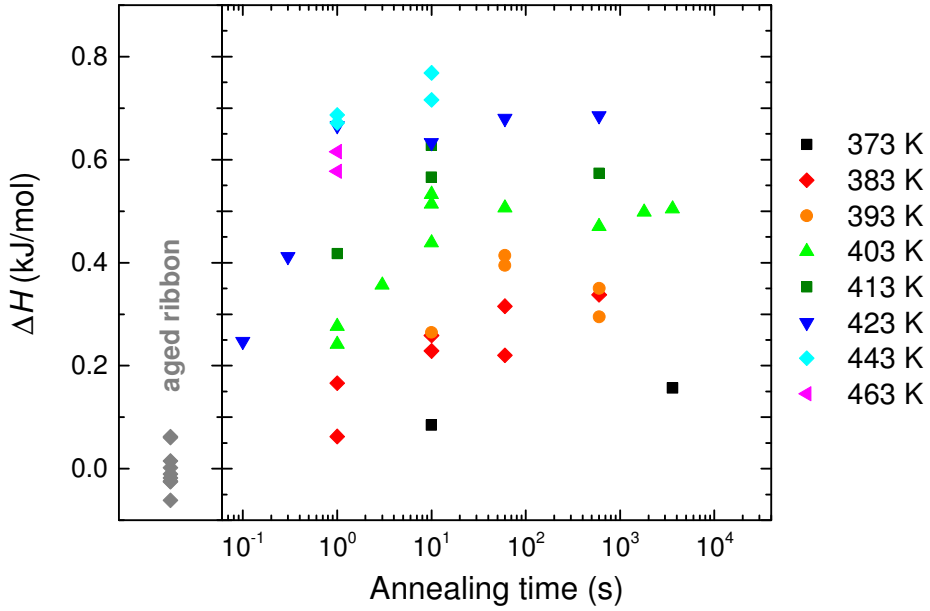

Fig. 7.13. The increase in energy ΔH of the aged ribbon after recovery annealing at different temperatures and times, followed by cooling at 100 K/s. ΔH was determined here as shown in Fig. 7.12.

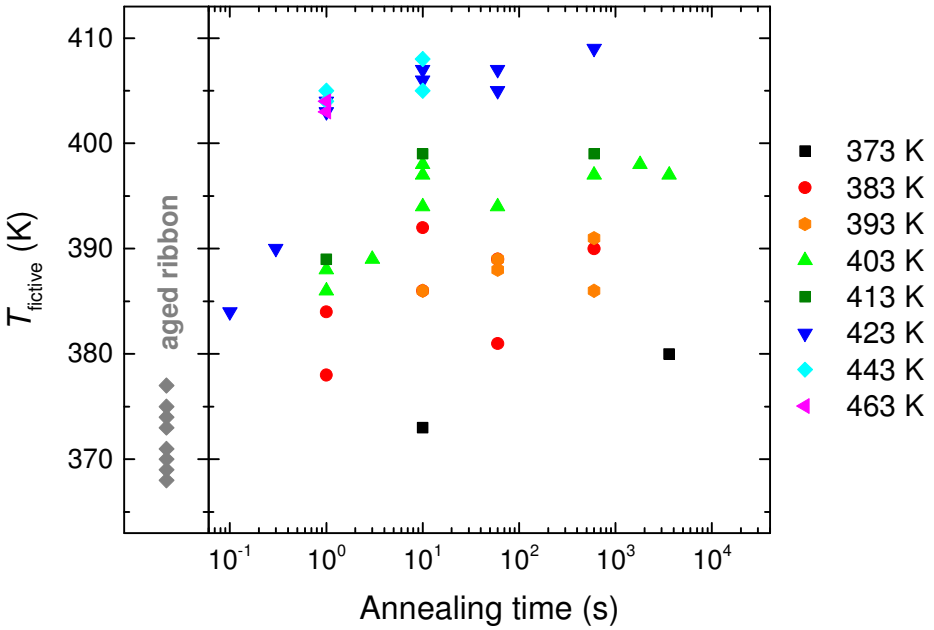

Fig. 7.14. Fictive temperature $T_{fictive}$ of the aged ribbon and after recovery annealing at different temperatures and times, followed by cooling at 100 K/s.

For every annealing temperature, there seemed to be a limit to the achievable rejuvenation: with time, the overshoot decreased (and ΔH increased) until a saturation value seemed to be reached, after which further annealing did not seem to have any further effect. The higher the annealing temperature was, the bigger was the achievable rejuvenation. By annealing at 423 K, the aged sample could seemingly be returned to the same state as the as-cast ribbon (for which $T_{fictive} \approx 403$ K and $\Delta H \approx 640$ J/mol). This temperature-dependent limit of the achievable rejuvenation may be explained by the fact that in the aged sample, there is a range of relaxed zones, with a wide spectrum of relaxation times, and the temperature at which the disordering (i.e. rejuvenation) takes place depends on the zone.

It should be noted that the data in Figs. 7.13 and (especially) 7.14 are quite noisy, and give only a rough idea of how rejuvenation occurred as a function of annealing temperature and time. Considering the relatively large spread in ΔH and $T_{fictive}$ values obtained for the aged sample from 9 measurements (around 120 J/mol for ΔH and 9 K for $T_{fictive}$), more measurements per annealing treatment would have been necessary to obtain a clearer trend of how ΔH and $T_{fictive}$ change upon annealing. Another problem concerning these results, besides the error in defining ΔH and $T_{fictive}$, is that the temperature is not uniform across the FDSC sensor (§3.3.7). This implies that even though the annealing temperature was set to the same value among several measurements, the samples may have been heated to different temperatures, depending on their position on the sensor.

Although recovery annealing of this glass composition did not seem to have been reported yet in the literature, several recent studies did deal with the relaxation of this metallic glass through annealing below T_g [193, 196, 200]. It would be interesting to be able to compare the process of

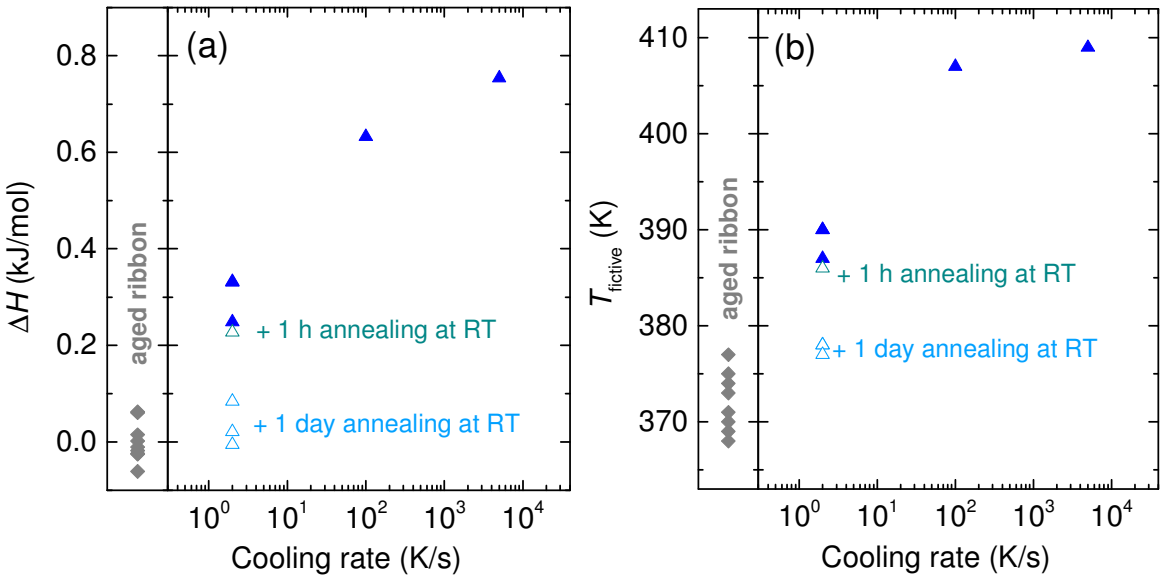

Fig. 7.15. Effect of cooling rate on the excess energy above the aged state ΔH (a) and $T_{fictive}$ (b) after annealing the aged ribbon at 423 K for 10 s in the FDSC.

relaxation through 'conventional' annealing with that of rejuvenation obtained here. In Appendix D, an attempt is made to obtain the activation energies for these two processes. But due to the sparse and noisy data in the present results, a reliable activation energy could not be obtained, and it is not conclusive if there is a difference between these processes or not.

Besides the temperature and time, a crucial parameter for rejuvenation through recovery annealing is the cooling rate at the end of the anneal. The principle of recovery annealing is to bring the glass into the supercooled-liquid state, then to form a new glass by quenching it again, whose structure and energy depend on the cooling rate. In the case of the results shown in Figs. 7.13 and 7.14, a cooling rate of 100 K/s was applied. As mentioned above, by annealing the aged ribbon at 423 K for 1 s or more, followed by 100 K/s cooling, the as-cast state could be reached. But as expected, when a lower rate was used (e.g. 2 K/s), the rejuvenation effect was considerably smaller (Fig. 7.15). By increasing the rate from 100 to 5000 K/s, a slightly higher energy could be reached, though it seems the achievable energy increase will saturate at higher cooling rates.

It should be noted that as T_g is relatively low for this glass composition, the induced rejuvenation cannot be retained at RT; instead it decreased again upon RT storage due to relaxation of the glass. For the above results, the induced energy was determined from FDSC curves measured practically

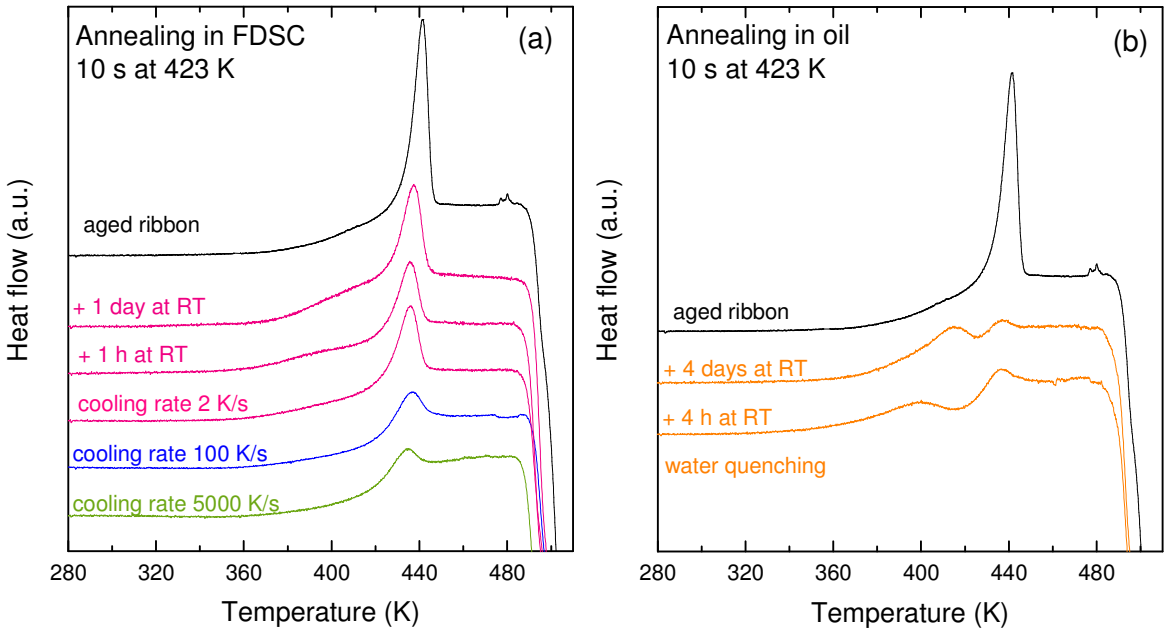

Fig. 7.16. FDSC traces of the aged sample annealed at 423 K for 10s in the FDSC, followed by different quenching rates (a). FDSC curves of the sample used for nanoindentation, after annealing in 423 K hot oil for 10 s followed by water quenching (b). After some hours at RT, the rejuvenated samples relaxed again, and the sub-T_g peak re-appeared (visible in (a) as a shoulder below the overshoot instead of a well-defined peak as in (b)). FDSC curves in (a) and (b) were measured at 100 K/s.

instantaneously after the annealing treatment. But if the rejuvenated sample is left at RT for some time after the treatment, the freshly formed soft zones relax again, leading again to the appearance of an endothermic sub-T_g peak in the heat flow curves at around 400 K (Fig. 7.16), and to a decrease in energy (Fig. 7.15).

In order to determine how this annealing-induced rejuvenation of the aged ribbon affected the mechanical properties, nanoindentation measurements were performed before and after annealing on a 2 cm-long sample. This sample, which was too big to be heat treated by FDSC, was instead annealed in oil at 423 K for 10 s followed by quenching in water. Nanoindentation obviously could not be carried out instantaneously after annealing; in addition, since several indents are required to accurately characterize the properties, indentation took place over several hours. The indents were effectively performed between 8 h and 28 h after annealing. During this waiting time at RT, the sample relaxed. In order to estimate the energy the sample had during indentation, FDSC heat flow curves were measured 4 h after annealing, as well as 4 days afterwards (i.e. sometime before and sometime after nanoindentation). After annealing, the overshoot peak disappeared, though a sub-T_g peak was present after 4 h, which became bigger after 4 days (Fig. 7.16b). After 4 h at RT, $\Delta H \approx 0.44$ kJ/mol and $T_{fictive} \approx 394$ K, and after 4 days, $\Delta H \approx 0.36$ kJ/mol and $T_{fictive} \approx 393$ K.

The cooling rate applied after annealing through quenching in water is not known, but was estimated to be around 30–200 K/s by comparing the ΔH and $T_{fictive}$ obtained for this sample with those of the FDSC-annealed samples (see Appendix D for more details).

Representative nanoindentation load–displacement curves of the aged ribbon before and after annealing are shown in Fig. 7.17 and the cumulative distributions of the measured mechanical

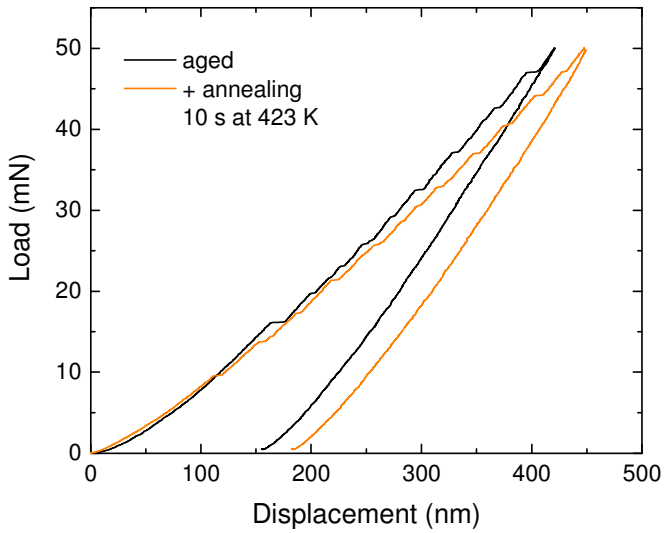

Fig. 7.17. Nanoindentation load–displacement curves of the aged ribbon before and after recovery annealing.

properties in Fig. 7.18. After annealing, a general softening of the sample was observed: the median values of the hardness H and of the indentation modulus, determined from the unloading curve $E_{r,unloading}$ and from the Hertzian equation $E_{r,Hertzian}$, decreased by around 13%, 14% and 8%, respectively. The obtained values for H are similar to the value found for this glass composition in the literature (a Vickers hardness of 360 Hv was measured [192], which corresponds to ≈ 3.5 GPa). But the Young's modulus measured here is considerably lower than the literature value of 74.4 GPa from ultrasonic measurements [192] — an indentation modulus of $E_r \approx 65$ GPa corresponds to a Young's modulus of around 58 GPa. The reason for this difference is not completely understood. But it should be noted that the ribbon seemed to contain some pores (enclosed bubbles), which may partly explain the low measured values of E.

The 13% decrease in H observed here is similar to the degree of softening obtained from rejuvenation through inhomogeneous plastic deformation (e.g. through cold-rolling [47, 51] or through uniaxial compression [59]), but larger than the decrease in H of ≈ 5% observed by Saida et al. [95] after recovery annealing of their pre-relaxed Zr-based sample. In their work, they first relaxed the sample by pre-annealing it below T_g, followed by cooling at a rate α_i. This pre-annealed sample was then subjected to recovery annealing, i.e. annealing at $T_a > T_{g(20\ K/min)}$ followed by cooling at a higher rate α_c. According to their findings, the degree of rejuvenation obtained is higher for larger $T_a/T_{g(20\ K/min)}$ and α_c/α_i ratios [95]. Their 5% decrease in H was obtained for $T_a/T_{g(20\ K/min)} = 1.07$ and $\alpha_c/\alpha_i = 25$. In our case, annealing at 423 K corresponds to $T_a/T_{g(20\ K/min)} = 1.08$, which is similar that used by Saida et al. But our α_c/α_i ratio is much larger. Our α_c can be estimated to be around 0.333 K/s (which is the effective cooling rate of the annealed sample during nanoindentation, estimated from the VFT fitting of the Angel plot in Fig. 7.9 if assuming $T_{fictive} \approx 393$ K) and $\alpha_i \approx 3 \cdot 10^{-4}$ K/s. This corresponds to $\alpha_c/\alpha_i \approx 1000$, which may explain the larger H decrease observed.

The median values of the other mechanical properties, i.e. of the initial yield load F_y and pressure P_y and of the size Δh of the first pop-in, also decreased upon recovery annealing (by around 34%, 19% and 29%, respectively). But interestingly, the effect of annealing on the entire distribution curves was different. In the case of H, $E_{r,unloading}$ and $E_{r,Hertzian}$, the whole distribution curve was shifted to lower values. In comparison, mainly the upper parts of the curves of the initial pop-in related properties were decreased to lower values, whereas the lower parts were barely affected by annealing. Pop-ins are considered to be related to the activation of shear transformation zones (STZs). Annealing seems to have removed the large pop-ins, which require a higher stress to be activated, implying that probably the 'harder' regions in the sample, which need a higher energy to activate shear events, were removed in the recovery-annealed sample. This is consistent with the findings from the FDSC measurements. As mentioned above, the aged Au-based glass has a large

spectrum of zones relaxed to different degrees, with a range of relaxation times. Upon recovery annealing, the glass was rejuvenated, and probably all zones became unrelaxed. However, zones

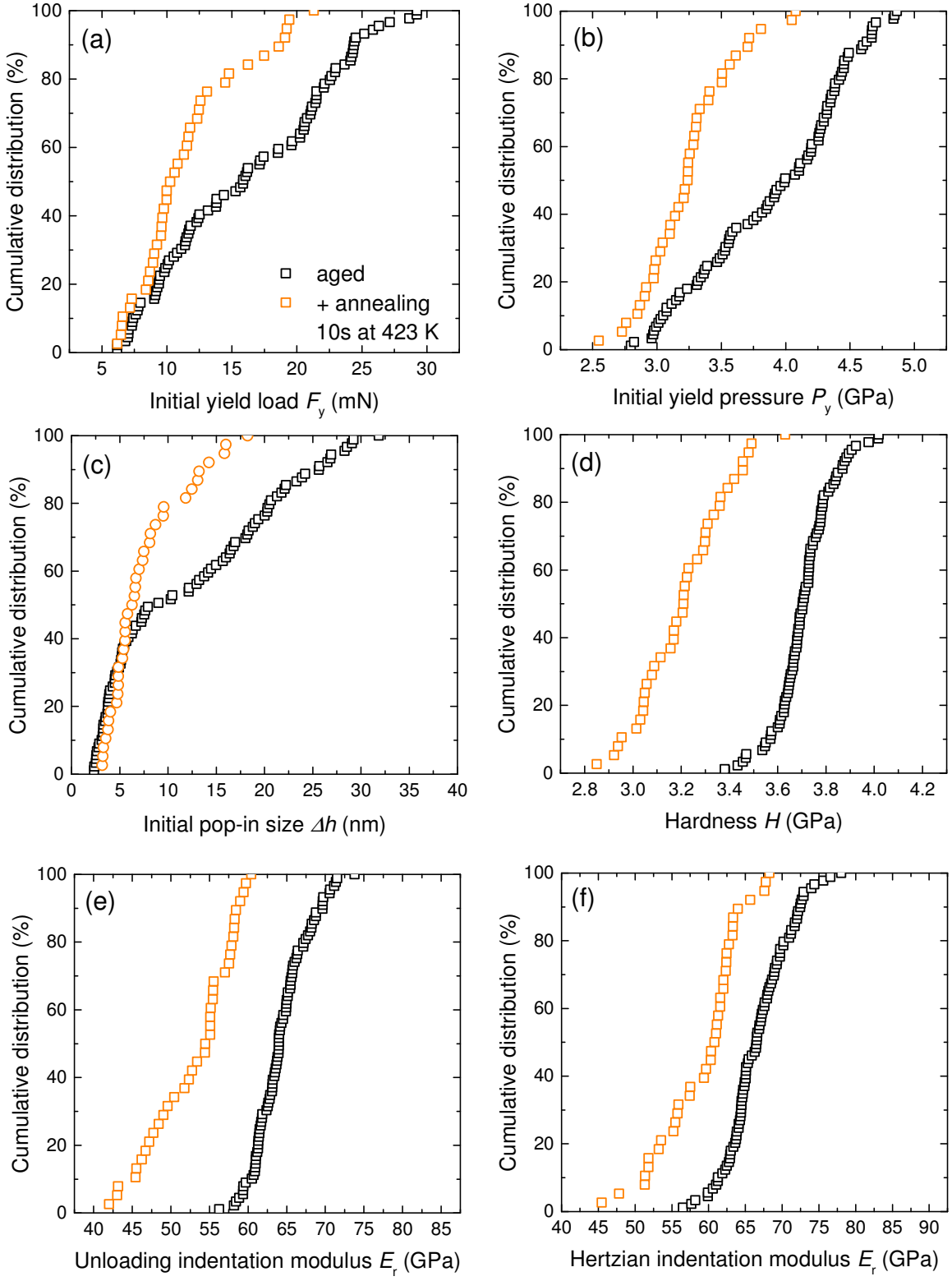

Fig. 7.18. Cumulative distribution curves of the mechanical properties, measured by nanoindentation, of the aged ribbon before and after recovery annealing.

with short relaxation times relaxed quickly again upon RT annealing, and thus an endothermic sub-T_g peak was observed in the FDSC curves although the large overshoot had disappeared (Fig. 7.16b).

7.4 Conclusions

The composition $Au_{49}Cu_{26.9}Si_{16.3}Ag_{5.5}Pd_{2.3}$ studied here has a good glass-forming ability, high stability and a large supercooled-liquid region, which makes it interesting for potential bulk applications of Au-based metallic glasses. However, it has a relatively low glass-transition temperature of around 393–403 K, and thus storage at room temperature leads to significant relaxation. This room-temperature ageing gives rise to an endothermic sub-T_g peak in the heat flow curves measured by DSC, which corresponds to the disordering of highly relaxed zones in the glass upon heating.

The kinetics of this disordering event was analysed here by DSC for samples aged to different degrees. The disordering process was found to have a spectrum of activation energies which depend on the energy of the sample. The more relaxed the sample is, the higher is the measured activation energy. The effective activation energies of the glass transition and crystallization were also determined for an as-cast and an aged ribbon. Though the dependence of the crystallization peak temperature on the heating rate is similar for both ribbons, the onset of glass transition behaves differently for these two samples. Due to the substantial relaxation of the aged ribbon, the overshoot effect upon heating is quite extreme for this sample, especially at high rates. This implied that the transformation rate of T_g of the aged sample does not follow anymore the trend given by the liquid viscosity, meaning that instead of following 'liquid-like' kinetics as is expected, and as is the case for the T_g of as-cast ribbon, the T_g of the aged sample seems to follow 'glass-like' kinetics.

By annealing the aged glass for short times above its fictive temperature, it could be successfully returned to a state thermally equivalent to that of a freshly formed glass. The effect of this rejuvenation on the mechanical properties was explored by nanoindentation; on average, lower hardness, Young's modulus, and initial yield stress are obtained. In addition, the average size of the first pop-in also decreased, meaning that the initial shear event occurs in a less abrupt manner. Furthermore, the distribution width of the measured values of the pop-in size and initial yield stress decreased. This may indicate that although recovery annealing probably rejuvenated the entire sample, subsequent room temperature annealing may have relaxed again the softer zones, whereas the harder zones stayed unrelaxed, and therefore there is a smaller variation among the different zones compared to the heavily aged glass.

8 Overall Conclusions and Suggestions for Further Work

8.1 Overall conclusions

Once a metallic glass is formed, its structure and properties can be changed through various thermomechanical processing methods. Numerous studies in the literature showed the possibility of inducing relaxation or rejuvenation of metallic glasses with the related property changes.

In this work, the effects of five different methods were explored on several metallic-glass samples by measuring the induced changes in mechanical properties and through thermal analysis. The treatments tested here were (1) plastic deformation through uniaxial compression, (2) elastic cycling, (3) thermal cycling, (4) recovery annealing, and (5) ageing/annealing.

The introduction of large plastic strains is a well-known approach to create damage and thereby increase the energy and change the properties of metallic glasses. Here, a yet infrequently-used method to reach large deformation was tested on a $La_{55}Ni_{20}Al_{25}$ bulk metallic glass. Brittle fracture was avoided by uniaxial compression of samples with a low aspect ratio, and up to 85% plastic strain was achieved. By ultra-fast differential scanning calorimetry (FDSC), the introduced deformation was found to increase the energy of the samples by up to 670 J/mol on average, which is in the range of values typically obtained by other plastic deformation methods in the literature. A large spread in the increase of energy was observed (i.e. a difference of up to 600 J/mol between the maximum and minimum value within a same sample was measured), indicating that deformation and rejuvenation was not introduced homogeneously throughout the sample during compression. Furthermore, the induced deformation was found to bring the bulk sample to a similar state as the melt-spun ribbon: not only did the deformed bulk sample reach the same internal energy as the ribbon, but it also showed a similar endothermic disordering event below the glass transition after ageing at room temperature, which did not occur in the undeformed bulk sample.

Due to the amorphous structure of metallic glasses, deformation even below the macroscopic yield point can lead to atomic rearrangements which do not fully recover upon stress removal. Several methods making use of macroscopically elastic strains are known which can change the energy state and properties of metallic glasses. One example, which was tested here on a $Cu_{46}Zr_{46}Al_7Gd_1$ bulk sample, is the application of load cycles within the elastic regime by nanoindentation. Elastic cycling was found to increase the stress required for the first pop-in to occur and to increase the average pop-in velocity, which correspond to an increase in the yield

stress and in the propagation speed of shear bands, respectively. But the hardness and elastic modulus were not significantly affected. In the literature, elastic cycling by nanoindentation was sometimes proposed to have a similar effect to relaxation through thermal annealing. The present results showed that this was however probably not the case; annealing was applied on the same sample and its effects could be directly compared to those of elastic cycling. The two treatments were found to affect the sample in different manners: annealing had a stronger strengthening effect and also increased the elastic modulus. In addition, elastic cycling affected an already relaxed sample by a greater degree than a less relaxed sample; this result opposes the supposition that elastic cycling is a mechanical relaxation method, because a glass of an initially higher energy should be more prone to relaxation than one of lower energy.

The third processing method explored here was thermal cycling, which is a relatively recently discovered technique to rejuvenate metallic glasses and consists of cycling between cryogenic and room temperatures and thereby introducing non-affine thermal strains. Three metallic-glass compositions were treated to thermal cycling, and different aspects were investigated. Nanoindentation measurements showed that thermal cycling of a $Cu_{46}Zr_{46}Al_7Gd_1$ glass decreased the yield stress but did not significantly change the hardness or elastic modulus. Consequently, by applying thermal cycling to a sample relaxed by annealing, its mechanical properties were only partially restored to their pre-annealed values.

The effect of thermal cycling was also tested on the anelastic deformation behaviour of $La_{25}Ni_{20}Al_{25}$ ribbons. The ribbons were elastically bent around mandrels for several minutes, then released and the relaxation rate of the strain was measured. Thermal cycling, whether applied during or before bending, was found to speed up the recovery rate of anelastic strain, which depends mainly on the 'flow units' within the glassy sample.

$Fe_{73.5}Cu_1Nb_3Si_{15.5}B_7$ metallic-glass ribbons, which are interesting application-wise due to their extraordinarily good soft magnetic properties, were also treated to thermal cycling. The mechanical properties, determined by nanoindentation, were affected in a similar manner as those of other metallic-glass compositions (e.g. $Cu_{46}Zr_{46}Al_7Gd_1$, $La_{25}Ni_{20}Al_{25}$). But a larger number of cycles were required; to obtain an equivalent change in the yield stress, more than 100 cycles were needed, in comparison to the usual 10 cycles for the other compositions. However, the magnetic properties such as the Curie temperature, coercivity and saturation magnetization were barely affected.

The results on thermal cycling of the three different samples demonstrate that this treatment seemed to target mainly the soft spots of the glass, which are responsible for the initiation of shearing and for anelastic flow, whereas the global structure was barely affected.

For metallic glass compositions with a low glass-transition temperature T_g, storage at room temperature (RT) can considerably change their structure and properties. RT ageing was studied here on $Au_{49}Cu_{26.9}Si_{16.3}Ag_{5.5}Pd_{2.3}$ metallic-glass ribbons by FDSC. For this composition, RT corresponds to around 0.75 T_g, and storage at RT led to significant relaxation, causing a characteristic endothermic sub-T_g peak in the heat-flow curves measured by FDSC which corresponds to the disordering of highly relaxed zones in the glass upon heating. This disordering event was found to have a spectrum of activation energies, which depend on the energetic state of the sample: the activation energy was higher for more relaxed samples. Furthermore, the effective activation energy of T_g was also found to be affected by ageing. The kinetics of T_g of the as-cast ribbon seemed to be governed by the liquid viscosity, as is usually expected. But after more than 7 years of RT ageing, the transformation rate of T_g did not seem to follow liquid-like kinetics anymore.

Through recovery annealing, which consisted of heating above the fictive temperature followed by fast cooling, the 7-years RT-aged Au-based sample could be successfully returned to a state thermally equivalent to that of a freshly formed glass, which corresponds to an increase in energy of almost 700 J/mol. Nanoindentation measurements showed that this rejuvenation treatment also decreased the average yield stress, hardness and elastic modulus.

Besides knowing the effects of separate thermomechanical methods, it is also important to understand how the combination of different types of treatments may affect the properties of metallic glasses. For example, one might expect that by first relaxing a metallic-glass sample, followed by a rejuvenating treatment (or the reverse) the initial glassy state would be reached again, with the same properties. But in this work, two situations showed that this is not necessarily the case, or that sometimes care should be taken when considering a treatment to cause relaxation or rejuvenation. For example, after plastically deforming the $La_{25}Ni_{20}Al_{25}$ bulk-metallic-glass sample, the energy was found to increase, indicating that rejuvenation occurred. After RT ageing of this deformed sample, the energy decreased again, as expected. But although the energy returned to almost the same value as before deformation, its heat flow curve resembled rather that of a RT-aged ribbon than of the undeformed bulk sample (i.e. an endothermic sub-T_g peak occurred upon heating in the FDSC, which was not present before deformation). Another example is the combination of annealing followed by thermal cycling of the $Cu_{46}Zr_{46}Al_7Gd_1$ bulk sample. After annealing, the mechanical properties measured by nanoindentation changed as would be expected upon relaxation: the yield stress and elastic modulus increased. But after subsequent thermal cycling, which is expected to cause rejuvenation, only the yield stress was restored to its initial value. On the one hand, this result may seem disappointing, because the effect of annealing could not be reversed. But on the other hand, the combination of these two treatments led to interesting

properties, namely a lower yield stress at the same time as a higher modulus than of the pre-treated state was obtained.

8.2 Suggestions for further work

In many studies in the literature, as well as in the present work, a wide-ranging investigation of the effects of a treatment (i.e. effect on structure, energy, mechanical properties, etc.) is not carried out, sometimes because this is simply not feasible. In addition, the structure of metallic glasses is difficult to characterize with precision and certainty. One therefore often tends to rely only on the changes in properties which are more easily measured in order to describe the state of the glass. However, there is the danger of relying too much on the approach of linking certain property changes with an increase or a decrease in energy, and using this to conclude if relaxation or rejuvenation occurred as a result of the treatment. Furthermore, it should be kept in mind that the same energy, or the same property, can be obtained through different routes. Although two glasses of a given composition may have equivalent energies or certain properties that are identical, they are not necessarily in the same state.

A lot of research has been made recently in improving the properties of metallic glasses and in trying to reach extraordinarily unrelaxed or relaxed states. However, many fundamental aspects are not yet well understood (e.g. what is the exact mechanism underlying the changes in the properties induced by the treatment, what characteristics does the metallic glass need to have to be affected by a specific treatment, or how do the parameters of the treatment have to be tuned in order to affect a specific sample, …).

Regarding the research carried out in the present work, several areas could be further investigated. The experiments undertaken here did not focus on exploring the full potential of each treatment, for example by tuning the different parameters, but there would be an interest in developing the following aspects.

First, plastic deformation by uniaxial compression of the La-based metallic glass was here carried out at room temperature. But it is known from the literature that a higher increase in energy should be expected if plastic deformation is performed at lower temperatures, since this reduces thermally activated ordering which otherwise competes with the deformation-induced disordering. Therefore, it would be interesting to compress the samples at e.g. liquid-nitrogen temperature in order to achieve more rejuvenation.

Second, thermal cycling is still a relatively unexplored treatment, and the importance of the different parameters (e.g. lower and upper temperature limits, holding times at the lower and upper temperatures, heating and cooling rate, number of cycles…) is not yet known. The present results showed that the effect of thermal cycling seemed to be much weaker and more limited on the Fe-based ribbons. In order to observe a change in the mechanical properties, the number of cycles was significantly increased here. In the literature, rejuvenation was proposed to be due to non-affine thermal strains which are introduced upon the change in temperature. Fe-based metallic glasses have a significantly higher elastic modulus and yield stress than La- or Cu-based compositions, therefore a same temperature difference may have a weaker influence. Therefore, instead of increasing the number of cycles, it would be interesting to apply a larger temperature difference during the cycling and observe if this causes a more pronounced effect.

The third point to be further explored is not directly related to thermomechanical processing of metallic glasses, but is instead important to better understand some fundamental aspects of glasses. The experiments carried out here on the Au-based metallic glass showed that, after significant ageing, its T_g did not seem to be governed by the liquid viscosity anymore; it would be interesting to further investigate and confirm this finding. This could be done by measuring the kinetics of T_g for a much wider range of glass states, obtained for example through the recovery annealing procedure investigated here.

References

[1] W. Klement, R. H. Willens, P. Duwez, Non-crystalline structure in solidified gold-silicon alloys, *Nature* **187** (1960) 869–870.

[2] A. L. Greer, 'Metallic Glasses', in Physical Metallurgy, D. E. Laughlin, K. Hono. Oxford: Elsevier, 2014, 305–385.

[3] N. Nishiyama, K. Takenaka, H. Miura, N. Saidoh, Y. Zeng, A. Inoue, The world's biggest glassy alloy ever made, *Intermetallics* **30** (2012) 19–24.

[4] C. Suryanarayana, A. Inoue, Bulk Metallic Glasses. Boca Raton, FL: CRC Press, 2011.

[5] Y. Sun, A. Concustell, A.L. Greer, Thermomechanical processing of metallic glasses: extending the range of the glassy state, *Nat. Rev. Mater.* **1** (2016) 16039.

[6] A. Inoue, Stabilization of metallic supercooled liquid and bulk amorphous alloys, *Acta Mater.* **48** (2000) 279–306.

[7] M.F. Ashby, A. L. Greer, Metallic glasses as structural materials, *Scripta Mater.* **54** (2006) 321–326.

[8] C.A. Schuh, T.C. Hufnagel, U. Ramamurty, Mechanical behavior of amorphous alloys, *Acta Mater.* **55** (2007) 4067–4109.

[9] W.H. Wang, C. Dong, C.H. Shek, Bulk metallic glasses, *Mater. Sci. Eng. R* **44** (2004) 45–89.

[10] Y. Zhang, A. L. Greer, Thickness of shear bands in metallic glasses, *Appl. Phys. Lett.* **89** (2006) 071907.

[11] R. Hasegawa, Applications of amorphous magnetic alloys, *Mater. Sci. Eng. A* **375–377** (2004) 90–97.

[12] J. Schroers, T.M. Hodges, G. Kumar, H. Raman, .J. Barnes, Q. Pham, T.A. Waniuk, Thermoplastic blow molding of metals, *Mater. Today* **14** (2011) 14–19.

[13] G. Kumar, P.A. Staffier, J. Blawzdziewicz, U.D. Schwarz, J. Schroers, Atomically smooth surfaces through thermoplastic forming of metallic glass, *Appl. Phys. Lett.* **97** (2010) 101907.

[14] Y.Q. Cheng, E. Ma, Atomic-level structure and structure-property relationship in metallic glasses, *Prog. Mater. Sci.* **56** (2011) 379–473.

[15] P. Lamparter, Structure of metallic glasses, *Phys. Scripta* **57** (1995) 45–63.

[16] F. C. Frank, Supercooling of liquids, *Proc. Roy. Soc. Lond. A* (1952) 43–46.

[17] Y.Q. Cheng, H. W. Sheng, E. Ma, Relationship between structure, dynamics, and mechanical properties in metallic glass-forming alloys, *Phys. Rev. B* **78** (2008) 014207.

[18] C. Liu, R. Maaß, Elastic fluctuations and structural heterogeneities in metallic glasses, *Adv. Funct. Mater.* **28** (2018) 1800388.

[19] X.F. Zhang, K.B. Kim, J. Das, S. Yi, J. Eckert, Influence of additional elements on the development of nanoscale heterogeneities in (TiCu)-based bulk metallic glasses with enhanced ductility, *J. Mater. Res.* **22** (2007) 2223–2229.

[20] Y.H. Liu, D. Wang, K. Nakajima, W. Zhang, A. Hirata, T. Nishi, A. Inoue, M.W. Chen, Characterization of nanoscale mechanical heterogeneity in a metallic glass by dynamic force microscopy, *Phys. Rev. Lett.* **106** (2011) 125504.

[21] Y.B. Wang, D.D. Qu, X.H. Wang, Y. Cao, X.Z. Liao, M. Kawasaki, S.P. Ringer, Z.W. Shan, T.G. Langdon, J. Shen, Introducing a strain-hardening capability to improve the ductility of bulk metallic glasses via severe plastic deformation, *Acta Mater.* **60** (2012) 253–260.

[22] J. G. Wang, D. Q. Zhao, M. X. Pan, C. H. Shek, W. H. Wang, Mechanical heterogeneity and mechanism of plasticity in metallic glasses, *Appl. Phys. Lett.* **94** (2009) 031904.

[23] J.C. Ye, J. Lu, C.T. Liu, Q. Wang, Y. Yang, Atomistic free-volume zones and inelastic deformation of metallic glasses, *Nat. Mater.* **9** (2010) 619–623.

[24] H.B. Ke, J.F. Zeng, C.T. Liu, Y. Yang, Structure heterogeneity in metallic glass: modeling and experiment, *J. Mater. Sci. Technol.* **30** (2014) 560–565.

[25] M.H. Cohen, D. Turnbull, Molecular transport in liquids and glasses, *J. Chem. Phys.* **31** (1959) 1164.

[26] H.B. Yu, W.H. Wang, H.Y. Bai, K. Samwer, The β-relaxation in metallic glasses, *Nat. Sci. Rev.* **1** (2014) 429–461.

[27] J.C. Qiao, J.M. Pelletier, Dynamic mechanical relaxation in bulk metallic glasses: a review, *J. Mater. Sci. Technol.* **30** (2014) 523–545.

[28] R.D. Conner, W.L. Johnson, N.E. Paton, W.D. Nix, Shear bands and cracking of metallic glass plates in bending, *J. Appl. Phys.* **94**, (2003) 904–911.

[29] M.W. Chen, Mechanical behavior of metallic glasses: microscopic understanding of strength and ductility, *Annu. Rev. Mater. Res.* **38** (2008) 445–69.

[30] F. Spaepen, A microscopic mechanism for steady state inhomogeneous flow in metallic glasses, *Acta Metall.* **25** (1977) 407–415.

[31] A.S. Argon, Plastic deformation in metallic glasses, *Acta Metall.* **27** (1979) 47–58.

[32] M. Zink, K. Samwer, W.L. Johnson, S.G. Mayr, Plastic deformation of metallic glasses: Size of shear transformation zones from molecular dynamics simulations, *Phys. Rev. B* **73** (2006) 172203.

[33] A. L. Greer, Y. Q. Cheng, E. Ma, Shear bands in metallic glasses, *Mater. Sci. Eng. R* **74** (2013) 71–132.

[34] J. Lu, G. Ravichandran, W. L. Johnson, Deformation behavior of the $Zr_{41.2}Ti_{13.8}Cu_{12.5}Ni_{10}Be_{22.5}$ bulk metallic glass over a wide range of strain-rates and temperatures, *Acta Mater.* **51** (2003) 3429–3443.

[35] T.C. Hufnagel, Cryogenic rejuvenation, *Nat. Mater.* **14** (2015) 867–868.

[36] T. Egami, T. Iwashita, W. Dmowski, Mechanical properties of metallic glasses, *Metals* **3** (2013) 77–113.

[37] C.C. Hays, C.P. Kim, W.L. Johnson, Microstructure controlled shear band pattern formation and enhanced plasticity of bulk metallic glasses containing *in situ* formed ductile phase dendrite dispersions, *Phys. Rev. Lett.* **84** (2000) 2901–2904.

[38] K.K. Song, X.L. Han, S. Pauly, Y.S. Qin, K. Kosiba, C.X. Peng, J.H. Gong, P.X. Chen, L. Wang, B. Sarac, S. Ketov, M. Mühlbacher, F. Spieckermann, I. Kaban, J. Eckert, Rapid and partial crystallization to design ductile CuZr-based bulk metallic glass composites, *Mater. Des.* **139** (2018) 132–140.

[39] H.B. Yu, Y. Luo , K. Samwer, Ultrastable metallic glass, *Adv. Mater.* **25** (2013) 5904–5908.

[40] D.P.B. Aji, A. Hirata, F. Zhu, L. Pan, K.M. Reddy, S. Song, Y. Liu, T. Fujita, S. Kohara, M. Chen, Ultrastrong and ultrastable metallic glass, preprint at http://arxiv.org/abs/1306.1575 (2013).

[41] Q.P. Cao, J.F. Li, Y.H. Zhou, A. Horsewell, J.Z. Jiang, Free-volume evolution and its temperature dependence during rolling of $Cu_{60}Zr_{20}Ti_{20}$ bulk metallic glass, *App. Phys. Lett.* **87** (2005) 101901.

[42] H.S. Chen, Stored energy in a cold-rolled metallic glass, *Appl. Phys. Lett.* **29** (1976) 328–330.

[43] B. Jessen, E. Woldt, Stored energy of the deformed metallic glass $Ni_{78}Si_8B_{14}$, *Thermochim. Acta* **151** (1989) 179–186.

[44] Q.P. Cao, J.F. Li, J.Z. Jiang, Y.H. Zhou, Microstructure and stored energy evolutions during rolling of $Cu_{60}Zr_{20}Ti_{20}$ bulk metallic glass, *J. Non-Cryst. Solids* **354** (2008) 5353–5362.

[45] J.W. Liu, Q.P. Cao, L.Y. Chen, X.D. Wang, J.Z. Jiang, Shear band evolution and hardness change in cold-rolled bulk metallic glasses, *Acta Mater.* **58** (2010) 4827–4840.

[46] O. Haruyama, K. Kisara, A. Yamashita, K. Kogure, Y. Yokoyama, K. Sugiyama, Characterization of free volume in cold-rolled $Zr_{55}Cu_{30}Ni_5Al_{10}$ bulk metallic glasses, *Acta Mater.* **61** (2013) 3224–3232.

[47] M. Stolpe, J.J. Kruzic, R. Busch, Evolution of shear bands, free volume and hardness during cold rolling of a Zr-based bulk metallic glass, *Acta Mater.* **64** (2014) 231–240.

[48] Q.P. Cao, J.W. Liu, K.J. Yang, F. Xu, Z.Q. Yao, A. Minkow, H.J. Fecht, J. Ivanisenko, L.Y. Chen, X.D. Wang, S.X. Qu, J.Z. Jiang, Effect of pre-existing shear bands on the tensile mechanical properties of a bulk metallic glass, *Acta Mater.* **58** (2010) 1276–1292.

[49] K.K. Song, S. Pauly, Y. Zhang, S. Scudino, P. Gargarella, K.B. Surreddi, U. Kühn, J. Eckert, Significant tensile ductility induced by cold rolling in $Cu_{47.5}Zr_{47.5}Al_5$ bulk metallic glass, *Intermetallics* **19** (2011) 1394–1398.

[50] S. Scudino, B. Jerliu, K.B. Surreddi, U. Kühn, J. Eckert, Effect of cold rolling on compressive and tensile mechanical properties of $Zr_{52.5}Ti_5Cu_{18}Ni_{14.5}Al_{10}$ bulk metallic glass, *J. Alloys Comp.* **509S** (2011) S128–S130.

[51] W.H. Jiang, F.E. Pinkerton, M. Atzmon, Mechanical behavior of shear bands and the effect of their relaxation in a rolled amorphous Al-based alloy, *Acta Mater.* **53** (2005) 3469–3477.

[52] F. Meng, K. Tsuchiya, S. II, Y. Yokoyama, Reversible transition of deformation mode by structural rejuvenation and relaxation in bulk metallic glass, *Appl. Phys. Lett.* **101** (2012) 121914.

[53] X.D. Wang, Q.P. Cao, J.Z. Jiang, H. Franz, J. Schroers, R.Z. Valiev, Y. Ivanisenko, H. Gleiter, H.J. Fecht, Atomic-level structural modifications induced by severe plastic shear deformation in bulk metallic glasses, *Scripta Mater.* **64** (2011) 81–84.

[54] J. Qiang, K. Tsuchiya, Composition dependence of mechanically-induced structural rejuvenation in Zr-Cu-Al-Ni metallic glasses, *J. Alloys Comp.* **712** (2017) 250–255.

[55] W. Dmowski, Y. Yokoyama, A. Chuang, Y. Ren, M. Umemoto, K. Tsuchiya, A. Inoue, T. Egami, Structural rejuvenation in a bulk metallic glass induced by severe plastic deformation, *Acta Mater.* **58** (2010) 429–438.

[56] Y. Zhang, W.H. Wang, A.L. Greer, Making metallic glasses plastic by control of residual stress, *Nat. Mater.* **5** (2006) 857–860.

[57] F.O. Méar, B. Lenk, Y. Zhang, A.L. Greer, Structural relaxation in a heavily cold-worked metallic glass, *Scripta Mater.* **59** (2008) 1243–1246.

[58] A. Concustell, F.O. Méar, S. Suriñach, M.D. Baró, A.L. Greer, Structural relaxation and rejuvenation in a metallic glass induced by shot-peening, *Philos. Mag. Lett.* **89** (2009) 831–840.

[59] H. Bei, S. Xie, E.P. George, Softening caused by profuse shear banding in a bulk metallic glass, *Phys. Rev. Lett.* **96** (2006) 105503.

[60] D.V. Louzguine-Luzgin, S.V. Ketov, Z. Wang, M.J. Miyama, A.A. Tsarkov, A.Y. Churyumov, Plastic deformation studies of Zr-based bulk metallic glassy samples with a low aspect ratio, *Mater. Sci. Eng. A* **616** (2014) 288–296.

[61] L. He, M.B. Zhong, Z.H. Han, Q. Zhao, F. Jiang, J. Sun, Orientation effect of pre-introduced shear bands in a bulk-metallic glass on its “work-ductilising”, *Mater. Sci. Eng. A* **496** (2008) 285–290.

[62] J. Pan, Y.X. Wang, Q. Guo, D. Zhang, A.L. Greer, Y. Li, Extreme rejuvenation and softening in a bulk metallic glass, *Nat. Commun.* **9** (2018) 560.

[63] Z.T. Wang, J. Pan, Y. Li, C.A. Schuh, Densification and strain hardening of a metallic glass under tension at room temperature, *Phys. Rev. Lett.* **111** (2013) 135504.

[64] K.W. Park, C.M. Lee, M. Wakeda, Y. Shibutani, E. Fleury, J.C. Lee, Homogeneous deformation of bulk amorphous alloys during elastostatic compression and its packing density dependence, *Scripta Mater.* **59** (2008) 710–713.

[65] K.W. Park, C.M. Lee, M. Wakeda, Y. Shibutani, M.L. Falk, J.C. Lee, Elastostatically induced structural disordering in amorphous alloys, *Acta Mater.* **56** (2008) 5440–5450.

[66] S.C. Lee, C.M. Lee, J.C. Lee, H.J. Kim, Y. Shibutani, E. Fleury, M.L. Falk, Structural disordering process of an amorphous alloy driven by the elastostatic compression at room temperature, *Appl. Phys. Lett.* **92** (2008) 151906.

[67] S.C. Lee, C.M. Lee, J.W. Yang, J.C. Lee, Microstructural evolution of an elastostatically compressed amorphous alloy and its influence on the mechanical properties, *Scripta Mater.* **58** (2008) 591–594.

[68] K. S. Yoon, M. Lee, E. Fleury, J. C. Lee, Cryogenic temperature plasticity of a bulk amorphous alloy, *Acta Mater.* **58** (2010) 5295–5304.

[69] H.B. Ke, P. Wen, H.L. Peng, W.H. Wang, A.L. Greer, Homogeneous deformation of metallic glass at room temperature reveals large dilatation, *Scripta Mater.* **64** (2011) 966–969.

[70] Y.M. Wang, M. Zhang, L. Liu, Mechanical annealing in the homogeneous deformation of bulk metallic glass under elastostatic compression, *Scripta Mater.* **102** (2015) 67–70.

[71] J. Gu, M. Song, S. Ni, X. Liao, S. Guo, Improving the plasticity of bulk metallic glasses via pre-compression below the yield stress, *Mater. Sci. Eng. A* **602** (2014) 68–76.

[72] M. Zhang, Y.M. Wang, F.X. Li, S.Q. Jiang, M.Z. Li, L. Liu, Mechanical relaxation-to-rejuvenation transition in a Zr-based bulk metallic glass, *Sci. Rep.* **7** (2017) 625.

[73] P. Deng, X.C. Wang, F. Zhang, X.M. Qin, P. Gao, Y.D. Sui, J. Tan, Effect of mechanical-annealing on the mechanical properties of a Zr-based bulk metallic glass, *Int. J. Mod. Phys. B* **33** (2019) 1940052.

[74] C.E. Packard, E.R. Homer, N. Al-Aqeeli, C.A. Schuh, Cyclic hardening of metallic glasses under Hertzian contacts: Experiments and STZ dynamics simulations, *Philos. Mag.* **90** (2010) 1373–1390.

[75] C.E. Packard, L.M. Witmer, C.A. Schuh, Hardening of a metallic glass during cyclic loading in the elastic range, *Appl. Phys. Lett.* **92** (2008) 171911.

[76] N. Al-Aqeeli, Strengthening behavior due to cyclic elastic loading in Pd-based metallic glass, *J. Alloys Comp.* **509** (2011) 7216–7220.

[77] C. Deng, C.A. Schuh, Atomistic mechanisms of cyclic hardening in metallic glass, *Appl. Phys. Lett.* **100** (2012) 251909.

[78] N. Wang, F. Yan, L. Li, Mesoscopic examination of cyclic hardening in metallic glass, *J. Non-Cryst. Solids* **428** (2015) 146–150.

[79] A. Caron, A. Kawashima, H.J. Fecht, D.V. Louzguine-Luzgin, A. Inoue, On the anelasticity and strain induced structural changes in a Zr-based bulk metallic glass, *Appl. Phys. Lett.* **99** (2011) 171907.

[80] D.V. Louzguine-Luzgin, V.Y. Zadorozhnyy, S.V. Ketov, Z. Wang, A.A. Tsarkov, A.L. Greer, On room-temperature quasi-elastic mechanical behaviour of bulk metallic glasses, *Acta Mater.* **129** (2017) 343–351.

[81] W. Jiao, P. Wen, H.Y. Bai, Q.P. Kong, W.H. Wang, Transiently suppressed relaxations in metallic glass, *Appl. Phys. Lett.* **103** (2013) 161902.

[82] T. Ichitsubo, S. Kai, H. Ogi, M. Hirao, K. Tanaka, Elastic and anelastic behavior of $Zr_{55}Al_{10}Ni_5Cu_{30}$ bulk metallic glass around the glass transition temperature under ultrasonic excitation, *Scripta Mater.* **49** (2003) 267–271.

[83] T. Ichitsubo, E. Matsubara, S. Kai, M. Hirao, Ultrasound-induced crystallization around the glass transition temperature for $Pd_{40}Ni_{40}P_{20}$ metallic glass, *Acta Mater.* **52** (2004) 423–429.

[84] T. Ichitsubo, E. Matsubara, T. Yamamoto, H.S. Chen, N. Nishiyama, J. Saida, K. Anazawa, Microstructure of fragile metallic glasses inferred from ultrasound-accelerated crystallization in Pd-based metallic glasses, *Phys. Rev. Lett.* **95** (2005) 245501.

[85] T. Ichitsubo, E. Matsubara, K. Anazawa, N. Nishiyama, M. Naito, Y. Hirotsu, Low-temperature crystallization caused by ultrasound in $Pd_{42.5}Ni_{7.5}Cu_{30}P_{20}$ and $Pd_{40}Ni_{40}P_{20}$ bulk metallic glasses, *Mater. Sci. Eng. A* **442** (2006) 273–277.

[86] A. Gupta, S. Lai, R.P. Verma, On the ultrasonic-induced instability in metallic glasses, *J. Magn. Magn. Mater.* **44** (1984) 329–323.

[87] Y. Wang, W. Zhao, G. Li, R. Liu, Effects of ultrasonic treatment on the structure and properties of Zr-based bulk metallic glasses, *J. Alloy. Comp.* **544** (2012) 46–49.

[88] A.L. Greer, J.A. Leake, Structural relaxation and crossover effect in a metallic glass, *J. Non-Cryst. Solids* **33** (1979) 291–297.

[89] S.G. Zaichenko, N.S. Perov, A.M. Glezer, E.A. Gan'shina, V.M. Kachalov, M. Calvo-Dalborg, U. Dalborg, Low-temperature irreversible structural relaxation of amorphous metallic alloys, *J. Magn. Magn. Mater.* **215–216** (2000) 297–299.

[90] S.G. Zaichenko, A.M. Glezer, Physical model of the low-temperature-induced change in the structure and properties of amorphous alloys, *Doklady Phys.* **47** (2002) 846–848.

[91] S. Zaichenko, S. Roth, A. Glezer, Influence of the internal stresses relaxation on magnetic properties of Finemet-type amorphous alloy, *J. Magn. Magn. Mater.* **258–259** (2003) 571–573.

[92] K. Bán, A. Lovas, J. Kováč, Cryogenic effects in the amorphous Curie temperature shift of Fe-based glassy alloys, *Czech. J. Phys.* **54** (2004) D141–D144.

[93] A.M. Glezer, A.I. Potekaev, A.O. Cheretaeva, *Thermal and Time Stability of Amorphous Alloys*, Boca Raton: CRC Press, 2017.

[94] M. Wakeda, J. Saida, J. Li, S. Ogata, Controlled rejuvenation of amorphous metals with thermal processing, *Sci. Rep.* **5** (2015) 10545.

[95] J. Saida, R. Yamada, M. Wakeda, S. Ogata, Thermal rejuvenation in metallic glasses, *Sci. Technol. Adv. Mater.* **18** (2017) 152–162.

[96] W. Guo, R. Yamada, J. Saida, S. Lü, S. Wu, Thermal rejuvenation of a heterogeneous metallic glass, *J. Non-Cryst. Solids* **498** (2018) 8–13.

[97] W. Guo, J. Saida, M. Zhao, S. Lü, S. Wu, Thermal rejuvenation of an Mg-based metallic glass, *Metall. Mater. Trans. A* **50** (2019) 1125–1129.

[98] S. Küchemann, P.M. Derlet, C. Liu, D. Rosenthal, G. Sparks, W.S. Larson, R. Maaß, Energy storage in metallic glasses via flash annealing, *Adv. Funct. Mater.* **28** (2018) 1805385.

[99] S.V. Ketov, Y.H. Sun, S. Nachum, Z. Lu, A. Checchi, A.R. Beraldin, H.Y. Bai, W.H. Wang, D.V. Louzguine-Luzgin, M.A. Carpenter, A.L. Greer, Rejuvenation of metallic glasses by non-affine thermal strain, *Nature* **524** (2015) 200–203.

[100] H. Wagner, D. Bedorf, S. Küchemann, M. Schwabe, B. Zhang, W. Arnold, K. Samwer, Local elastic properties of a metallic glass, *Nat. Mater.* **10** (2011) 439–442.

[101] W. Song, X. Meng, Y. Wua, D. Cao, H. Wang, X. Liu, X. Wang, Z. Lu, Improving plasticity of the $Zr_{46}Cu_{46}Al_8$ bulk metallic glass via thermal rejuvenation, *Sci. Bull.* **63** (2018) 840–844.

[102] W. Guo, R. Yamada, J. Saida, Rejuvenation and plasticization of metallic glass by deep cryogenic cycling treatment, *Intermetallics* **93** (2018) 141–147.

[103] D. Grell, F. Dabrock, E. Kerscher, Cyclic cryogenic pretreatments influencing the mechanical properties of a bulk glassy Zr-based alloy, *Fatigue Fract. Eng. Mater. Struct.* **41** (2018) 1330–1343.

[104] F. Bu, J. Wang, L. Li, H. Kou, X. Xue, J. Li, The effect of thermal cycling treatments on the thermal stability and mechanical properties of a Ti-based bulk metallic glass composite, *Metals* **6** (2016) 274.

[105] S.V. Ketov, A.S. Trifonov, Y.P. Ivanov, A.Y. Churyumov, A.V. Lubenchenko, A.A. Batrakov, J. Jiang, D.V. Louzguine-Luzgin, J. Eckert, J. Orava, A.L. Greer, On cryothermal cycling as a method for inducing structural changes in metallic glasses, *NPG Asia Mater.* **10** (2018) 137–145.

[106] W. Guo, R. Yamada, J. Saida, S. Lü, S. Wu, Various rejuvenation behaviors of Zr-based metallic glass by cryogenic cycling treatment with different casting temperatures, *Nanoscale Res. Lett.* **13** (2018) 398.

[107] M.C. Ri, S. Sohrabi, D.W. Ding, B.S. Dong, S.X. Zhou, W.H. Wang, Serrated magnetic properties in metallic glass by thermal cycle, *Chin. Phys. B* **26** (2017) 066101.

[108] Y. Meng, Y.G. Wang, L. Zhu, C.C. Cao, Y.D. Dai, Effect of thermal cycling treatment on local structure, thermal stability and magnetic properties of $Fe_{80}Si_{8.75}B_{10}Cu_{1.25}$ metallic glass, *J. Non-Cryst. Solids* **471** (2017) 406–409.

[109] C. Wang, Z.Z. Yang, T. Ma, Y.T. Sun, Y.Y. Yin, Y. Gong, L. Gu, P. Wen, P.W. Zhu, Y.W. Long, X.H. Yu, C.Q. Jin, W.H. Wang, H.Y. Bai, High stored energy of metallic glasses induced by high pressure, *Appl. Phys. Lett.* **110** (2017) 111901.

[110] T.P. Ge, C. Wang , J. Tan, T. Ma, X.H. Yu, C.Q. Jin, W.H. Wang, H.Y. Bai, Unusual energy state evolution in Ce-based metallic glass under high pressure, *J. Appl. Phys.* **121** (2017) 205109.

[111] Y. Tong, W. Dmowski, Y. Yokoyama, G. Wang, P.K. Liaw, T. Egami, Recovering compressive plasticity of bulk metallic glasses by high-temperature creep, *Scr. Mater.* **69** (2013) 570–573.

[112] Y. Tong, T. Iwashita, W. Dmowski, H. Bei, Y. Yokoyama, T. Egami, Structural rejuvenation in bulk metallic glasses, *Acta Mater.* **86** (2015) 240–246.

[113] Y. Tong, W. Dmowski, H. Bei, Y. Yokoyama, T. Egami, Mechanical rejuvenation in bulk metallic glass induced by thermo-mechanical creep, *Acta Mater.* **148** (2018) 384–390.

[114] E.A. Kramer, W.L. Johnson, C. Cline, The effects of neutron irradiation on a superconducting metallic glass, *Appl. Phys. Lett.* **35** (1979) 815–818.

[115] Q. Xiao, L. Huang, Y. Shi, Suppression of shear banding in amorphous ZrCuAl nanopillars by irradiation, *J. Appl. Phys.* **113** (2013) 083514.

[116] R. Raghavan, K. Boopathy, R. Ghisleni, M.A. Pouchon, U. Ramamurty, J. Michler, Ion irradiation enhances the mechanical performance of metallic glasses, *Scripta Mater.* **62** (2010) 462–465.

[117] R. Gerling, F.P. Schimansky, R. Wagner, Restoration of the ductility of thermally embrittled amorphous alloys under neutron-irradiation, *Acta Metall.* **35** (1987) 1001–1006.

[118] Y. Huang, H. Fan, X. Zhou, P. Xue, Z. Ning, D. Daisenberger, J. Sun, J. Shen, Structure and mechanical property modification of a Ti-based metallic glass by ion irradiation, *Scripta Mater.* **103** (2015) 41–44.

[119] J. Carter, E.G. Fu, G. Bassiri, B.M. Dvorak, N.D Theodore, G. Xie, D.A. Lucca, M. Martin, M. Hollander, X. Zhang, L. Shao, Effects of ion irradiation in metallic glasses, *Nucl. Instrum. Methods Phys. Res. B* **267** (2009) 1518–1521.

[120] T. Nagase, Y. Umakoshi, Thermal stability and electron irradiation effect on Zr-based amorphous alloys, *J. Appl. Phys.* **93** (2003) 912–918.

[121] S.G. Mayr, Impact of ion irradiation on the thermal, structural, and mechanical properties of metallic glasses, *Phys. Rev. B* **71** (2005) 144109.

[122] A.L. Greer, Y.H. Sun, Stored energy in metallic glasses due to strains within the elastic limit, *Philos. Mag.* **96** (2016) 1643–1663.

[123] H. Kuhn, D. Medlin, ASM Handbook Volume 8: Mechanical Testing and Evaluation, ASM Handbooks Online, ASM International, 2000. DOI: https://doi.org/10.31399/asm.hb.v08.9781627081764.

[124] A.C. Fischer-Cripps, *Nanoindentation*, 3rd ed. New York; London: Springer, 2011.

[125] J.L. Hay, G.M. Pharr, 'Instrumented Indentation Testing', in ASM Handbook Volume 8: Mechanical Testing and Evaluation, H. Kuhn, D. Medlin, ASM Handbooks Online, ASM International, 2000. DOI: https://doi.org/10.31399/asm.hb.v08.a0003273.

[126] J. S. Field, M. V. Swain, A simple predictive model for spherical indentation, *J. Mater. Res.* **8** (1993) 297–306.

[127] W.C. Oliver, G.M. Pharr, An improved technique for determining hardness and elastic modulus using load and displacement sensing indentation experiments, *J. Mater. Res.* **7** (1992) 1564–1583.

[128] J. H. Perepezko, S. D. Imhoff, M. W. Chen, J. Q. Wang, and S. Gonzalez, Nucleation of shear bands in amorphous alloys, *Proc. Natl. Acad. Sci. USA* **111** (2014) 3938–3942.

[129] M.D. Ediger, Spatially heterogeneous dynamics in supercooled liquids, *Annu. Rev. Phys. Chem.* **51** (2000) 99–128.

[130] T. Ichitsubo, E. Matsubara, Structural inhomogeneity of metallic glass observed by ultrasonic and inelastic X-ray scattering measurements, *Mater. Sci. Eng. A* **521–522** (2009) 236–242.

[131] C.E. Packard, O. Franke, E.R. Homer, C.A. Schuh, Nanoscale strength distribution in amorphous versus crystalline metals, *J. Mater. Res.* **25** (2010) 2251–2263.

[132] W. Dmowski, T. Iwashita, C.P. Chuang, J. Almer, T. Egami, Elastic heterogeneity in metallic glasses, *Phys. Rev. Lett.* **105** (2010) 205502.

[133] A.L. Greer, The use of DSC to determine the Curie temperature of metallic glasses, *Thermochim. Acta* **42** (1980) 193–222.

[134] P. Gabbott, *Principles and Applications of Thermal Analysis*, Oxford: Blackwell, 2008.

[135] A.A. Minakov, C. Schick, Ultrafast thermal processing and nanocalorimetry at heating and cooling rates up to 1 MK/s, *Rev. Sci. Instrum.* **78** (2007) 073902.

[136] E. Zhuravlev, C. Schick, Fast scanning power compensated differential scanning nano-calorimeter: 1. The device, *Thermochim. Acta* **505** (2010) 1–13.

[137] C. Schick, V. Mathot, *Fast Scanning Calorimetry*, Switzerland: Springer International Publishing, 2016.

[138] J.E.K. Schawe, Flash DSC 1: A novel fast differential scanning calorimeter, *Proceedings of the 27th International Conference of the Polymer Processing Society (PPS)*, Marrakech, Morocco, 2011.

[139] Operating instructions manual of Flash DSC 1, Mettler-Toledo AG.

[140] S. Pogatscher, D. Leutenegger, A. Hagmann, P.J. Uggowitzer, J.F. Löffler, Characterization of bulk metallic glasses via fast differential scanning calorimetry, *Thermochim. Acta* **590** (2014) 84–90.

[141] S. van Herwaarden, E. Iervolino, F. van Herwaarden, T. Wijffels, A. Leenaers, V. Mathot, Design, performance and analysis of thermal lag of the UFS1 twin-calorimeter chip for fast scanning calorimetry using the Mettler-Toledo Flash DSC1, *Thermochim. Acta* **522** (2011) 46–52.

[142] J. Fornell, A. Concustell, A.L. Greer, S. Suriñach, M.D. Baró, J. Sort, Effects of shot peening on the nanoindentation response of $Cu_{47.5}Zr_{47.5}Al_5$ metallic glass, *J. Alloy. Compd.* **586** (2014) S36–S40.

[143] H.E. Kissinger, Variation of peak temperature with heating rate in differential thermal analysis, *J. Res. Nat. Bur. Stand.* **57** (1956) 217–221.

[144] M. Lasocka, The effect of scanning rate on glass transition temperature of splat-cooled $Te_{85}Ge_{15}$, *Mater. Sci. Eng.* **23** (1976) 173–177.

[145] R. Jia, X.F. Bian, Y.Y. Wang, Thermodynamic determination of fragility in La-based glass-forming liquid, *Chinese Sci. Bull.* **56** (2011) 3912–3918.

[146] Y. Kawamura, T. Nakamura, A. Inoue, T. Masumoto, High-strain-rate superplasticity due to Newtonian viscous flow in $La_{55}Al_{25}Ni_{20}$ metallic glass, *Mater. T. JIM* **40** (1999) 794–803.

[147] Z.P. Lu, T.T. Goh, Y. Li, S.C. Ng, Glass formation in La-based La–Al–Ni–Cu–(Co) alloys by Bridgman solidification and their glass forming ability, *Acta Mater.* **47** (1999) 2215–2224.

[148] Z.P. Lu, Y. Li, C.T. Liu, Glass-forming tendency of bulk La–Al–Ni–Cu–(Co) metallic glass-forming liquids, *J. Appl. Phys.* **93** (2003) 286–290.

[149] I.M. Hodge, Enthalpy relaxation and recovery in amorphous materials, *J. Non-Cryst. Solids* **169** (1994) 211–266.

[150] K.B. Kim, X.F. Zhang, S. Yi, M.H. Lee, J. Das, J. Eckert, Effect of local chemistry, structure and length scale of heterogeneities on the mechanical properties of a $Ti_{45}Cu_{40}Ni_{7.5}Zr_5Sn_{2.5}$ bulk metallic glass, *Phil. Mag. Lett.* **88** (2008) 75–81.

[151] B. Huang, H.Y. Bai, P. Wen, D.W. Ding, D.Q. Zhao, M.X. Pan, W.H. Wang, The heterogeneous structure of metallic glasses revealed by superconducting transitions, *J. Appl. Phys.* **114** (2013) 113508.

[152] M.H. Lee, J.K. Lee, K.T. Kim, J. Thomas, J. Das, U. Kühn, J. Eckert, Deformation-induced microstructural heterogeneity in monolithic $Zr_{44}Ti_{11}Cu_{9.8}Ni_{10.2}Be_{25}$ bulk metallic glass, *Phys. Status Solidi. RRL* **3** (2009) 46–48.

[153] R.D. Conner, Y. Li, W.D. Nix, W.L. Johnson, Shear band spacing under bending of Zr-based metallic glass plates, *Acta Mater.* **52** (2004) 2429–2434.

[154] C.T. Moynihan, A.J. Easteal, M.A. DeBolt, J. Tucker, Dependence of the fictive temperature of glass on cooling rate, *J. Am. Ceram. Soc.* **59** (1976) 12–16.

[155] J.C. Qiao, Q. Wang, D. Crespo, Y. Yang, J.M. Pelletier, Secondary relaxation and dynamic heterogeneity in metallic glasses: A brief review, *Chin. Phys. B* **26** (2017) 016402.

[156] H. Okumura, H.S. Chen, A. Inoue, T. Masumoto, Sub-T_g mechanical relaxation of a $La_{55}Al_{25}Ni_{20}$ amorphous alloy, *J. Non-Cryst. Solids* **130** (1991) 304–310.

[157] P.T. Vianco, J.C.M. Li, Analysis of the endothermic peak in an annealed metallic glass, *J. Non-Cryst. Solids* **107** (1989) 225–232.

[158] H.S. Chen, A. Inoue, Sub-T_g enthalpy relaxation in PdNiSi alloy glasses, *J. Non-Cryst. Solids* **61**–**62** (1984) 805–810.

[159] H.S. Chen, Kinetics of low temperature structural relaxation in two (Fe-Ni)-based metallic glasses, *J. Appl. Phys.* **52** (1981) 1868–1870.

[160] H.S. Chen, On the mechanisms of structural relaxation in a $Pd_{48}Ni_{32}P_{20}$ glass, *J. Non-Cryst. Solids* **46** (1981) 289–305.

[161] L. Hu, C. Zhou, C. Zhang, Y. Yue, Thermodynamic anomaly of the sub-T_g relaxation in hyperquenched metallic glasses, *J. Chem. Phys.* **138** (2013) 174508.

[162] Y. Yue, C.A. Angell, Clarifying the glass-transition behaviour of water by comparison with hyperquenched inorganic glasses, *Nature* **427** (2004) 717–720.

[163] L. Hu, Y. Yue, Secondary relaxation in metallic glass formers: its correlation with the genuine Johari-Goldstein relaxation, *J. Phys. Chem. C* **113** (2009) 15001–15006.

[164] J. Orava, A.L. Greer, B. Gholipour, D.W. Hewak, C.E. Smith, Characterization of supercooled liquid $Ge_2Sb_2Te_5$ and its crystallization by ultrafast-heating calorimetry, *Nat. Mater.* **11** (2012) 279–283.

[165] S. Pogatscher, P.J. Uggowitzer, J. F. Löffler, In-situ probing of metallic glass formation and crystallization upon heating and cooling via fast differential scanning calorimetry, *Appl. Phys. Lett.* **104** (2014) 251908.

[166] A. Inoue, T. Masumoto, H.S. Chen, Enthalpy relaxation behaviour of $(Fe, Co, Ni)_{75}Si_{10}B_{15}$ amorphous alloys upon low temperature annealing, *J. Mater. Sci.* **19** (1984) 3953–3966.

[167] H.S. Chen, A method for evaluating viscosities of metallic glasses from the rates of thermal transformations, *J. Non-Cryst. Solids* **27** (1978) 257–263.

[168] C.A. Angell, Formation of glasses from liquids and biopolymers, *Science* **267** (1995) 1924–1935.

[169] R. Böhmer, K.L. Ngai, C.A. Angell, D J. Plazek, Nonexponential relaxations in strong and fragile glass formers, *J. Chem. Phys.* **99** (1993) 4201–4209.

[170] C.A. Schuh, T.G. Nieh, A nanoindentation study of serrated flow in bulk metallic glasses, *Acta Mater.* **51** (2003) 87–99.

[171] P. Yu, H.Y. Bai, W.H. Wang, Superior glass-forming ability of CuZr alloys from minor additions, *J. Mater. Res.* **21** (2006) 1674–1679.

[172] J. Wen, H.W. Yang, H. Guo, B. Wu, M.L. Sui, J.Q. Wang, E. Ma, Fluctuation electron microscopy of Al-based metallic glasses: effects of minor alloying addition and structural relaxation on medium-range structural homogeneity, *J. Phys. Condens. Matter* **19** (2007) 455211.

[173] H.B. Ke, C.T. Liu, Y. Yang, Structural heterogeneity and deformation rheology in metallic glasses, *Sci. China Technol. Sci.* **58** (2015) 47–55.

[174] W. Dmowski, C. Fan, M.L. Morrison, P.K. Liaw, T. Egami, Structural changes in bulk metallic glass after annealing below the glass-transition temperature, *Mater. Sci. Eng. A* **471** (2007) 125–129.

[175] S. Xie, E.P. George, Hardness and shear band evolution in bulk metallic glasses after plastic deformation and annealing, *Acta Mater.* **56** (2008) 5202–5213.

[176] P. Denis, C.M. Meylan, C. Ebner, A.L. Greer, M. Zehetbauer, H.J. Fecht, Rejuvenation decreases shear band sliding velocity in Pt-based metallic glasses, *Mate. Sci. Eng. A* **684** (2017) 517–523.

[177] C.A. Schuh, T.G. Nieh, Y. Kawamura, Rate dependence of serrated flow during nanoindentation of a bulk metallic glass, *J. Mater. Res.* **17** (2002) 1651–1654.

[178] W.H. Wang, The elastic properties, elastic models and elastic perspectives of metallic glasses, *Prog. Mater. Sci.* **57** (2012) 487–656.

[179] K. Fujita, A. Inoue, T. Zhang, N. Nishiyama, Anelastic behavior under tensile and shearing stresses in bulk metallic glasses, *Mater. Trans.* **43** (2002) 1957–1960.

[180] T.W. Wu, F. Spaepen, The relation between embrittlement and structural relaxation of an amorphous metal, *Philos. Mag. B* **61** (1990) 739–750.

[181] A.I. Taub, F. Spaepen, The kinetics of structural relaxation of a metallic glass, *Acta Metall.* **28** (1980) 1781–1788.

[182] J.D. Ju, D. Jang, A. Nwankpa, M. Atzmon, An atomically quantized hierarchy of shear transformation zones in a metallic glass, *J. Appl. Phys.* **109** (2011) 053522.

[183] Z. Lu, W. Jiao, W.H. Wang, H.Y. Bai, Flow unit perspective on room temperature homogeneous plastic deformation in metallic glasses, *Phys. Rev. Lett.* **113** (2014) 045501.

[184] R.S. Williams, T. Egami, Effects of deformation and annealing on magnetic amorphous alloys, *IEEE Trans. Magn.* **12** (1976) 927–929.

[185] W.L. Johnson, K. Samwer, A universal criterion for plastic yielding of metallic glasses with a $(T/T_g)^{2/3}$ temperature dependence, *Phys. Rev. Lett.* **95** (2005) 195501.

[186] Z. Lu, B.S. Shang, Y.T. Sun, Z.G. Zhu, P.F. Guan, W.H. Wang, H.Y. Bai, Revealing β-relaxation mechanism based on energy distribution of flow units in metallic glass, *J. Chem. Phys.* **144** (2016) 144501.

[187] A.L. Greer, Effect of quench rate on the structural relaxation of a metallic glass, *J. Mater. Sci.* **17** (1982) 1117–1124.

[188] S. Sabolek, E. Babić, Domain structure, pinning centres and magnetization processes in amorphous and nanocrystalline $Fe_{73.5}Cu_1Nb_3Si_{15.5}B_7$ ribbon, *Phys. Stat. Sol. (a)* **160** (1997) 205–214.

[189] Y. Nishi, T. Kai, M. Tachi, T. Ishidaira, E. Yajima, Cooling condition dependence of saturated magnetic flux density in Fe-5at%Si-20at%B alloy glass, *Scr. Metall.* **20** (1986) 1099–1100.

[190] S.W. Hwang, S.J. Kim, C.S. Yoon, C.K. Kim, Crystallization and structural relaxation of $Fe_{78-x}Pt_xB_{10}Si_{12}$ metallic glasses, *Phys. Stat. Sol. (a)* **201** (2004) 1875–1878.

[191] M. Miglierini, Mössbauer-effect study of the hyperfine field distributions in the residual amorphous phase of the Fe-Cu-Nb-Si-B nanocrystalline alloys, *J. Phys.: Condens. Matter* **6** (1994) 1431–1438.

[192] J. Schroers, B. Lohwongwatana, W.L. Johnson, A. Peker, Gold based bulk metallic glass, *Appl. Phys. Lett.* **87** (2005) 061912.

[193] I. Gallino, D. Cangialosi, Z. Evenson, L. Schmitt, S. Hechler, M. Stolpe, B. Ruta, Hierarchical aging pathways and reversible fragile-to-strong transition upon annealing of a metallic glass former, *Acta Mater.* **144** (2018) 400–410.

[194] Z. Evenson, S.E. Naleway, S. Wei, O. Gross, J.J. Kruzic, I. Gallino, W. Possart, M. Stommel, R. Busch, β relaxation and low-temperature aging in a Au-based bulk metallic glass: From elastic properties to atomic-scale structure, *Phys. Rev. B* **89** (2014) 174204.

[195] H.B. Yu, W.H. Wang, H.Y. Bai, Y. Wu, M.W. Chen, Relating activation of shear transformation zones to β relaxations in metallic glasses, *Phys. Rev. B* **81** (2010) 220201(R).

[196] L. Song, W. Xu, J. Huo, J.Q. Wang, X. Wang, R. Li, Two-step relaxations in metallic glasses during isothermal annealing, *Intermetallics* **93** (2018) 101–105.

[197] G. Fiore, I. Ichim, L. Battezzati, Thermal analysis, fragility and viscosity of Au-based metallic glasses, *J. Non-Cryst. Solids* **356** (2010) 2218–2222.

[198] Supplementary material of L. Song, W. Xu, J. Huo, J.Q. Wang, X. Wang, R. Li, Two-step relaxations in metallic glasses during isothermal annealing, *Intermetallics* **93** (2018) 101–105.

[199] J. Schroers, On the formability of bulk metallic glass in its supercooled liquid state, *Acta Mater.* **56** (2008) 471–478.

[200] J.Q. Wang, Y. Shen, J.H. Perepezko, M.D. Ediger, Increasing the kinetic stability of bulk metallic glasses, *Acta Mater.* **104** (2016) 25–32.

[201] S.F. Swallen, K.L. Kearns, M.K. Mapes, Y.S. Kim, R.J. McMahon, M.D. Ediger, T. Wu, L. Yu, S. Satija, Organic glasses with exceptional thermodynamic and kinetic stability, *Science* **315** (200) 353–356.

Appendix A Additional Information on Chapter 4

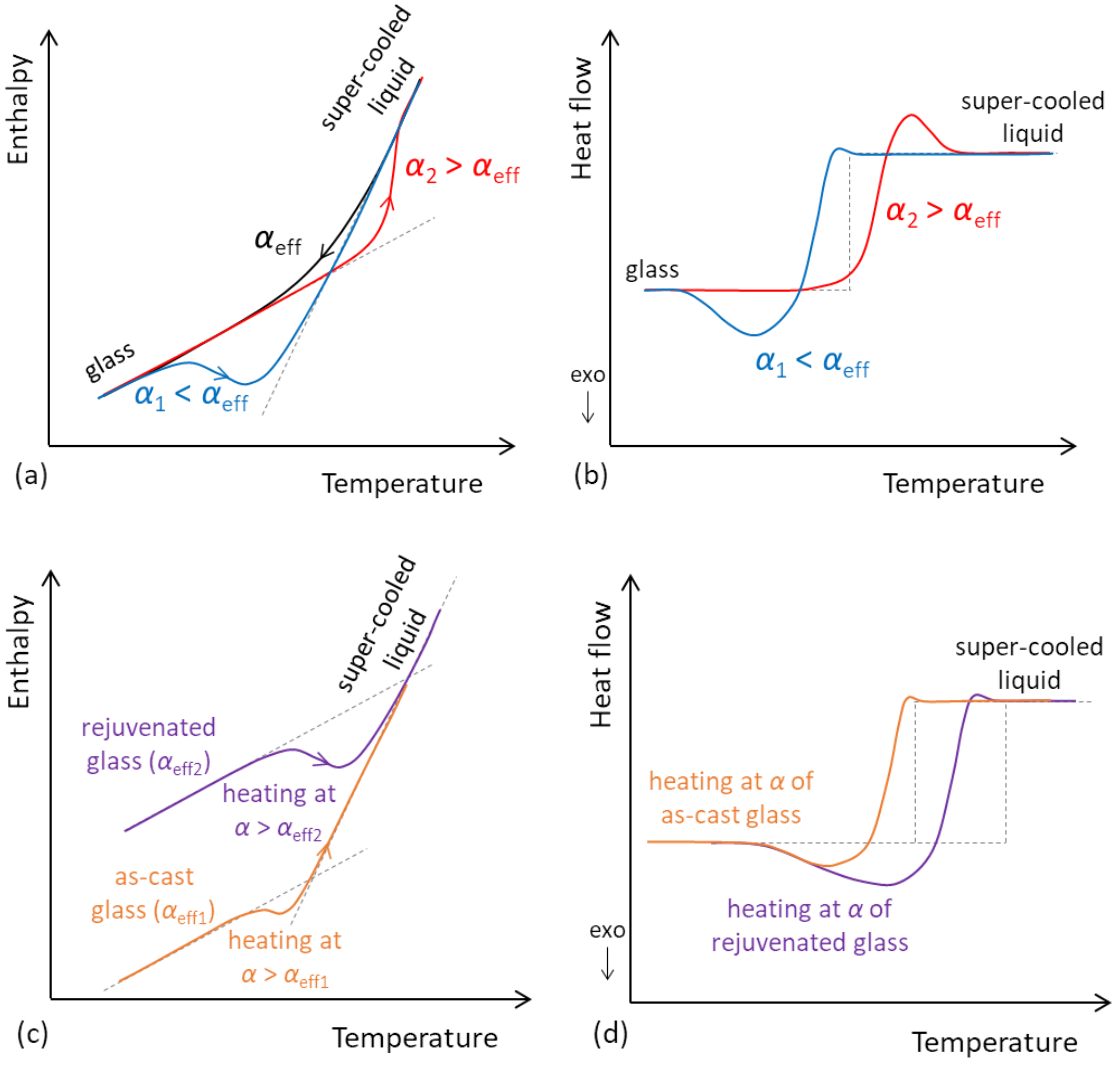

Fig. A.1. Schematic diagram of the enthalpy vs. temperature curve of a glass formed upon cooling at a rate of α_{eff1} (black line) and upon subsequent heating at a rate of $\alpha_1 < \alpha_{eff}$ (blue line) and $\alpha_2 > \alpha_{eff}$ (red line) (a). When the glass is heated at a rate of $\alpha_1 < \alpha_{eff}$, the glass can relax before the glass transition takes place, giving rise to an exothermic structural relaxation peak in the heat flow curve measured by DSC (shown schematically by the blue line in (b)); but if heating at a rate of $\alpha_2 > \alpha_{eff}$, an overshoot peak appears at the glass transition (red line in (b)). If an as-cast glass (formed at a cooling rate of α_{eff1}) is rejuvenated, its energy increases, and its effective cooling rate is now $\alpha_{eff2} > \alpha_{eff1}$ (c). Upon heating in the DSC at a rate of $\alpha < \alpha_{eff1} < \alpha_{eff2}$, the rejuvenated glass will relax more, and will show a larger exothermic relaxation peak in its heat flow curve (d).

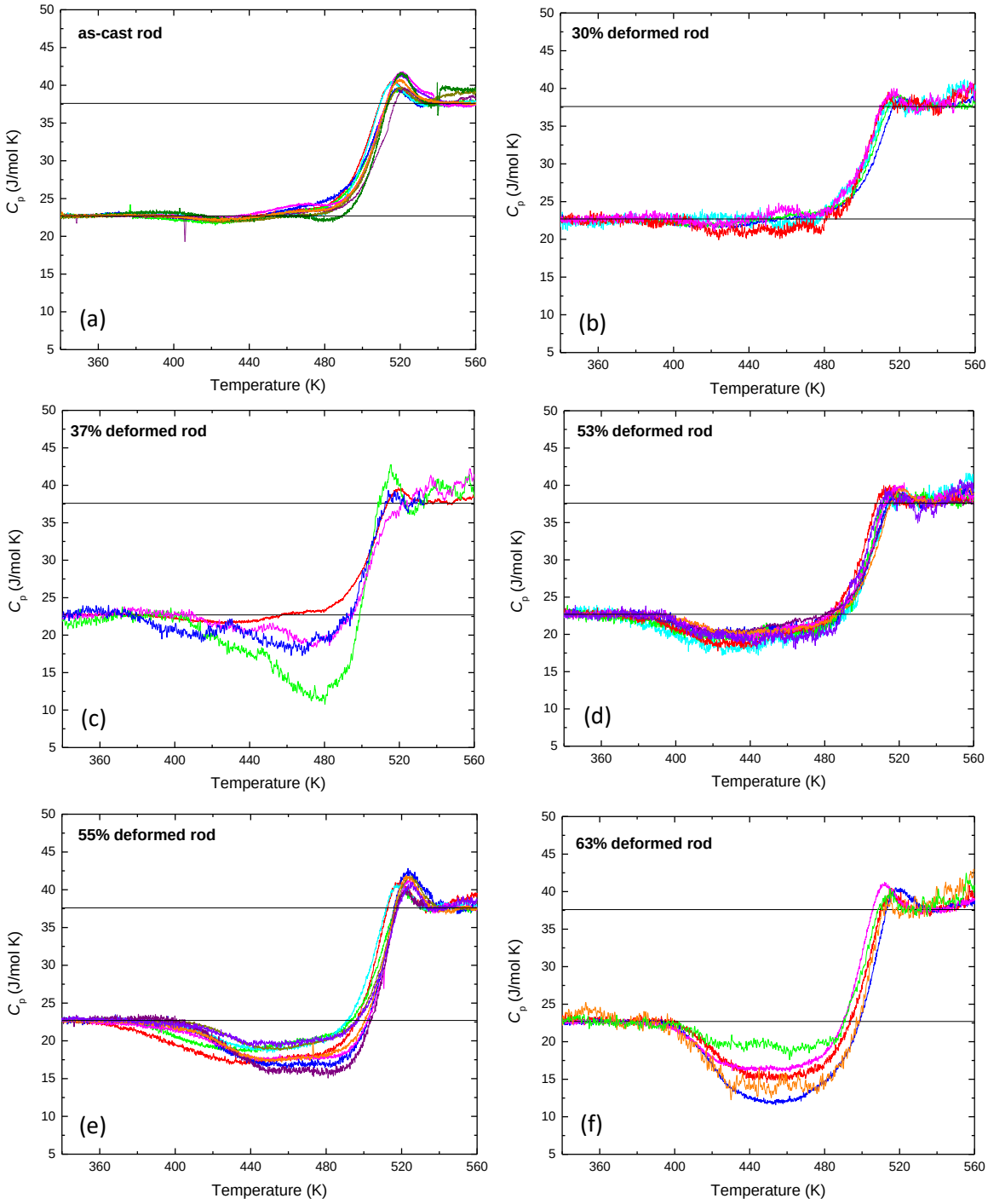

Fig. A.2. *(continued on next page)*

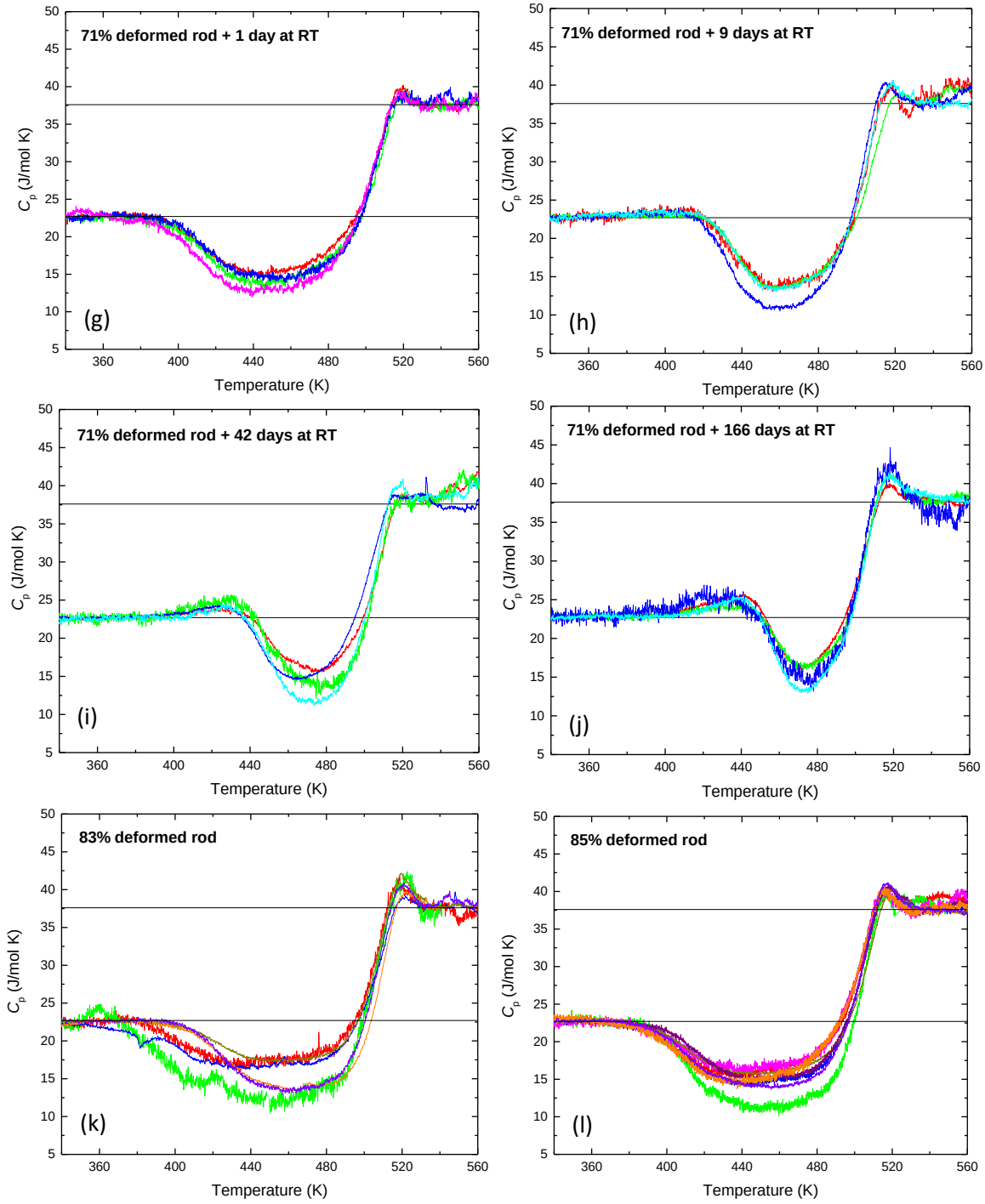

Fig. A.2. *(continued on next page)*

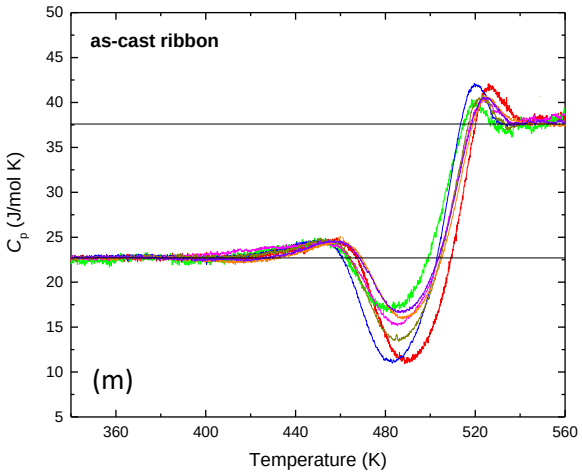

Fig. A.2. Calculated specific-heat curves C_p of all FDSC-measured samples of the as-cast rod (a), the rod after different degrees of plastic deformation (b–l) and the as-cast ribbon (m).

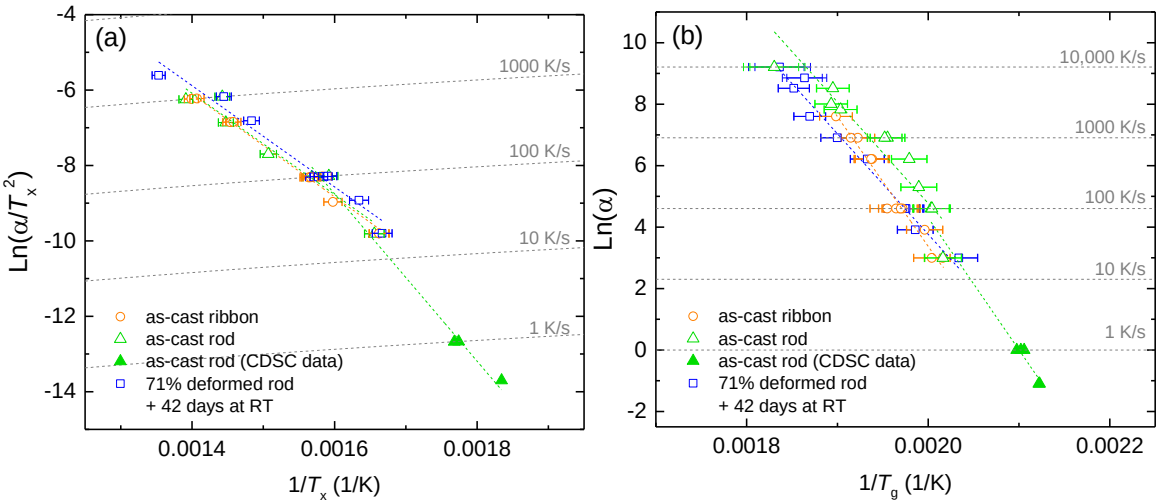

Fig. A.3. Kissinger plots of the crystallization peak T_x (a) and onset of glass transition T_g (b) for the as-cast ribbon, as-cast rod and the rod deformed by 71% and aged for 42 days at RT. Data were obtained by FDSC when measuring with heating rates above 10 K/s, and by conventional DSC (CDSC) at 1 K/s and lower. Linear fits were applied to these data in order to deduce activation energies of these processes, which are presented in the main text in Table 4.2.

Table A.1. Fitting parameters of the Vogel–Fulcher–Tammann equation for our data, as well as the parameters given by Lu et al. [A1].

	D^*	T_0 (K)	m
Fitting of the present work	11.3	341.3	46.9
Lu et al. [A1]	18	306.5	41.7

Calculation of work done during compression

The work done (WD) during plastic deformation can be estimated from the area under the stress–strain curve $\sigma(\varepsilon)$ upon loading, excluding the elastic part of the deformation:

$$\text{Work done (WD)} = V_{\text{molar}} \cdot \left(\left(\int_0^{\epsilon_{\max}} \sigma(\varepsilon)\, \mathrm{d}\varepsilon \right) - \left(\frac{1}{2} \frac{{\sigma_{\max}}^2}{E} \right) \right)$$

where V_{molar} is the molar volume ($1.54 \cdot 10^{-5}$ m^3/mol), $\varepsilon_{\max}$ and $\sigma_{\max}$ are the strain and stress at the final load, and E is the Young's modulus found in the literature (47 GPa [A2]).

For the rod sample deformed to 55%, the WD was estimated to be roughly 17 kJ/mol. For this sample, an average increase in energy of ≈ 500 J/mol was measured; this corresponds to ≈ 3% of WD.

Determination of errors

a) Errors in the values of the onset of glass transition T_g, onset of crystallization T_x and crystallization peak T_p measured as a function of heating rate:
   - Error in chip temperature calibration is ± 5°C.
   - Error due to thermal lag is not known for these measurements, but can be estimated. The thermal lag was considered here to be:

$$\text{thermal lag} = \alpha \cdot \tau_{\text{lag}} \propto \alpha \cdot m \cdot C_{\text{p}}$$

   where α is the heating rate, τ_{lag} the time lag, m the sample mass C_p the heat capacity of the sample, and therefore:

$$\frac{{\tau_{\text{lag}}}_{\text{sample1}}}{m_{\text{sample1}} \cdot C_{\text{p, sample1}}} = \frac{{\tau_{\text{lag}}}_{\text{sample2}}}{m_{\text{sample2}} \cdot C_{\text{p, sample2}}}$$

   τ_{lag} of a nickel sample (with a known size of 150 µm x 150 µm x 10 µm, and therefore a known mass of 2 µg) was determined from T_{Curie} measurements at various heating rates as 0.007 s. The mass of the La-based metallic-glass samples is not known, but was estimated to be around 1.2 ± 0.5 µg. From this, τ_{lag} of the La-based samples should be around

0.0023 ± 0.0009 s. The temperature error corresponding to this time lag is e.g. 0.23 K when heating at 100 K/s, and 2.3 K when heating at 1000 K/s.

b) Concerning the errors in the determination of the fictive temperature $T_{fictive}$:
   - Error due to thermal lag: The FDSC curves used for determining $T_{fictive}$ were measured at a heating rate of 100 K/s, at which thermal lag is negligible (<1°C according to the estimation above).
   - Error of temperature calibration: A temperature calibration was not done for the sensors used; instead each FDSC curve was calibrated separately using the onset of melting T_m of the measured La-based metallic-glass sample. From a separate measurement on a calibrated sensor, we found T_m ≈ 460°C. The variation of the temperature corrections among all the curves is around ± 5°C; the error in temperature calibration is considered equal to this variation.

c) Measurement of enthalpy change ΔH_{diff}:
   - Error of ΔH_{diff} due to variation of baseline definition. For some selected FDSC curves, the baselines were determined twice. Difference of ΔH_{diff} for the different baselines was on average ≈ 40 J/mol.
   - Error of ΔH_{diff} due to error in temperature calibration. A temperature calibration error of ± 5 K leads to a variation in ΔH_{diff} of around ± 75 J/mol.

[A1] Z.P. Lu, Y. Li, C.T. Liu, Glass-forming tendency of bulk La–Al–Ni–Cu–(Co) metallic glass-forming liquids, *J. Appl. Phys.* **93** (2003) 286–290.

[A2] S. Takeuchi, T. Kakegawa, T. Hashimoto, A.P. Tsai, A. Inoue, Low temperature mechanical properties of bulk metallic glasses, *Mat. T. JIM* **41** (2000) 1443–1447.

Appendix B : Additional Information on Chapter 5

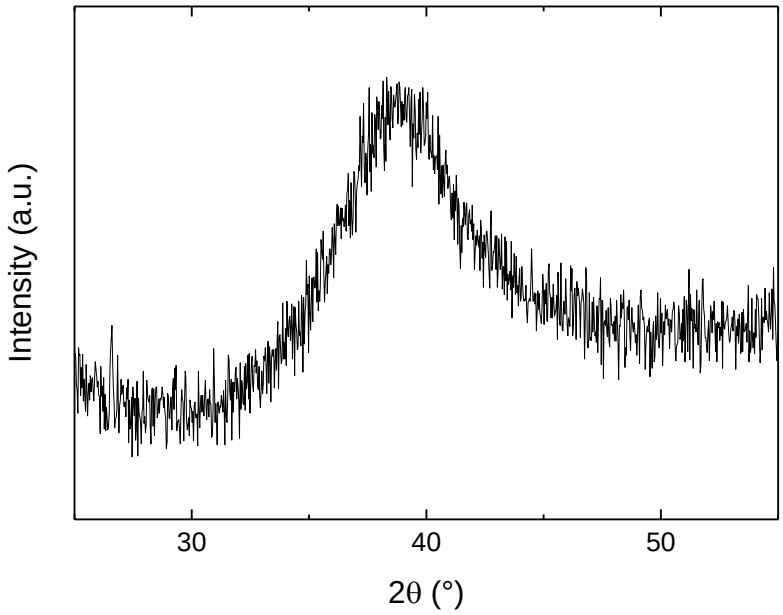

Fig. B.1. X-ray diffractogram of the $Cu_{46}Zr_{46}Al_7Gd_1$ bulk-metallic-glass sample after annealing for 24 h at 630 K (≈ 0.9 T_g), showing a broad diffraction maximum characteristic of amorphous structures. No sharp crystalline peaks are visible in this pattern.

Table B.1. Nanoindentation measurement of the initial yield load F_y and pressure P_y, the size of the initial pop-in Δh, the hardness H and the indentation modulus extracted from the unloading curve, $E_{r,unloading}$, as well as from fitting of the loading curve with the Hertzian equation, $E_{r,Hertzian}$. For each property, the median is given, as well as the values at the 5th percentile (P_5) and 95th percentile (P_{95}). The range of the distribution corresponds to the difference $P_{95} - P_5$.

F_y (mN)	median	5th percentile	95th percentile	range
as-cast	41.2	25.1	60.3	35.3
	+ 39%	+ 28%	+ 6%	- 9%
as-cast + EC	57.2	32.2	64.1	31.9
	- 28%	- 32%	- 30%	-29%
10 TCs	29.7	17.1	42.3	25.2
	+ 19%	+ 41%	+ 18%	+ 2%
10 TCs + EC	35.5	24.1	49.7	25.6
	+ 54%	+ 44%	+ 79%	+ 103%
annealed	45.8	24.7	75.7	51.1
	+ 42%	+ 28%	+ 3%	- 9%
annealed + EC	65.0	31.6	77.9	46.3
P_y (GPa)	median	5th percentile	95th percentile	range
as-cast	7.1	6.0	8.0	2.0
	+ 12%	+ 9%	+ 3%	-17%
as-cast + EC	7.9	6.6	8.2	1.6
	-10%	-15%	-10%	6%
10 TC	6.4	5.1	7.2	2.1
	+ 8%	+ 18%	+ 7%	-18%
10 TC + EC	6.9	6.0	7.7	1.7
	+ 22%	+ 26%	+ 29%	+ 36%
annealed	7.8	6.4	9.3	2.8
	+ 11%	+ 6%	+ 1%	-10%
annealed + EC	8.6	6.8	9.4	2.6

Table B.1. *Continued.*

Δ*h* (nm)	median	5th percentile	95th percentile	range
as-cast	9.0	2.0	25.0	23.0
	+ 118%	+ 82%	+ 13%	+ 7%
as-cast + EC	19.6	3.7	28.2	24.5
	-62%	-9%	-48%	-52%
10 TCs	3.4	1.8	12.9	11.1
	+ 53%	+ 23%	+ 41%	+ 44%
10 TCs + EC	5.2	2.3	18.3	16.0
	+ 465%	+ 127%	+ 277%	+ 302%
annealed	19.3	4.2	48.8	44.6
	+ 72%	-42%	+ 4%	+ 8%
annealed + EC	33.2	2.4	50.8	48.3
H (GPa)	median	5th percentile	95th percentile	range
as-cast	6.4	6.1	6.6	0.5
	0%	+ 1%	+ 3%	+ 27%
as-cast + EC	6.4	6.2	6.8	0.7
	-1%	0%	0%	-6%
10 TC	6.3	6.1	6.6	0.5
	0%	-4%	+ 1%	+ 69%
10 TC + EC	6.3	5.9	6.7	0.8
	+ 9%	+ 8%	+ 8%	+ 10%
annealed	6.9	6.6	7.1	0.5
	0%	0%	0%	+ 4%
annealed + EC	6.9	6.6	7.1	0.5

Table B.1. *Continued.*

$E_{r,unloading}$ (GPa)	median	5th percentile	95th percentile	range
as-cast	104.5	101.9	106.8	4.9
	0%	0%	-1%	-28%
as-cast + EC	104.3	102.1	105.7	3.5
	+ 9%	+ 10%	+ 8%	-35%
10 TCs	113.6	111.7	114.9	3.2
	0%	-2%	+ 1%	+ 108%
10 TCs + EC	113.2	109.0	115.6	6.6
	+ 5%	+ 6%	+ 6%	+ 3%
annealed	119.4	118.2	121.4	3.3
	0%	-1%	0%	+ 32%
annealed + EC	119.1	117.1	121.4	4.3
$E_{r,Hertzian}$ (GPa)	median	5th percentile	95th percentile	range
as-cast	98.8	96.3	101.5	5.2
	0%	0%	-1%	-19%
as-cast + EC	99.0	96.4	100.7	4.2
	+ 1%	-2%	+ 3%	+ 94%
10 TC	99.5	94.3	104.4	10.1
	+ 3%	+ 2%	+ 2%	+ 3%
10 TC + EC	102.2	95.8	106.2	10.4
	+ 9%	+ 12%	+ 7%	-41%
annealed	108.2	105.2	111.2	6.0
	-1%	-10%	0%	+ 183%
annealed + EC	106.7	94.7	111.7	17.0

Appendix C : Additional Information on Chapter 6

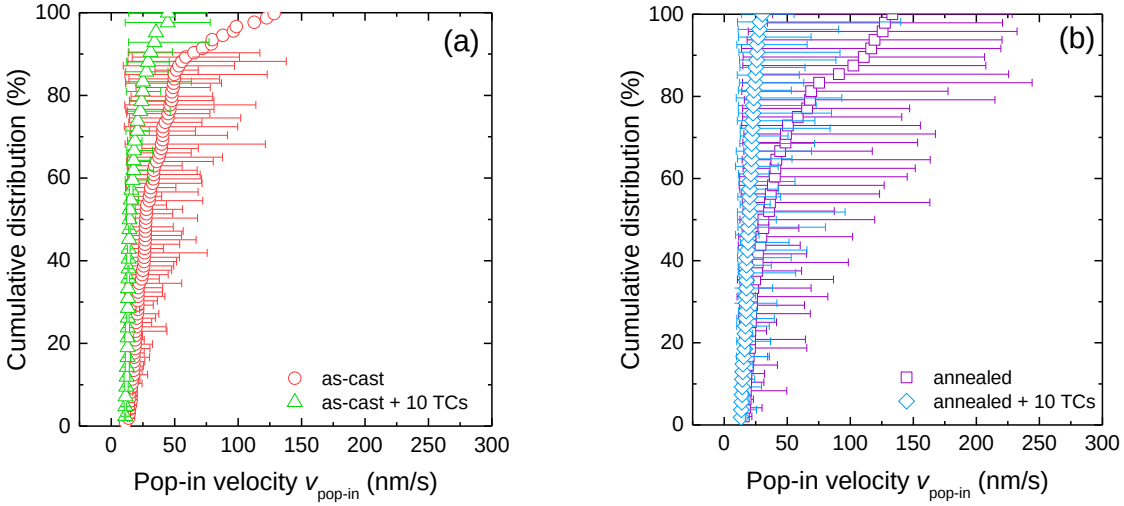

Fig. C.1. Velocity $v_{pop\text{-}in}$ of every individual pop-in, presented as cumulative distribution curves (where the data point is the mean $v_{pop\text{-}in}$ of a single indent, and the error bars are the minimum and maximum $v_{pop\text{-}in}$ found in that indentation curve) for the sample as-cast and after the first thermal cycling treatment (a), as well as after annealing and further thermal cycling (b).

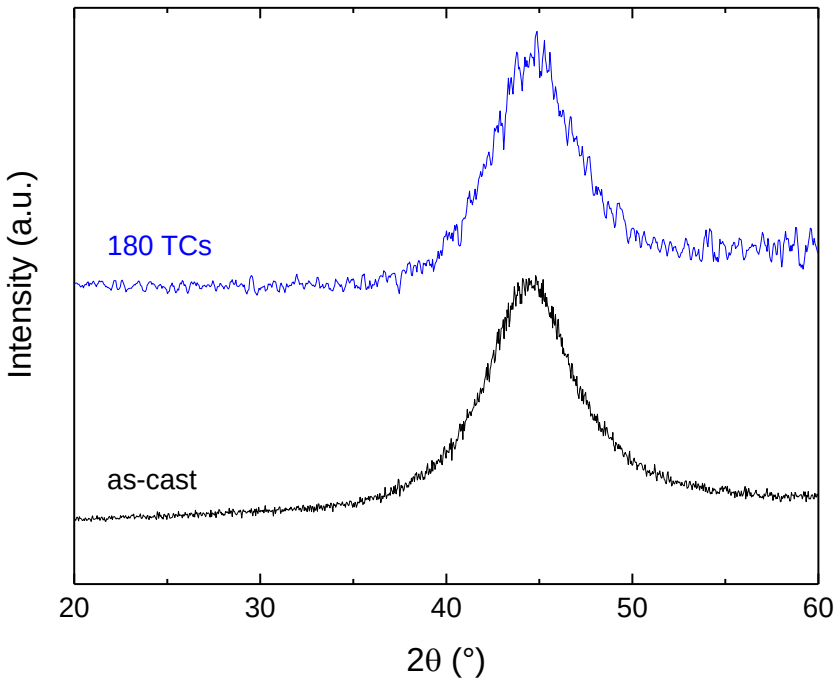

Fig. C.2. X-ray diffraction of the as-cast $Fe_{73.5}Cu_1Nb_3Si_{15.5}B_7$ ribbon and after 180 thermal cycles (TCs). In both cases, a broad diffraction maximum is observed, which is characteristic for amorphous structures.

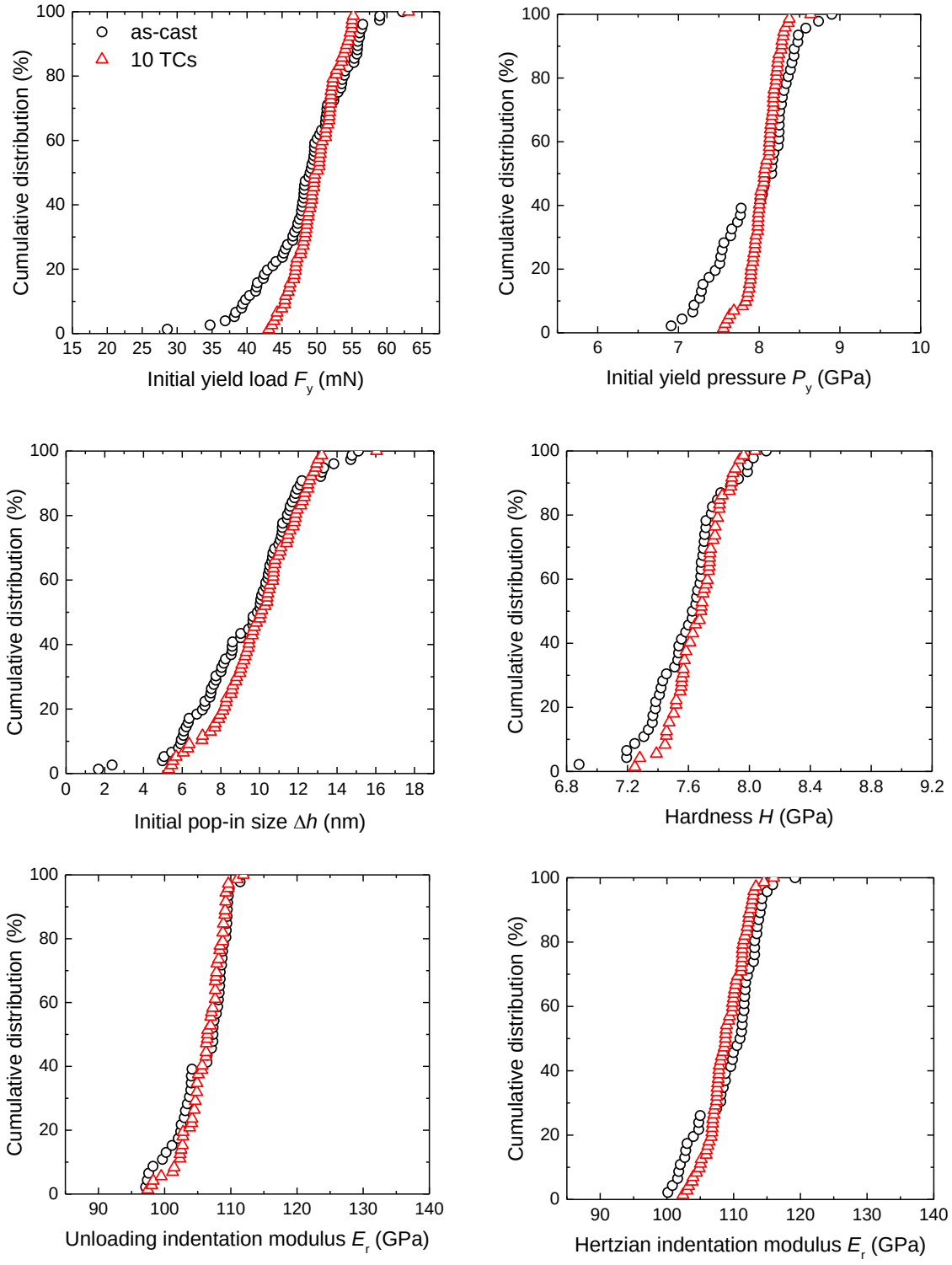

Fig. C.3. Cumulative distribution curves of the mechanical properties determined by spherical nanoindentation of a $Fe_{73.5}Cu_1Nb_3Si_{15.5}B_7$ metallic glass ribbon as-cast and after 10 thermal cycles.

Mössbauer spectroscopy of Fe-based ribbons

Mössbauer spectroscopy of the amorphous $Fe_{73.5}Cu_1Nb_3Si_{15.5}B_7$ ribbons was kindly performed by Prof. M. Miglierini from the Slovak University of Technology in Bratislava (Slovakia). Experimental details of the measurement, provided by him, are as follows: "Mössbauer spectra were recorded in transmission geometry at room temperature. Standard constant-acceleration driver equipped with a $^{57}Co(Rh)$ radioactive source was employed. Velocity calibration was accomplished by a 12.5 μm thick bcc-Fe foil. Isomer shifts are given with respect to a calibration Mössbauer spectrum recorded at room temperature. Analysis of the obtained spectra was performed by the Confit software [C1]."

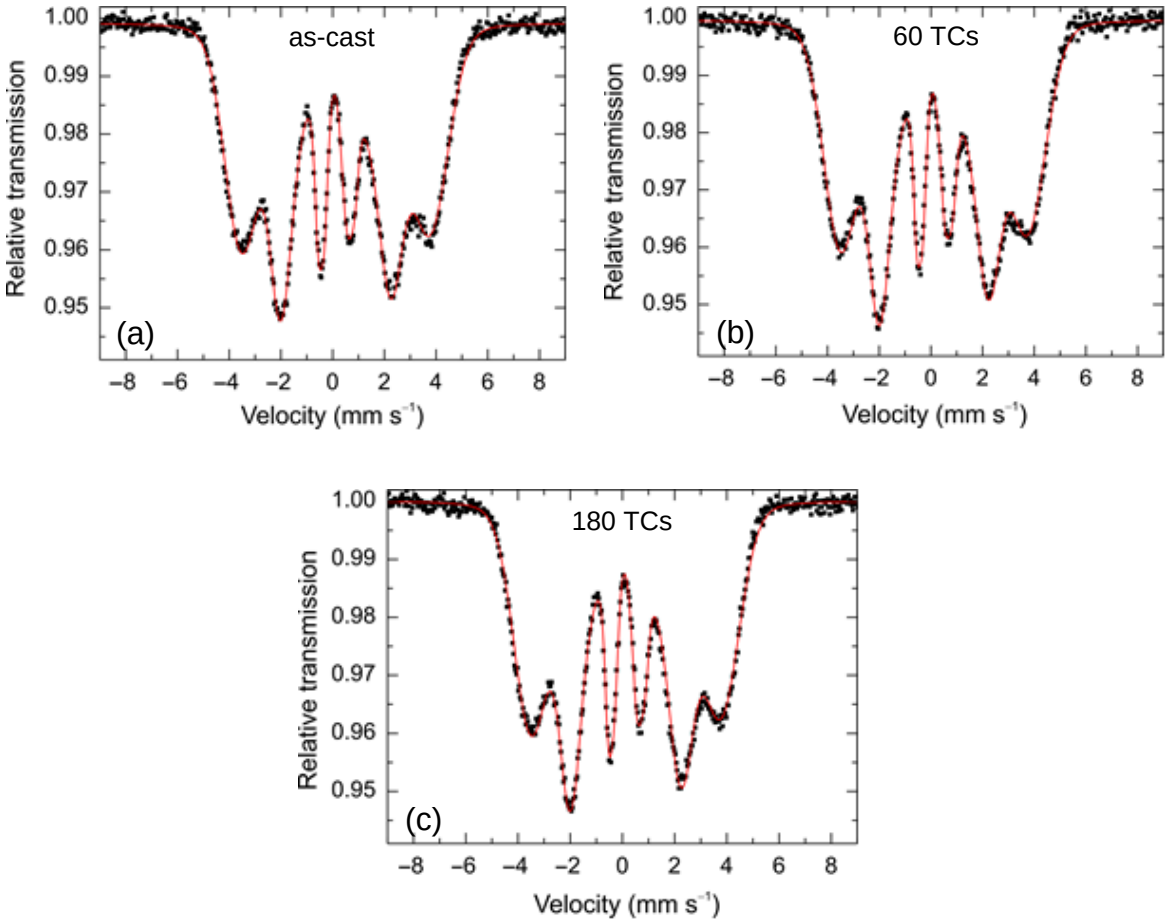

Fig. C.4. Mössbauer spectra of the amorphous $Fe_{73.5}Cu_1Nb_3Si_{15.5}B_7$ ribbon as-cast (a) and after 60 (b) and 180 (c) thermal cycles (TCs). The spectra indicate that the ribbon is amorphous and magnetically ordered, before as well as after thermal cycling.

[C1] T. Žák, Y. Jirásková, CONFIT: Mössbauer fitting program, *Surf. Interface Anal.* **38** (2006) 710–714.

Appendix D : Additional Information on Chapter 7

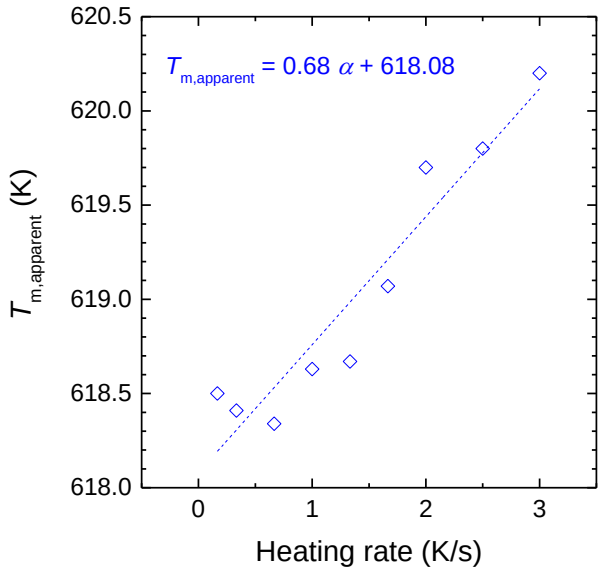

Fig. D.1. Apparent onset of melting temperature $T_{m,apparent}$ of the Au-based ribbon measured by conventional DSC in Chapter 7 at different heating rates α.

FDSC measurement of Au-based ribbons: temperature calibration

Temperature errors in FDSC may arise from errors in sensor calibration, thermal lag due to sample mass, which becomes important at higher heating rates, and from a bad contact between the sample and the sensor. The advantage of the Au-based metallic glass as a material to be measured by FDSC is that the onset of its melting, T_m, is well below the maximum-temperature limit and that it does not oxidise or evaporate easily, meaning that it can be repeatedly heated, melted and cooled without decomposing.

The melting point onsets T_m of pure metals are independent of the heating rate and can be used for temperature calibration. But in the case of the Au-based metallic glass, T_m measured during the first heating run cannot be reliably used for calibration, because at higher heating rates, different crystalline phases may form (though this was not shown here) which may lead to a different T_m. Furthermore, at very high rates, crystallization of the glass is avoided (Fig. D.2b), and no melting peak can be observed. Instead, T_m measured during the second heating run was used as calibration point.

After the first heating above melting, the sample was cooled always at the same rate of 100 K/s, thereby crystallizing the sample always in the same manner (Fig. D.2). During the second heating run, the melting point onset $T_{m(cryst.)}$ of this crystallized sample is measured, which should not depend on the heating rate and can be used for calibration.

$T_{m(cryst.)}$ was defined for more than 20 samples on two thoroughly pre-calibrated sensors; the average was 625 K. All FDSC curves of the Au-based samples were shifted in order for $T_{m(cryst.)}$ to be 625 K.

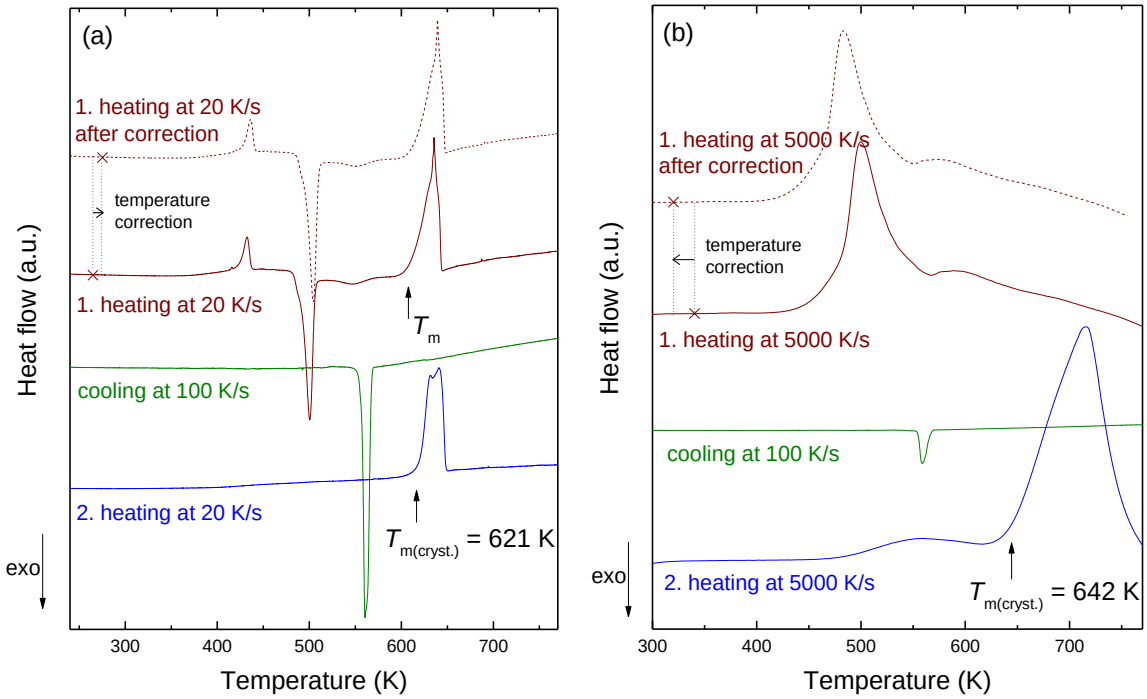

Fig. D.2. Example heat-flow curves of the heating – cooling – heating procedure during FDSC measurement of the aged Au-based ribbon. The samples were first heated at the desired heating rate. When measuring at 20 K/s (a), the glass transition occurred at around 420 K (during which a large overshoot is visible), followed by crystallization at around 480 K; melting started at around 610 K. But when heating the sample at 5000 K/s (b), only T_g and the overshoot are visible. At this heating rate, crystallization is avoided, meaning that the sample stayed in the liquid state and there is no melting peak. The sample crystallized upon cooling at 100 K/s. During the second heating run, the melting point onset $T_{m(cryst.)}$ of the crystallized sample could be measured for both heating rates. $T_{m(cryst.)}$ = 621 K in (a), meaning that the heating curves had to be corrected by +4 K, whereas in (b) $T_{m(cryst.)}$ = 642 K, and so a correction of −17 K was needed.

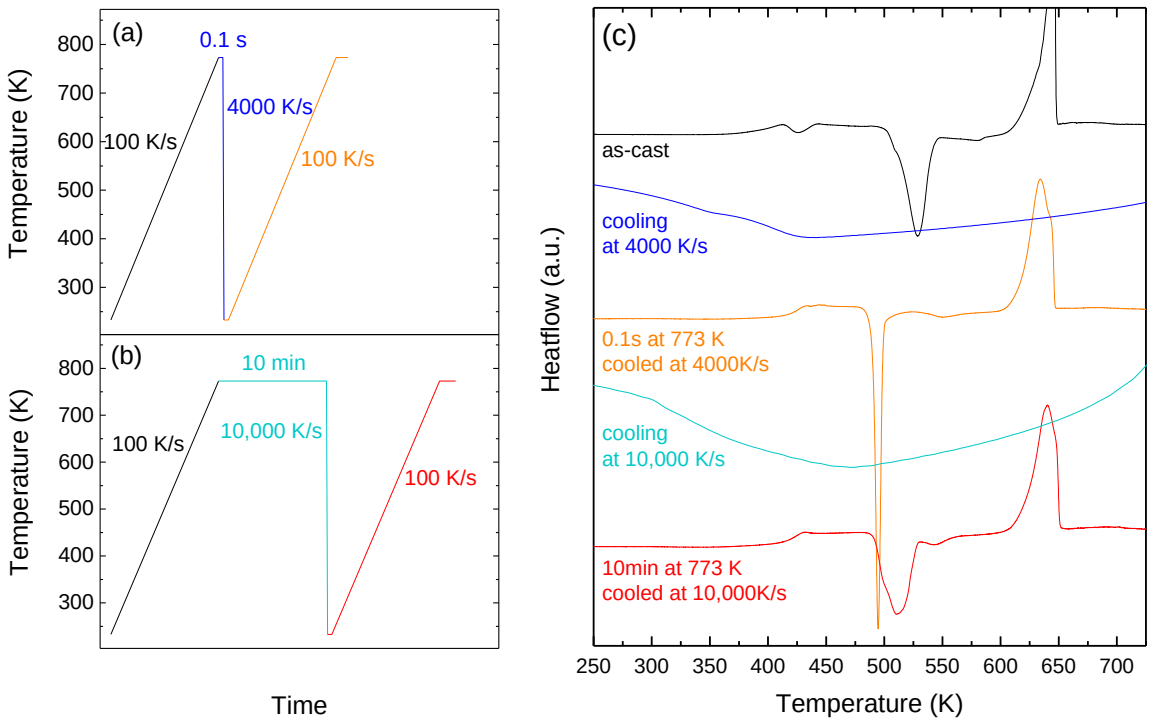

Fig. D.3. By heating the $Au_{49}Cu_{26.9}Si_{16.3}Ag_{5.5}Pd_{2.3}$ to 773 K into the liquid state, followed by rapid cooling, a fresh glass, called here "re-melted", can be formed by FDSC. The re-melted samples used for the results in Chapter 7 were formed according to the thermal history in (a). But even by cooling at 4000 K/s, which is above the critical cooling rate defined in ref.[D1] and during which no crystallization was observed on the DSC curve (c), the re-melted sample probably contained some crystals, since the crystallization peak occurred earlier and was sharper than for the as-cast sample. By keeping the melted sample at 773 K for longer (10 min instead of only 0.1 s) and by cooling faster (10,000 K/s instead of 4000 K/s), the crystallization peak was not as sharp and resembled more the as-cast one. However, even this re-melted sample contained some Pd–Si crystals, observed by transmission electron microscopy (not shown here).

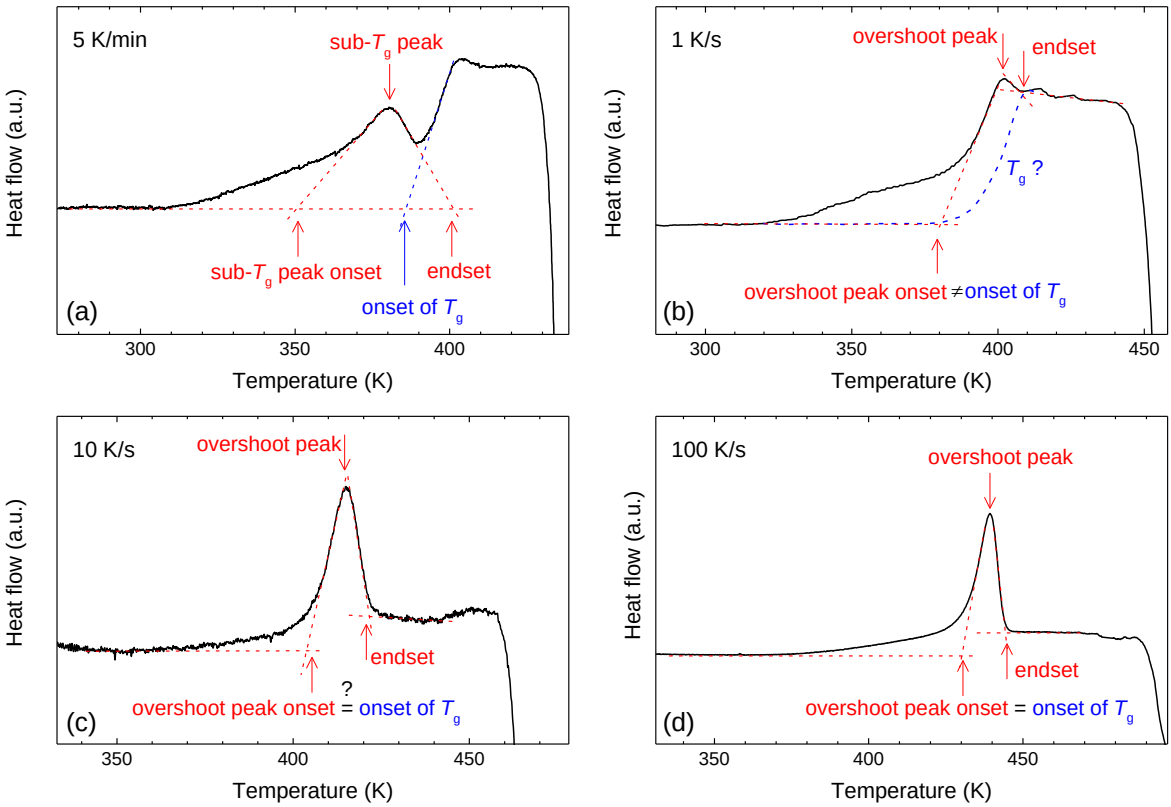

Fig. D.4. Examples of how the onset and endset temperatures of the endothermic sub-T_g or overshoot peak were determined, as well as the onset of T_g, in the case of the aged Au-based ribbon. If the sub-T_g peak is well below the glass-transition step, such as at 5 K/min (a), then the onset of T_g is easily defined. At higher heating rates, e.g. 1 K/s (b), this peak overlapped with the glass transition, and T_g is not visible. The overshoot peak onset in (b) can clearly not be also the onset of T_g, because otherwise T_g would decrease with increasing heating rate instead of increasing (see Fig. D.5). The blue dashed curve in (b) shows an assumption of where the glass transition may have occurred, if no sub-T_g peak/overshoot had been present. At 10 K/s (c), it is still not clear where T_g lies. At 100 K/s (d), the onsets of the overshoot peak and of T_g were assumed to be the same.

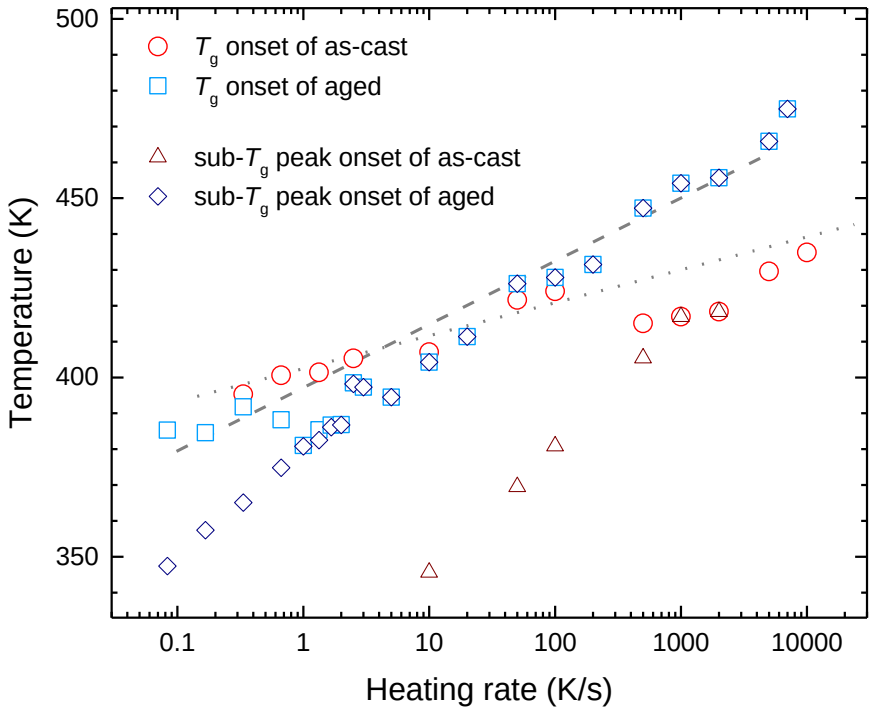

Fig. D.5. Onsets of the glass transition T_g and of the sub-T_g (or overshoot) peak as a function of heating rate, for the as-cast and aged Au-based metallic-glass ribbons. At some heating rates (e.g. at 1 K/s in the case of the aged ribbon), the apparent onset of T_g seemed to decrease with increasing heating rate, which is not possible. This is because the sub-T_g peak started overlapping with the glass transition, and the measured T_g onset value was therefore considered as not valid. At higher rates, T_g increased again. But it is not clear if T_g was still affected by the sub-T_g/overshoot peak or not. If it is assumed that T_g increases linearly with the logarithm of the heating rate (shown as dashed grey line), one can see that the T_g data points of the aged ribbon lie lower than expected in the range 0.667–20 K/s. From 50 K/s on, T_g returned to the line, and we assumed the measured onsets of T_g are valid again. In the case of the as-cast ribbon, the measured T_g decreased at 500 K/s. It is not clear if T_g of the as-cast sample follows the same trend as the aged sample (dashed line), implying that the as-cast values between 500–10,000 K/s were all influenced by the sub-T_g/overshoot peak, or if the as-cast T_g increases by a different degree with heating rate (following e.g. the dotted line), which would mean that the values at 5000 and 10,000 K/s are valid.

Determination of the activation energy of the recovery-annealing-induced rejuvenation

Several recent studies observed the relaxation of the metallic-glass composition $Au_{49}Cu_{26.9}Si_{16.3}Ag_{5.5}Pd_{2.3}$ through annealing below T_g [D2, D3, D4]. Fig. D.6a shows the decrease in energy obtained by Wang et al. [D4] upon sub-T_g annealing of this Au-based metallic glass. A relaxation time τ can be obtained for each annealing temperature T_a by fitting the data points with a stretched exponential Kohlrausch-Williams-Watts (KWW) function [D5]:

$$f(t) = f_0 \cdot \left(1 - \exp\left(-(t/\tau)^{\beta}\right)\right)$$

where f_0 is the value at equilibrium ($t \to \infty$) and $0 < \beta < 1$ is the stretching exponent. By knowing τ for various T_a, the activation energy E_a of this relaxation process can be obtained from the slope of $\ln \tau$ vs. $1/T_a$ (Fig. D.7), and was found to be around 192 ± 28 kJ/mol.

It would be interesting to know how the relaxation induced by conventional (sub-T_g) annealing compares to the recovery-annealing-induced rejuvenation observed in §7.3.2 for an aged Au-based metallic-glass ribbon. Therefore, even though the obtained data in §7.3.2 are quite sparse, a KWW fitting of the data was attempted (shown in dashed lines in Fig. D.6b). But an acceptable fitting, from which a reliable τ could be derived, was only obtained for 383 K, 403 K and 423 K. A linear fitting of these three points in Fig. D.7 would lead to an activation energy E_a of 119 ± 7 kJ/mol, which would imply that the recovery-annealing-induced rejuvenation was easier to activate than relaxation. But because only three points were obtained for our results in Fig. D.7, one may also well imagine that these points follow the same line as the relaxation data of Wang et al [D4]. Considering Wang et al.'s and our data together, an E_a of 178 ± 20 kJ/mol would be obtained (which is close to the E_a determined from only Wang et al.'s data). It is therefore not possible to conclude if there is a convincing difference between the two processes. But in any case, these energies seem broadly compatible with the activation energy of the disordering event $E_{sub\text{-}Tg} \approx 156$ kJ/mol of the aged ribbon determined from Fig. 7.6 in §7.3.1.

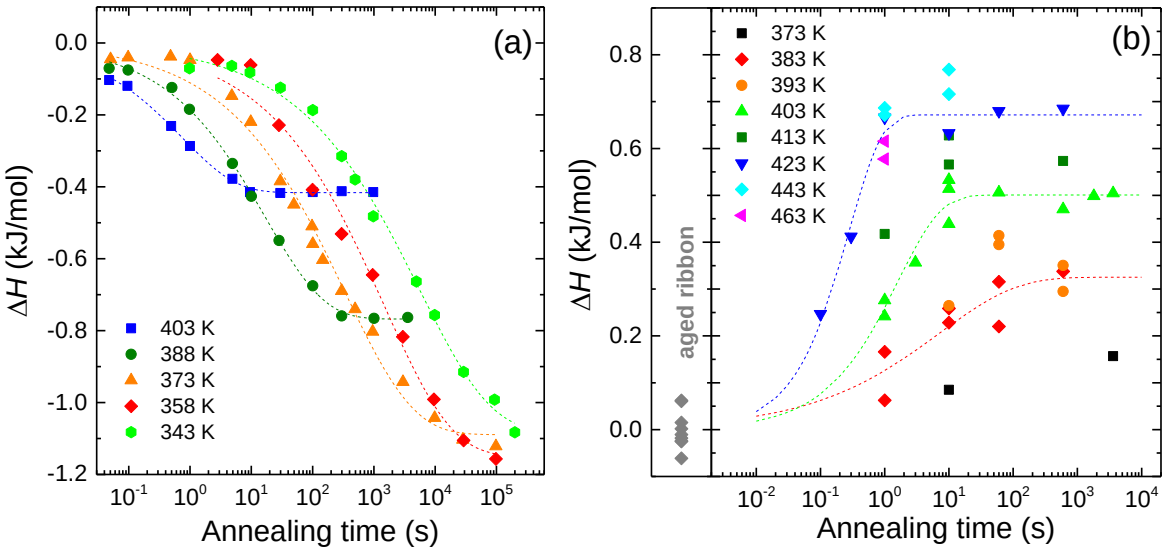

Fig. D.6. Decrease in enthalpy upon sub-T_g annealing given by Wang et al.[D4] (a), and increase upon annealing above the fictive temperature $T_{fictive}$ obtained in §7.3.2 (b). The data were fitted with a KWW function.

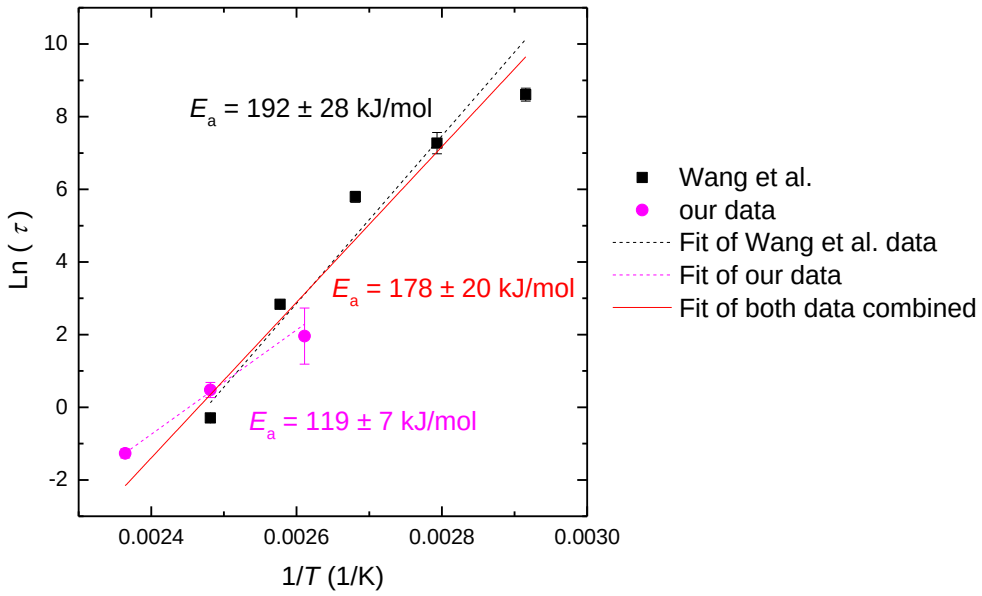

Fig. D.7. The relaxation times τ determined from the KWW fittings in Fig. D.6 are plotted as $\ln \tau$ vs. $1/T$ in order to estimate the activation energies E_a needed to decrease the energy of the glass upon sub-T_g annealing (Wang et al.'s data [D4]) and to increase the energy by recovery annealing (our data).

Estimation of the quench rate after annealing in oil of the aged Au-based ribbon

The $Au_{49}Cu_{26.9}Si_{16.3}Ag_{5.5}Pd_{2.3}$ aged metallic-glass ribbon used for nanoindentation measurements in §7.3.2 was annealed in oil, then quenched in water. The cooling rate during quenching was not measured, but can be estimated. FDSC measurements on this sample were made after annealing, after being stored at RT for 4 h as well as for 4 days. From these measurements, the increase in enthalpy ΔH compared to the aged sample and the fictive temperature $T_{fictive}$ were determined and are shown in Fig. D.8. But ΔH and $T_{fictive}$ of the sample directly after oil annealing are not known. The effect of RT ageing on the as-cast ribbon, as well as on the aged ribbon annealed in the FDSC for 10 s at 423 K, followed by cooling at 2 K/s, are also shown in Fig. D.8. By comparing the decrease in energy for these two samples with the oil-annealed sample, one can estimate that $\Delta H \approx 0.65$ kJ/mol and $T_{fictive} \approx 404$ K if no RT ageing had occurred. By placing these values into Fig. D.9, which shows the dependency of the degree of rejuvenation on cooling rate, one finds that the values of the oil-annealed sample correspond to a cooling rate of 30–200 K/s.

The quench rate can also be estimated by knowing that the rate of heat transfer $\dot{Q}$ is

$$\dot{Q} = h \cdot A \cdot (T_2 - T_1) = m \cdot C_p \cdot \mathrm{d}T/\mathrm{d}t$$

where h is the heat-transfer coefficient, A the surface through which heat is transferred between the sample and the water, T_2 and T_1 the temperatures of the sample (= 423 K) and of the water (= 293 K), m the sample mass (≈ 7 mg), C_p the heat capacity (≈ 40 J/mol K), and $\mathrm{d}T/\mathrm{d}t$ the cooling rate. Taking h to be 3000 W/m^2 K [D6], the calculated cooling rate would be ≈ 60 K/s, which is in the same order of magnitude as the cooling rates (10–20 K/s at 423 K) measured upon water quenching of steel probes by ref.[D6].

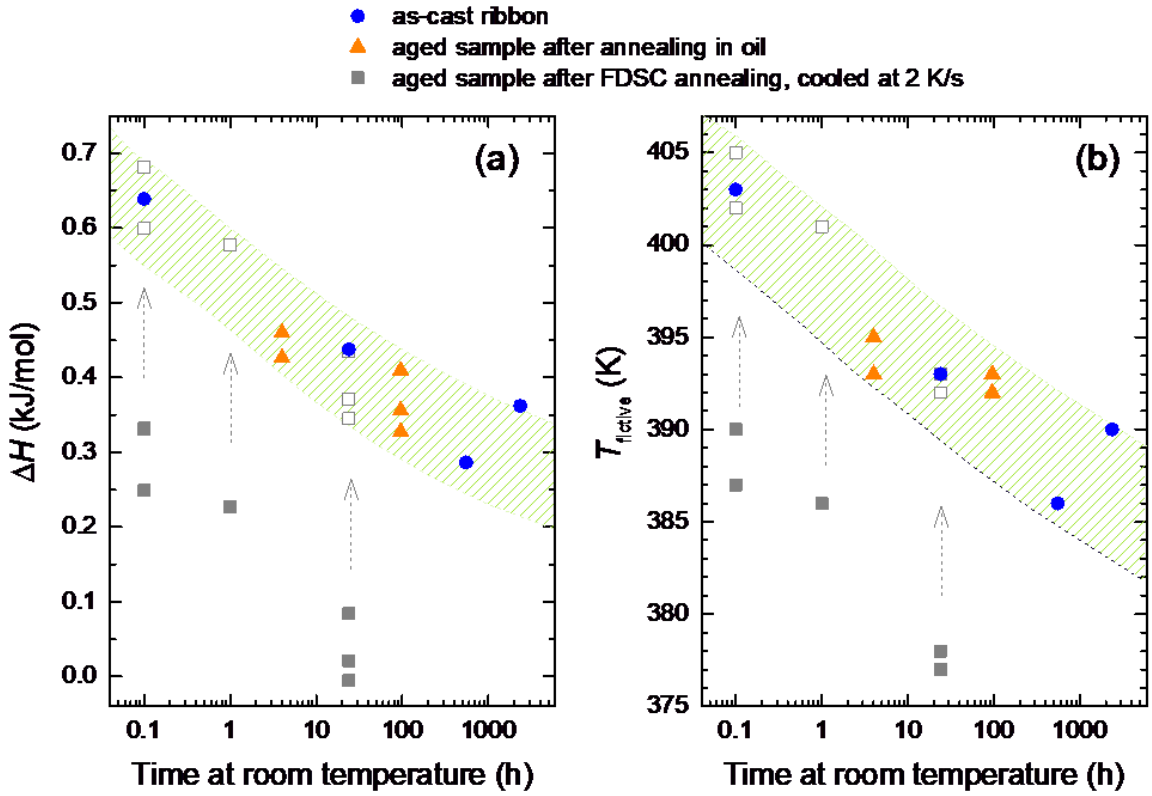

Fig. D.8. Effect of RT ageing on Δ*H* (a), which is the increase in enthalpy compared to the aged Au-based ribbon, and on the fictive temperature $T_{fictive}$ (b) of the oil-annealed sample, the as-cast sample, and the sample annealed for 10 s at 423 K and cooled at 2 K/s in the FDSC. By combining the data from the as-cast sample and from the FDSC-annealed sample (shifted upwards and shown as empty grey square symbols) with the data points of the oil-annealed sample, a trend can be estimated (shown by the shaded band). According to this trend, the oil-annealed sample should have $\Delta H \approx 0.65$ kJ/mol and $T_{fictive} \approx 404$ K if negligible RT ageing had occurred.

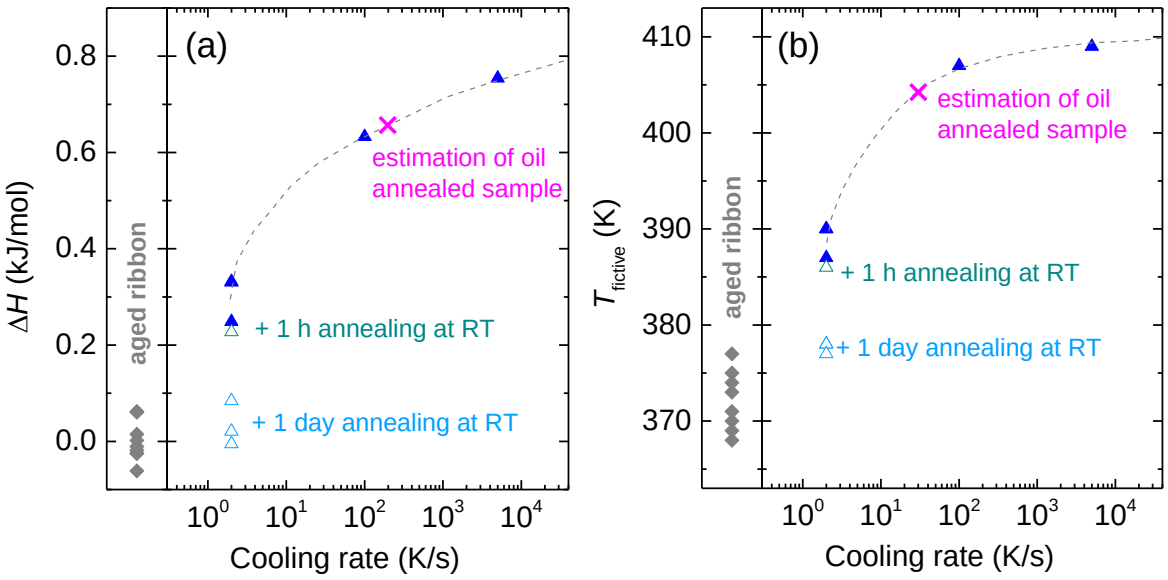

Fig. D.9. Effect of cooling rate on Δ*H* (a) and $T_{fictive}$ (b) after annealing the aged ribbon at 423 K for 10 s in the FDSC (blue triangle symbols). By placing the Δ*H* and $T_{fictive}$ values estimated for the oil-annealed sample (pink cross symbols) on the trend line (grey dashed curve), effective cooling rates of around 200 K/s (according to the Δ*H* value) and of 30 K/s (according to the $T_{fictive}$ value) are obtained.

[D1] S. Pogatscher, P.J. Uggowitzer, J. F. Löffler, In-situ probing of metallic glass formation and crystallization upon heating and cooling via fast differential scanning calorimetry, *Appl. Phys. Lett.* **104** (2014) 251908.

[D2] I. Gallino, D. Cangialosi, Z. Evenson, L. Schmitt, S. Hechler, M. Stolpe, B. Ruta, Hierarchical aging pathways and reversible fragile-to-strong transition upon annealing of a metallic glass former, *Acta Mater.* **144** (2018) 400–410.

[D3] L. Song, W. Xu, J. Huo, J.Q. Wang, X. Wang, R. Li, Two-step relaxations in metallic glasses during isothermal annealing, *Intermetallics* **93** (2018) 101–105.

[D4] J.Q. Wang, Y. Shen, J.H. Perepezko, M.D. Ediger, Increasing the kinetic stability of bulk metallic glasses, *Acta Mater.* **104** (2016) 25–32.

[D5] R. Busch, Z. Evenson, I. Gallino, S. Wei, 'Thermodynamics, Kinetics and Fragility of Bulk Metallic Glass Forming Liquids', in Fragility of Glass-forming Liquids, A.L. Greer, K. Kelton, S. Sastry. New Delhi: Hindustan Book Agency, 2014, 227–266.

[D6] H.S. Hasan, M.J. Peet, J.M. Jalil, H.K.D.H. Bhadeshia, Heat transfer coefficients during quenching of steels, *Heat Mass Transf.* **47** (2011) 315–321.